

9-15-2017

Characterization and Scaling Study of Energy Pathways in Small Four-Stroke Internal Combustion Engines

Jason R. Blantin

Follow this and additional works at: <https://scholar.afit.edu/etd>

Part of the [Aerospace Engineering Commons](#)

Recommended Citation

Blantin, Jason R., "Characterization and Scaling Study of Energy Pathways in Small Four-Stroke Internal Combustion Engines" (2017). *Theses and Dissertations*. 1732.
<https://scholar.afit.edu/etd/1732>

This Thesis is brought to you for free and open access by the Student Graduate Works at AFIT Scholar. It has been accepted for inclusion in Theses and Dissertations by an authorized administrator of AFIT Scholar. For more information, please contact richard.mansfield@afit.edu.



**CHARACTERIZATION AND SCALING STUDY OF ENERGY PATHWAYS IN
SMALL FOUR-STROKE INTERNAL COMBUSTION ENGINES**

THESIS

Jason R. Blantin, Captain, USAF

AFIT-ENY-MS-17-S-054

**DEPARTMENT OF THE AIR FORCE
AIR UNIVERSITY**

AIR FORCE INSTITUTE OF TECHNOLOGY

Wright-Patterson Air Force Base, Ohio

DISTRIBUTION STATEMENT A.
APPROVED FOR PUBLIC RELEASE; DISTRIBUTION UNLIMITED.

The views expressed in this thesis are those of the author and do not reflect the official policy or position of the United States Air Force, Department of Defense, or the United States Government. This material is declared a work of the U.S. Government and is not subject to copyright protection in the United States.

AFIT-ENY-MS-17-S-054

CHARACTERIZATION AND SCALING STUDY OF ENERGY PATHWAYS IN
SMALL FOUR-STROKE INTERNAL COMBUSTION ENGINES

THESIS

Presented to the Faculty

Department of Aeronautics and Astronautics

Graduate School of Engineering and Management

Air Force Institute of Technology

Air University

Air Education and Training Command

In Partial Fulfillment of the Requirements for the
Degree of Master of Science in Aeronautical Engineering

Jason R. Blantin, BS

Captain, USAF

August 2017

DISTRIBUTION STATEMENT A.
APPROVED FOR PUBLIC RELEASE; DISTRIBUTION UNLIMITED.

AFIT-ENY-MS-17-S-054

CHARACTERIZATION AND SCALING STUDY OF ENERGY PATHWAYS IN
SMALL FOUR-STROKE INTERNAL COMBUSTION ENGINES

Jason R. Blantin, BS

Captain, USAF

Committee Membership:

Dr. Marc D. Polanka
Chair

Maj James L. Rutledge, PhD
Member

Capt Adam L. Comer, PhD
Member

Abstract

A study of the efficiency and energy losses of a selection of five small (40 – 200 cm³ displacement) single cylinder, four-stroke engines was accomplished. The study was performed as part of a larger effort to improve the range and endurance of small internal combustion engines (ICE) that power Group II Unmanned Aerial Vehicles (UAVs). Little is known about the performance, efficiency, and allocation of energy losses for four-stroke ICEs in this size range. The goal of the study was to characterize these parameters for use in future research efforts. Three research objectives were developed to guide the study contained herein. The first objective was to reliably measure the brake power output of each engine and compare the measurements to the manufacturer's advertised power ratings. The second objective was to perform an energy balance, experimentally measuring the fuel energy entering the system (engine), and all of the energy exiting the system. Energy exiting the system was categorized as useable energy (brake power), or energy losses due to exhaust sensible enthalpy, thermal losses, or incomplete combustion. The third objective (which encompassed the first two) was to perform a series of parametric sweeps on the engines, examining the effects of varying engine speed, equivalence ratio, combustion phasing, cylinder head temperature, and throttle position. The characterization data from the five engines was then used to develop a set of correlations that could be used to predict brake mean effective pressure (BMEP), fuel conversion efficiency (η_f), exhaust sensible enthalpy losses, thermal (cooling load) losses, and incomplete combustion losses as a percentage of fuel energy

for small four-stroke engines with displacement volumes of 40 – 200 cm³. Accurate correlations for this size class currently do not exist in the literature.

Acknowledgments

I would like to sincerely express my deep gratitude to all those who have helped me to complete this goal. First and foremost, I would like to thank my wife Caren, who has provided unending support and encouragement, and who was the person who inspired me to undertake this endeavor in the first place. My deepest appreciation is also extended to my research advisor, Dr. Marc Polanka, for his guidance and wisdom. I would also like to thank many individuals at AFRL/RQTC for supporting this effort by providing the laboratory facilities and expertise necessary to complete the research. This group includes but is not limited to Capt Joseph Ausserer, PhD, Mr. Paul Litke, Mr. Jacob Baranski, Dr. John Hoke, Dr. Fred Schauer, Mr. Rich Ryman, and Mr. Matthew Rice.

Capt Jason R. Blantin

Table of Contents

	Page
Abstract.....	1
Table of Contents	4
List of Figures	6
List of Tables	16
Abbreviations	18
Nomenclature.....	20
1. Introduction	23
1.1. General Issue	23
1.2. Research Objectives	25
1.3. Organization	26
2. Literature Review.....	28
Chapter Overview	28
2.1. ICE Classification	28
2.2. ICE Geometry.....	31
2.3. ICE Operation.....	32
2.4. Relevant Research In Small ICE Testing	52
3. Methodology.....	63
Chapter Overview	63
3.1. Small Engine Research Bench (SERB).....	63
3.2. Engine Selection and Preparation	75
3.3. Energy Balance Methodology	78
3.4. Experimental Uncertainty.....	87

3.5.	Repeatability	97
4.	Analysis and Results	100
	Chapter Overview	100
4.1.	GX120	100
4.2.	GX120, GX160, GX200.....	136
4.3.	GF40, TP70	180
5.	Conclusions and Recommendations	219
	Chapter Overview	219
5.1.	Research Objectives	219
5.2.	Key Findings and Conclusions	222
5.3.	Recommendations for Future Research	223
	Appendix A.....	225
	Bibliography	235

List of Figures

	Page
Figure 1. The four-stroke engine operating cycle. Images courtesy of https://www.grc.nasa.gov	30
Figure 2. The two-stroke engine operating cycle. Image courtesy of https://www.britannica.com	31
Figure 3. ICE engine geometry. Adapted from Heywood [11].	32
Figure 4. Valve lift (L_v) and in-cylinder pressure (p) versus crank angle (θ) for a typical four-stroke ICE. Figure adapted from Heywood [11].	35
Figure 5. In-cylinder pressure versus crank angle for a loop-scavenged two-stroke engine. Figure adapted from Taylor [12].	36
Figure 6. Piston Ring Crevices (from Heywood) [11].	38
Figure 7. Effect of engine speed on flame development angle ($\Delta\theta_d$) and overall burning angle ($\Delta\theta_o$). Adapted from Heywood [11].	40
Figure 8. (a) In cylinder pressure versus crank angle for ignition timing of 50° , 30° , and 10° bTDC. (b) Brake torque versus ignition timing at constant speed [14].	42
Figure 9. Exhaust gas species concentration of a typical SI engine as a function of equivalence ratio [11].....	47
Figure 10. Combustion efficiency as a function of equivalence ratio [11].	49
Figure 11. Performance map of a typical automotive SI ICE [12].	51
Figure 12. Menon and Cadou BMEP plot [9].	58
Figure 13. Menon and Cadou fuel conversion efficiency plot [9].	59

Figure 14. Small engine research bench (SERB) schematic.	64
Figure 15. Small engine research bench (SERB) photograph.	65
Figure 16. Engine air intake of the SERB. Intake air is inducted through a parallel array of three TSI flow meters.	66
Figure 17. SERB exhaust manifold for measuring exhaust pressure and temperature and taking exhaust samples.....	68
Figure 18. SERB drivetrain schematic.	71
Figure 19. SERB cooling subsystem schematic.....	72
Figure 20. The SERB engine cooling air enclosure.....	73
Figure 21. Honda GX120 in stock configuration (left), and as tested on the SERB (right).	78
Figure 22. Power dissipation by SERB drivetrain measured as the difference between power delivered at the electric motor cradle and power dissipated at the dynamometer. For the fit, $R^2=0.96$ [10].....	80
Figure 23. GC-TCD calibration curve for nitrogen.....	84
Figure 24. GC-TCD calibration curve for carbon monoxide.....	85
Figure 25. GC-TCD calibration curve for hydrogen.....	85
Figure 26. GC-TCD calibration curve for oxygen.	86
Figure 27. Repeatability of GX120 engine.....	98
Figure 28. SERB exhaust validation plot from Ausserer [10].....	101
Figure 29. SERB exhaust validation plot from GX120 engine.	103

Figure 30. GX120 power curve with the SERB exhaust versus the manufacturer's advertised power curve.	105
Figure 31. GX120 power curve with the SERB exhaust and stock exhaust versus the manufacturer's advertised power curve.	106
Figure 32. GX120 speed sweep energy pathways (in kW).	107
Figure 33. GX120 speed sweep incomplete combustion losses.	108
Figure 34. GX120 speed sweep IMEP and CoV of IMEP.	110
Figure 35. GX120 speed sweep combustion phasing.....	111
Figure 36. GX120 speed sweep combustion duration.....	112
Figure 37. Honda GX120 speed sweep energy balance.	114
Figure 38. GX120 equivalence ratio sweep energy pathways (in kW).....	116
Figure 39. GX120 equivalence ratio sweep IMEP and CoV of IMEP.....	117
Figure 40. GX120 equivalence ratio sweep combustion phasing.....	118
Figure 41. GX120 equivalence ratio sweep combustion duration.	119
Figure 42. Honda GX120 equivalence ratio sweep energy balance.	120
Figure 43. GX120 combustion phasing sweep energy pathways (in kW).	122
Figure 44. GX120 combustion phasing sweep IMEP and CoV of IMEP.	123
Figure 45. GX120 combustion phasing sweep combustion phasing.	124
Figure 46. GX120 combustion phasing sweep combustion duration.....	124
Figure 47. GX120 combustion phasing energy balance.....	125
Figure 48. GX120 cooling load sweep cooling air speed versus cylinder head temperature.....	126

Figure 49. GX120 cooling load sweep energy pathways (in kW).	127
Figure 50. GX120 cooling load sweep IMEP and CoV of IMEP.....	128
Figure 51. Honda GX120 cooling load sweep energy balance.....	129
Figure 52. GX120 throttle sweep volumetric efficiency versus mass flow rate of intake air.	130
Figure 53. GX120 throttle sweep energy pathways (in kW).	132
Figure 54. GX120 throttle sweep H ₂ and CO concentration in exhaust gases.	133
Figure 55. GX120 throttle sweep IMEP and CoV of IMEP.....	134
Figure 56. GX120 throttle sweep combustion phasing.	134
Figure 57. GX120 throttle sweep combustion duration.	135
Figure 58. GX120 throttle sweep energy balance.....	136
Figure 59. GX160 and GX200 power curves with the SERB exhaust versus the manufacturer's advertised power curves.....	138
Figure 60. GX160 speed sweep using various equipment configurations.	139
Figure 61. Combined speed sweep energy pathways (in kW).....	140
Figure 62. Combined speed sweep IMEP and CoV of IMEP.	141
Figure 63. Combined speed sweep combustion phasing and combustion duration.....	142
Figure 64. GX160 speed sweep energy balance.	143
Figure 65. GX200 speed sweep energy balance.	143
Figure 66. Combined speed sweep percentage of fuel energy in each energy pathway.	145
Figure 67. BMEP and fuel conversion efficiency (η_f) at peak power versus displacement volume for the Honda GX120, GX160, and GX200 engines.	146

Figure 68. Menon and Cadou BMEP versus displacement plot [9] with data points from the Honda GX120, GX160, and GX200 added in red.	147
Figure 69. Menon and Cadou fuel conversion efficiency versus displacement plot [9] with data points from the Honda GX120, GX160, and GX200 added in red.	147
Figure 70. Mean piston speed versus engine speed for the Honda GX120, GX160 and GX200 engines.	148
Figure 71. Fuel conversion efficiency as a function of mean piston speed and displacement volume.	149
Figure 72. BMEP as a function of mean piston speed and displacement volume.	150
Figure 73. GX160 equivalence ratio sweep energy balance.....	152
Figure 74. GX200 equivalence ratio sweep energy balance.....	152
Figure 75. Combined equivalence ratio sweep energy pathways (in kW).	154
Figure 76. Combined equivalence ratio sweep IMEP and CoV of IMEP.....	155
Figure 77. Combined equivalence ratio sweep combustion phasing and combustion duration.	156
Figure 78. Combined equivalence ratio sweep percentage of fuel energy in each energy pathway.	157
Figure 79. Fuel conversion efficiency as a function of equivalence ratio and displacement volume.	158
Figure 80. BMEP as a function of equivalence ratio and displacement volume.	159
Figure 81. GX160 combustion phasing sweep energy balance.	160
Figure 82. GX200 combustion phasing sweep energy balance.	161

Figure 83. Combined combustion phasing sweep energy pathways (in kW).....	162
Figure 84. Combined combustion phasing sweep IMEP and CoV of IMEP.	163
Figure 85. Combined combustion phasing sweep combustion phasing and combustion duration.	164
Figure 86. Combined combustion phasing sweep percentage of fuel energy in each energy pathway.....	164
Figure 87. Fuel conversion efficiency and BMEP as functions of CA50 and displacement volume.....	165
Figure 88. Equivalent air speed of cooling air versus cylinder head temperature for the Honda GX120, GX160, and GX200 engines.	167
Figure 89. GX160 cooling load sweep energy balance.....	168
Figure 90. GX200 cooling load sweep energy balance.....	169
Figure 91. Average BMEP versus displacement volume for the combined cooling load sweeps.	170
Figure 92. Average brake power, exhaust enthalpy, cooling load, and incomplete combustion losses as a percentage of fuel energy versus displacement volume for the combined cooling load sweeps.....	171
Figure 93. Combined throttle sweep volumetric efficiency versus mass flow rate of intake air.....	173
Figure 94. GX160 throttle sweep energy balance.....	174
Figure 95. GX200 throttle sweep energy balance.....	174
Figure 96. Combined throttle sweep energy pathways (in kW).	175

Figure 97. Combined throttle sweep IMEP and CoV of IMEP.....	176
Figure 98. Combined throttle sweep combustion phasing and combustion duration. ...	177
Figure 99. Combined throttle sweep percentage of fuel energy in each energy pathway.	178
Figure 100. Fuel conversion efficiency and BMEP as functions of volumetric efficiency and displacement volume.	179
Figure 101. OS GF40 and Torqpro TP70 engines.	181
Figure 102. GF40 and TP70 power curves with the SERB exhaust versus the manufacturer’s advertised power curves.....	182
Figure 103. Combined GF40 and TP70 speed sweep IMEP and CoV of IMEP.	183
Figure 104. Mean piston speed (m/s) versus engine speed (rpm) for the GF40 and TP70 engines.....	184
Figure 105. Combined GF40 and TP70 speed sweep energy pathways (in kW).	185
Figure 106. Combined GF40 and TP70 speed sweep combustion phasing and combustion duration.....	186
Figure 107. GF40 speed sweep energy balance.	187
Figure 108. TP70 speed sweep energy balance.	187
Figure 109. Combined GF40 and TP70 speed sweep percentage of fuel energy in each energy pathway.....	188
Figure 110. BMEP and fuel conversion efficiency (η_f) at peak power versus displacement volume for the GF40, TP70, GX120, GX160, and GX200 engines. .	189

Figure 111. Menon and Cadou BMEP versus displacement plot [9] with data points from the GF40, TP70, GX120, GX160, and GX200 added in red.	190
Figure 112. Menon and Cadou fuel conversion efficiency versus displacement plot [9] with data points from the GF40, TP70, GX120, GX160, and GX200 added in red.	191
Figure 113. Fuel conversion efficiency and BMEP for the GF40, TP70, GX120, GX160, and GX200 engines as functions of mean piston speed and displacement volume..	192
Figure 114. GF40 equivalence ratio sweep energy balance.	194
Figure 115. TP70 equivalence ratio sweep energy balance.....	194
Figure 116. Combined GF40 and TP70 equivalence ratio sweep IMEP and CoV of IMEP.	196
Figure 117. Combined equivalence ratio sweep combustion phasing and combustion duration.	197
Figure 118. Combined GF40 and TP70 equivalence ratio sweep percentage of fuel energy in each energy pathway.	198
Figure 119. Fuel conversion efficiency and BMEP as functions of equivalence ratio and displacement volume.	199
Figure 120. GF40 combustion phasing sweep energy balance.....	201
Figure 121. TP70 combustion phasing sweep energy balance.	201
Figure 122. Combined GF40 and TP70 combustion phasing sweep IMEP and CoV of IMEP.	202
Figure 123. Combined GF40 and TP70 combustion phasing sweep percentage of fuel energy in each energy pathway.	204

Figure 124. Fuel conversion efficiency and BMEP as functions of CA50 and displacement volume.	205
Figure 125. Equivalent air speed of cooling air versus cylinder head temperature for the GF40 and TP70 engines.	207
Figure 126. GF40 cooling load sweep energy balance.....	208
Figure 127. TP70 cooling load sweep energy balance.	208
Figure 128. Average BMEP versus displacement volume for the cooling load sweeps of all five engines.....	209
Figure 129. Average brake power, exhaust enthalpy, cooling load, and incomplete combustion losses as a percentage of fuel energy versus displacement volume for the combined cooling load sweeps of all five engines.	210
Figure 130. Combined GF40 and TP70 throttle sweep volumetric efficiency versus mass flow rate of intake air.	212
Figure 131. GF40 throttle sweep energy balance.....	213
Figure 132. TP70 throttle sweep energy balance.	213
Figure 133. Combined GF40 and TP70 throttle sweep energy pathways (in kW).....	214
Figure 134. Combined GF40 and TP70 throttle sweep IMEP and CoV of IMEP.....	215
Figure 135. Combined GF40 and TP70 throttle sweep combustion phasing and combustion duration.....	216
Figure 136. Combined GF40 and TP70 throttle sweep percentage of fuel energy in each energy pathway.....	216

Figure 137. Fuel conversion efficiency and BMEP as functions of volumetric efficiency and displacement volume for all five engines.217

List of Tables

	Page
Table 1. Typical air-to-fuel ratio (AFR) and equivalence ratio (ϕ) of SI engines operating on gasoline fuel and CI engines operating on Diesel fuel [11].....	34
Table 2. Typical BMEP values of automotive ICES [11].....	44
Table 3. Test engine design and performance characteristics.....	77
Table 4. Repeatability analysis results for GX120 engine.	99
Table 5. BMEP and η_f coefficients for use with Equation (60).....	150
Table 6. Exhaust enthalpy, cooling load, and incomplete combustion losses as a percentage of fuel energy coefficients for use with Equation (60).....	151
Table 7. BMEP, η_f , exhaust enthalpy, cooling load, and incomplete combustion losses as a percentage of fuel energy coefficients for use with Equation (61).....	159
Table 8. BMEP, η_f , exhaust enthalpy, cooling load, and incomplete combustion losses as a percentage of fuel energy coefficients for use with Equation (62).....	166
Table 9. BMEP, η_f , exhaust enthalpy, cooling load, and incomplete combustion losses as a percentage of fuel energy coefficients for use with Equation (63).....	171
Table 10. BMEP, η_f , exhaust enthalpy, cooling load, and incomplete combustion losses as a percentage of fuel energy coefficients for use with Equation (64).....	180
Table 11. BMEP, η_f , exhaust enthalpy, cooling load, and incomplete combustion losses as a percentage of fuel energy coefficients for use with Equation (60).....	193
Table 12. BMEP, η_f , exhaust enthalpy, cooling load, and incomplete combustion losses as a percentage of fuel energy coefficients for use with Equation (61).....	200

Table 13. BMEP, η_f , exhaust enthalpy, cooling load, and incomplete combustion losses
as a percentage of fuel energy coefficients for use with Equation (62).....206

Table 14. BMEP, η_f , exhaust enthalpy, cooling load, and incomplete combustion losses
as a percentage of fuel energy coefficients for use with Equation (63).....210

Table 15. BMEP, η_f , exhaust enthalpy, cooling load, and incomplete combustion losses
as a percentage of fuel energy coefficients for use with Equation (64).....218

Abbreviations

AFIT	Air Force Institute of Technology
AFR	Air to Fuel Ratio
AFRL	Air Force Research Laboratory
AKI	Anti-Knock Index
ANSI	American National Standards Institute
aTDC	After Top Dead Center
BC	Bottom Center
BDC	Bottom Dead Center
BHP	Brake Horsepower
BMEP	Brake mean effective pressure
BSFC	Brake Specific Fuel Consumption
bTDC	Before Top Dead Center
BTE	Brake Thermal Efficiency
CA	Crank Angle
CFR	Cooperative Fuels Research
CHT	Cylinder Head Temperature
CI	Compression Ignition
DOF	Degrees of Freedom
ECU	Engine Control Unit
EFI	Electronic Fuel Injection
EFI	Electronic Fuel Injection
EGR	Exhaust Gas Recirculation
EGT	Exhaust Gas Temperature
EPC	Exhaust Port Close
EPO	Exhaust Port Open
EVC	Exhaust Valve Close
EVO	Exhaust Valve Open
FAR	Fuel to Air Ratio
FID	Flame Ionization Detector
GC	Gas Chromatograph
GPIB	General Purpose Interface Bus
HC	Hydrocarbon
HP	Horsepower
ICE	Internal Combustion Engine
IMEP	Indicated Mean Effective Pressure
IPC	Intake Port Close

IPO	Intake Port Open
ISFC	Indicated Specific Fuel Consumption
ITE	Indicated Thermal Efficiency
IVC	Intake Valve Close
IVO	Intake Valve Open
LSDAQ	Low Speed Data Acquisition
MBT	Maximum Brake Torque
MW	Molecular Weight
NI	National Instruments
NIST	National Institute of Standards and Technology
PFI	Port Fuel Injection
PLC	Programmable Logic Controller
PRF	Primary Reference Fuel
RMS	Root Mean Squared
RPA	Remotely Piloted Aircraft
RPM	Revolutions per Minute
RSS	Root-Sum-Square
RTD	Resistance Temperature Detector
SERB	Small Engine Research Bench
SERL	Small Engine Research Laboratory
SFC	Specific Fuel Consumption
SI	Spark Ignition
SLPM	Standard Liters per Minute
STP	Standard Temperature and Pressure
TC	Top Center
TCD	Thermal Conductivity Detector
TDC	Top Dead Center
UAV	Unmanned Aerial Vehicle
UHC	Unburned Hydrocarbon
USAF	United States Air Force
VDC	Volts Direct Current
WOT	Wide Open Throttle

Nomenclature

a	Radius, crank (m)
B	Bore (m)
CA10	Crank angle, 10% fuel burned
CA50	Crank angle, 50% fuel burned
CA90	Crank angle, 90% fuel burned
C_p	Specific heat, constant pressure (J/mol-K)
h_a	Specific enthalpy, air (J/kg)
h_c	Specific enthalpy, combustion (J/kg)
h_f	Specific enthalpy, fuel (J/kg)
\tilde{h}_f^o	Enthalpy of formation, “ith” species (J/kg)
H_P	Enthalpy, products (J)
H_R	Enthalpy, reactants (J)
l	Length, connecting rod (m)
L	Stroke (m)
L_v	Lift, valve (m)
m_a	Mass of air (kg)
m_f	Mass of fuel (kg)
\dot{m}_a	Mass flow rate, air (kg/s)
\dot{m}_{cool}	Mass flow rate, cooling air (kg/s)
\dot{m}_f	Mass flow rate, fuel (kg/s)
\dot{m}_i	Mass flow rate, “ith” species (kg/s)
n	Polytropic exponent
n_i	Number of moles, “ith” species (kg/s)
n_R	Number of crank revolutions for each power stroke
\dot{n}_{ex}	Molar flow rate, exhaust (mol/s)
N	Engine speed (rpm)
p	Pressure (N/m ²)
p_e	Pressure, exhaust (N/m ²)
p_f	Pressure, end of combustion (N/m ²)
p_i	Pressure, intake (N/m ²)
p_o	Pressure, spark (N/m ²)
P	Power (W)
P_b	Power, brake (W)
P_I	Power, indicated (W)
Q_{exh}	Energy, exhaust sensible enthalpy (J)

Q_f	Energy, friction (J)
Q_{in}	Energy entering a system (J)
Q_{inc}	Energy, incomplete combustion (J)
$Q_{l,tot}$	Total energy loss of a system (J)
Q_{LHV}	Lower heating value (J/kg)
Q_{sc}	Energy, short circuiting (J)
Q_{th}	Energy, thermal (J)
\dot{Q}_{in}	Energy entering a system per unit time (W)
$\dot{Q}_{l,tot}$	Total energy loss of a system per unit time (W)
r_c	Compression ratio
\bar{S}_p	Speed, mean piston (m/s)
T_A	Temperature, ambient (°)
v_{exh}	Valve, exhaust
v_{int}	Valve, intake
V	Volume (m ³)
V_c	Volume, clearance (m ³)
V_d	Volume, displacement (m ³)
V_f	Volume, end of combustion (m ³)
V_o	Volume, spark (m ³)
W_{out}	Useful work done by a system (J)

Greek

γ	Polytropic exponent
γ_b	Polytropic exponent, burned mixture
γ_u	Polytropic exponent, unburned mixture
δ	Error, absolute
Δ	Change
$\Delta\theta_b$	Angle, rapid burning (°)
$\Delta\theta_d$	Angle, flame development (°)
$\Delta\theta_o$	Angle, overall burning (°)
ε	Error, relative
η_c	Efficiency, combustion
η_f	Efficiency, fuel conversion
η_m	Efficiency, mechanical
η_{th}	Efficiency, thermal
η_v	Efficiency, volumetric
θ	Crank angle (°)

λ	Relative air/fuel ratio
$\rho_{a,i}$	Density, intake air (kg/m ³)
τ	Torque (N-m)
τ_b	Torque, brake (N-m)
ϕ	Equivalence ratio
χ	Mass fraction
χ_b	Mass fraction, fuel burned

CHARACTERIZATION AND SCALING STUDY OF ENERGY PATHWAYS IN SMALL FOUR-STROKE INTERNAL COMBUSTION ENGINES

1. Introduction

1.1. General Issue

Globally, the unmanned aerial vehicle (UAV) or remotely piloted aircraft (RPA), market is growing at an exponential pace. Recent estimates have forecasted economic impact from the UAV market to be anywhere from \$82 to \$85 billion per year by 2025 in the United States alone [1, 2]. The United States Air Force (USAF) considers RPA technology to be vitally important to its Global Integrated Intelligence, Surveillance, & Reconnaissance (ISR) Operations [3]. Recently, Air Force Research Laboratory (AFRL), the research and development (R&D) branch of the USAF, has been tasked with studying the power, efficiency, and alternative fuel exploration for Group II (10 – 25 kg) UAVs. These studies are to be used to facilitate improvements in the design and implementation of future propulsion methods for Group II UAVs. More powerful and efficient propulsion systems has a direct impact on the capabilities of these small aircraft, improving range and endurance. Small improvements, often considered negligible to the individual, can add up to massive savings when they are scaled up and implemented department wide across the entire USAF or Department of Defense (DoD). For the last decade, research into UAV propulsion has been mentioned as key focus areas in several high level government reports [4-6].

Typically, Group II UAVs are powered by electric motors or small internal combustion engines (ICEs). For the purposes of this study the term “small ICEs” will

refer to internal combustion engines with displacement volumes of 200 cm³ or less. Both of these propulsion systems have their own unique advantages and disadvantages. Electric motors are quiet and highly efficient, typically converting 80 – 90% of the electrical energy provided to the engine into mechanical energy useful for propulsion. Small ICEs have a much lower energy conversion efficiency, which can be anywhere from approximately 4 – 25% [7-9], but they tend to offer much higher endurance and range when used to power small UAVs. This critical difference stems from the difference in the specific energy of batteries versus hydrocarbon (HC) fuels. The specific energy of a typical high powered battery such as a Lithium-Sulfur (Li-S) is around 0.6 kW-hr/kg. By contrast, most HC fuels have specific energies in the neighborhood of 13 kW-hr/kg. Small improvements in ICE efficiency can yield increases in range and endurance that would require orders of magnitude improvements over the current state of the art in battery technology.

In order to begin improving small engine performance and efficiency, a survey of what current small ICEs are generally capable of regarding these operating characteristics is needed. Unfortunately, most manufacturers of small ICEs typically only publish the engine speed range and peak power output of their products, with little to no information on fuel consumption. AFRL has found through prior small ICE testing that the published peak power ratings of small hobbyist aircraft ICEs are sometimes much higher than what was measured in the laboratory.

In order to establish a useful model for predicting small engine efficiency and other important operating characteristics, a representative sample of reliable small ICE test data

is necessary. Vast amounts of time and money have been dedicated over the last century into the study of ICE improvements; however the large majority of the focus in these efforts has been in the transportation industry, which typically entails engine displacements much larger than 200 cm³. The study of small ICEs must also be divided into the different types of small ICEs, two-stroke versus four-stroke for instance. In 2016, Ausserer took an in-depth look at these subjects in his research of 28 – 85 cm³ displacement volume two-stroke ICEs [10]. The focus of the current study will be four-stroke engines of similar size and power output.

1.2. Research Objectives

To guide the research in the current study, a set of research objectives was established to understand the performance and efficiency of small ICEs. The objectives are:

- 1) Comparison of actual measured power to manufacturer's advertised power ratings for a selection of single cylinder, 40 – 200 cm³ displacement volume, four-stroke ICEs. The engines studied will have displacement volumes of 40, 70, 120, 160, and 200 cm³, with maximum rated power ranging from 2.8 kW (3.75 hp) to 4.1 kW (5.5 hp).
- 2) First law of thermodynamics energy balances for five engines. All energy pathways are to be measured experimentally. Examined energy pathways will be:
 - a) Brake power
 - b) Cooling load
 - c) Sensible enthalpy of exhaust gases
 - d) Incomplete combustion

- 3) Parametric studies to characterize the impact of five variables (equivalence ratio, combustion phasing, cylinder head temperature, engine speed, and throttle setting) on the loss pathways.

1.3. Organization

Chapter two is a literature review. The chapter is written in a manner that describes all of the concepts to be discussed throughout the remainder of the paper. The chapter begins by discussing very basic internal combustion engine topics such as classification and geometry in Section 2.1 and Section 2.2. Chapter two then discusses internal combustion engine operation concepts and terminology in Section 0. Chapter two then finishes with a discussion of small internal combustion engine testing and research in Section 2.4.

Chapter three discusses the methodology used in the study. The chapter begins by discussing the Small Engine Research Bench (SERB) used for engine testing in Section 3.1. After that, the engine selection and preparation is discussed in Section 3.2, followed by a description of the methods and techniques used to perform the energy balances in Section 3.3. Experimental uncertainty is discussed in Section 3.4. The last section of Chapter three addresses the repeatability of experimental measurements, found in Section 3.5.

Chapter four discusses the analysis and results of the engines tested, beginning with the Honda GX120 engine in Section 4.1. A discussion of the test results and scaling of the energy pathways in three geometrically similar engines is the subject of Section 4.2.

Section 4.3 contains the analysis and results of two additional engines, which were not geometrically similar to the three Honda engines discussed in Section 4.1 and Section 4.2.

Chapter five provides conclusions for the current research and recommendations for future research. The chapter begins in Section 5.1 with a review of the research objectives defined in Section 1.2. Section 5.2 summarizes the key findings and conclusions. Finally, Section 5.3 provides recommendations for future research.

2. Literature Review

Chapter Overview

The purpose of this chapter is to provide the background information necessary to understand the concepts and processes behind the research objectives described in Section 1.2. The chapter begins with overviews of engine classification and geometry in Sections 2.1 and 2.2. Section 0 discusses various topics related to ICE operation such as: fuel/air mixtures, gas exchange, combustion phasing, torque, power and efficiency. Section 2.4.1 introduces the concept of the energy balance, while Section 2.4.2 to 2.4.4 discuss related work in small engine testing from the 1950s up to modern day.

2.1. ICE Classification

There are numerous ways to categorize ICEs. One such category is the mechanism used to ignite fuel inside the combustion chamber. The two primary categories of engine ignition are compression ignition (CI) and spark ignition (SI). In a CI engine (also known as Diesel cycle) fuel and air are introduced into the combustion chamber separately with no premixing and compressed to very high pressure and temperature (often with the help of a glow plug to raise the temperature) until the mixture ignites (a process called autoignition). The ignition releases energy which drives the piston down in the engine block, which in turn produces power for whatever purpose the engine is used for. CI engines run on “heavy fuels”, the most common of which is known as Diesel fuel, that have a lower autoignition temperature than the fuels used in SI engines (gasoline being the most familiar). In a SI engine, air and fuel are premixed

before entering the combustion chamber in a carburetor or electronic fuel injection (EFI) system, then the air-fuel mixture (often referred to as fresh charge) are driven into the combustion chamber and compressed using the mechanical motion of the piston being driven upward in the engine cylinder. Once the fresh charge has been compressed sufficiently inside the cylinder, an ignition catalyst is introduced in the form of an electric spark provided by the spark plug.

SI and CI engines can both be further classified into engines with a two-stroke or four stroke (sometimes referred to as two-cycle or four-cycle) operating cycle. The four-stroke ICE operating cycle is shown in Figure 1. As seen in the figure, the four-stroke operating cycle consists of an intake stroke where fresh charge is drawn into the cylinder, a compression stroke where the fresh charge is compressed, a power stroke where energy is released after the ignition of the charge, and an exhaust stroke where the hot combustion gases are pushed out of the engine cylinder.

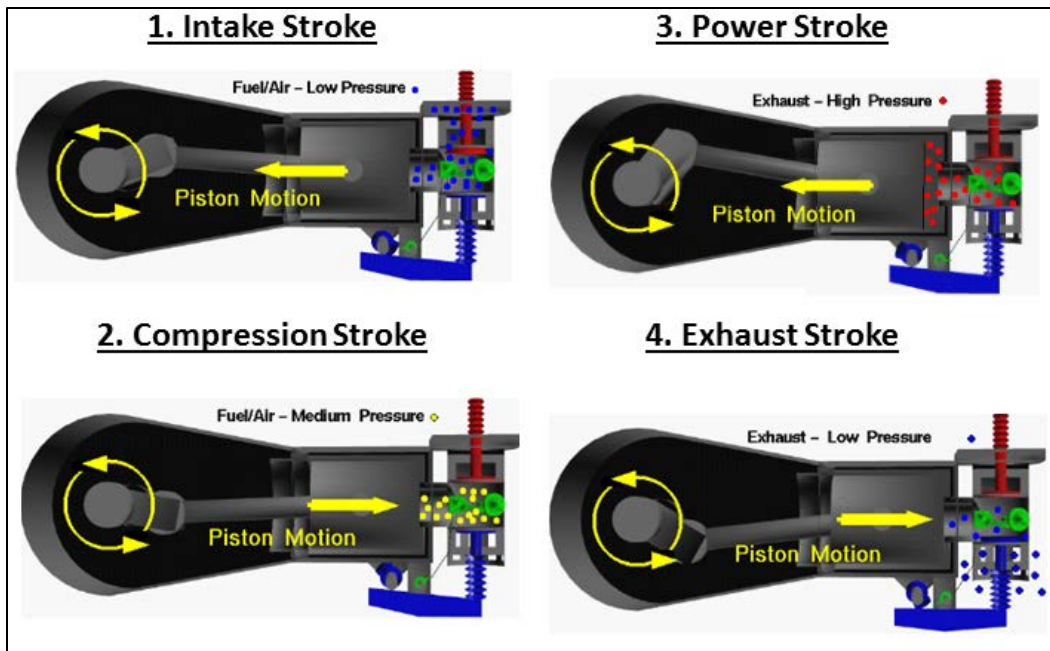


Figure 1. The four-stroke engine operating cycle. Images courtesy of <https://www.grc.nasa.gov>.

A two-stroke engine operation cycle is shown in Figure 2. In a two-stroke engine, there is a compression stroke (or upstroke), where fresh charge is drawn in to the engine crankcase while charge from the previous cycle is compressed in the combustion chamber, and a power stroke (or downstroke), where the hot combustion gases release energy, driving the piston downward. A critical difference between two-stroke and four-stroke engines is illustrated in Figure 1 and Figure 2. The four-stroke engine of Figure 1 has intake and exhaust valves which are timed to open and close separately to allow fresh charge at ambient pressure to enter the engine independently of the burned exhaust gases leaving the engine. The two-stroke engine of Figure 2 has ports rather than valves, which are simply openings in the cylinder sidewalls. In order to bring fresh charge into the cylinder and remove the exhaust gases, the fresh charge must be compressed in the crankcase to a higher pressure than the exhaust and the intake (or transfer) port and

exhaust port are open *at the same time*. This combined intake and exhaust process is called scavenging¹. More discussion of scavenging can be found in Section 2.3.2. Key concepts pertaining to ICE operation are discussed next in Section 2.2.

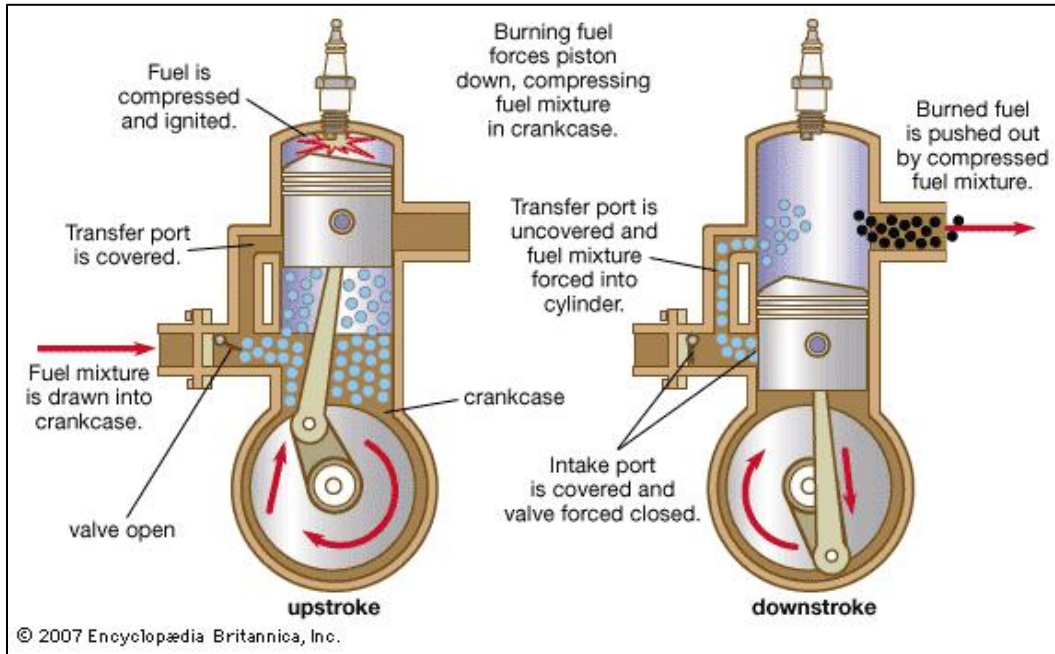


Figure 2. The two-stroke engine operating cycle. Image courtesy of <https://www.britannica.com>

2.2. ICE Geometry

With few exceptions, the cylinder of an ICE is similar to the configuration shown in Figure 3. In the figure, V_c is the clearance volume of the cylinder, V_d is the displacement or swept volume, B is the bore (diameter of the cylinder), L is the stroke (distance the piston is swept), l is the connecting rod length, a is the crank radius, s is the distance between the crank axis and the piston pin axis and θ is the crank angle. TC stands for top center (sometimes called TDC, or top dead center), this is when the piston is at its highest

¹ Some two-stroke engines utilize intake ports and exhaust valves but still must employ scavenging for gas exchange; they are called uniflow scavenged two-strokes.

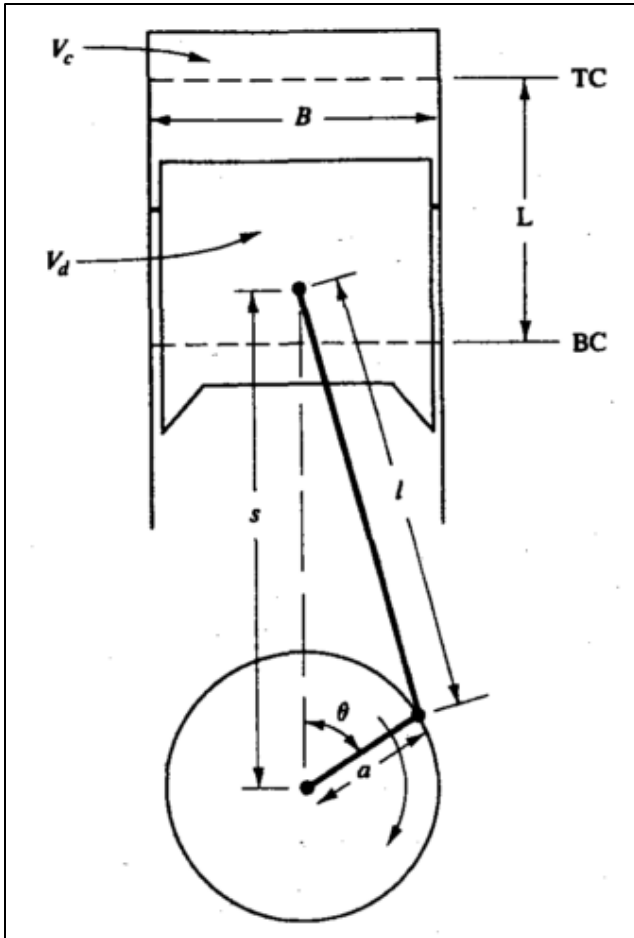


Figure 3. ICE engine geometry. Adapted from Heywood [11].

2.3. ICE Operation

2.3.1. Fuel/Air Mixtures

An ICE cannot operate on fuel alone. The fuel must be mixed with an appropriate quantity of air for the combustion process to occur. The amount of air needed for a particular fuel to burn varies among different fuels and engine types. Typically this is quantified using air-fuel-ratio (AFR) or fuel-air-ratio (FAR). AFR and FAR are defined as follows:

point. BC stands for bottom center (sometimes called BDC, or bottom dead center), this is when the piston is at its lowest point. The compression ratio (r_c) is an important design consideration for ICEs and influences many operating characteristics. Compression ratio is the ratio of maximum cylinder volume to minimum cylinder volume. Compression ratio in equation form is written:

$$r_c = \frac{V_c + V_d}{V_c} \quad (1)$$

$$AFR = \frac{m_a}{m_f} \quad (2)$$

$$FAR = \frac{m_f}{m_a} \quad (3)$$

It is important to note that AFR and FAR are defined on a mass basis where m_a and m_f are masses of air and fuel, respectively. If molar amounts of air and fuel are known, such as in a chemical equation, they must be converted to mass before calculating an AFR or FAR. AFR and FAR may also be defined as mass per unit time:

$$AFR = \frac{\dot{m}_a}{\dot{m}_f} \quad (4)$$

$$FAR = \frac{\dot{m}_f}{\dot{m}_a} \quad (5)$$

A *stoichiometric* AFR or FAR is where exactly the right amount of oxygen is present to completely burn all of the fuel present in the mixture with no excess oxygen. Stoichiometric AFR² is typically denoted as $(AFR)_{st}$. Gasoline has an $(AFR)_{st}$ of 14.6. It is sometimes preferable to run ICEs with a fresh charge AFR at or near $(AFR)_{st}$, but this is not always the case. The term equivalence ratio is used to quantify the degree to which an ICE is operating in a lean or rich condition. Equivalence ratio (ϕ) is defined:

$$\phi = \frac{FAR}{(FAR)_{st}} = \frac{(AFR)_{st}}{AFR} \quad (6)$$

When $\phi < 1$, the engine is in a lean condition, while when $\phi > 1$, the engine is running rich. For instance, CI engines are typically run with less fuel than the stoichiometric ratio (a condition known as lean), and simple small carbureted SI engines (such as a

² Although both AFR and FAR are used in engine research, AFR is used more commonly.

lawnmower engine) are typically run with slightly more fuel than the stoichiometric ratio (a condition known as rich).

Sometimes the term relative air/fuel ratio is used to describe the operating condition. Relative air/fuel ratio (λ) is defined:

$$\lambda = \frac{1}{\phi} \quad (7)$$

Since relative air/fuel ratio is the inverse of equivalence ratio, $\lambda > 1$ means the engine is in a lean condition, while $\lambda < 1$ indicates the engine is running rich.

Typical ranges of AFR and ϕ for SI engines operating on gasoline fuel and CI engines operating on Diesel fuel are shown in Table 1 [11]. The table shows that CI engines are typically run at lean conditions while SI engines operate near the stoichiometric AFR. Although this study does not focus on CI engines, the distinctions are worth noting and provide a useful comparison when describing the concepts of AFR and ϕ . Another topic related to air-fuel mixtures is the flow of fresh charge into the cylinder and the flow of burned exhaust gases out of the cylinder, which are discussed in Section 2.3.2.

Table 1. Typical air-to-fuel ratio (AFR) and equivalence ratio (ϕ) of SI engines operating on gasoline fuel and CI engines operating on Diesel fuel [11].

Engine Type	AFR	ϕ
SI	12 - 18	0.81 - 1.22
CI	18 - 70	0.21 - 0.81

2.3.2. Gas Exchange in SI ICEs

Air flow into and out of an ICE is critical to its operation and heavily influences the engine's output power and efficiency. As discussed in section 2.1, two-stroke and four-stroke engines utilize different processes to induct fresh charge into the cylinder. In a four-stroke engine, the intake valve opens 10 - 20° before TC, while the piston is travelling upward in the cylinder. At this time the exhaust valve is still open and expelling gases from the previous combustion cycle. The exhaust valve remains open until approximately 15 - 30° after TC. The short period of time where the intake and exhaust valves are slightly open at the same time is referred to as the overlap period, highlighted in Figure 4:

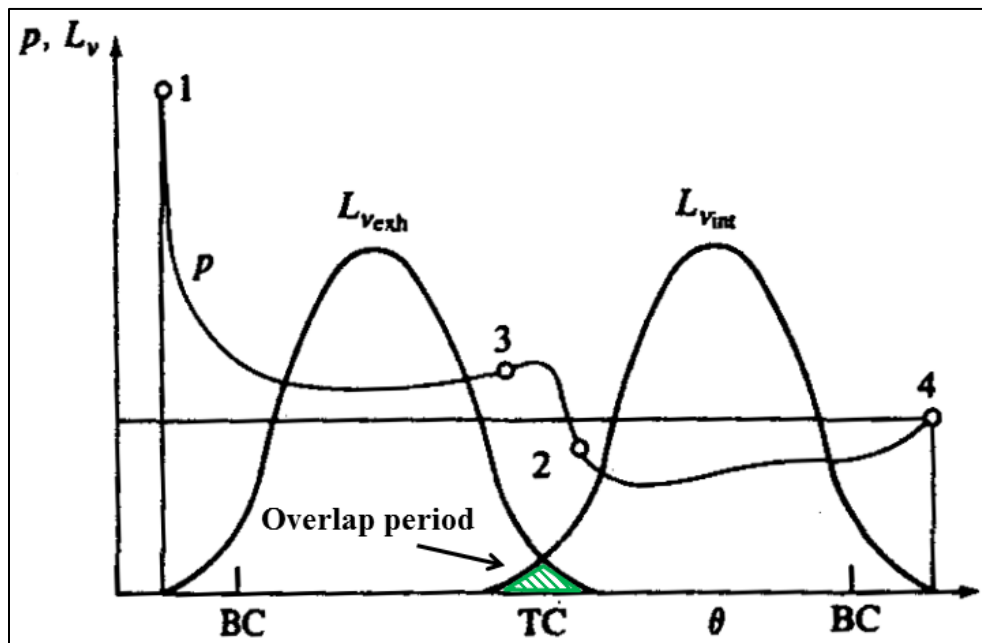


Figure 4. Valve lift (L_v) and in-cylinder pressure (p) versus crank angle (θ) for a typical four-stroke ICE. Figure adapted from Heywood [11].

In Figure 4, valve lift (L_v) and in-cylinder pressure (p) are plotted versus crank angle (θ) for a typical four-stroke ICE [11]. During the overlap period, when the intake valve (v_{int}) and exhaust valve (v_{exh}) are open simultaneously, the burned exhaust gases are at a higher pressure than the intake fresh charge, which often leads to a backflow of exhaust gases into the cylinder and cylinder gases into the intake.

What happens during the overlap period in a two-stroke engine is quite different than the phenomena described above in four-stroke ICEs. Because two-stroke ICEs utilize scavenging (combined intake-exhaust process), the overlap period is much longer, as shown in Figure 5. The curve represented by the letter p represents in-cylinder pressure, p_e is the exhaust gas pressure, p_i is the intake pressure, EPO is the exhaust port opening, IPO is the intake port opening, IPC is the intake port closing, and EPC is the exhaust port closing.

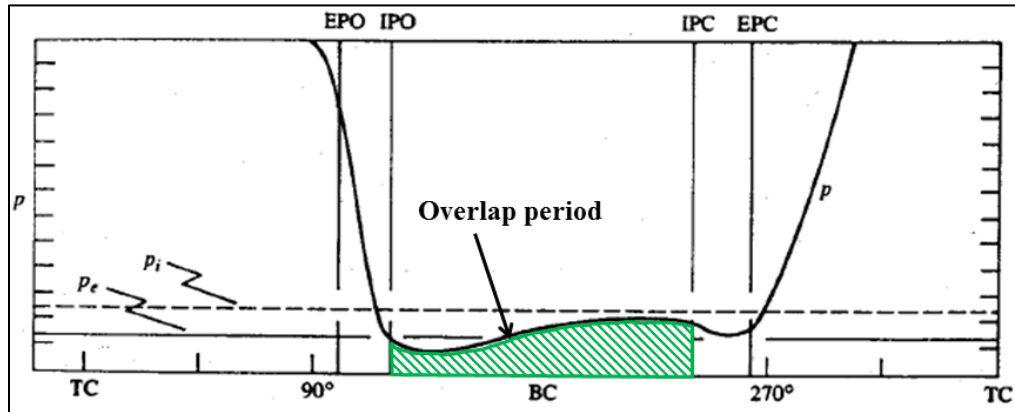


Figure 5. In-cylinder pressure versus crank angle for a loop-scavenged two-stroke engine. Figure adapted from Taylor [12].

In Figure 5 it is shown that the typical overlap period of a two-stroke engine is greater than 100 crank angle degrees, as opposed to the 25 - 50° of a four-stroke. Furthermore, in two-stroke engines the intake charge pressure (p_i) is elevated, often by trapping it in the engine crankcase during the downstroke. The fresh charge at higher pressure is then used to “push” the burned exhaust gases out of the cylinder. During this process it is impossible to ensure that exhaust gases are the only thing “pushed” out of the cylinder, varying amounts of fresh charge will always escape the cylinder through the exhaust ports as well. The passing of fresh charge through the cylinder and out of the exhaust prior to combustion is called short circuiting, and occurs in all two-stroke engines. By contrast, four-stroke engines typically exhibit negligible levels of short circuiting.

Both two-stroke and four-stroke engines lose a small amount of unburned fuel energy to crevice flows and blowby. Crevice flows are the flow of gases into and out of small volumes within the cylinder, such as the gap between the piston and cylinder wall, gaps around piston rings, and area between the threads and around the electrode of spark plugs. Blowby is the flow of cylinder gases past the piston rings and into the crankcase. Piston ring crevices are shown below in Figure 6. Crevice volumes change as a result of thermal expansion as an engine warms up.

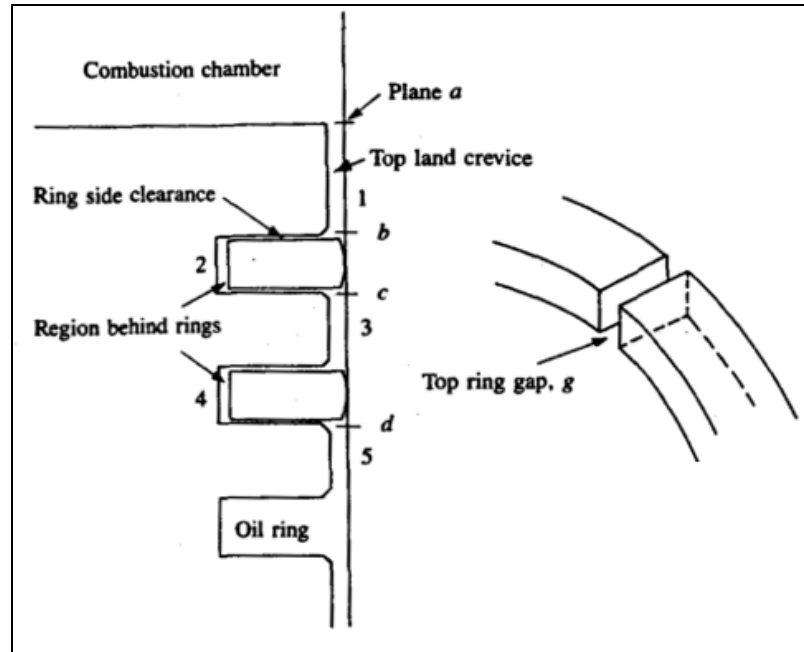


Figure 6. Piston Ring Crevices (from Heywood) [11].

As fresh charge is inducted into an engine and undergoes compression, a small portion of the mixture is forced into the crevices. Due to a large surface area to volume ratio in the crevices, some heat transfer occurs out of the charge, into the surfaces surrounding the crevices, raising the amount of energy needed to ignite the charge trapped in the crevices. During combustion the charge starts to burn around the spark plug electrode, expanding in a roughly spherical pattern. The combusted mixture is a higher pressure than the uncombusted mixture surrounding it, so it “pushes” more of the charge into the crevices. As the flame front reaches the crevices, some burned gases flow into the crevices, and some combustion of the trapped fresh charge occurs. At this time, with high pressures inside the cylinder, some trapped gases (unburned and exhaust gas) are ejected into the crankcase as blowby. When the flame front encounters the high surface area to volume ratio, there is heat transfer from the flame to the cylinder wall and

other surrounding surfaces. The flame front also encounters gaps that are too small to pass through, the result of which is quenching. After combustion the exhaust valve opens, lowering the pressure inside the cylinder. The gases trapped in the crevices are now at a higher pressure and flow back into the cylinder and out the exhaust. Crevice flow and blowby are a source of energy losses, and can account for 5 – 10% [11] or even 20% [13] of the total cylinder charge at peak pressure, according to various sources.

2.3.3. Combustion Phasing

In a SI ICE, the timing of the combustion process, or combustion phasing, has a large influence on the overall engine performance and efficiency. Typically, the process is divided into two phases, which are named according to the number of crank angle degrees the engine progresses during each phase. The phases are called the flame development angle ($\Delta\theta_d$) and the rapid burning angle ($\Delta\theta_b$). The flame development angle is the number of crank angle degrees the engine has progressed between the ignition spark and when a small amount of the fuel in the cylinder has burned (usually 10%), this angle is also sometimes represented as θ_{10} , θ_{0-10} , or $\theta_{10\%}$. The rapid burning angle is the number of crank angle degrees the engine has progressed when the majority of the fuel in the cylinder has burned (usually from 10% to 90%). The sum of the flame development angle and the rapid burning angle is the overall burning angle ($\Delta\theta_o$), which is also sometimes represented as θ_{90} , θ_{0-90} , or $\theta_{90\%}$. As seen in Figure 7, the flame development angle and rapid burning angle are roughly equivalent for most conditions, with an increase in the number of crank angle degrees required for both as engine speed is increased.

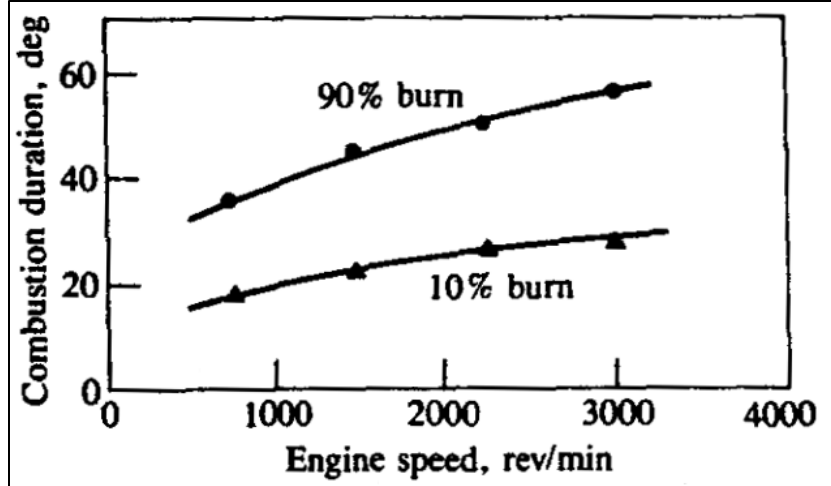


Figure 7. Effect of engine speed on flame development angle ($\Delta\theta_d$) and overall burning angle ($\Delta\theta_o$). Adapted from Heywood [11].

To determine $\Delta\theta_d$ and $\Delta\theta_b$, it is necessary to know the mass fraction of fuel burned inside the cylinder. This quantity is very difficult to obtain through direct measurement but it can be closely approximated. If in-cylinder pressure (p) and instantaneous volume (V) are known, the following equation can be used to calculate mass fraction of fuel burned (χ_b) [11]:

$$\chi_b = \frac{p^{1/n}V - p_o^{1/n}V_o}{p_f^{1/n}V_f - p_o^{1/n}V_o} \quad (8)$$

where p_o is the in-cylinder pressure at the time of spark, p_f is the in-cylinder pressure at the end of combustion, V_o is the in-cylinder volume at the time of spark, V_f is the in-cylinder volume at the end of combustion, and n is a polytropic exponent which is similar to, although slightly different from γ , which is used for adiabatic isentropic processes. The polytropic exponent n used for conventional fuels is typically 1.3 ± 0.05 , which is close to the average of γ_u for the unburned mixture over the compression process, but

larger than γ_b , for the burned gas mixture during the expansion process [11]. Equation (8) utilizes some inherent approximations. First, heat transfer effects are largely not considered. Second, the pressure rise due to combustion is known to be proportional to the amount of fuel chemical energy released rather than the mass of mixture burned. Finally, the polytropic exponent is not constant during real combustion. Nevertheless, it is a widely used technique in combustion analysis [11]. The crank angles relative to TDC where 10%, 50% and 90% of the mass of fuel has been burned are known as CA10, CA50, and CA90, respectively. These terms are sometimes used when referring to the spark timing of an ICE.

It is important to understand the effect of spark timing on the combustion process. If the spark is too early in the compression stroke, or too far advanced, the energy released in the combustion process can counteract the upward movement of the piston in the cylinder, reducing the power output and efficiency of the engine. If the spark occurs too late, the combustion energy is released after the engine's momentum has already begun pushing the piston down in the cylinder, again reducing the power output and efficiency of the engine. This effect is shown in Figure 8. It can be seen in Figure 8(b) that, generally, when spark timing is between 30° and 40° bTDC, engine output is at or very near maximum brake torque (MBT). Peak efficiency occurs when the engine reaches MBT.

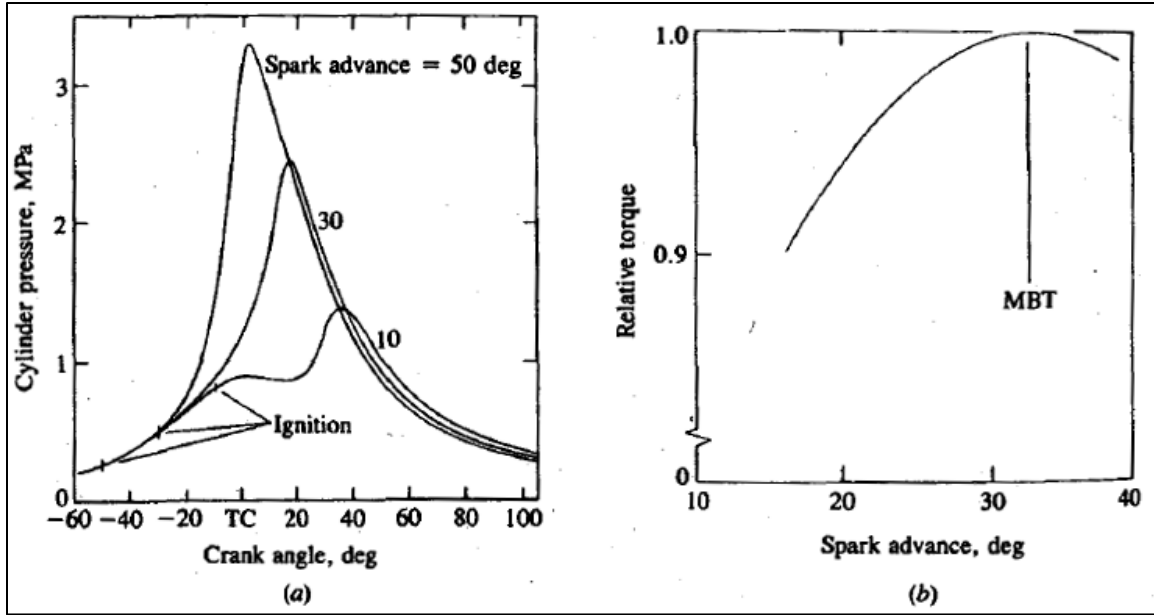


Figure 8. (a) In cylinder pressure versus crank angle for ignition timing of 50°, 30°, and 10° bTDC. (b) Brake torque versus ignition timing at constant speed [14].

The timing advance setting where MBT occurs is referred to as MBT timing. MBT timing varies from engine to engine and changes based on the operating condition of the engine. An empirical rule of thumb is that MBT timing generally occurs when CA50 is approximately 10° aTDC [11].

2.3.4. Torque and Power

When measuring ICE performance torque and power are the most commonly used metrics. Torque (τ) is the twisting force produced by an ICE, while power (P) is the rate at which an ICE is capable of providing force. Power and torque are related by the equation:

$$P = 2\pi N\tau \quad (9)$$

where N is the engine speed. Torque may be measured using a dynamometer, which is a device capable of providing a resistance to the rotating output shaft of an ICE. The

amount of force needed to resist the shaft rotation is recorded as the torque of the engine. There are various types of dynamometers available which employ different methods of resistance. An eddy current dynamometer, for instance, uses magnetic force to resist the rotation of the spinning ICE driveshaft. The amount of electrical current needed to provide the required amount of resistance (applied load) is proportional to the torque provided by the ICE.

Power or torque are often prefixed with the words indicated or brake. Indicated power (P_I) is the power output of an ICE before any losses are subtracted due to heat transfer, friction, etc. Brake power (P_b) is the power output of an ICE after all losses have been subtracted from the indicated power; therefore, indicated power is always greater than brake power. Brake power is the power output of an ICE that is capable of performing useful work.

A measure of engine performance that is very useful for comparing ICEs of different sizes and types is mean effective pressure (MEP). Mean effective pressure is a quantity (with units of pressure) that is “equal to that constant pressure which, if exerted on the piston for the whole outward stroke, would yield work equal to the work of the cycle” [12]. MEP is calculated using the following equation:

$$MEP = \frac{Pn_R}{V_d N} \quad (10)$$

where n_R is a constant used to indicate the number of crank revolutions needed for each power stroke ($n_R =$ two for four-stroke ICEs, or one for two-stroke ICEs). When using

indicated or brake power in Equation (10), MEP is referred to as indicated mean effective pressure (IMEP) or brake mean effective pressure (BMEP):

$$IMEP = \frac{P_I n_R}{V_d N} \quad (11)$$

$$BMEP = \frac{P_b n_R}{V_d N} \quad (12)$$

It is clear by examining Equations (10), (11), or (12) that, when comparing a two-stroke ICE to a four-stroke ICE, displacement volume (V_d) of the four-stroke engine must be double that of the two-stroke to obtain the same MEP (for a given engine speed). Some typical values for BMEP for automotive ICEs are listed below in Table 2.

Table 2. Typical BMEP values of automotive ICEs [11].

BMEP at MBT, (bar)		
	SI Engines	CI Engines
Naturally Aspirated	8.5-10.5	7-9
Turbocharged	12.5-17	10-12

Another quantity that is useful for making comparisons of different ICEs is mean piston speed (\bar{S}_p), which is calculated using the equation:

$$\bar{S}_p = 2LN \quad (13)$$

Utilizing mean piston speed rather than engine rotational speed (N) is advantageous because values such as gas flow velocities in the intake and cylinder scale with \bar{S}_p . Maximum mean piston speeds for ICEs are typically 8 – 15 m/s. These practical limits are encountered due to factors such as gas flow resistance into the engine or internal stresses [11].

2.3.5. Efficiency

There are several different types of efficiencies discussed in the study of ICEs. The following paragraphs discuss some of the efficiency types relevant to the research in this document. It is useful to start with a quantity known as the maximum theoretical engine efficiency (η_{max}). Using an ideal Otto cycle model and assuming air is a calorically perfect ideal gas, it can be shown that the maximum theoretical efficiency of an ICE is a function of compression ratio and the ratio of specific heats [12]:

$$\eta_{max} = 1 - \left(\frac{1}{r_c}\right)^{\gamma-1} \quad (14)$$

Although the maximum theoretical efficiency of an ICE is not physically achievable, it sets the upper bound for engine designers and gives the first set of parameters for optimization (r_c and γ).

Typically, when referring to the overall efficiency of an ICE, the fuel conversion efficiency (η_f) is what is being discussed. Fuel conversion efficiency is calculated using the equation:

$$\eta_f = \frac{P_b}{\dot{m}_f Q_{LHV}} \quad (15)$$

where \dot{m}_f is the mass flow rate of fuel and Q_{LHV} is the lower heating value of the fuel. Closely related to fuel conversion efficiency is the quantity known as specific fuel consumption (*sfc*). Specific fuel consumption measures how efficiently an ICE is using the fuel to produce useful work. To maximize ICE efficiency, it is desirable to minimize sfc. Brake specific fuel consumption is calculated as the ratio of the fuel mass flow rate to brake power:

$$bsfc = \frac{\dot{m}_f}{P_b} \quad (16)$$

or, when combined with Equation (15):

$$bsfc = \frac{1}{\eta_f Q_{LHV}} \quad (17)$$

Traditional automotive SI engines typically have a maximum bsfc of around 270 g/kWh ($\eta_f = 30.3\%$) [11], while some large CI engines can have a bsfc below 200 g/kWh ($\eta_f = 40.9\%$) [11]. Small two-stroke SI engines have been shown to operate with bsfc exceeding 1000 g/kWh ($\eta_f = 8.2\%$) [10, 15].

Mechanical efficiency (η_m) is the ratio of brake power to indicated power:

$$\eta_m = \frac{P_b}{P_I} \quad (18)$$

Typically, for a modern automotive engine running at wide open throttle, mechanical efficiency is approximately 90% at moderate engine speeds (1800–2400 rpm), decreasing to approximately 75% at maximum rated speed. WOT provides the highest η_m for a given engine speed, but as the throttle is closed (reducing intake air and fuel flow), mechanical efficiency drops, ultimately reaching zero when the engine is idling [11].

The efficiency which describes how well the fuel is burning is known as the combustion efficiency (η_c). Combustion efficiency is an indication of how much energy remains in the exhaust gases of an ICE. Although there are many constituents in the exhaust gases, much of the chemical energy in the exhaust of an ICE is contained in CO, H₂, and unburned hydrocarbons (UHCs) found in the exhaust gas. Figure 9 shows how the concentrations of exhaust gas species in SI engines change as equivalence ratio is

varied. As seen in the figure, CO and H₂ concentrations increase steadily under rich conditions. It goes without saying that UHC emissions increase under rich conditions as well.

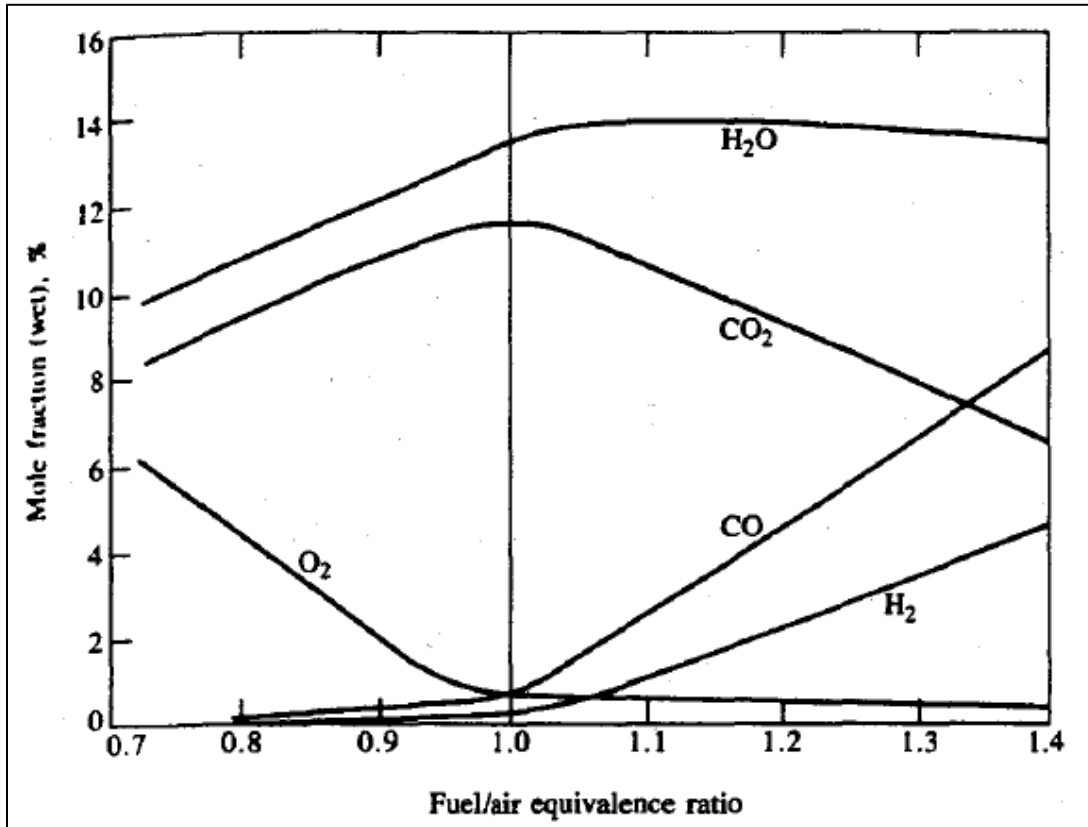


Figure 9. Exhaust gas species concentration of a typical SI engine as a function of equivalence ratio [11].

To fully define combustion efficiency, the net chemical energy release rate due to engine combustion must first be discussed, using the following equation [11]:

$$[H_R(T_A) - H_P(T_A)] = \dot{m}_i \left(\sum_{i, \text{ reactants}} n_i \Delta \tilde{h}_{f,i}^o - \sum_{i, \text{ products}} n_i \Delta \tilde{h}_{f,i}^o \right) \quad (19)$$

Equation (19) represents the rate of change in enthalpy (H) from the reactants (R) to the products (P), where n_i is the number of moles of a given species per unit mass of working fluid and $\tilde{h}_{f,i}^o$ is the standard enthalpy of formation of species i at a given ambient temperature T_A . The ratio of the net chemical energy release rate to the rate of fuel energy entering the engine ($\dot{m}_f Q_{LHV}$) is the combustion efficiency [11]:

$$\eta_c = \frac{[H_R(T_A) - H_P(T_A)]}{\dot{m}_f Q_{LHV}} \quad (20)$$

Combustion efficiency in SI ICEs is highly dependent on the fuel mixture of the engine, or equivalence ratio. Figure 10 shows the effect of equivalence ratio on combustion efficiency for both SI and CI (Diesel) engines. In SI engines, combustion efficiency at lean conditions is typically 95 – 98%. As the fuel/air mixture approaches the stoichiometric ratio and becomes rich, combustion efficiency in SI engines declines as the amount of fuel in the cylinder becomes too large for the amount of available oxygen to react. CI engines are always run with a lean mixture, and have typical combustion efficiencies around 98%. For a given engine under stable operating conditions, equivalence ratio is the primary driver in changes to combustion efficiency, with most other design variables having little effect [11].

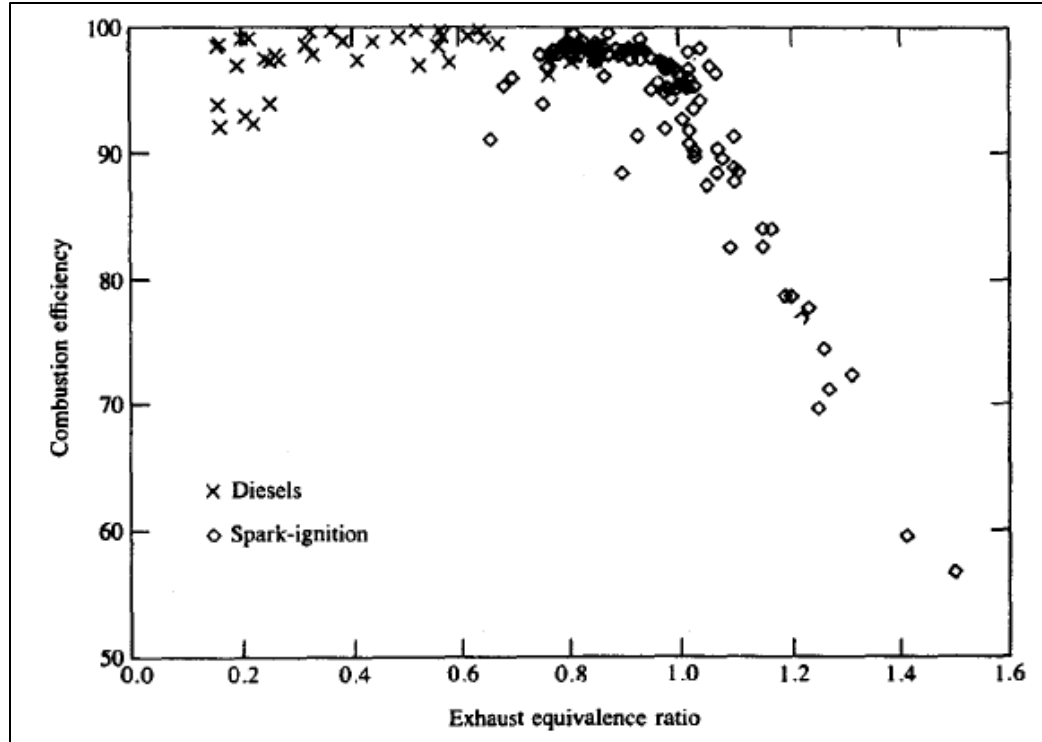


Figure 10. Combustion efficiency as a function of equivalence ratio [11].

It is sometimes desirable to examine incomplete combustion effects on efficiency using the brake power produced by the engine. The ratio of brake power to the net chemical energy release rate is defined as thermal efficiency (η_t) and is calculated using Equation (21) [11].

$$\eta_t = \frac{P_b}{[H_R(T_A) - H_P(T_A)]} \quad (21)$$

Combining Equations (20) and (21):

$$\eta_t \eta_c = \frac{P_b}{\dot{m}_f Q_{LHV}} = \eta_f \quad (22)$$

Finally, volumetric efficiency (η_v) is an indicator of how effectively an ICE is utilizing the air it inducts, and it is specific to four-stroke engines. Volumetric efficiency is the ratio of the volumetric flow rate of intake air to the rate at which the volume is displaced by the piston [11]:

$$\eta_v = \frac{2\dot{m}_a}{\rho_{a,i}V_dN} \quad (23)$$

where $\rho_{a,i}$ is the density of the intake air. Typical maximum values of volumetric efficiency for automotive SI ICEs are approximately 80-90%, with significant decreases as the intake air of the engine becomes more throttled [11]. The performance map shown in Figure 11 illustrates the complex interrelationships of the various types of efficiency as engine speed (represented as piston speed), and power (represented as BMEP) are varied.

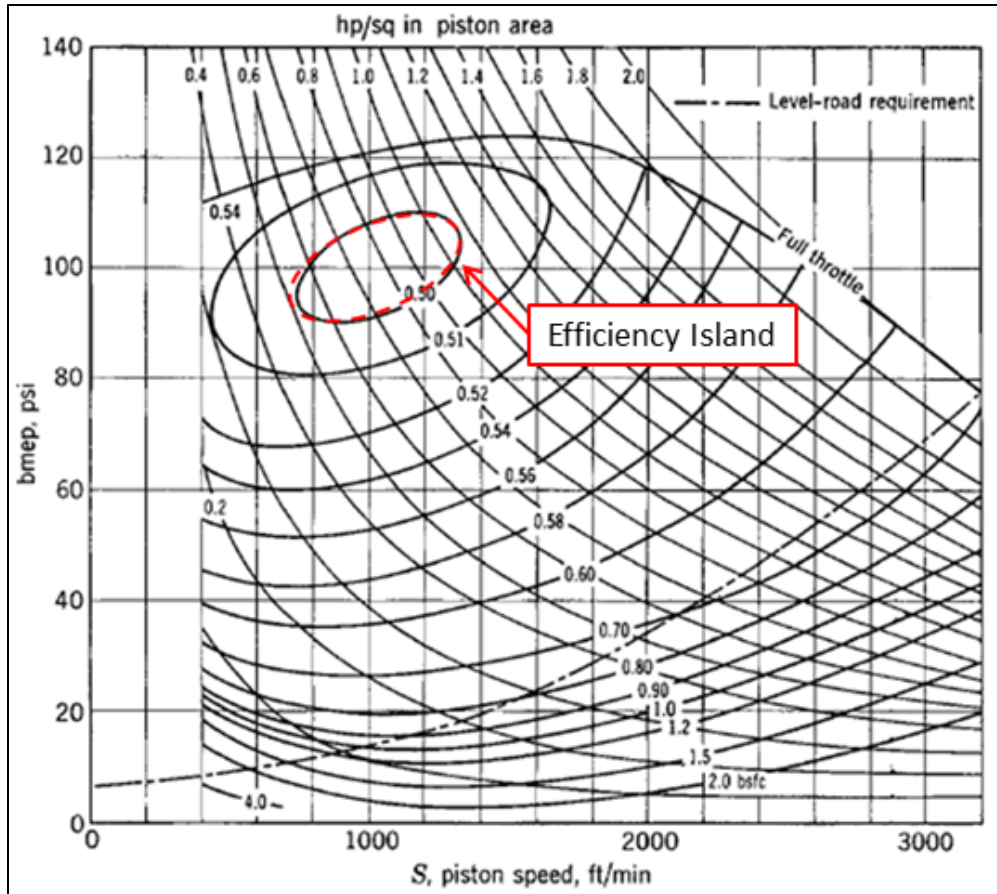


Figure 11. Performance map of a typical automotive SI ICE [12].

Examining the lines of constant bsfc, an “efficiency island” (highlighted in red) is found where bsfc is at a minimum and fuel conversion efficiency is at a maximum. Starting from the efficiency island and moving to the right (increasing engine speed), increased friction losses reduce mechanical efficiency. While there is generally a small increase in gross *indicated* fuel conversion efficiency with increased engine speed, the friction losses are more dominant, ultimately increasing bsfc and reducing the overall fuel conversion efficiency. Starting from the efficiency island and moving to the left (decreasing engine speed), losses due to heat transfer tend to increase while combustion

and thermal efficiencies decrease (higher incomplete combustion), reducing overall fuel conversion efficiency. Moving down from the efficiency island (closing the throttle or decreasing engine load), tends to reduce volumetric efficiency (due to increased pumping losses), decrease mechanical efficiency (due to increased friction losses), and increase heat transfer losses, reducing the overall fuel conversion efficiency once again. Every ICE has a unique performance map, but the general shape and trends are fairly consistent for most automotive SI ICEs.

2.4. Relevant Research In Small ICE Testing

2.4.1. Energy Balance

A useful tool in the study of internal combustion engines is the first law of thermodynamics energy balance, sometimes called a first law energy balance or simply “energy balance.” An energy balance is, as the name implies, an accounting of all energy entering and leaving a system. In its most simple form:

$$Q_{in} = W_{out} + Q_{l,tot} \quad (24)$$

Where Q_{in} is the energy entering the system, W_{out} is the useful work produced by the system, and $Q_{l,tot}$ is the total energy losses of the system. For the analysis performed in this study, a control volume energy balance approach was used, where the values of quantities crossing the control volume borders were steady state, averaged test data. The system was defined as the test engine and a cooling air enclosure which completely surrounded the engine, with openings for the engine intake, exhaust, driveshaft, cooling air entry, and cooling air exit. Energy entered the system at the engine fuel/air intake and

the cooling enclosure intake, and exited via the engine exhaust, output driveshaft, and the cooling enclosure exit.

For this study it was beneficial to describe the terms in Equation (24) on a per unit time basis:

$$\dot{Q}_{in} = P_b + \dot{Q}_{l,tot} \quad (25)$$

The energy entering the engine (Q_{in}) was the sum of the energy in the air and fuel in the engine intake, or:

$$Q_{in} = m_a h_a + m_f h_f \quad (26)$$

again, on a per unit time basis:

$$\dot{Q}_{in} = \dot{m}_a h_a + \dot{m}_f h_f \quad (27)$$

where h_a was the specific enthalpy of the intake air and h_f was the specific enthalpy of the fuel. Generally speaking, the specific enthalpy of the intake air (h_a) is much smaller than the specific enthalpy of the intake fuel (h_f) and can often be considered negligible.

Energy losses ($Q_{l,tot}$) come in many different forms. There are thermal losses from heat escaping the engine through the cylinder walls and cylinder head (Q_{th}), friction losses from the physical contact of parts inside the engine (Q_f), sensible enthalpy losses in the exhaust associated with the temperature rise of combustion (Q_{exh}), chemical enthalpy losses in the exhaust from incomplete combustion (Q_{inc}), and short circuiting losses from the scavenging process (Q_{sc}). Short circuiting losses are generally considered negligible for four-stroke ICEs but are quite significant in two-stroke ICEs. It

is important to note that the energy lost to friction is primarily converted to heat energy, which exits the engine as thermal losses.

2.4.2. Early Work

As described in Section 1.2, the ICE displacement volume range of 10-200 cm³ is of interest to many who study the propulsion of Group 2 RPAs. Understanding how changes in various operating conditions affects the performance and efficiency of these small ICEs opens the door to future improvements in design and operation. Historically speaking, scientific testing of small ICEs has been relatively scant when compared to larger ICEs, especially those used in the transportation industry.

A study of miniature engine generator sets performed by Smith et al. in 1956 measured the thermal efficiency (η_{th}) of a selection of hobbyist ICEs [16]. Results of the study showed thermal efficiencies of 7.5 - 9% for two-stroke engines with displacement volumes of 7.7 and 10 cm³ and ~18% for three four-stroke engines ranging in size from 9 – 25 cm³. Engine reliability and operation at various temperatures and altitudes were examined, but no determination of energy losses was determined beyond overall engine efficiency.

In 1965, Bishop studied the effects of various design variables on friction losses and overall fuel efficiency using experimental data collected on single cylinder cooperative fuels research (CFR) and 4, 6, and 8 cylinder Ford engines [17]. The observed indicated thermal efficiency (ITE) of the multi-cylinder engines taken at various speeds and throttle conditions ranged from approximately 17.5% at 800 rpm to

approximately 35% at 4000 rpm. These efficiencies correlated to indicated sfc of 471 g/kWh at 800 rpm to 234 g/kWh at 4000 rpm. He then developed general “corrected” trends for IMEP and ITE for all of the engines based on a speed correction factor. Using the corrected IMEP and ITE, along with engine design factors such as bore, stroke, compression ratio, etc. he developed equations for predicting BMEP, BSFC, BHP, and BTE. Using the model, Bishop predicted the effect of various parameters on overall fuel economy. His predictions showed that factors such as the number of piston rings, number of cylinders, relative valve area, bearing size and barometric pressure produced changes of generally less than 10% to fuel economy. On the other hand, engine displacement volume and compression ratio changed fuel economy by 10 – 20% as they were varied in the model. In the end, Bishop concluded that the sfc of automotive engines at moderate engine speeds (above 1200 rpm) and loading (60% of max) could be predicted within 5% of the actual value. Furthermore, Bishop stated that friction losses and fuel economy could be predicted to within 1%, with the caveats that these predictions break down at low speeds, low loading (highly throttled), and small displacement volumes [17]. The Bishop study is a valuable resource for the study of ICE energy pathways, but the equations are cumbersome, involving up to 15 variables, and the models developed within the study are not reliable for small ICEs.

In 1973 a series of articles written by Geirke was released in a remote control aircraft hobbyist magazine named “Flying Models [18-20].” In the first article, Gierke detailed the design and construction of a small dynamometer and tested a 40 cm³ displacement volume two-stroke glow engine. The engine produced from 1.67 – 1.95

brake horsepower across an engine speed range of 16.3 – 21.8 krpm. In the second article, Gierke discussed techniques for running dynamometer testing including atmospheric correction factors and analysis of test results, as well as a discussion of energy flow in two-stroke engines and methods for measuring air and fuel flow. The third article by Gierke contained discussions on various types of efficiency and results indicating a fuel conversion efficiency of 15.5% at 15000 rpm.

Throughout the 1960s and 70s several studies were performed on the methods, reproducibility, and accuracy of in-cylinder pressure measurements [21-26] where high-speed data acquisition began to appear through the use of computers. The use of highly accurate in-cylinder pressure measurements greatly aided the field of ICE performance and efficiency studies moving into the modern era. In 1976 Blair developed computer predictions of power, MEP, and sfc of 250 cm³ and 380 cm³ two-stroke ICEs and compared them with experimental data [27, 28]. Exhaust enthalpy, cooling losses, and incomplete combustion effects were not examined.

In 1980 Lavoie and Blumberg developed models to predict fuel consumption (ISFC), NO_x levels, and unburned hydrocarbons (UHCs) in a four-stroke, single-cylinder, 611 cm³ displacement volume ICE [29]. The paper contained experimental data showing indicated specific fuel consumption (ISFC) variation as ignition timing, equivalence ratio, percent of exhaust gas recirculation (%EGR), engine speed, and engine load were varied. ISFC values ranged from approximately 220 – 320 g/kWh across the range of test conditions.

2.4.3. Scaling Studies

In 2002, Menon and Cadou at the University of Maryland began studying the performance and efficiency of small internal combustion engines, with an emphasis on ICEs with an overall mass of less than 1 kg. Although the aforementioned studies examined some of the various subjects related to small engine efficiency and energy losses, no previous comprehensive studies of the performance and efficiency of ICEs smaller than 1 kg existed at that time. The first paper published by Menon and Cadou contained details of the test rig dynamometer and fuel measurement system as well as methods for predicting the power, fuel conversion efficiency, and power density of small ICEs based on engine mass [30]. The following year (2003), Menon and Cadou published information regarding refinements to the dynamometer and fuel measurement system, as well as data collected from a 7.45 cm³ displacement volume, single cylinder, glow fuel, two-stroke hobby aircraft engine. Fuel conversion efficiency ranged from approximately 0.5 – 4% [31]. In 2004 Menon and Cadou measured fuel conversion efficiency of approximately 3 – 6.5% for the same engine from the previous study, and fuel conversion efficiencies of 5 – 6.3% and 1.5 – 6% for 2.26 and 0.99 cm³ displacement volume single cylinder, glow fuel, two-stroke hobby aircraft engines, respectively [32].

In 2013, Menon and Cadou expanded upon their previous work, producing a two-part study [9, 33]. In the first paper, scaling laws were developed for ICE power and fuel conversion efficiency as a function of displacement volume, for all types of ICEs from the micro scale (0.16 cm³ displacement volume) to the macro scale (> 1E7 cm³

displacement volume) [9]. Figure 11 and Figure 12 show a slightly modified version from the original paper. The micro glow engine data points shown on the left side of the figures were obtained by Menon and Cadou through experimentation. Nine two-stroke, micro scale (0.16 – 7.54 cm³ displacement volume) hobbyist engines were tested and plotted, while the remaining data points were obtained using a combination of manufacturer data and information found in Heywood [11] and Heywood and Sher [34].

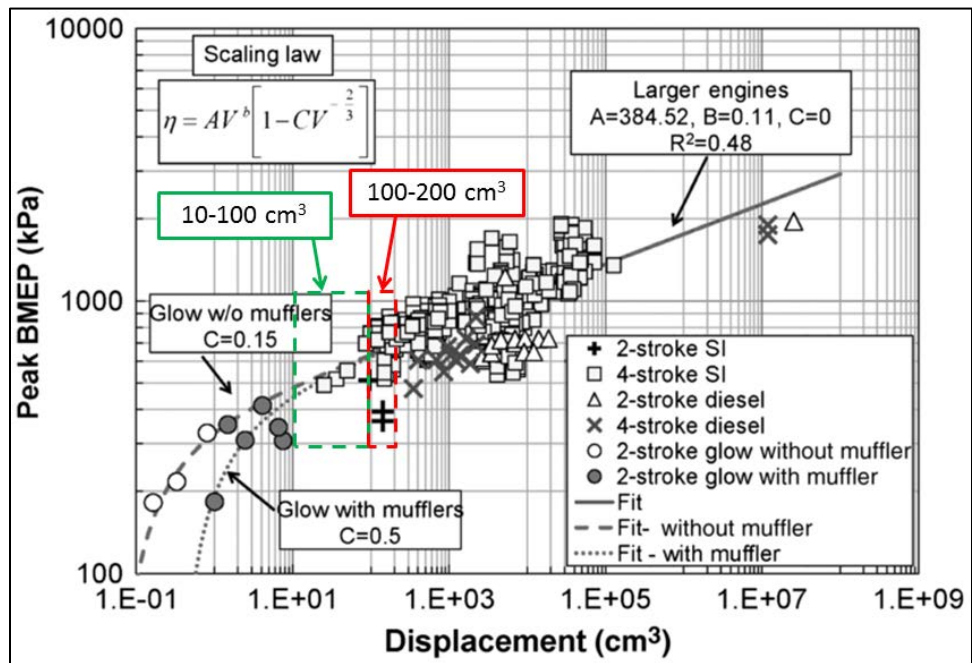


Figure 12. Menon and Cadou BMEP plot [9].

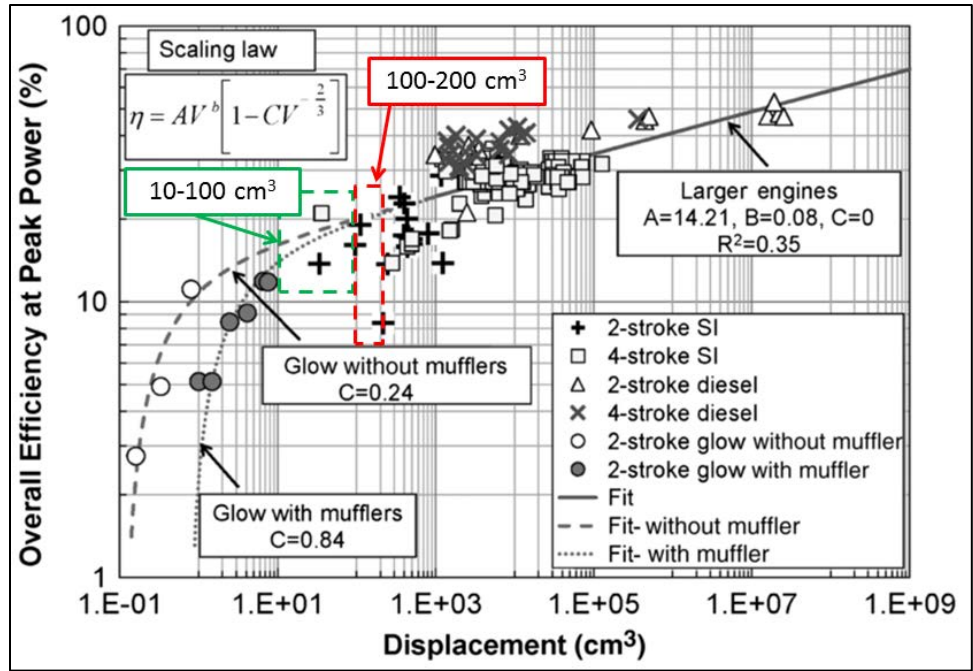


Figure 13. Menon and Cadou fuel conversion efficiency plot [9].

Figure 12 shows that most publicly available data for SI engine power ratings lies in the displacement range of 100 – 10,000 cm³. This data typically consists of a single peak power rating at a single rpm. It is clear from a comparison of Figure 11 and Figure 12 that efficiency data is far less common than power ratings. Examining the range of interest for this study in Figure 13 (10 - 200 cm³ displacement), the 10 – 100 cm³ range contains one point representing a two-stroke SI engine and one point representing a four-stroke SI engine. In the 100 – 200 cm³ range, two data points are shown, both representing two-stroke SI engines. The lack of data in this displacement volume range was a key driving factor for the work done in this study.

In Part Two of the 2013 Menon and Cadou study, energy balances were performed on the nine micro size, glow fuel, two-stroke engines discussed in [9]. Energy

losses were categorized as thermal losses, mechanical losses (due to friction), exhaust gas enthalpy losses, or incomplete combustion losses. It is important to note that the incomplete combustion losses discussed in the study included both scavenging (short circuiting) losses and the chemical enthalpy losses due to incomplete combustion discussed in Sections 2.1 and 2.3.2. The study showed that incomplete combustion losses were dominant in the micro two-stroke ICEs, ranging from 54 – 65% of the fuel energy entering the engine at 10,000 rpm and a ϕ of 1.0 [33].

Additionally, in 2013 Menon and Cadou produced a study on the combustion process in micro scale piston engines using cylinder pressure measurements, in-cylinder flame imaging, and a regime diagram analysis [35]. The study showed that combustion is dependent on scale, that the low combustion efficiency of micro scale ICEs may be attributed to intermittency associated with a two-stage combustion process, and that micro scale ICEs operate primarily in the “flamelet in eddy” regime rather than the “wrinkled laminar flame sheet” regime seen in conventional-scale ICEs.

2.4.4. Small Engine Research Laboratory (SERL)

In 2011, Air Force Research Laboratory (AFRL) began studying small ICEs with an initial focus on the use of heavy (low AKI) fuels in small ICEs designed to run on gasoline. At AFRL’s Small Engine Research Laboratory (SERL), Groenewegen et al. [36, 37] began development of the Small Engine Research Bench (SERB). In the first set of studies on the SERB, a 33.5cm³ displacement volume, four-stroke, single cylinder Fuji-Imvac BF-34EI hobbyist aircraft SI ICE was installed on the test bench and run

using various fuels to examine power output (BMEP) and efficiency (BSFC). Groenewegen et al. had difficulty maintaining a consistent air-fuel mixture using the stock carburetor and therefore developed an air-assisted port fuel injection (PFI) system. Results showed that running the engine on heavy fuels increased efficiency (reduced BSFC) slightly at lower engine speeds but made the engine more susceptible to knocking. To avoid knock, ignition timing was retarded, which decreased BMEP.

In 2013, after a re-design of the SERB (similar to the current configuration), Ausserer et al. began testing a 3W Modelmotoren 55i engine. The 3W-55i is a single-cylinder, two-stroke, 55cm³ displacement volume, SI small UAV engine. The engine was run with its stock carburetor from 3000 – 8000 rpm at throttle settings of ¼ open, ½ open, ¾ open, and wide open throttle (WOT). Results showed BSFC ranging from 0.9 – 2.1 kg/kW-h, with an overall fuel conversion efficiency of 6 – 14% [15]. Also in 2013, Baranski et al. developed the JABtronic engine control unit (ECU) in-house at the SERL [38, 39]. The JABtronic ECU allowed for precise control of fuel-air mixture and ignition timing. Although it was originally developed for a four-cylinder, turbocharged, 1200cm³ light aircraft engine, it was later integrated into to the SERB.

In 2014 Rittenhouse et al. attempted a complete energy balance on the SERB with the 3W-55i engine. As the engine was run through its speed range, energy pathways were categorized as brake power, friction power, exhaust enthalpy, and heat rejection. Each of the energy pathways was quantified as a percentage of the fuel energy entering the engine, with a maximum fuel conversion efficiency of 12.5% at 7500 rpm

[40]. Energy losses due to short circuiting and incomplete combustion were not measured.

Finally, for his PhD research, Ausserer performed a complete energy balance, knock studies, and alternative fuel studies for three two-stroke SI engines of 28, 55, and 85 cm³ displacement [10]. The results of Ausserer's work showed that 40 – 60 % of the fuel energy entering the two-stroke engines was lost to short circuiting. This was the predominant source of energy loss for all operating conditions in the study. The work of Ausserer provided a solid foundation for understanding the energy pathways of small, two-stroke ICEs, but it also raised some questions. Specifically, “What are the energy loss pathways of small four-stroke ICEs?” And “If small four-stroke ICEs do not lose 40 – 60% of the incoming fuel energy to short-circuiting, where does the energy go?”

3. Methodology

Chapter Overview

The purpose of this chapter is to describe the experimental setup and procedures used in this project. The chapter is divided into four subsections. Section 3.1. describes the layout and instrumentation used for testing the engines on the SERB. Section 3.2. discusses the engines selected for testing. Section 3.3. describes the processes and procedures used in testing the engines. Section 3.4. discusses the methods used for determining the experimental uncertainty associated with the data collected on the SERB.

3.1. Small Engine Research Bench (SERB)

The SERB has been adapted and reconfigured several times over the last 3 – 4 years to accommodate studies of various engines ranging in power output from 1 – 4 kW. A schematic of the current configuration of the SERB is shown in Figure 14 while a photograph is shown in Figure 15. The SERB was built from the ground up with the goal of performing first law energy balances on small displacement engines. The energy pathways considered were brake power, exhaust sensible enthalpy losses, cooling load losses, incomplete combustion losses, and (for two-stroke engines) short circuiting or scavenging losses. These concepts of these energy pathways were discussed in Section 2.4.1, and the equipment and techniques used to measure them are discussed in this Section and Section 3.3. Descriptions of the SERB layout and instrumentation are described in the following four subsections as follows: Section 3.1.1 discusses air and

fuel delivery, drivetrain and torque measurement in Section 3.1.2, the cooling subsystem in Section 3.1.3, and the data acquisition and engine control in Section 3.1.4.

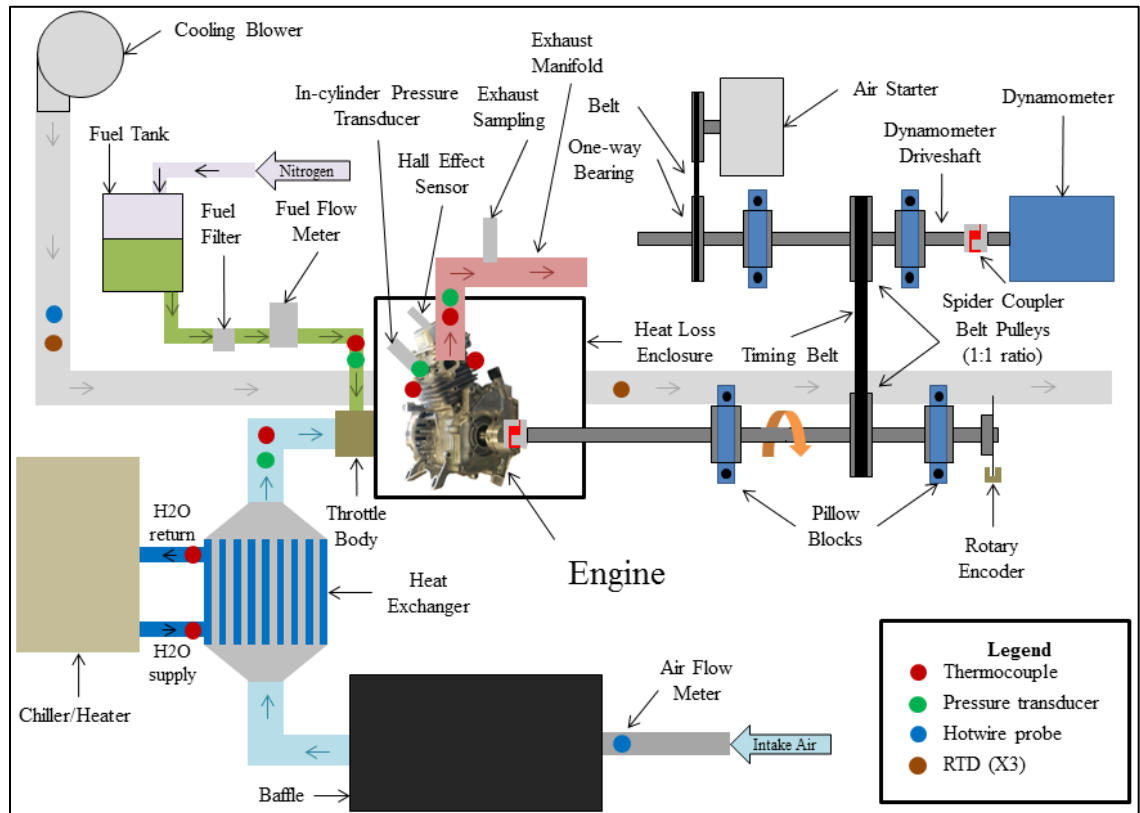


Figure 14. Small engine research bench (SERB) schematic.

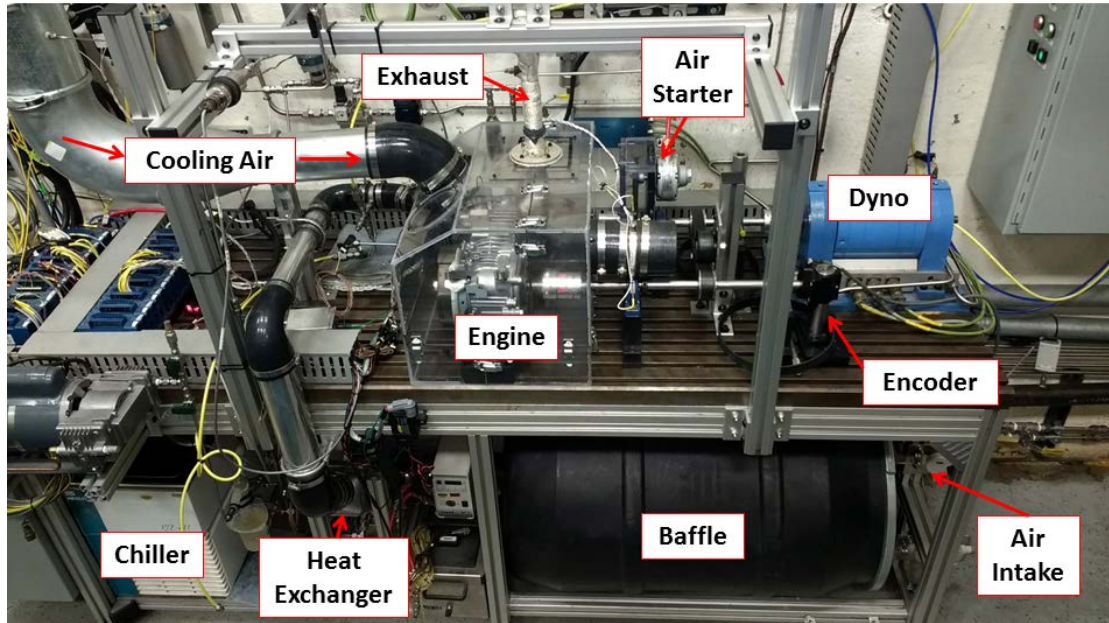


Figure 15. Small engine research bench (SERB) photograph.

3.1.1. Air/Fuel Delivery

Intake air to the engine first passed through a parallel array of three TSI 40211 high performance linear mass flow meters. The parallel array allowed for one or two of the flow meters to be capped under low airflow conditions (low rpm, low throttle), or all three to be open under higher demand test conditions. The flow meters were each rated for 300 SLPM, with $\pm 2\%$ accuracy. The flow meters were installed in one end of a 55 gallon baffle which provided dampening of the intake air flow oscillations, shown in Figure 16.

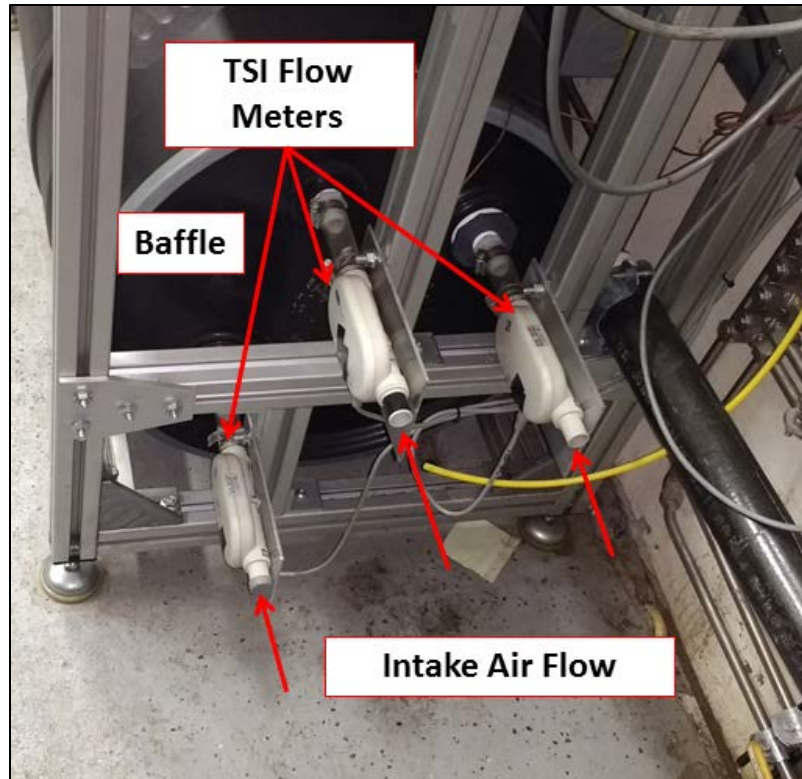


Figure 16. Engine air intake of the SERB. Intake air is inducted through a parallel array of three TSI flow meters.

After exiting the damping baffle, intake air was passed through 7.62 cm tubing into a heat exchanger. Heat exchanger temperature was maintained using a Thermo Neslab RTE-211 recirculating water bath chiller held at a constant 30° C. The chiller was rated for heating up to 0.8 kW or cooling up to 0.5 kW, and holding intake air temperature to $\pm 2^{\circ}\text{C}$. After passing through the heat exchanger, intake air was ducted through 5.08 cm tubing, with intake temperature and pressure being measured with a thermocouple and pressure transducer. All thermocouples on the SERB (unless noted otherwise) were Class 1, Type J, accurate to $\pm 1.5^{\circ}\text{C}$ from $-40 - 375^{\circ}\text{C}$ plus $\pm 0.004^{\circ}\text{C}$ per degree over 375°C . All pressure transducers on the SERB (unless noted otherwise)

were low bandwidth (maximum frequency of 2000 Hz) Honeywell TJE pressure transducers with an accuracy of $\pm 0.1\%$ of their full range.

Intake air velocity was measured using an Omega Engineering FMA 902A-V1-S hot-wire anemometer, capable of measuring 0 – 5.08 m/s air velocity. The hot-wire anemometer had an accuracy of $\pm 1.5\%$ of full scale plus $\pm 0.5\%$ of the reading. The 5.08 cm tubing was further reduced via connectors before the intake air was passed through an 18mm Ecotrons throttle body. The throttle body was purchased from the manufacturer with a pre-installed servo for throttle control. After exiting the engine, exhaust gases were routed through a custom built exhaust manifold fabricated at the SERB. The test exhaust manifold, shown in Figure 17, featured a 2.54 cm exhaust pipe with a thermocouple installed approximately 5 cm from the test engine exhaust port. The 2.54 cm exhaust pipe expanded into a 5.08 cm pipe, with eight additional ports which were used for installing additional thermocouples, a pressure transducer, and for exhaust sampling.

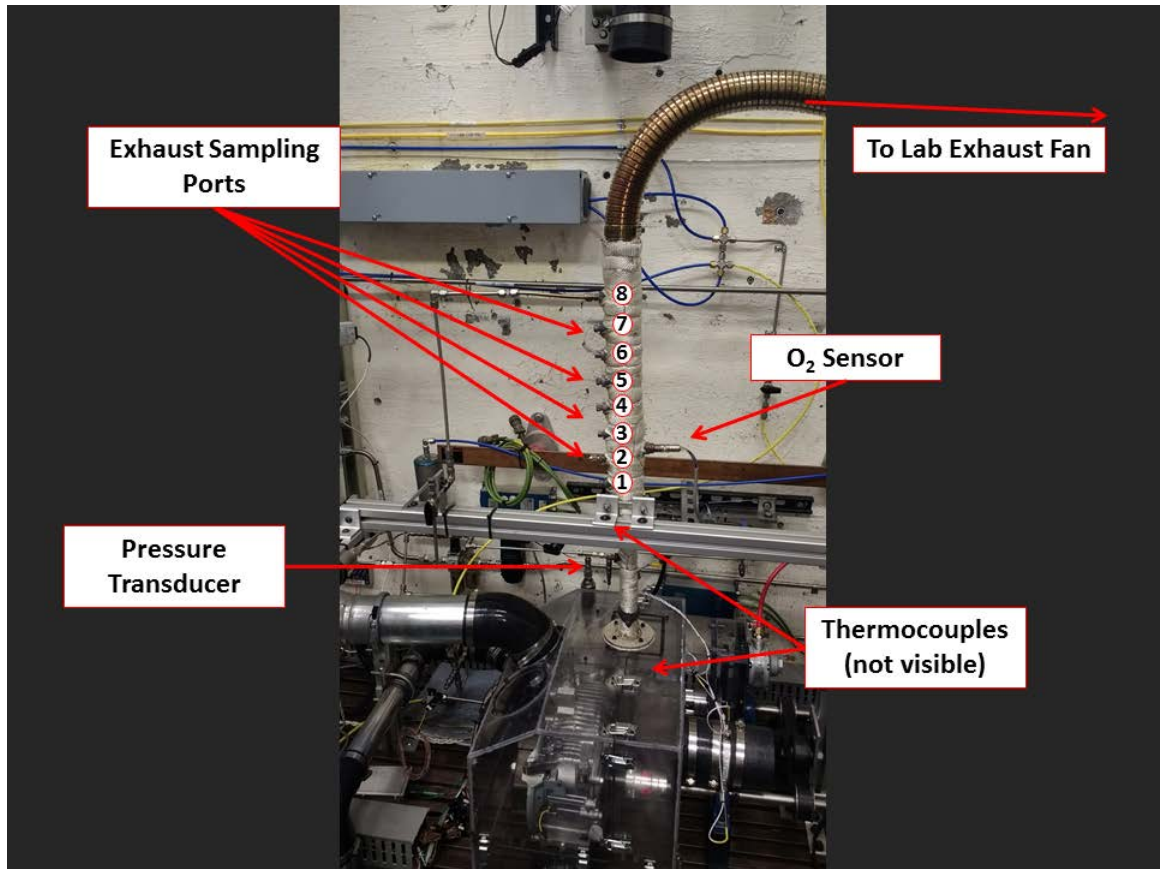


Figure 17. SERB exhaust manifold for measuring exhaust pressure and temperature and taking exhaust samples.

The exhaust manifold was wrapped entirely with fiberglass tape to minimize radiative heat losses. The exhaust manifold also contained an NGK 24300 O₂ sensor coupled with a Powerdex AFX automotive type AFR meter. The 5V analog output of the AFR meter was connected to the LSDAQ (discussed in Section 3.1.4) and displayed on a NI LabVIEW program used to monitor and control SERB functions (also discussed in Section 3.1.4). The AFR meter was configured as a lambda meter (the inverse of equivalence ratio), and was capable of measuring lambda values from 0.62 – 1.1 ($\phi = 0.9 – 1.6$). The AFR meter was used as a primary method of determining air/fuel

mixture when the test engines were run with stock carburetors and a back-up method when using the SERB EFI system. To prevent the laboratory exhaust fans from pulling a vacuum on the exhaust manifold, the 15.24 cm diameter laboratory exhaust was indirectly coupled to the SERB exhaust manifold.

The 98% iso-octane, 2% n-heptane primary reference fuel was stored in a 10 Liter bladder accumulator (which was pressurized with nitrogen) using a high precision regulator to 70 ± 0.58 psi. 0.635 cm stainless steel fuel lines were run from the accumulator to a 128 g/min Ecotrons EFIJ-2-128 fuel injector, with inline sequential 40 μ m and 7 μ m fuel filters. After the fuel filters, fuel flow rate was measured using a Max Machinery 213 positive displacement analog flow meter. The flow meter had a 0-10 VDC analog signal output and was capable of measuring 0.5 – 1800 cm³/min with an accuracy of $\pm 0.2\%$ of the reading or 0.027 cm³/min, whichever was larger. Fuel temperature and pressure were measured using a thermocouple and pressure transducer of the types previously mentioned. Two pneumatic solenoids were used as safety cutoff valves for the fuel line to the engine. Both solenoids were controlled from outside the test cell via the SERL's programmable logic controller (PLC) system.

3.1.2. Drivetrain and Torque Measurement

A schematic of the SERB drivetrain is shown in Figure 18. The 1.905 cm diameter ANSI keyed stainless steel primary driveshaft was either directly coupled to the 1.905 cm diameter output shaft of the test engines or coupled to a 304 stainless steel driveshaft adapter using Ruland jaw coupling hubs and a spider. The primary driveshaft was supported by two ABEC-1 class bearings, press fit into pillow-blocks which sat on

top steel riser blocks to maintain the proper clearance height from the bench. A US Digital 1800 count per revolution E6 optical encoder was installed on the primary driveshaft, which provided crank angle position to a resolution of 0.2° . The encoder also provided a once per revolution index signal.

The primary driveshaft was coupled to a secondary driveshaft using taper lock pulleys and a Power Grip G2 toothed belt. The pulleys were identically sized to maintain a 1:1 rotation speed ratio between the two shafts, and belt tension was provided using a spring loaded tensioner on the return side of the belt and an idler pulley on the tension side of the belt. One end of the secondary driveshaft was attached via a v-belt and pulley to a GAST 2AM-NCW-7B lubricated air motor, which was used for starting the engine. The air motor was connected to the SERL shop air with a one-way bearing installed between the pulley and secondary driveshaft to allow the driveshaft to spin freely after the engine was started. The other end of the secondary driveshaft was connected via Ruland jaw coupling hubs and spider to a water-cooled Magtrol 2-WB-65 eddy current dynamometer. The dynamometer was capable of measuring up to 20 N-m of torque at up to 10,000 rpm (12 kW continuous power). The measurement accuracy of the dynamometer for both speed and torque was $\pm 0.5\%$ of full scale. The dynamometer was controlled using a Magtrol DSP6001 dynamometer controller with an inline TSC 401 torque and speed conditioner, which was coupled to the data acquisition and control computer using a National Instruments (NI) General Purpose Interface Bus (GPIB). All dynamometer controls and monitoring were accomplished via the “low speed data acquisition and control” program (hereto referred to as the “LSDAQ”). Friction testing

of the SERB drivetrain in this configuration has shown friction losses for the system to be 69.2 ± 8.0 W per 1000 rpm [10].

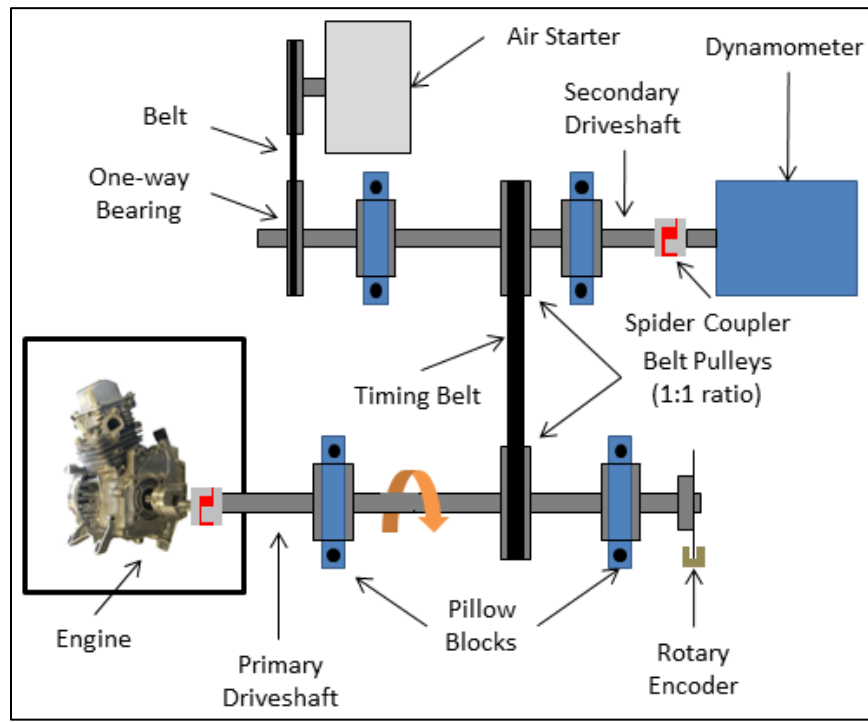


Figure 18. SERB drivetrain schematic.

3.1.3. Cooling Subsystem

To cool the test engines, a 2.24 kW Baldor cooling blower was used. Cooling air was forced through a 15.24 cm diameter duct, which tapered down to a 10.16 cm diameter before entering the sealed engine cooling enclosure which completely surrounded the engines. A schematic of the cooling system is shown in Figure 19. In the 15.24 cm diameter section of the cooling duct, an Omega Engineering FMA 905A-V1 hot-wire anemometer was installed to measure cooling air velocity. The hot-wire anemometer was capable of measuring 0-50.8 m/s velocity at an accuracy of $\pm 1.5\%$ of

full scale plus $\pm 0.5\%$ of the reading. Three Omega platinum class A Resistance Temperature Detectors (RTDs) were also installed in the 15.24 cm diameter section of the cooling duct to measure the temperature of the cooling air entering the sealed cooling enclosure. The RTDs were accurate to $\pm 0.15^\circ\text{C}$ plus $\pm 0.002^\circ\text{C}$ per degree from -100°C – 400°C .

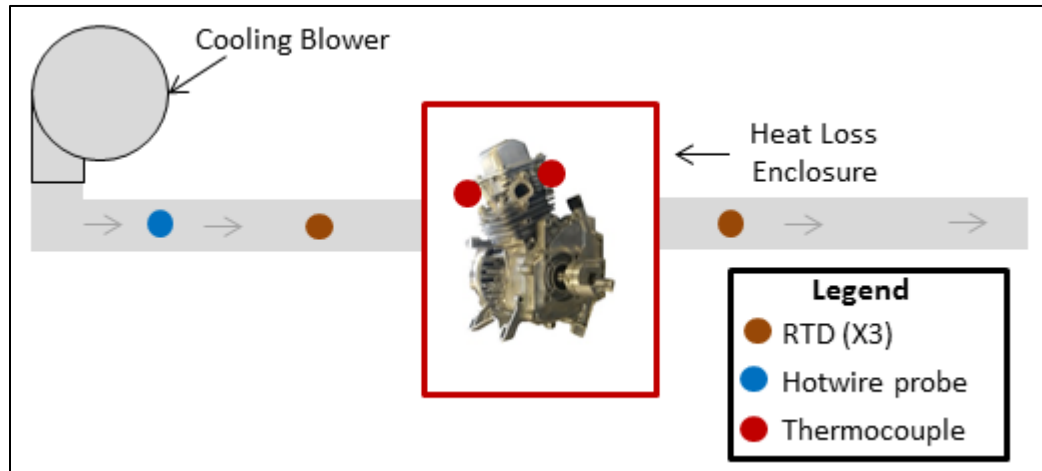


Figure 19. SERB cooling subsystem schematic.

The sealed cooling enclosure, shown in Figure 20, was constructed of 0.476 cm thick clear polycarbonate. The enclosure was constructed in four pieces to allow for partial removal in the event that access to the test engine was needed before or after test runs. The modular design also allowed the enclosure to be completely removed and reinstalled after the test engines had been aligned and secured to the test bench. Previous iterations of the cooling enclosure required removal of the engine from the test bench (and subsequent realignment) if the enclosure required complete removal. All seams on the cooling enclosure were sealed with 0.3175 cm thick foam tape to minimize air leaks. Three Omega platinum class A RTDs were installed at the outlet of the cooling enclosure

to obtain the temperature difference across the enclosure. Although slight modifications were made to the enclosure to allow for geometric differences in the test engines, the same enclosure was used for all of the engines tested in this study. The location of the exhaust and cooling air inlet access holes were relocated and a 3.81 cm thick piece of polystyrene foam insulation was added to block off empty space in the enclosure for test engines number four and five.

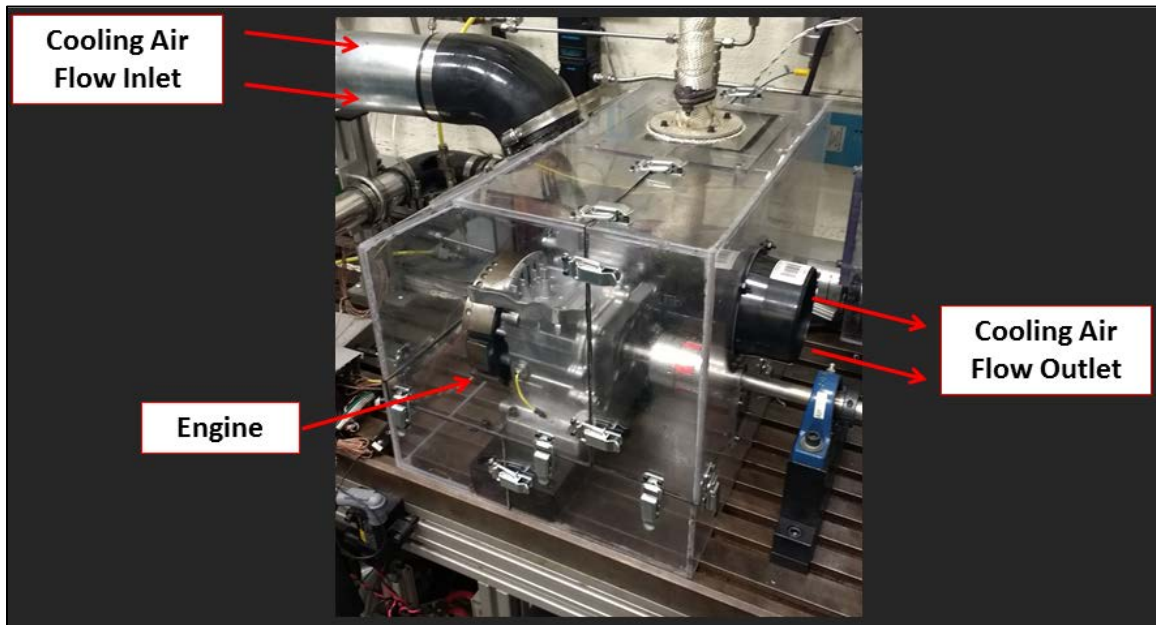


Figure 20. The SERB engine cooling air enclosure.

3.1.4. Data Acquisition/Engine Control

For data acquisition and engine control, three different systems were used: the LSDAQ, the JABtronic ECU, and the AVL program. The LSDAQ, previously mentioned in Sections 3.1.1 and 3.1.2, was used for low speed data acquisition and control. The LSDAQ consisted of two NI Compact Field Point backplanes, with eight slots available on each backplane for signal processing cards. For data acquisition, there

were six TC-120 thermocouple cards, two AI-100 and one AI-118 analog input cards. The cards were used to monitor all temperatures and pressures, intake and cooling air hot-wire anemometers, intake air mass flow meters, the fuel mass flow meter, and secondary dynamometer analog speed and torque signals. The LSDAQ had a maximum frequency of 10 Hz and was configured to collect and record data at a frequency of 4 Hz. For control purposes, an AO-210 analog output card and a RLY-425 relay card were used. The cooling blower motor and air starter motor were controlled using the analog output card. Safety interlocks for the air starter were controlled using the relay card. The LSDAQ also controlled the dynamometer using an NI General Purpose Input Bus (GPIB) and the heater/chiller used to maintain intake air temperature using an RS232 based communication protocol. All of the LSDAQ controls for the dynamometer, heater/chiller, and JABtronic ECU were performed using a NI LabVIEW software interface.

The JABtronic ECU, discussed briefly in Section 2.4.4, was developed at SERL by Baranski et al. [38, 39], and consisted of both hardware and software components. The JABtronic software communicated via RS232 protocol and was stored on an XMOS microcontroller, with an operating frequency of up to 1 GHz. Using the same NI LabVIEW interface as the LSDAQ, the JABtronic ECU allowed the user to control ignition timing, fuel injector timing and duration, and the EFI system throttle servo. Ignition signals were sent to an AEM Performance Electronics High Output Smart Coil (part # 30-2853). The spark plug was a Kistler Type 6118B pressure transducer spark plug, which had a linearity of $\pm 0.5\%$ of full scale and a sensitivity of $\pm 1\%$ at $200 \pm$

50°C. The pressure transducer spark plug allowed for the continuous measurement of in-cylinder pressure while the engine was in operation, a requirement for the AVL Indismart Combustion Analyzer discussed next. All timing signals from the JABtronic ECU were accurate to $\pm 0.2^\circ$ of crank angle.






The AVL Indismart Combustion Analyzer provided IMEP, CoV of IMEP, and mass fraction of fuel burned using input signals from the Kistler pressure transducer spark plug and the US digital optical encoder. Operating on an 800 kHz sampling frequency, the AVL program converted the signal from the piezoelectric pressure transducer spark plug into an analog voltage signal using a Kistler SCP 2852A12 signal conditioning chassis fitted with a 5064C charge amplifier. The AVL program user interface allowed the user to monitor ignition and fuel injector signals and provided real time measurements of IMEP, CA10, CA50, and CA90 on a PC. Displayed values were averages of the last 10 cycles, and a manual data collection feature allowed the user to sample and export data for the previous 400 cycles.

3.2. Engine Selection and Preparation

There were three primary requirements for the selection of test engines for use in this study. First, the engines needed to be four-stroke gasoline engines. Second, the test engines were to be small (less than 250 cm³) displacement volume. Third, to minimize changes to the SERB, the engines needed to be single cylinder. Other considerations for engine selection were the intended use (Were they built for use on small aircraft or something else?), power rating, and displacement volume. To maintain similarity with

the prior SERB study (Ausserer [10]), the maximum rated power of the test engines was to be in the range of 2.5 – 6.7 kW, and displacement volume was to be as close as possible to 28 – 85 cm³. Due to the inherent differences between two-stroke and four-stroke engines (discussed in Section 2.1), the displacement volume of a four-stroke engine with the same rated power as a two-stroke engine is typically double. Recalling Figure 13 from Section 2.4.3, there is very little data publicly available regarding the efficiency of ICEs with 10 – 200 cm³ of displacement volume. Taking these factors into consideration, a survey of small aircraft four-stroke single cylinder engines was performed. It was discovered that there are few four-stroke single cylinder engines commercially available at the higher end of the aforementioned power range. Consequently, the five engines chosen for the study were a mix of two engines designed and built for small aircraft (Torqpro 70 and OS GF40) and three engines designed for powered equipment (Honda GX120, GX160, and GX200). A summary of the test engine design parameters and performance characteristics is shown in Table 3.

Table 3. Test engine design and performance characteristics.

Engine	OS GF40	Torqpro TP70	Honda GX120	Honda GX160	Honda GX200
					
Displacement (cm³)	39.96	70.69	118	163	196
Bore (mm)	40	50	60	68	68
Stroke (mm)	31.8	36	42	45	54
Max Rated Power (kW)	2.8	4.6	2.6	3.6	4.2
Speed @ Max. Power (rpm)	8600	6800	3600	3600	3600
Speed Range (rpm)	1800-9000	1300-6800	2000-3600	2000-3600	2000-3600
Compression Ratio	9:1	9.5:1	8.5:1	9.0:1	8.5:1
Mean Piston Speed (m/s)	9.116	8.16	5.04	5.4	6.48
BMEP (bar)	9.78	11.53	7.34	7.36	6.97
Mass (kg)	1.17	2.04	13	15.1	16.1
Specific Power (kW/kg)	2.39	2.26	0.20	0.24	0.25
Cylinder Surface Area to Volume Ratio (1/cm)	1.63	1.36	1.14	1.03	0.96

From the images and mass values listed in Table 2 it is clear that the OS GF40 and Torqpro TP70 engines were built to be as light as possible, while the Honda engines were much larger. The GF40 and TP70 engines were built for hobby aircraft and therefore lack an internal oil sump, pull start, or integrated fuel tank. The Honda GX120, GX160, and GX200 engines were built primarily for the purpose of running small powered equipment and are therefore completely self-contained. Furthermore, the Honda engines were not manufactured to be flight worthy. Since the SERB was designed and built for small aircraft engines like the GF40 and TP70, some components were removed

from the Honda engines prior to installing them on the SERB. Specifically, the stock pull starts, carburetors, air cleaners, ignition systems, fuel tanks, and exhaust systems were removed from the Honda engines. Figure 15 shows a side-by-side comparison of the Honda GX120 engine in its stock configuration and how it was configured to run on the SERB. Only the stock carburetors and exhaust were removed from the GF40 and TP70 engines.

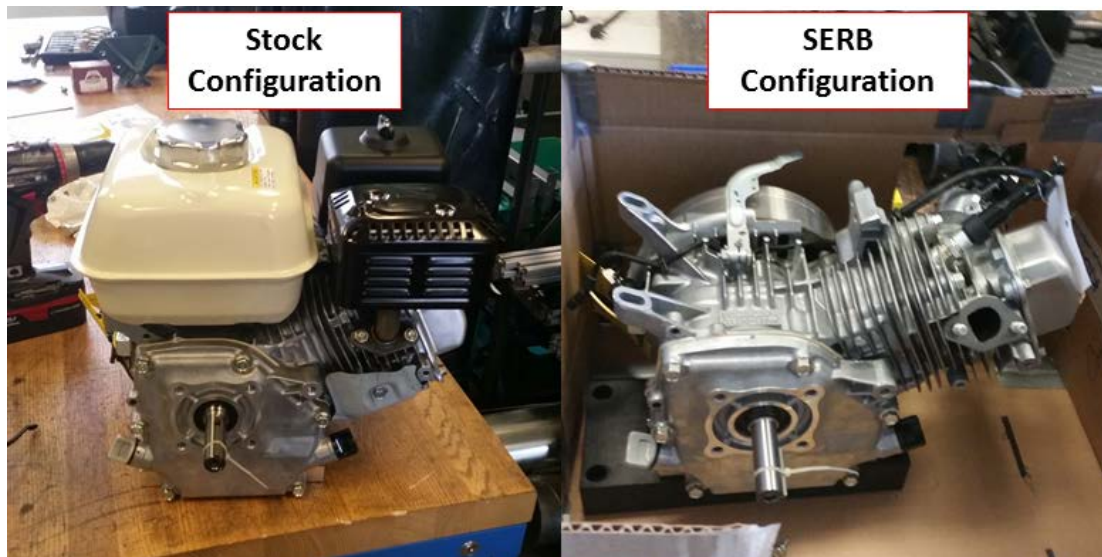


Figure 21. Honda GX120 in stock configuration (left), and as tested on the SERB (right).

3.3. Energy Balance Methodology

As discussed in Section 2.4, the primary objective of this project was to characterize the energy pathways of small displacement volume four-stroke ICEs. This objective was accomplished using the first law of thermodynamics energy balance approach. Recall from Section 2.4 that energy losses (or pathways) can be categorized as thermal losses (Q_{th}), friction losses (Q_f), exhaust sensible enthalpy losses (Q_{exh}), incomplete combustion losses (Q_{inc}), and short circuiting losses (Q_{sc}). To simplify the analysis for

this study, internal engine friction losses were not measured independently; they were included in the category of thermal losses. Additionally, short circuiting losses were considered negligible due to the differences of two-stroke and four-stroke engines discussed in Section 2.1 and experimental findings throughout the study (typically 0.5 – 2.0% of fuel energy entering the engine). Rather than measuring the energy quantities lost in each pathway (Q_{th} , Q_{inc} , etc.) the *rates* of energy losses (or power losses) were measured. Energy power losses were categorized as brake power (P_b , also known as useable energy), power lost to thermal energy (P_{th}), power lost to exhaust sensible enthalpy (P_{exh}), and power lost to incomplete combustion (P_{inc}). Five parametric studies were performed for each engine to examine the effects of varying engine speed, cooling load, combustion phasing, fuel mixture, and throttle position. For each test point an energy balance was performed. While Section 3.1 detailed the equipment and instrumentation used to perform the energy balances, Section 3.3 examines the equations and some of the procedures used in accomplishing them.

3.3.1. Brake Power, Thermal Losses, and Exhaust Enthalpy Losses

Brake power (P_b) was determined using the measured (or brake) torque (τ_b), and the engine speed (N) obtained from the dynamometer output signal. Drivetrain friction losses of 69.2 W per 1000 rpm (measured previously by Ausserer [10]) were added to the brake power measured from the dynamometer. Figure 22 shows the results of the test used to determine drivetrain friction. For the test, an electric motor was used to spin the drivetrain (with no engine attached) while dynamometer measurements were taken. A load cell was attached to a cradle for the electric motor to measure the torque being

applied by the motor. The dyno torque measurement was then subtracted from the torque applied at the electric motor cradle to determine the drivetrain torque losses. The torques were then converted to power and plotted at various speeds. Further details of the drivetrain friction correction determination can be found in Horn et al. [41].

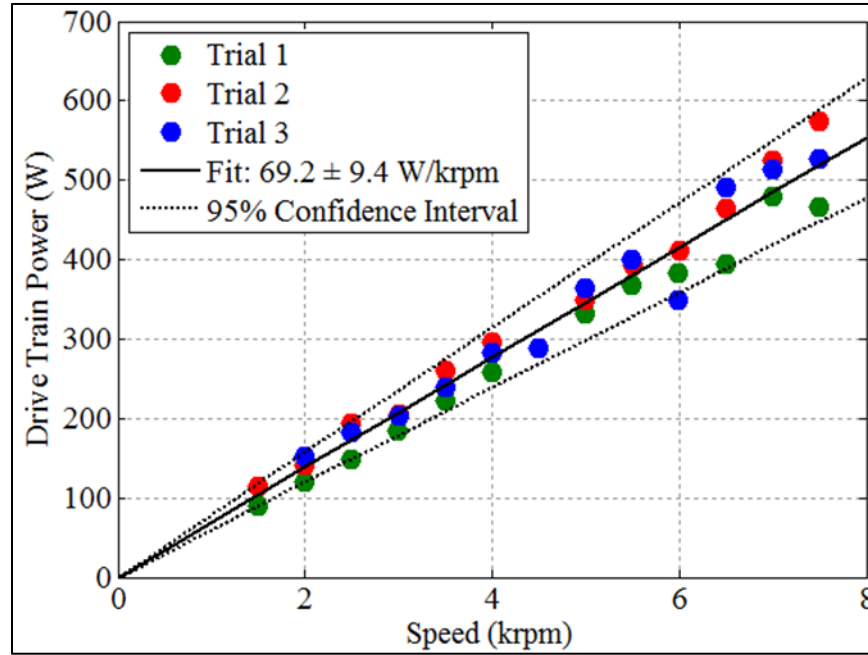


Figure 22. Power dissipation by SERB drivetrain measured as the difference between power delivered at the electric motor cradle and power dissipated at the dynamometer. For the fit, $R^2=0.96$ [10].

The following equation, including the drivetrain friction correction factor and a torque offset term (τ_{offset}), was used to calculate brake power:

$$P_b = \left[\frac{2\pi \left(\tau_b(N \cdot m) - \tau_{offset}(N \cdot m) \right) + (6.92 * 10^{-5})}{1000 * 60} \right] N(rpm) \quad (28)$$

The torque offset term (τ_{offset}) was inserted into Equation (28) to remove the small baseline torque reading that the dynamometer displayed prior to applying a load. The baseline reading was due to small fluctuations in the output signal voltage.

Power lost to thermal energy (P_{th}), was calculated using a control volume approach. The mass flow rate of cooling air (\dot{m}_{cool}) entering the cooling enclosure was determined using the air velocity of the cooling air, measured from the hot-wire anemometer, the cross-sectional area of the cooling air duct, and the density of the cooling air (assuming an ideal gas and calculated using the temperature and pressure of the cooling air). The hot wire anemometer was installed in the center of the cooling duct upstream of the engine, with approximately ten diameters of the cooling duct both upstream and downstream to ensure a fully developed flow profile. Radiative heat losses were neglected as were heat losses through the cooling enclosure. Prior testing on the SERB by Rittenhouse et al. showed heat losses through a similarly constructed cooling enclosure to be negligible [40, 42]. The specific heat of the cooling air ($C_{p,cool}$), was obtained using the temperature of the cooling air and National Institute of Standards and Technology (NIST) Shomate equation coefficients [43]. The temperature difference across the cooling enclosure while the engine was running (ΔT_{cool}) was determined using the RTD arrays at the inlet and exit of the cooling enclosure. After an engine run, the engine was stopped while the cooling blower motor was left at a nominal speed for several minutes. During this time, the temperature change across the enclosure was monitored as it gradually dropped until a steady state was reached. The drop in ambient temperature across the cooling enclosure when the engine was stopped and cool ($\Delta T_{amb,cool}$),

typically 0.2 – 0.6 °C) was then subtracted from ΔT_{cool} before calculating the final P_{th} .

The final equation of P_{th} was:

$$P_{th} = \dot{m}_{cool} C_{p,cool} (\Delta T_{cool} - \Delta T_{amb}) \quad (29)$$

Power lost to exhaust sensible enthalpy (P_{exh}) is the energy associated with cooling the hot exhaust products to the temperature of the fuel and air entering the engine. The exhaust composition was assumed using an incomplete perfect combustion model with Ar, CO, CO₂, H₂O, and N₂ as products. To measure P_{exh} a thermocouple was placed in the SERB exhaust manifold 5 cm downstream of the test engine exhaust port. This location was decided upon when it was found to have produced the highest exhaust temperature from several locations that were tested in the SERB exhaust system. Using the exhaust temperature, the enthalpy per mole of each of the exhaust products, referenced to 298.15 K, ($\bar{h}_i^\circ - \bar{h}_{i,298.15}^\circ$) was calculated using NIST Shomate equation coefficients [43]. The enthalpy per mole for each exhaust product was then multiplied by the mole fraction of each product (χ_i). The resulting quantities were then combined to obtain the total enthalpy per mol for the exhaust products, which was then multiplied by the total molar flow rate of the exhaust gases (\dot{n}_{exh}) to provide the power losses as shown in the following equation:

$$P_{exh} = \dot{n}_{exh} \sum_i^{n,products} \chi_i (\bar{h}_i^\circ - \bar{h}_{i,298.15}^\circ) \quad (30)$$

3.3.2. Incomplete Combustion Losses

Incomplete combustion losses were calculated using two different methods involving the use of an HP 6890 gas chromatograph (GC). Carbon monoxide, hydrogen, nitrogen, and oxygen concentrations in the exhaust gases were determined using an Agilent brand HP MOLSIV column connected to a thermal conductivity detector (GC-TCD), while unburned hydrocarbon concentrations in the exhaust gases were determined using a J&W Scientific 115-3532 alumina column connected to a flame ionization detector (GC-FID). Both methods were developed and used previously at the SERL by Ausserer et al. [10, 44]. All exhaust samples were collected from the SERL exhaust manifold sampling ports (shown in Figure 16) in accordance with SAE standard J254 [45], using a R254-AT-AA1 Dia-Vac inert sampling (vacuum) pump and collected in 2 L Supel inert foil gas sampling bags. Before collecting each exhaust sample the air in the exhaust sampling system's ¼ inch stainless steel lines was purged for 90 seconds using the vacuum pump. 0.1 mL samples were extracted from the sampling bags and injected into the GC using 0.5mL Vici precision sampling syringes.

Using intake air nitrogen concentration as an internal standard, exhaust samples were first run through the GC-TCD to determine CO, H₂, and O₂ concentrations in the exhaust gases. Prior to exhaust testing, gas bags with known concentrations of CO, H₂, N₂, and O₂ were injected into the GC-TCD to determine the TCD response. Calibration curves for each of the gases detected by the GC-TCD are included below in Figure 23 - Figure 26. The N₂ and H₂ calibrations were generated by Ausserer [10], and were also used in the current study due to similarities in the levels of N₂ and H₂ (Figure 23 and

Figure 25) found in the exhaust samples of both Ausserer and the current study. The O₂ levels of the current study were significantly lower than those found by Ausserer and the CO levels of the current study were significantly higher than those found by Ausserer. Consequently, O₂ and CO calibration curves were re-accomplished for the current study using different gas mixtures which more accurately reflected the concentrations of O₂ and CO seen in the current study. The new calibration curves for O₂ and CO are shown in Figure 24 and Figure 26. All four of the calibration linear curve fits had an R² value greater than 0.99.

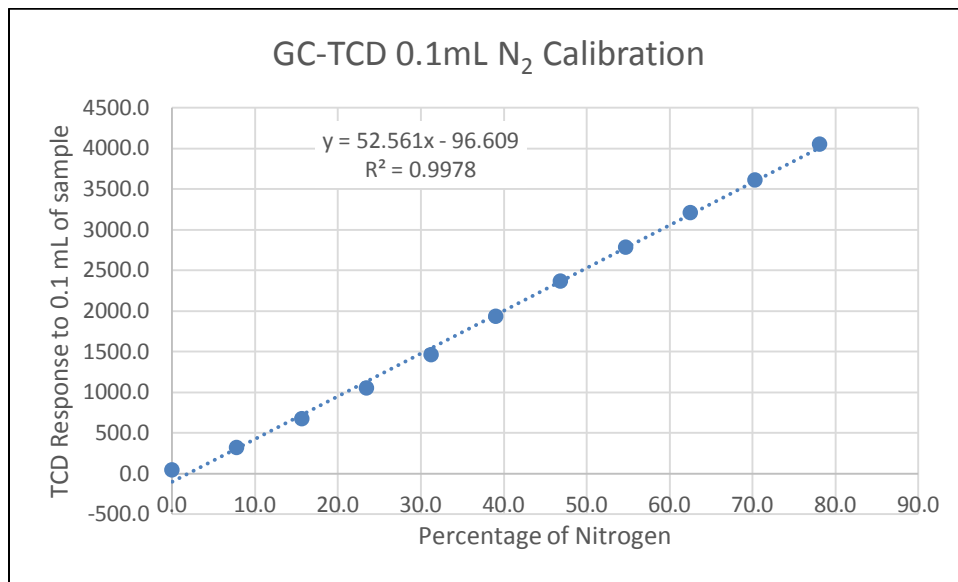


Figure 23. GC-TCD calibration curve for nitrogen.

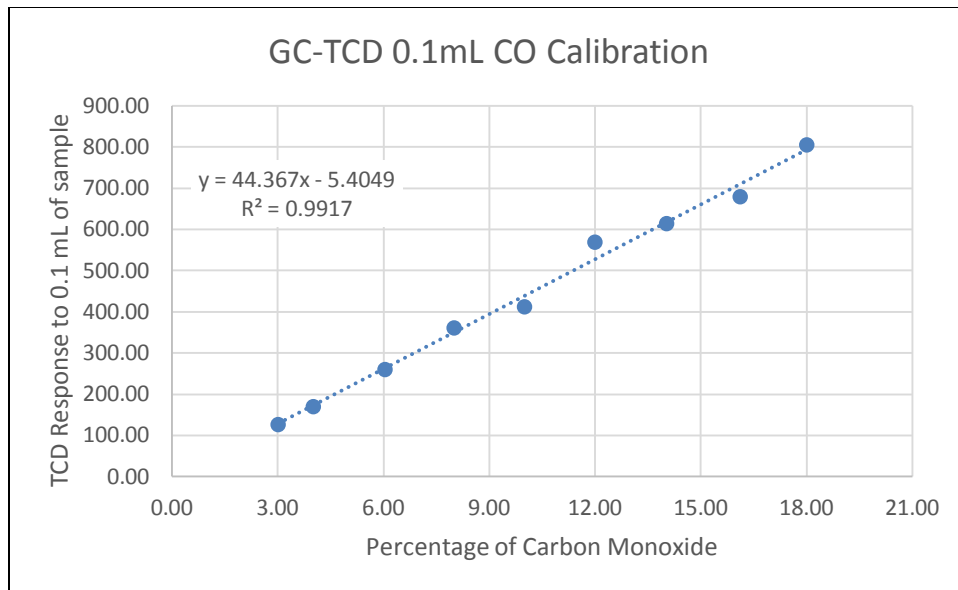


Figure 24. GC-TCD calibration curve for carbon monoxide.

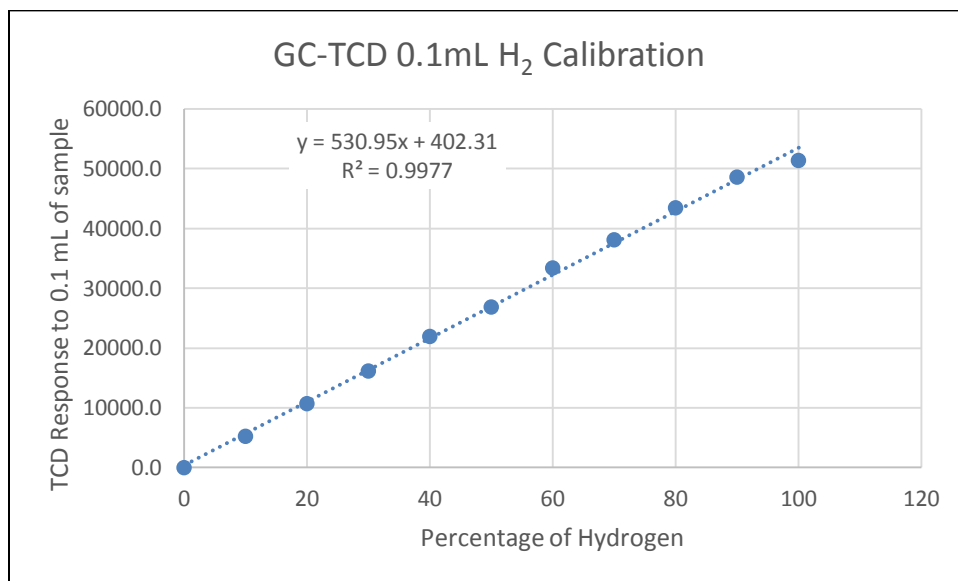


Figure 25. GC-TCD calibration curve for hydrogen.

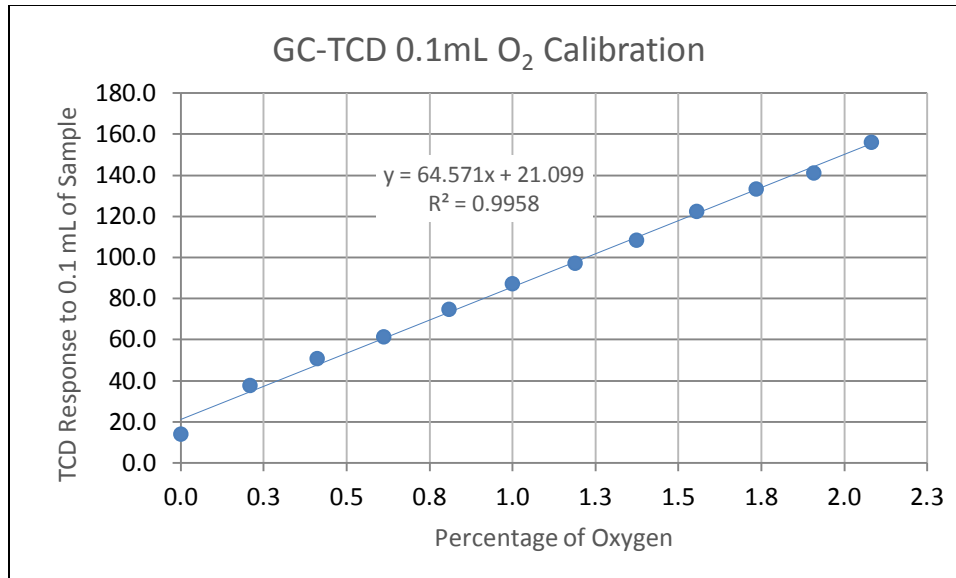


Figure 26. GC-TCD calibration curve for oxygen.

The following equation was then used to determine the mass flow rate of each species:

$$\dot{m}_i = \left(\frac{\%_i}{\%N_2} \right) \frac{\dot{m}_{air} \chi_{N_2}}{MW_{N_2}} MW_i \quad (31)$$

where \dot{m}_i was the mass flow rate of species “i” in the exhaust sample, $\%_i$ was the percent of species “i” in the exhaust sample, $\%N_2$ was the percent of nitrogen in the exhaust sample, χ_{N_2} was the mass fraction of nitrogen in the ambient air, MW_i was the molecular weight of species “i” in the exhaust sample, and MW_{N_2} was the molecular weight of nitrogen. The vast majority of the energy in the exhaust gases is contained in the hydrogen and carbon monoxide, which made up the bulk of the calculated incomplete combustion losses.

Using the iso-octane in the exhaust as an internal standard, the exhaust samples were then injected into the GC-FID to determine the concentrations of UHCs in the

exhaust samples. The mass flow rate of each UHC species was calculated using the following equation:

$$\dot{m}_i = \left(\frac{y_{i,ex}}{y_{iso-octane,ex}} \right) \frac{\dot{m}_f \chi_{iso-octane,f}}{MW_{iso-octane}} MW_i \quad (32)$$

where $y_{i,ex}$ was the mole fraction of species “ i ” in the exhaust sample, $y_{iso-octane,ex}$ was the mole fraction of iso-octane in the exhaust sample, \dot{m}_f was the mass flow rate of fuel, $\chi_{iso-octane,f}$ was the mass fraction of iso-octane in the fuel, and $MW_{iso-octane}$ was the molecular weight of iso-octane. This method had slightly higher uncertainty under lean running conditions. Power lost to incomplete combustion was then calculated using NIST standard enthalpy values [43] with the following equation:

$$P_{inc} = \sum \dot{n}_i (\bar{h}_{c,i}) \quad (33)$$

where \dot{n}_i was the molar flow rates of H₂, CO, and UHCs in the exhaust and $\bar{h}_{c,i}$ was the enthalpy of combustion per mole for H₂, CO, and UHCs in the exhaust.

3.4. Experimental Uncertainty

Experimental uncertainty was calculated using methods from Moffatt [46, 47] and t-distribution analysis. The calculation of the uncertainty in brake power, cooling load, exhaust sensible enthalpy, and incomplete combustion as a percentage of fuel energy are detailed in the following paragraphs. For the example calculations, the GX120 engine was operated with the following conditions: engine speed of 2800 rpm, WOT, ϕ of 1.05, CA50 of 8° aTDC, and cylinder head temperature of 140° C.

The measurement uncertainties seen in the results and analysis of Chapter 4 were calculated largely as relative uncertainties (as a percentage of the measurement), then multiplied by the measurement to determine the absolute uncertainty of the measurements. This method allowed for the calculation of uncertainty of unitless parameters such as fuel conversion efficiency (η_f) or volumetric efficiency (η_v). Some of the uncertainties were converted from absolute uncertainty to relative uncertainty or from relative uncertainty to absolute uncertainty so that they may be combined with other absolute uncertainties before being converted back to total relative uncertainties again. As seen in Section 3.1, many different types of instrumentation were used on the SERB, which quantified measurement uncertainty using several different units and techniques.

As stated previously, a combination of absolute and relative uncertainties was used in the analysis, with all final combined uncertainty determinations as unitless relative uncertainties. Moffat defines absolute and relative uncertainties as follows [47]:

$$\text{absolute uncertainty: } x_i = \hat{x}_i \pm \delta x_i \quad (34)$$

$$\text{relative uncertainty: } x_i = \hat{x}_i \pm \delta x_i / x_i \quad (35)$$

Where x_i is the input data for the desired quantity (R), \hat{x}_i is the best estimate of the value (or measured value), and δx_i is the uncertainty interval of the value. The basic form of Equation (35) was the primary method used to calculate relative uncertainty in this study. Determining the uncertainty interval is frequently accomplished using another of Moffat's general equations [46]:

$$\delta R = \left\{ \sum_{i=1}^N \left(\frac{\partial R}{\partial X_i} \delta X_i \right)^2 \right\}^{1/2} \quad (36)$$

Referring back to Section 3.3.1 and 3.3.2, all of the final power loss energy pathway equations were linear, which somewhat simplified the uncertainty analysis. According to Moffat [46], “it is sometimes possible to do the calculation of relative uncertainty directly.” This is possible when the equation is in a pure “product form,” or in the form shown in Equation (37):

$$R = x_1^a x_2^b x_3^c \dots x_M^m \quad (37)$$

In this case, relative uncertainty is calculated using the following general equation:

$$\frac{\delta R}{R} = \left\{ \left(a \frac{\delta x_1}{x_1} \right)^2 + \left(b \frac{\delta x_2}{x_2} \right)^2 + \dots + \left(m \frac{\delta x_M}{x_M} \right)^2 \right\}^{1/2} \quad (38)$$

The calculation of brake power (P_b) uncertainty serves as an example, where the base form of the brake power equation (in kW) was:

$$P_b = \tau N$$

Referring back to Equation (37), $P_b = R$, $\tau_b = x_1$, $N = x_2$, and the exponents a and b were unity, therefore the general equation for brake power relative uncertainty was:

$$\frac{\delta P_b}{P_b} = \left\{ \left(\frac{\delta \tau_b}{\tau_b} \right)^2 + \left(\frac{\delta N}{N} \right)^2 \right\}^{1/2} \quad (39)$$

The values of τ_b and N were determined using a 15 second sampling of dynamometer measurements (taken at a sampling rate of 4 Hz, 60 samples over a 15 second period), thus the mean values of the 60 torque and engine speed measurements were 7.10 N-m and 2772.79 rpm, respectively. $\delta \tau_b$ and δN were the instrument uncertainties (according

to the manufacturer) of 0.10 N-m and 50 rpm, respectively. Inserting these values into Equation (39), the total dynamometer relative uncertainty for the brake power measurement was:

$$\frac{\delta P_{b,measured}}{P_{b,measured}} = \left\{ \left(\frac{0.10 N \cdot m}{7.10 N \cdot m} \right)^2 + \left(\frac{50 rpm}{2772.79 rpm} \right)^2 \right\}^{1/2} = 2.29\% \quad (40)$$

In order to determine the total relative uncertainty of the brake power *as a percentage of fuel energy* ($\frac{\delta P_{b,\% fuel}}{P_{b,\% fuel}}$), the total brake power measurement with the drivetrain friction correction (discussed in Section 3.3.1) was required ($P_{b,measured} + P_{b,correction}$), as well as the total absolute uncertainty of the measurement, including the uncertainty of the drivetrain friction correction ($\delta P_{b,measured} + \delta P_{b,correction}$). After obtaining those values, the final relative uncertainty of the brake power as a percentage of fuel energy ($\frac{\delta P_{b,\% fuel}}{P_{b,\% fuel}}$) was calculated by combining the brake power relative uncertainty ($\varepsilon_{P_{b,total}}$) with the relative uncertainty of the mass flow rate of fuel ($\varepsilon_{\dot{m}_f}$) using the root-sum-square (RSS) method:

$$\frac{\delta P_{b,\% fuel}}{P_{b,\% fuel}} = \left\{ (\varepsilon_{P_{b,total}})^2 + (\varepsilon_{\dot{m}_f})^2 \right\}^{1/2} \quad (41)$$

where

$$\varepsilon_{P_{b,total}} = \frac{(\delta P_{b,measured} + \delta P_{b,correction})}{(P_{b,measured} + P_{b,correction})} \quad (42)$$

The combined measured brake power and drivetrain friction correction could be directly calculated from Equation (28), however it was split into two equations for measured brake power ($P_{b,measured}$), and the drivetrain friction correction brake power

($P_{b,correction}$) to facilitate the calculation of the absolute uncertainty of the measured brake power ($\delta P_{b,measured}$). The following equations show these calculations:

$$P_{b,measured} = \frac{2\pi(\tau_b - \tau_{offset})N}{1000 * 60} = \frac{2\pi(7.10N \cdot m - 0.136N \cdot m) * 2772.79rpm}{1000 * 60} = 2.022kW \quad (43)$$

$$P_{b,correction} = (6.92 * 10^{-5}) * N = (6.92 * 10^{-5}) * 2772.79rpm = 0.192kW \quad (44)$$

$$\delta P_{b,measured} = P_{b,measured} * \frac{\delta P_{b,measured}}{P_{b,measured}} = 2.022kW * 2.29\% = 0.0463kW \quad (45)$$

Determination of the absolute uncertainty of the drivetrain friction correction ($\delta P_{b,correction}$) started by examining the curve shown in Figure 22. The slope of the curve fit was determined to be 69.2 W/krpm with a standard error of 4.08 W/krpm, which was calculated using statistical tools in Microsoft Excel. This provided a relative slope variation error of (4.08 W/krpm) / (69.2 W/krpm), or 5.90%. Using an inverse t-statistic analysis with a two-tailed probability of $P = 0.05$, and 8 degrees of freedom (DOF) (9 data points from Figure 22), the t value was 2.306. The relative uncertainty of the drivetrain friction correction ($\varepsilon_{drivetrain}$) was then calculated to be:

$$\varepsilon_{drivetrain} = 5.90\% * 2.306 = 13.61\% \quad (46)$$

$\delta P_{b,correction}$ was calculated next using:

$$\delta P_{b,correction} = \varepsilon_{drivetrain} * P_{b,correction} = 13.61\% * 0.192kW = 0.0261kW \quad (47)$$

Total brake power relative uncertainty ($\varepsilon_{P_{b,total}}$) was then calculated using the general form of Equation (35):

$$\varepsilon_{P_{b,total}} = \frac{(\delta P_{b,measured} + \delta P_{b,correction})}{(P_{b,measured} + P_{b,correction})} = \frac{(0.0463kW + 0.0261kW)}{(2.022kW + 0.192kW)} = 3.27\% \quad (48)$$

The last uncertainty needed to complete the analysis was the relative uncertainty of the mass flow rate of fuel ($\varepsilon_{\dot{m}_f}$). The fuel mass flow rate was determined by multiplying the volumetric flow rate of fuel (measured directly using a piston type flow meter) by the calculated density of the fuel. The mass flow rate of fuel was 0.205 g/s. The relative uncertainty in the mass flow rate of fuel measurement was determined by combining the relative uncertainty of the volumetric fuel flow rate (1.50%) and the relative uncertainty in the fuel density calculation (0.18%)³, providing a relative uncertainty in the mass flow rate of fuel ($\varepsilon_{\dot{m}_f}$) of 1.68%. Finally, the total relative uncertainty of the brake power as a percentage of fuel energy calculation was:

$$\frac{\delta P_{b,\% fuel}}{P_{b,\% fuel}} = \left\{ (\varepsilon_{P_{b,total}})^2 + (\varepsilon_{\dot{m}_f})^2 \right\}^{1/2} = \{(3.27\%)^2 + (1.68\%)^2\}^{1/2} = \underline{3.67\%} \quad (49)$$

The cooling load loss as a percentage of fuel energy relative uncertainty was calculated using similar methods to those previously discussed. The equation for cooling load losses (in kW) was:

$$P_{th} = \dot{m}_{cool} C_{p,cool} (\Delta T_{cool} - \Delta T_{amb}) \quad (29)$$

The sources of measurement uncertainty were the hot wire anemometer used to measure the velocity of the cooling air (which was then used to calculate \dot{m}_{cool}) and the thermocouples used to measure the temperature of the cooling air. The device absolute uncertainty for the hot wire anemometer velocity measurement (δV) (from the

³ Uncertainties in the volumetric flow rate and density of fuel were calculated using methods previously described, namely t-statistic analysis and the forms of Equation (35) and Equation (38).

manufacturer) was 1.016 m/s with a bias error ($\delta_{V,b}$) of 1.0%. The device absolute uncertainty for the thermocouple cooling air temperature measurement ($\delta\Delta T$) (from the manufacturer) was 0.34°C. Since the calculation of cooling load losses was a linear, “product form” equation, the calculation of the relative uncertainty of the cooling load as a percentage of fuel energy was straightforward, using the form of Equation (38). Utilizing the same test point analyzed for brake power, the measured cooling air velocity (V) was 8.8 m/s, the measured temperature drop across the cooling enclosure (ΔT) (minus an offset for the ambient temperature drop across the enclosure, ΔT_{amb}) was 13.6° C, and the relative uncertainty of the mass flow rate of fuel ($\varepsilon_{\dot{m}_f}$) again was 1.68%. The cooling load as a percentage of fuel energy relative uncertainty was then:

$$\frac{\delta P_{th,\% fuel}}{P_{th,\% fuel}} = \left\{ \left[\left(\frac{\delta V}{V} \right)^2 + \left(\frac{\delta \Delta T}{\Delta T} \right)^2 \right]^{1/2} + \left(\varepsilon_{\dot{m}_f} \right)^2 \right\}^{1/2} + \delta_{V,b} =$$

$$\left\{ \left[\left(\frac{1.016 m/s}{8.8 m/s} \right)^2 + \left(\frac{0.34^\circ C}{13.6^\circ C} \right)^2 \right]^{1/2} + (1.68\%)^2 \right\}^{1/2} + 1.0\% = \underline{12.93\%} \quad (50)$$

For the exhaust enthalpy losses, the base equation used to calculate the losses (in kW) was:

$$P_{exh} = \dot{n}_{exh} \sum_i^{n,products} \chi_i (\bar{h}_i^\circ - \bar{h}_{i,298.15}^\circ) \quad (30)$$

The primary sources of measurement uncertainty for this equation were the TSI flow meter used to directly measure the mass flow rate of intake air, the piston type flow meter used to measure the volumetric flow rate of the fuel, (which was converted to mass flow

rate of fuel), and the thermocouples used to measure the exhaust and intake temperatures. The relative uncertainty of the mass flow rate of fuel ($\varepsilon_{\dot{m}_f}$) was previously discussed and determined to be 1.68%. The relative uncertainty in the flow rate of intake air was calculated using similar methods to those described above and was determined to be 3.70%. The relative uncertainty of the mass flow rate of exhaust ($\varepsilon_{\dot{m}_{ex}}$) was then calculated using the RSS of the relative uncertainties in the mass flow rates of intake air and fuel and was found to be 4.06%⁴. The effects on the overall uncertainty of the exhaust enthalpy losses as a percentage of fuel energy ($\frac{\delta P_{exh, \% fuel}}{P_{exh, \% fuel}}$) due to uncertainties in the intake and exhaust temperature measurements were found to be negligible due to the large temperature change from intake temperature to exhaust temperature. Omitting the temperature measurement uncertainty terms, the final equation for the relative uncertainty of the exhaust enthalpy losses as a percentage of fuel energy was:

$$\frac{\delta P_{exh, \% fuel}}{P_{exh, \% fuel}} = \left\{ (\varepsilon_{\dot{m}_{ex}})^2 + (\varepsilon_{\dot{m}_f})^2 \right\}^{1/2} = \{(4.06\%)^2 + (1.68\%)^2\}^{1/2} = \underline{4.39\%} \quad (51)$$

The base form of the equation used to calculate incomplete combustion losses (in kW) was:

$$P_{inc} = \sum \dot{n}_i (\bar{h}_{c,i}) \quad (33)$$

Primary sources of uncertainty in the measurements of the incomplete combustion losses were driven by uncertainties in the exhaust gas analysis results (which determined the concentrations of H₂, CO, and UHCs in the exhaust). The contributions to the incomplete

⁴ The mass flow rate of the exhaust (\dot{m}_{ex}) was later converted to molar flow rate of exhaust (\dot{n}_{exh}) as seen in Equation (30).

combustion losses made by H₂ (P_{inc,H_2}), CO ($P_{inc,CO}$), and UHCs ($P_{inc,UHC}$), along with the absolute uncertainties of these contributions ($\delta P_{inc,H_2}$, $\delta P_{inc,CO}$, $\delta P_{inc,UHC}$) were used in the form of Equation (35) to calculate the overall relative uncertainty in the incomplete combustion loss ($\varepsilon_{P_{inc,total}}$):

$$\varepsilon_{P_{inc,total}} = \frac{(\delta P_{inc,H_2} + \delta P_{inc,CO} + \delta P_{inc,UHC})}{(P_{inc,H_2} + P_{inc,CO} + P_{inc,UHC})} \quad (52)$$

The contributions of H₂, CO, and UHCs to the incomplete combustion losses were calculated by multiplying the molar flow rate of each constituent by their respective enthalpies of formation, the result of which were $P_{inc,H_2} = 0.41$ kW, $P_{inc,CO} = 1.41$ kW, and $P_{inc,UHC} = 0.10$ kW. To determine the absolute uncertainties of each constituent to the incomplete combustion losses ($\delta P_{inc,H_2}$, $\delta P_{inc,CO}$, $\delta P_{inc,UHC}$), the relative uncertainty of the measurement of each constituent was first determined, then multiplied by the contribution of each constituent to the overall incomplete combustion losses (P_{inc,H_2} , $P_{inc,CO}$, $P_{inc,UHC}$). Recalling Equation (31), the mass flow rate of H₂ and CO (\dot{m}_i) was calculated using the mass flow rate of intake air (\dot{m}_a), the concentration of H₂ or CO ($\%_i$) in the exhaust sample, and the concentration of N₂ ($\%N_2$) in the exhaust sample. The relative uncertainty of \dot{m}_a was 3.70%, and the relative uncertainty of the concentrations of H₂, CO, and N₂ were 2.86%, 8.06%, and 2.99% respectively⁵. The absolute uncertainties for the H₂ and CO contributions to the incomplete combustion losses ($\delta P_{inc,H_2}$, $\delta P_{inc,CO}$) were then:

⁵ The concentration of the relative uncertainties of each exhaust constituent was calculated using the calibration curves shown in Figure 23 - Figure 26 and t-statistic analysis similar to the discussion of the drivetrain friction correction.

$$\begin{aligned}\delta P_{inc,H_2} &= P_{inc,H_2} * \left\{ (\varepsilon_{\dot{m}_a})^2 + (\varepsilon_{\%N_2})^2 + (\varepsilon_{\%H_2})^2 \right\}^{1/2} \\ &= 0.41kW * \{(3.70\%)^2 + (2.99\%)^2 + (5.56\%)^2\}^{1/2} = 0.0228kW\end{aligned}\quad (53)$$

$$\begin{aligned}\delta P_{inc,CO} &= P_{inc,CO} * \left\{ (\varepsilon_{\dot{m}_a})^2 + (\varepsilon_{\%N_2})^2 + (\varepsilon_{\%CO})^2 \right\}^{1/2} \\ &= 1.41kW * \{(3.70\%)^2 + (2.99\%)^2 + (8.06\%)^2\}^{1/2} = 0.1324kW\end{aligned}\quad (54)$$

Recalling Equation (32), the mass flow rate of UHCs (\dot{m}_i) was calculated using the mass flow rate of fuel (\dot{m}_f), the concentration of O₂ or (%O₂) in the exhaust sample, and the concentration of UHCs (%UHCs) in the exhaust sample. The relative uncertainty of \dot{m}_f was 1.68%, and the relative uncertainty of the concentrations of O₂ and UHCs were 13.9% and 5.0%, respectively. The absolute uncertainty for the UHC contribution to the incomplete combustion losses ($\delta P_{inc,UHC}$) was then:

$$\begin{aligned}\delta P_{inc,UHC} &= P_{inc,UHC} * \left\{ (\varepsilon_{\dot{m}_f})^2 + (\varepsilon_{\%O_2})^2 + (\varepsilon_{\%UHC})^2 \right\}^{1/2} \\ &= 0.10kW * \{(1.68\%)^2 + (13.90\%)^2 + (5.00\%)^2\}^{1/2} = 0.0154kW\end{aligned}\quad (55)$$

The total relative uncertainty for the incomplete combustion losses ($\varepsilon_{P_{inc,total}}$) was:

$$\begin{aligned}\varepsilon_{P_{inc,total}} &= \frac{(\delta P_{inc,H_2} + \delta P_{inc,CO} + \delta P_{inc,UHC})}{(P_{inc,H_2} + P_{inc,CO} + P_{inc,UHC})} \\ &= \frac{(0.0228kW + 0.1324kW + 0.0154kW)}{(0.41kW + 1.41kW + 0.10kW)} = 8.89\%\end{aligned}\quad (56)$$

Finally, the total relative uncertainty of the incomplete combustion losses ($\varepsilon_{P_{inc,total}}$) was combined with the fuel mass flow rate relative uncertainty ($\varepsilon_{\dot{m}_f}$) using the RSS method to

provide the total relative uncertainty of the incomplete combustion losses as a fraction of fuel energy ($\frac{\delta P_{inc, \% fuel}}{P_{inc, \% fuel}}$):

$$\frac{\delta P_{inc, \% fuel}}{P_{inc, \% fuel}} = \left\{ \left(\varepsilon_{P_{inc, total}} \right)^2 + \left(\varepsilon_{\dot{m}_f} \right)^2 \right\}^{1/2} = \{ (8.89\%)^2 + (1.68\%)^2 \}^{1/2} = \underline{9.05\%} \quad (57)$$

3.5. Repeatability

To determine the variability of the SERB test results from different tests, a repeatability analysis was done on the results from all of the engines tested. The parametric sweeps were performed in a manner such that one test point from each of the five sweeps (engine speed, equivalence ratio, combustion phasing, head temperature, and throttle) had the same operating conditions. The results of the Honda GX120 repeatability analysis are discussed in the following pages. The results of the repeatability analysis for the remaining four engines are contained in Appendix A.

3.5.1. GX120 Repeatability Analysis

Five test sweeps were performed to examine the effect of engine speed (Sweep 1), equivalence ratio (Sweep 2), combustion phasing (Sweep 3), cooling load (Sweep 4), and throttle setting (Sweep 5). Each of the five sweeps contained one baseline test point where engine speed was 2800 ± 120 rpm, throttle setting was WOT, ϕ was 1.05 ± 0.02 , CA50 was $8^\circ \pm 0.4^\circ$ aTDC, and cylinder head temperature was $140^\circ \pm 1^\circ$ C. The sweeps were performed on different days where environmental conditions in the test cell varied from day to day. Temperature variations in the cooling and intake air were unavoidable, as the test cell where the SERB was located had a large garage door that was open during testing to allow for ventilation of undesirable exhaust emissions. Figure 27 shows the

results of the measured brake power, exhaust enthalpy, cooling load, and incomplete combustion for the same test point in each of the five sweeps on the GX120 engine.

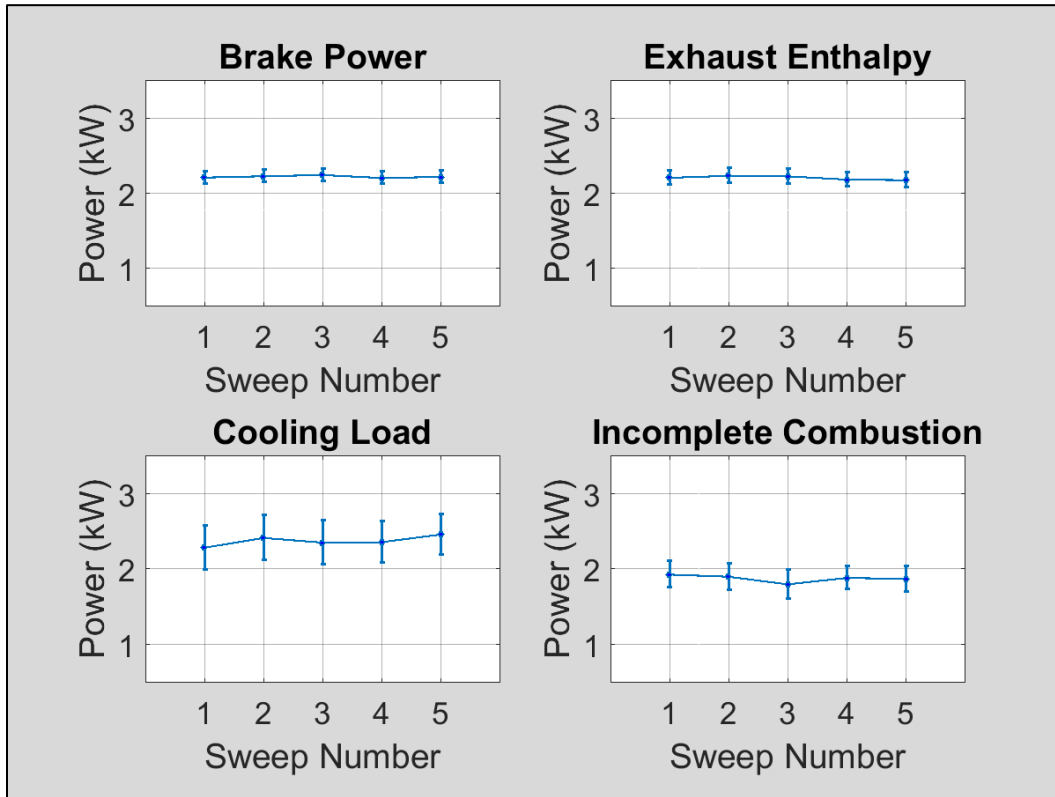


Figure 27. Repeatability of GX120 engine.

Table 4 contains the values plotted in Figure 27, as well as the mean values of the energy measured in each pathway for all five sweeps, the standard deviation of the mean values, and the 95% confidence interval of the mean values. The results of the analysis showed a 1.6% variation in brake power measurement, a 2.7% variation in exhaust enthalpy measurement, 6.4% variation in cooling load measurement, and a 5.9% variation in incomplete combustion measurement. A similar analysis was performed for the remaining four engines, the results of which can be found in Appendix A.

Table 4. Repeatability analysis results for GX120 engine.

Sweep	Brake Power (kW)	Exhaust Enthalpy (kW)	Cooling Load (kW)	Incomplete Combustion (kW)
1	2.214	2.211	2.288	1.932
2	2.232	2.237	2.417	1.903
3	2.247	2.231	2.356	1.803
4	2.209	2.187	2.362	1.888
5	2.222	2.180	2.462	1.875
Mean (kW)	2.225	2.209	2.377	1.880
Std Dev (kW)	0.014	0.023	0.059	0.043
95% CI (kW)	0.035	0.059	0.152	0.111
Variation (%)	1.6	2.7	6.4	5.9

4. Analysis and Results

Chapter Overview

The following chapter is divided into three primary subsections. Section 4.1 details the testing results of the Honda GX120 engine. Section 4.2 contains the results, analysis, and comparison of the three geometrically similar Honda engines (GX120, GX160, and GX200), focusing on how the results scale as engine displacement increases. Section 4.3 discusses the results of the TP70 and GF40 engine testing and further compares these smaller engines to their larger counterparts.

4.1. GX120

The first engine tested in the study was the Honda GX120. The GX120 is a single cylinder, four-stroke engine which is primarily used as the powerplant for small to medium sized powered equipment such as snow blowers or portable water pumps. The engine has a displacement volume of 118 cm³ and a maximum rated power of 2.6 kW at 3600 rpm. A list of engine performance and design characteristics was provided in Section 3.2, Table 3. The testing of the GX120 was done in three stages. First, the SERB exhaust system was validated as discussed in Section 4.1.1. Next, the power of the GX120 engine was examined as discussed in Section 4.1.2. Finally, a series of parametric sweeps was performed as discussed in Sections 4.1.3.1 to 4.1.3.4.

4.1.1. GX120 Exhaust Validation

The first test run on the Honda GX120 engine was an examination of the exhaust gas composition as samples were taken from different exhaust sampling ports on the

SERB exhaust manifold. Previously, when two-stroke engines were tested on the SERB by Ausserer, results showed that the makeup of the exhaust gases changed as the exhaust travelled downstream in the exhaust manifold [10]. In the two-stroke study, 3W-28i (28cm³ displacement), 3W-55i (55cm³ displacement), and 3W-85i (85cm³ displacement) engines were tested on the SERB. Figure 28 shows that O₂ concentrations dropped from approximately 13.2% to 10% from exhaust sampling Port One to Three for the 3W-55i engine, then remained relatively stable at 10% from exhaust Ports Three to six. A similar but less pronounced trend was seen with the 3W-28i engine; while results for the 3W-85i showed O₂ concentration varying from approximately 7% to 9.3% from exhaust Ports one to five before settling at approximately 8.5% from exhaust Ports six through eight. These results indicate that there continued to be significant mixing and reactions occurring in the exhaust gases after exiting the engine combustion chamber.

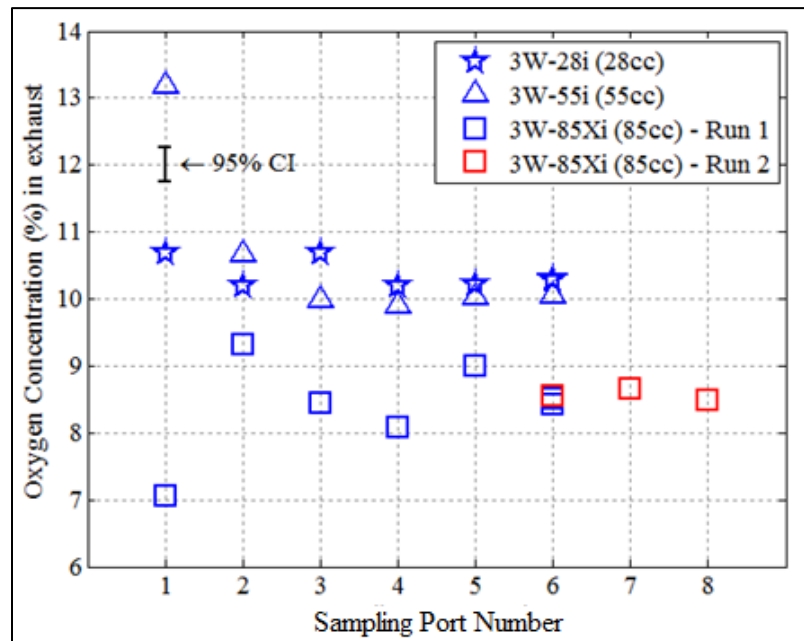


Figure 28. SERB exhaust validation plot from Ausserer [10].

This phenomena was discussed in Heywood and Sher [34], and is generally more of an issue with two-stroke engines as opposed to four-stroke engines. Nevertheless, in order to validate that exhaust samples were being taken at a distance sufficiently downstream of the engine exhaust port to ensure there was no mixing or continued chemical reactions in the exhaust gases, the GX120 engine was run at a baseline condition while exhaust samples were collected from exhaust Ports Two, Four, Six, and Eight. The engine was run at wide open throttle, a speed of 2800 ± 50 rpm, ϕ of 1.05 ± 0.02 , CA50 of $8^\circ \pm 0.4^\circ$ aTDC, and a cylinder head temperature of $135^\circ \pm 1^\circ$ C. Due to the extremely low concentration of oxygen found in the exhaust samples (0.02% - 0.27%), carbon monoxide concentration was used for the GX120 exhaust validation. Figure 29 shows that carbon monoxide concentration had little variation (6.34% – 6.62%) from exhaust Port two through eight. The results of the exhaust validation test showed that there was no mixing in the exhaust and any of the exhaust ports could be used for sampling without concern of exhaust species concentration changes as a function of distance from the engine exhaust port. All exhaust samples for the GX120 engine were collected using exhaust Port four.

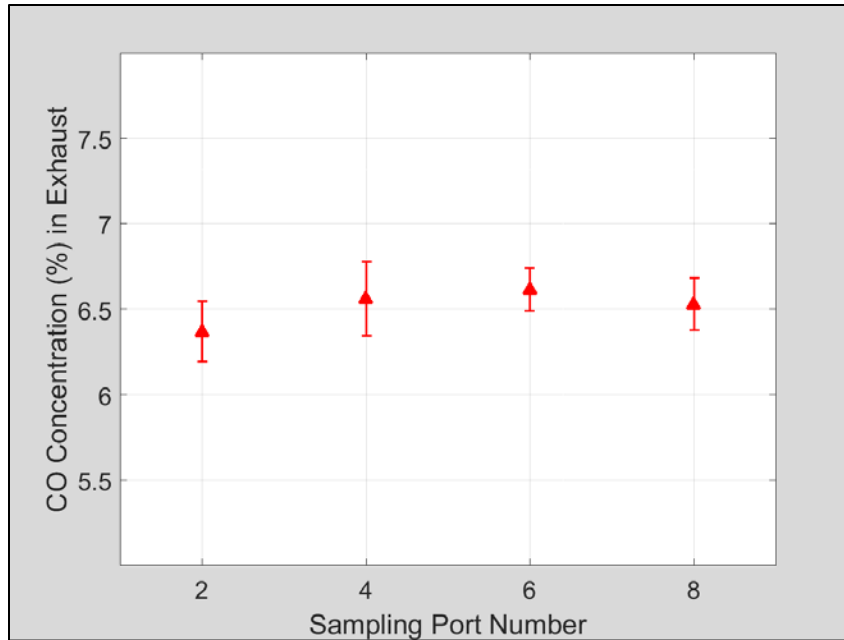


Figure 29. SERB exhaust validation plot from GX120 engine.

4.1.2. GX120 Power Study (Speed Sweep)

The GX120 engine was then run through its manufacturer recommended operating range from 1800 – 3600 rpm. Other conditions held constant were: WOT, ϕ of 1.05 ± 0.02 , CA50 of $8^\circ \pm 0.4^\circ$ aTDC, and cylinder head temperature of $140^\circ \pm 1^\circ$ C. Recall research Objective one from Section 1.2, which aimed to compare the measured brake power from the engine to the manufacturer’s advertised brake power data. This comparison is shown in Figure 30 [48]. Prior to testing, the stock carburetor, ignition system, and exhaust were removed. This was done to allow for precise control and adjustment of equivalence ratio and ignition timing, and to allow for exhaust sampling while the engine was running. While previous SERB small engine testing had shown that test engines typically produced less power than advertised by the manufacturer [7, 10, 15,

36, 37, 44, 49, 50], the results of the GX120 testing showed the engine producing more brake power than advertised. At low engine speeds the SERB measured brake power was similar, with a percent difference of approximately 1.9% and 2.5% at 2000 and 2400 rpm, respectively. However, as engine speed increased, the increase in power above the manufacturer data grew as well, with percent differences of approximately 4.4%, 7.4%, and 15.8% at 2800, 3200 and 3600 rpm, respectively.

There were several factors which could have led to the increase in brake power above the manufacturer's data. First, there may have been a small increase (~1%) in the heating value of the PRF used in this study versus the gasoline that was likely used to test the engine by the manufacturer. Second, as seen in later results, the ignition timing of the engine in its stock configuration was 18 - 19° bTDC while on the SERB it was set to 26 - 33° bTDC. The ignition timing was advanced on the SERB to maintain a CA50 of 8° aTDC, which is generally where MBT is achieved for a given engine speed. The manufacturer's decision to retard the stock ignition timing to 18 - 19° bTDC allowed the engine to have a much greater resistance to knock, while sacrificing a small amount (~3-5%) of brake power and torque. Third, to keep equipment costs down and reduce configuration changes to the SERB, a single 18mm diameter throttle body was purchased for the study of all five of the test engines used in this paper. The throat diameter of the stock carburetor for the Honda GX120 was 16mm. If the stock carburetor's throat diameter was slightly undersized for the engine design, the engine would be capable of producing more power (especially at higher engine speed) with a larger throat diameter. Finally, the stock exhaust of the GX120 engine consisted of a 7cm long, 2.54cm diameter

exhaust pipe connected to a muffler. The SERB exhaust by contrast was a 40cm long, 2.54cm diameter pipe connected to a 60cm long, 5.08cm diameter pipe with no internal baffling to reduce noise or provide a large amount of back pressure. The differences in the SERB exhaust system and the stock Honda exhaust was suspected to be the most significant cause of the differences in measured brake power versus the manufacturer data.

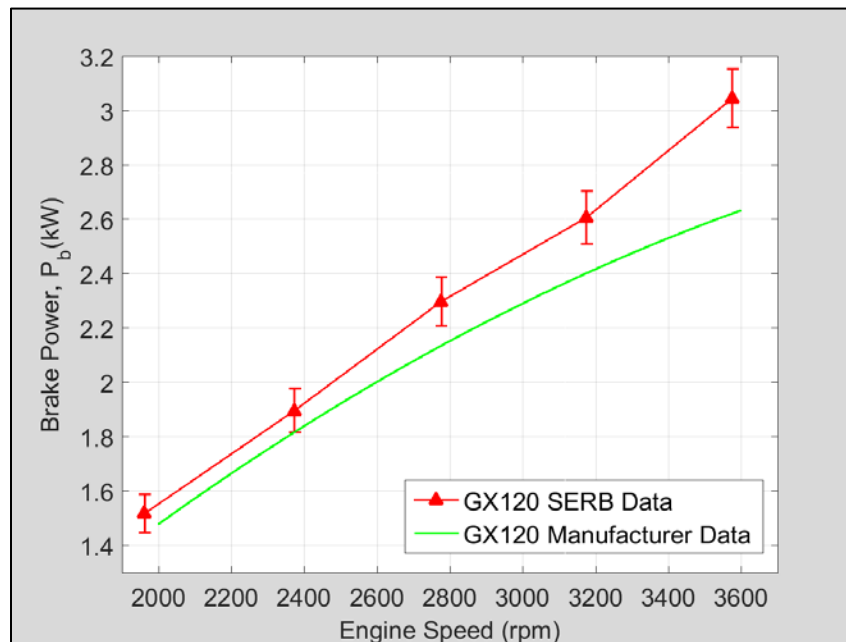


Figure 30. GX120 power curve with the SERB exhaust versus the manufacturer’s advertised power curve.

To determine the validity of the results, another speed sweep was conducted with the SERB exhaust system removed and the stock exhaust reinstalled on the engine. Figure 31 shows the results of running the engine with both the SERB exhaust and the stock exhaust, as well as the manufacturer’s advertised power curve. As shown in the figure, all of the brake power measurements taken with the stock muffler installed were closer to the manufacturer’s advertised power curve than the data points taken with the

SERB exhaust. From 2000 – 3200 rpm the measured brake power was nearly identical to the manufacturer power curve. At 3600 rpm the measured brake power was 2.84 kW, a percent difference of 8.8% from the advertised maximum power of 2.6kW at 3600 rpm. This is likely due to the result of the change in size between the stock carburetor throat and the SERB throttle body. The results indicate that the engine may have been breathing limited at high rpm using the smaller carburetor, but is more than capable of handling the increased air flow rate of the larger throttle body. Some testing of the GX160 was done using the stock ignition, carburetor and exhaust as discussed later in Section 4.2, but all of the remaining data in the study was taken using the SERB ignition, EFI (with the 18mm throttle body), and exhaust.

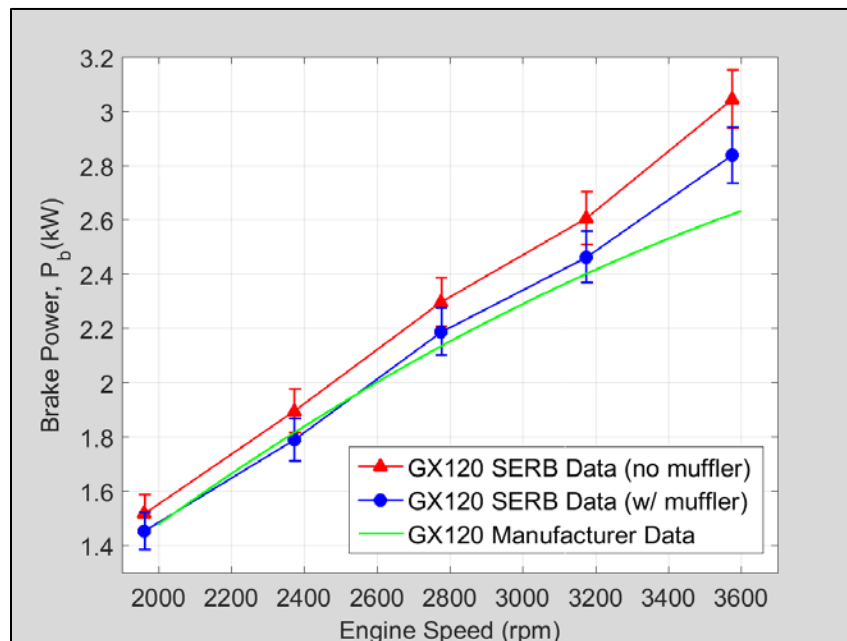


Figure 31. GX120 power curve with the SERB exhaust and stock exhaust versus the manufacturer’s advertised power curve.

After analyzing the power curve results for the two different exhaust systems, the engine was again run through its operating range of 2000 – 3600 rpm at WOT while

holding ϕ constant at 1.05 ± 0.02 , CA50 at $8^\circ \pm 0.4^\circ$ aTDC, and cylinder head temperature at $135^\circ \pm 1^\circ$ C. The amount of measured energy in each pathway (in kW) is shown below in Figure 32. While the amounts of brake power, exhaust sensible enthalpy, and cooling load increased with increasing engine speed, the amount of energy lost to incomplete combustion remained relatively stable near 2.2 kW throughout the entire operating range.

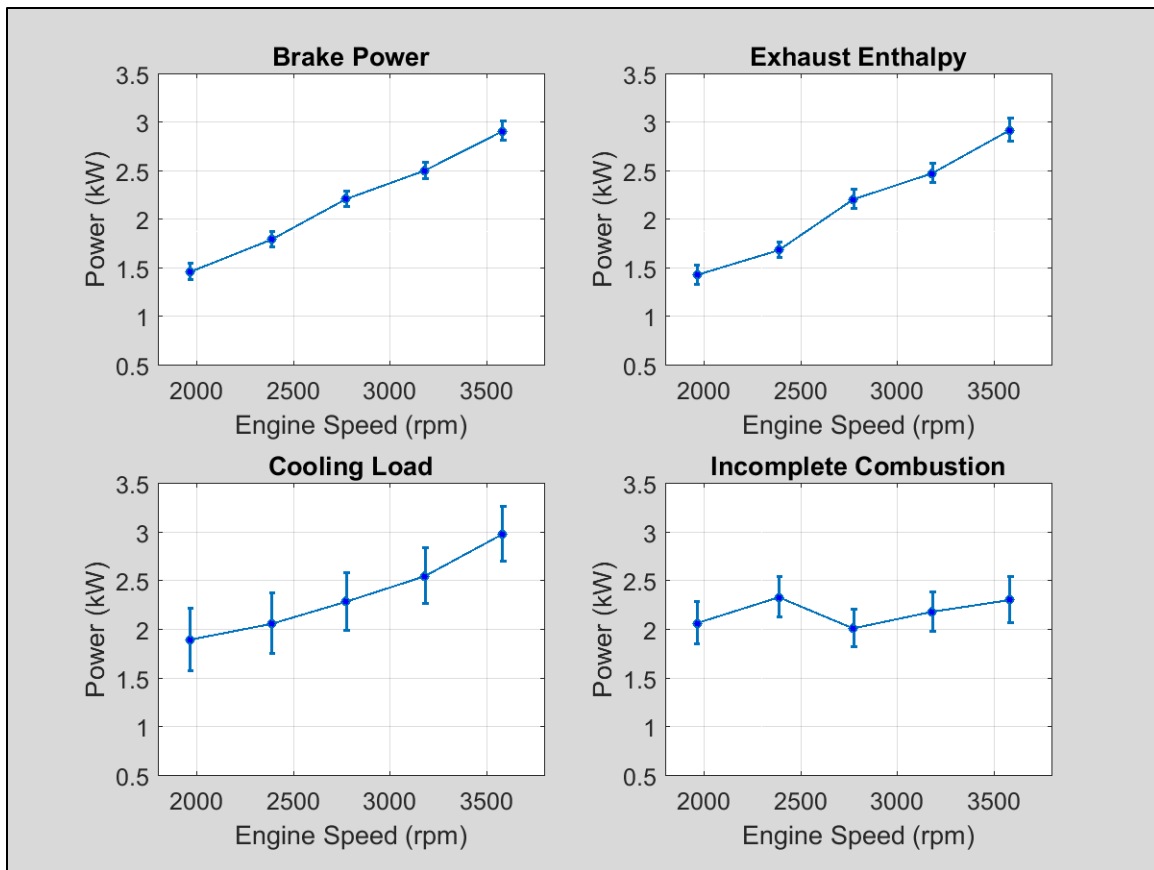


Figure 32. GX120 speed sweep energy pathways (in kW).

To examine this phenomenon more closely, the contributors to the incomplete combustion losses were examined. Figure 33 shows the energy losses (in kW) for the

UHCs, H₂ and CO in the exhaust, as well as the total incomplete combustion energy losses. It can be seen that while the UHC energy losses rose steadily with engine speed, the amount of energy lost was a small contributor to the overall incomplete combustion losses. H₂ and CO losses made up the majority of the incomplete combustion losses and remained relatively steady as engine speed increased. Although the H₂ and CO losses were steady, the levels of H₂ and CO in the exhaust samples was not. The exhaust samples contained 2.46% H₂ at 2000 rpm, which steadily decreased to 1.47% at 3600 rpm. Similarly, CO levels decreased from 6.73% at 2000 rpm to 4.34% at 3600 rpm. The increased concentrations of H₂ and CO at low rpm meant the exhaust gases contained more H₂ and CO energy per unit of volume, but the mass flow rate of the exhaust gases increased with increasing engine speed, keeping the total H₂ and CO losses within approx. 200 – 300 W of each other throughout the speed sweep.

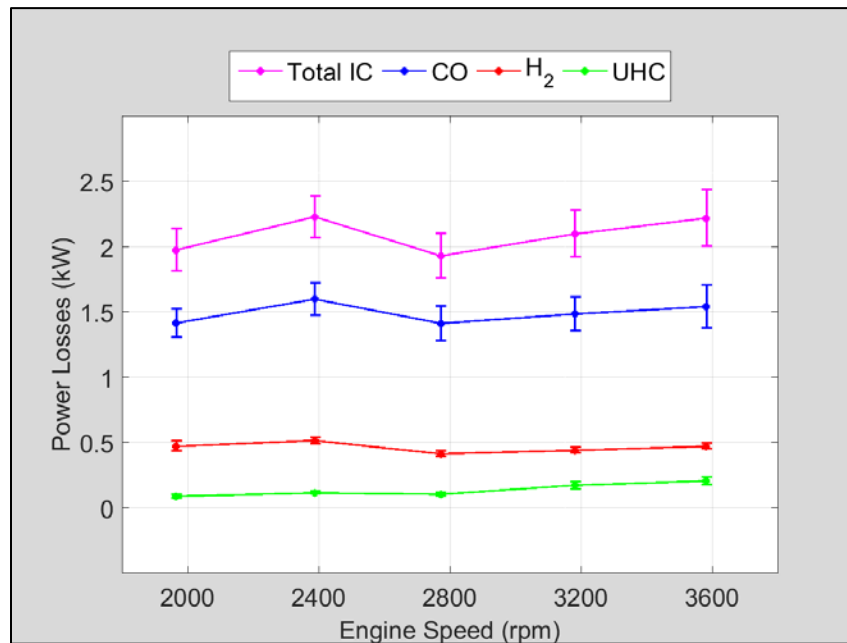


Figure 33. GX120 speed sweep incomplete combustion losses.

It is useful to examine the indicated (i.e. in-cylinder, before losses) power of the engine. Figure 34 shows the indicated mean effective pressure (IMEP) and CoV of IMEP for the GX120 speed sweep. As expected, IMEP increased steadily with increasing engine speed from 8.0 bar at 2000 rpm to 8.6 bar at 3600 rpm. The engine ran very consistently with low CoV of IMEP values (0.7% - 1.1%) throughout the entire operating range. BMEP also steadily increased from 7.6 bar at 2000 rpm to 8.3 bar at 3600 rpm. Indicated power increased from 3.1 kW at 2000 rpm to 6.1 kW at 3600 rpm while internal friction and pumping losses (indicated power – brake power) increased from 1.6 kW at 2000 rpm to 3.2 kW at 3600 rpm. Comparing the total change of BMEP and IMEP to the total change in brake power and indicated power illustrates the usefulness of using mean effective pressures rather than power when comparing different engines to each other – large changes in power (brake or indicated) translate to much smaller variations in mean effective pressures.

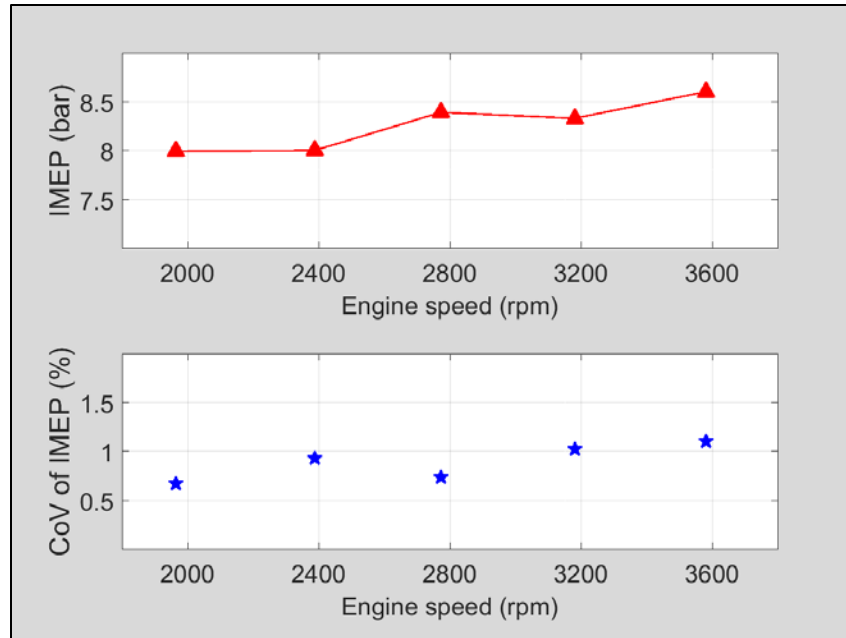


Figure 34. GX120 speed sweep IMEP and CoV of IMEP.

The combustion phasing and combustion duration for the speed sweep were plotted as shown in Figure 35 and Figure 36. As stated previously and seen in Figure 35, CA50 was held constant throughout the speed sweep at 8° aTDC. To accomplish this, the initial spark timing was advanced, increasing from 24.1° bTDC at 2000 rpm to 32.1° bTDC at 3600 rpm. Advancing the ignition timing was necessary because the duration of time needed for the initial combustion reactions remained relatively constant at all engine speeds. As engine speed increased, more crank angle degrees were traversed in the same amount of time, thus the initial spark was advanced to keep CA50 at the same crank angle. CA10 decreased from 4.2° bTDC to 5.9° bTDC and CA90 increased from 17.6° aTDC to 19.6° aTDC as engine speed increased from 2000 rpm to 3600 rpm. Figure 36 shows how the changes in CA10 and CA90 manifest themselves in the flame development angle and rapid burning angle with increasing engine speed. Both the flame

development angle and rapid burning angle increased with engine speed as expected. It should be noted that Figure 36 is very similar to Figure 7 (reprinted from Heywood [11]). Although Figure 35 and Figure 36 do not provide a large amount of insight into the performance and efficiency of the GX120 engine, they serve as a useful crosscheck with the literature to ensure the test results conformed to expectations.

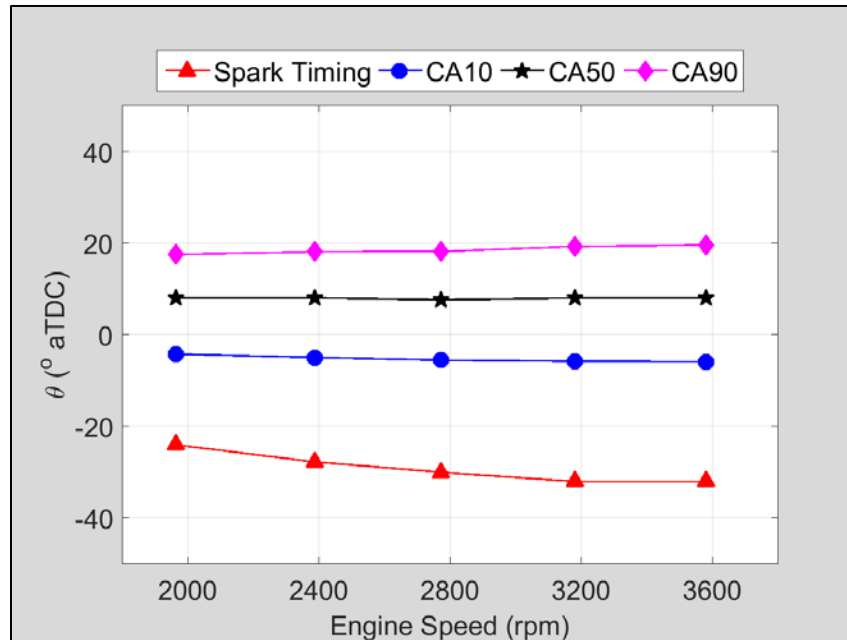


Figure 35. GX120 speed sweep combustion phasing.

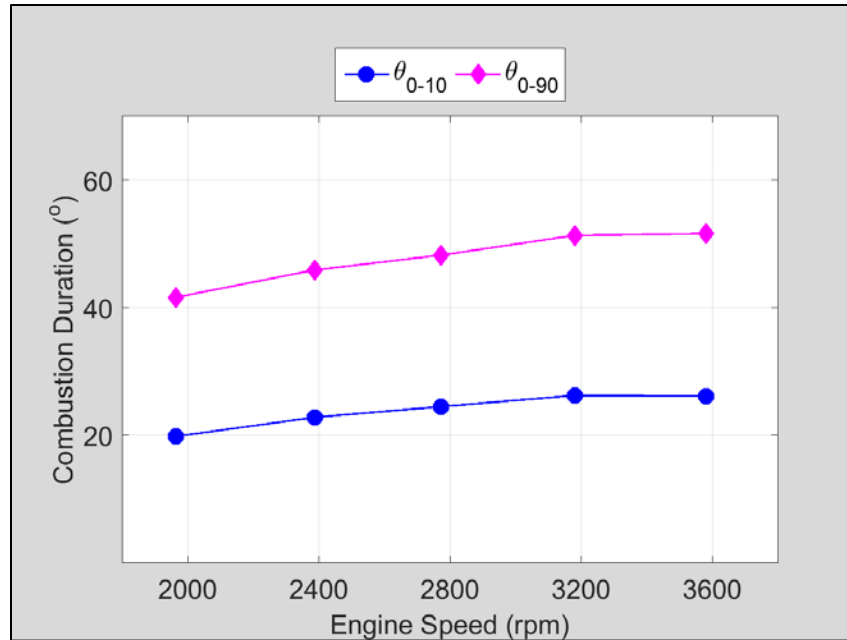
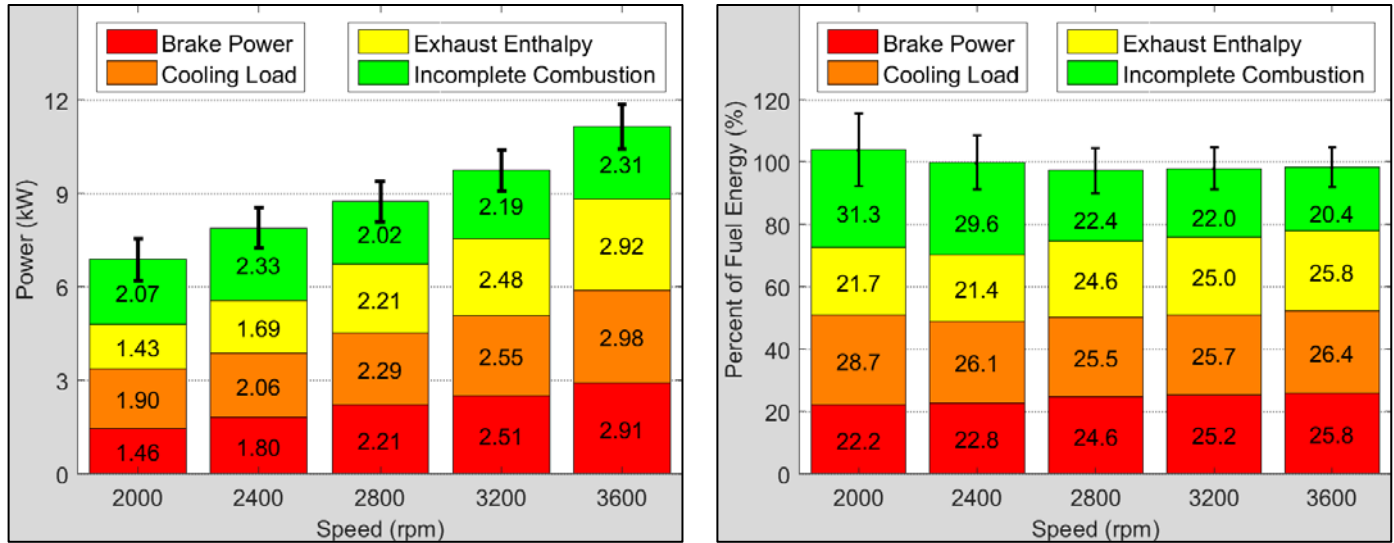


Figure 36. GX120 speed sweep combustion duration.

The GX120 speed sweep data was then used to address research Objective Two, a first law energy balance of all energy entering and exiting the system. Figure 37(a) shows the energy values in each pathway with error bars for the overall combined energy. Figure 37(b) shows the energy in each pathway as a percentage of fuel energy. The most pronounced trend is again in the incomplete combustion pathway. It was noted previously that the amount of energy lost to incomplete combustion (in kW) remained relatively flat throughout the speed sweep, however, the fuel energy entering the engine increased from 6.7 kW to 11.5 kW, causing the incomplete combustion losses as a percentage of fuel energy to decrease from 31.3% to 20.4% as engine speed increased from 2000 rpm to 3600 rpm. This was due to increased mixing of the fresh charge inside the cylinder and higher in-cylinder combustion temperatures. The increasing trend in exhaust enthalpy losses both in raw energy level (kW) and as a percentage of fuel energy

supports this theory because the exhaust enthalpy losses were driven primarily by the exhaust temperature.

Although cooling load increased in power level with engine speed, as a percentage of fuel energy it decreased from 28.7% at 2000 rpm, to 25.5% at 2800 rpm, only to rise again to 26.4% at 3600 rpm. The steady increase in measured brake power from 1.46 kW at 2000 rpm to 2.91 kW at 3600 rpm indicates that the engine would likely continue to produce more power if the engine speed was raised above the manufacturer recommended limit of 3600 rpm. To preserve the integrity of the engine and avoid damage to both the engine and SERB, it was not tested at speeds exceeding 3600 rpm. The brake power as a percentage of fuel energy, also known as fuel conversion efficiency (η_f), increased from 22.2% at 2000 rpm to 25.8% at 3600 rpm. Recalling Figure 11, an increase in engine speed while under constant load (or throttle setting) will typically result in an increase in η_f (or decrease in BSFC) until a peak is reached, with a decrease in η_f thereafter. The engine had most likely not reached its peak power (or peak η_f) at 3600 rpm. These results have made it apparent that the GX120 engine was capable of producing more power than it was rated for. As stated before, given the fact that the GX120 engine is used primarily for powered equipment, the engine was clearly designed with an emphasis on reliability and longevity rather than power output.



(a) Overall energy in each pathway (kW).

(b) Percentage of fuel energy in each pathway.

Figure 37. Honda GX120 speed sweep energy balance.

4.1.3. GX120 Parametric Studies

For research Objective Three, a parametric study was done to characterize the impact of five variables (equivalence ratio, combustion phasing, head temperature, engine speed and throttle setting) on the loss pathways. The speed sweep was discussed in Section 4.1.2; the remainder of Section 4.1.3 will discuss the remaining four parametric studies. The equivalence ratio sweep is in Section 4.1.3.1, the combustion phasing sweep is in Section 4.1.3.2, the cooling load (or head temperature) sweep is in Section 4.1.3.3, and the throttle sweep is in Section 4.1.3.4.

4.1.3.1. GX120 Equivalence Ratio Sweep

For the equivalence ratio (ϕ) sweep, the fuel air mixture of the fresh charge was varied from a ϕ of 0.85 to a ϕ of 1.25 ± 0.02 . Other conditions held constant were:

engine speed of 2800 ± 120 rpm, WOT, CA50 of $8^\circ \pm 0.4^\circ$ aTDC, and cylinder head temperature of $140^\circ \pm 1^\circ$ C.

Figure 38 shows the results of measuring the energy pathways in terms of the energy (in kW) contained in each of the four pathways. Brake power peaked at 2.23 kW near stoichiometric to slightly rich (ϕ of 1.05 and 1.15), and dipped slightly when lean (2.00 kW at $\phi = 0.85$, 2.19 kW at $\phi = 0.95$) and very rich (2.21 kW at $\phi = 1.25$). Exhaust enthalpy peaked at 2.24 kW when the engine was run slightly lean at $\phi = 0.95$. Not coincidentally, exhaust gas temperature (EGT) was also at a maximum (659° C) at the same condition. This is interesting when compared to the discussion in Turns [51] that the adiabatic flame temperature of a propane-air constant pressure (1 atm) combustion event reaches a maximum when the air-fuel mixture is slightly rich (1.05). However it should be noted that the Turns discussion is for a different hydrocarbon fuel in an idealized scenario with much lower pressure than those seen in the actual engine.

The cooling load losses followed roughly the same trend as the exhaust enthalpy losses, but tapered off more than the exhaust enthalpy losses at $\phi = 1.15$ and $\phi = 1.25$. This effect comes from the presence of excess unburned fuel inside the combustion chamber. Because there was not enough O_2 in the cylinder to react with all of the fuel, the unburned liquid fuel inside the cylinder was able to absorb more of the heat energy being released during the combustion event, thus the engine required less external cooling to maintain the same cylinder head temperature. The most striking trend in the energy pathways of the equivalence ratio sweep again occurred in the incomplete combustion. Incomplete combustion energy increased from 0.87 kW at $\phi = 0.85$ to 4.14

kW at $\phi = 1.25$. The substantial increase in incomplete combustion losses under rich conditions becomes a significant consideration when the engine is in its stock (carbureted) configuration, given the fact that most carburetors are tuned to run at a ϕ of $\sim 1.2 - 1.3$ under typical WOT conditions [11].

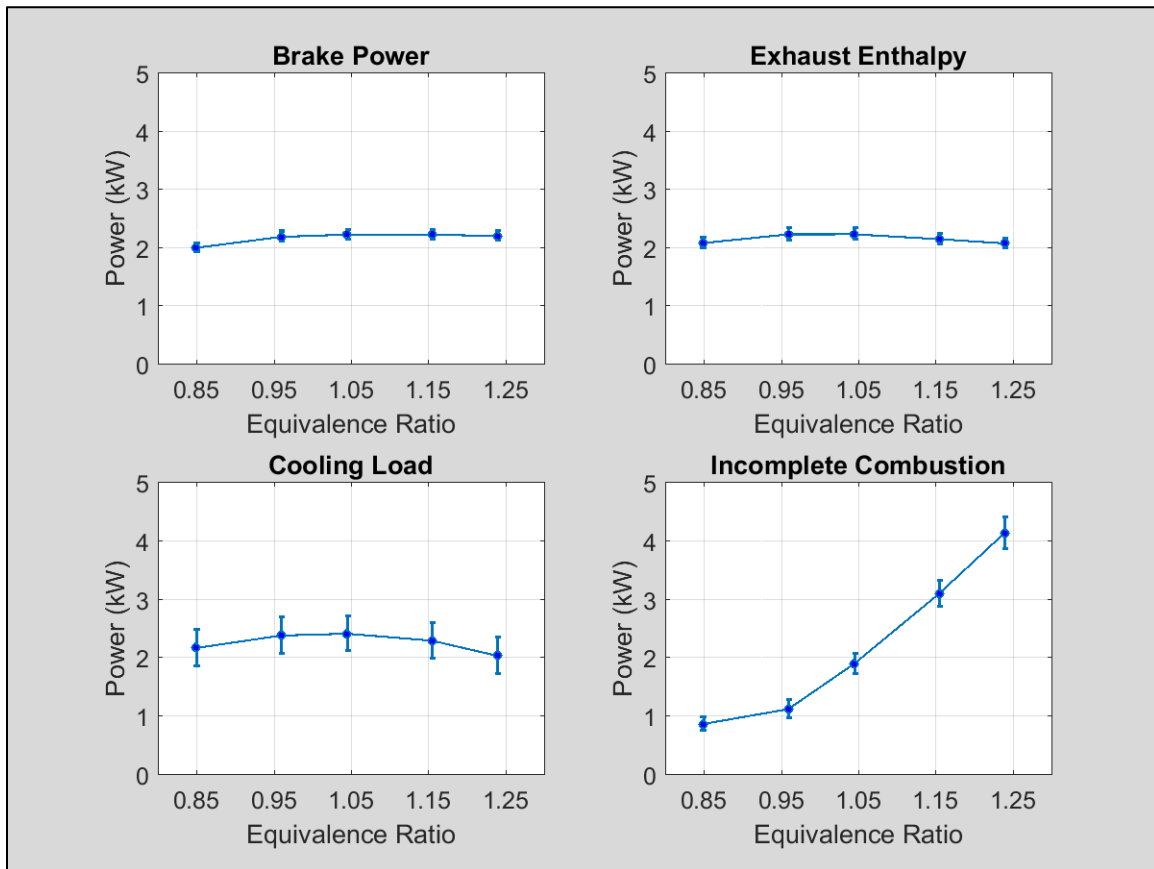


Figure 38. GX120 equivalence ratio sweep energy pathways (in kW).

Examining the IMEP and CoV of IMEP for the equivalence ratio sweep, a peak in IMEP of 8.5 bar is seen at $\phi = 1.05$ with a greater drop in IMEP under lean conditions than under rich conditions. The change in CoV of IMEP for the phi sweep is interesting. The engine ran very stable from $\phi = 1.05$ to $\phi = 1.25$, with CoV of IMEP of 0.89%,

0.93% and 1.09%, but nearly doubled at $\phi = 0.95$ with a CoV of IMEP of 1.74% and tripled at $\phi = 0.85$ with a CoV of IMEP of 2.60%. Although these values of CoV of IMEP are all still quite low⁶, leaning the fuel mixture decreased the consistency of combustion more than enriching it did.

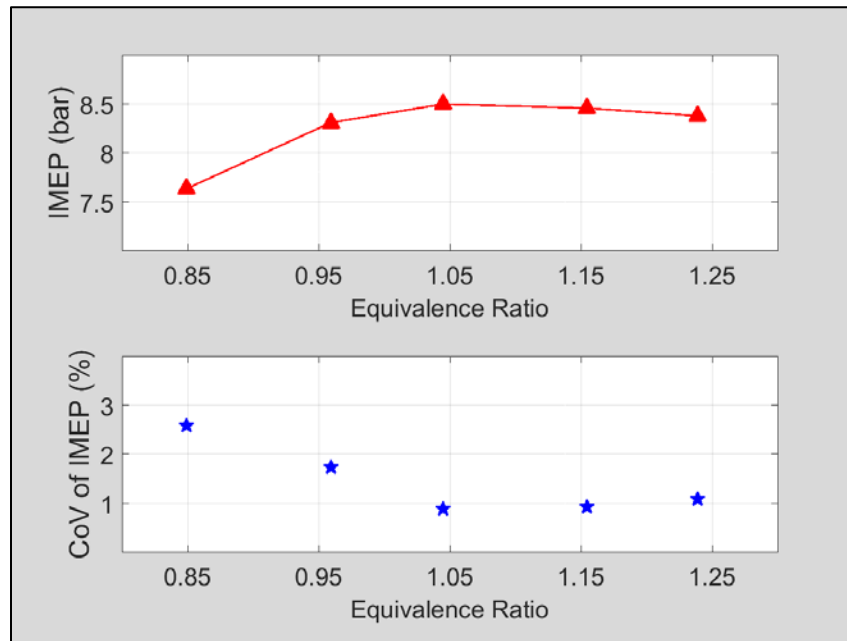


Figure 39. GX120 equivalence ratio sweep IMEP and CoV of IMEP.

Looking at the combustion phasing and combustion duration plots in Figure 40 and Figure 41, it is clear that running the engine under lean conditions increased the amount of time needed for combustion to occur. This increase in combustion time was seen in Figure 40, where the ignition timing was advanced from 28.0° bTDC to 41.2° bTDC as ϕ was decreased from 1.25 to 0.85 while holding CA50 constant at 8° aTDC. In Figure 41, the flame development angle increased from 22.8 crank angle degrees to

⁶ Noticeable differences in running consistency occur around 5%-10% CoV of IMEP. CoV of IMEP greater than 10% is for all practical purposes undriveable for an automobile engine[11].

34.6 crank angle degrees as ϕ decreased from 1.25 to 0.85 while the rapid burning angle increased only from 23.1 crank angle degrees to 28.5 crank angle degrees.

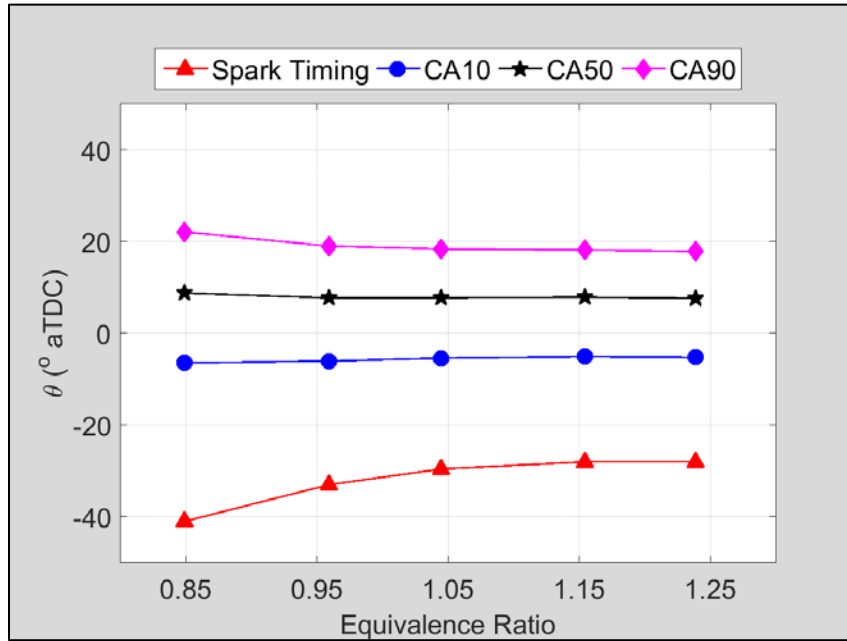


Figure 40. GX120 equivalence ratio sweep combustion phasing.

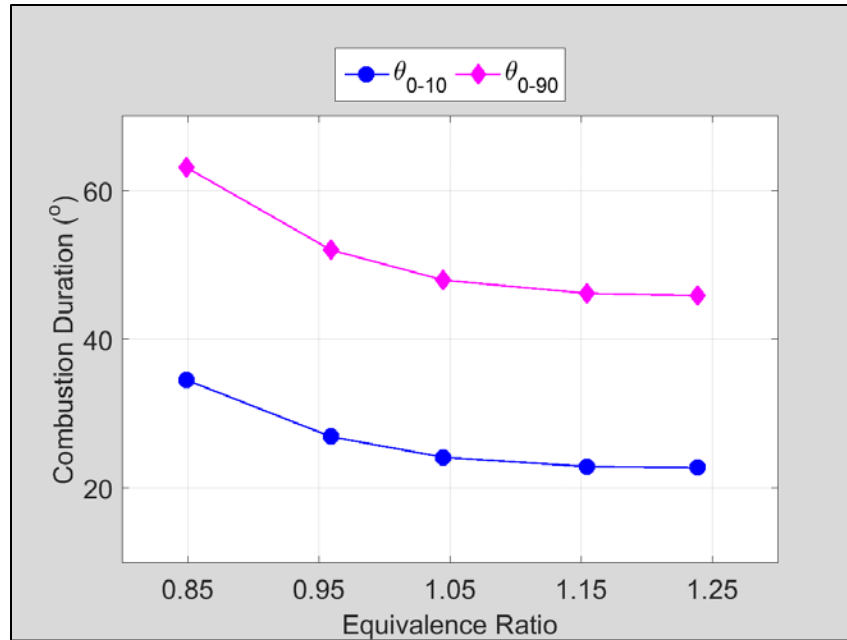
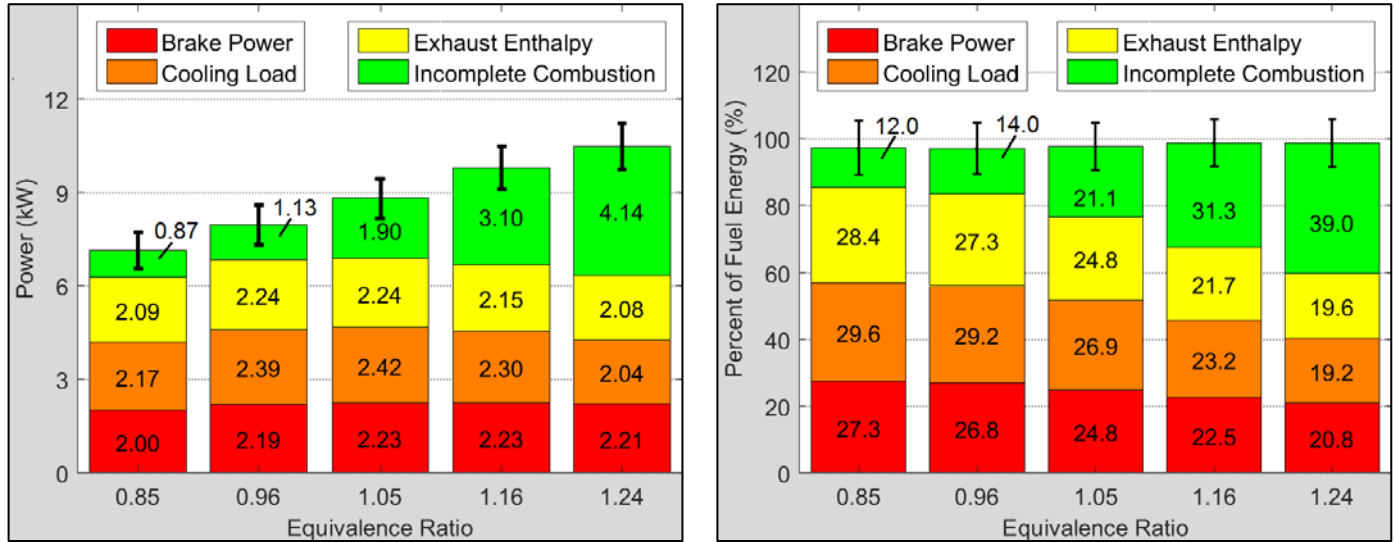


Figure 41. GX120 equivalence ratio sweep combustion duration.

Finally, the energy balance results for the equivalence ratio sweep are shown in Figure 42. Figure 42(a) shows the amount of energy in each pathway with the total uncertainty for the test point while Figure 42(b) shows the energy in each pathway as a percentage of fuel energy. Fuel conversion efficiency reached a high of 27.3% at a ϕ of 0.85 (which was also the peak fuel conversion efficiency of any test point for the GX120 engine), while steadily decreasing to 20.8% at a ϕ of 1.25. Exhaust enthalpy as a percentage of fuel energy was at its peak of 28.4% at $\phi = 0.85$, decreasing to 19.6% at $\phi = 1.25$, despite the magnitude of the exhaust sensible enthalpy losses being nearly identical at $\phi = 0.85$ and $\phi = 1.25$. This was mostly due to the large change in incomplete combustion as a percentage of fuel energy from 11.7% at $\phi = 0.85$ to 39.0% at $\phi = 1.25$. Cooling load losses decreased from a high of 29.6% at $\phi = 0.85$ to 19.2% at

$\phi = 1.25$. The decrease in cooling load losses was due in part to the large change in incomplete combustion losses along with a decrease in exhaust temperature and the cooling effects associated with excess fuel delivery.



(a) Overall energy in each pathway (kW).

(b) Percentage of fuel energy in each pathway.

Figure 42. Honda GX120 equivalence ratio sweep energy balance.

4.1.3.2. GX120 Combustion Phasing Sweep

For the combustion phasing sweep, CA50 was varied from 2° bTDC to 18° aTDC. This was accomplished by advancing and retarding the ignition timing with the JABtronic ECU. Other conditions held constant were: ϕ of 1.05 ± 0.02 , engine speed of 2800 ± 120 rpm, WOT, and cylinder head temperature of $140^\circ \pm 1^\circ$ C.

Figure 43 shows the results of measuring the energy pathways in terms of the energy (in kW) contained in each of the four pathways. Brake power reached a peak value of 2.25 kW at a CA50 of 8° aTDC, which was consistent with the statement in Heywood that “with optimum spark timing [...] half the charge is burned at about 10°

after TC. [11]” Brake power was slightly diminished at very advanced (CA50 of 2° bTDC) and very retarded (CA50 of 18° aTDC) ignition timing. At both of these test conditions, the brake power was 2.18 kW, a percent difference of 3.2%. The steady increase in exhaust enthalpy as the timing was retarded was the result of steadily increasing exhaust gas temperature (EGT). The EGT increase was the result of the steady movement of peak in-cylinder pressure and temperature later in the combustion process as the spark timing became increasingly retarded. The steady decrease in cooling load as spark timing was increasingly retarded was linked to the increase in exhaust enthalpy. This inverse relationship was the logical result of more energy exiting the engine via exhaust enthalpy, with less heat energy being retained in the engine, requiring less cooling load to maintain the same cylinder head temperature.

Incomplete combustion losses reached a minimum of 1.80 kW at a CA50 of 8° aTDC, and tended to rise as the timing was advanced or retarded to the extremes, showing a decrease in combustion quality as the ignition timing moved away from MBT timing. The slight decrease in incomplete combustion losses from 1.93 kW at CA50 = 13° aTDC to 1.90 kW at CA50 = 18° aTDC was very small and more likely the result of random variation than the start of a downward trend.

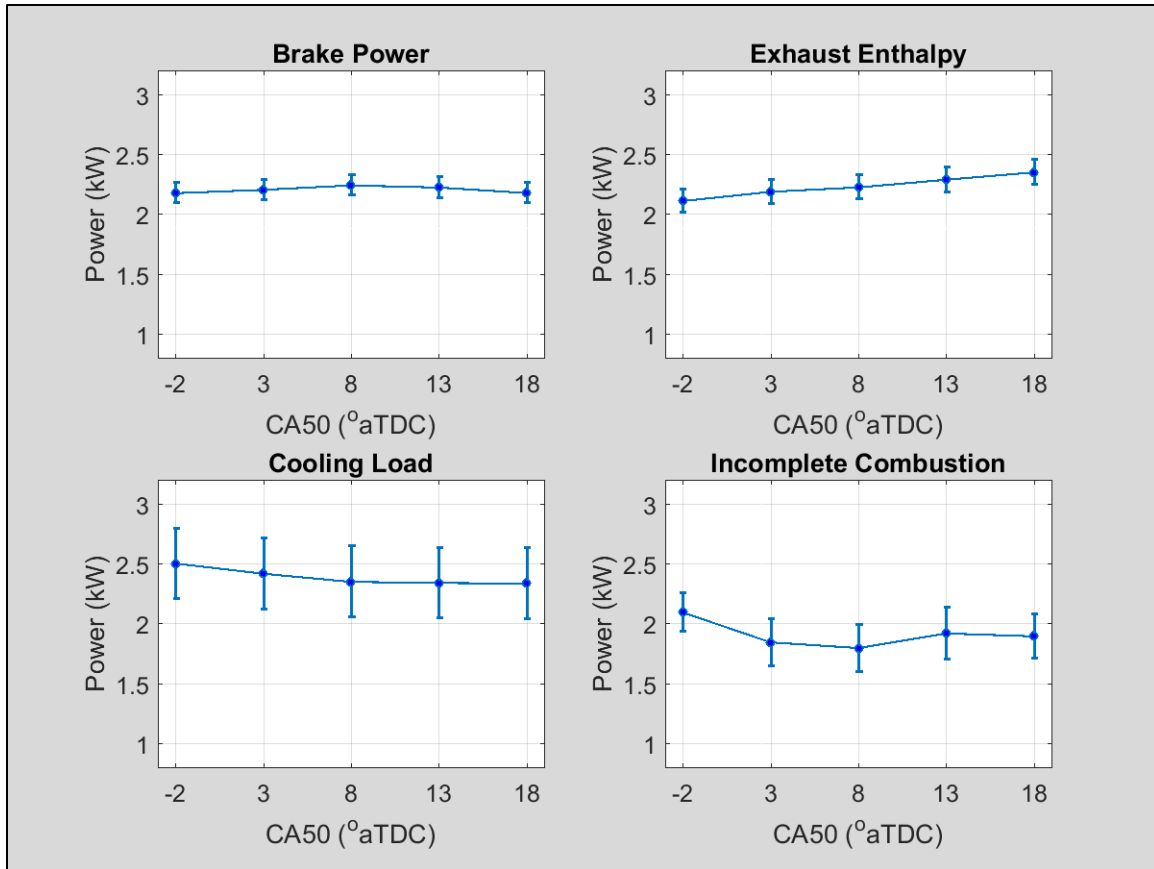


Figure 43. GX120 combustion phasing sweep energy pathways (in kW).

Examining the IMEP and CoV of IMEP from the combustion phasing sweep in Figure 44, the peak IMEP of 8.51 bar at CA50 = 8° aTDC follows the brake power plot in Figure 43. CoV of IMEP reached a minimum of 0.84% at CA50 = 8° aTDC, and steadily increased to 1.59% at CA50 = 2° bTDC and 2.38% at CA50 = 18° aTDC. This decrease in combustion quality as the spark timing was advanced and retarded away from MBT timing was previously discussed and seen in the incomplete combustion plot of Figure 43.

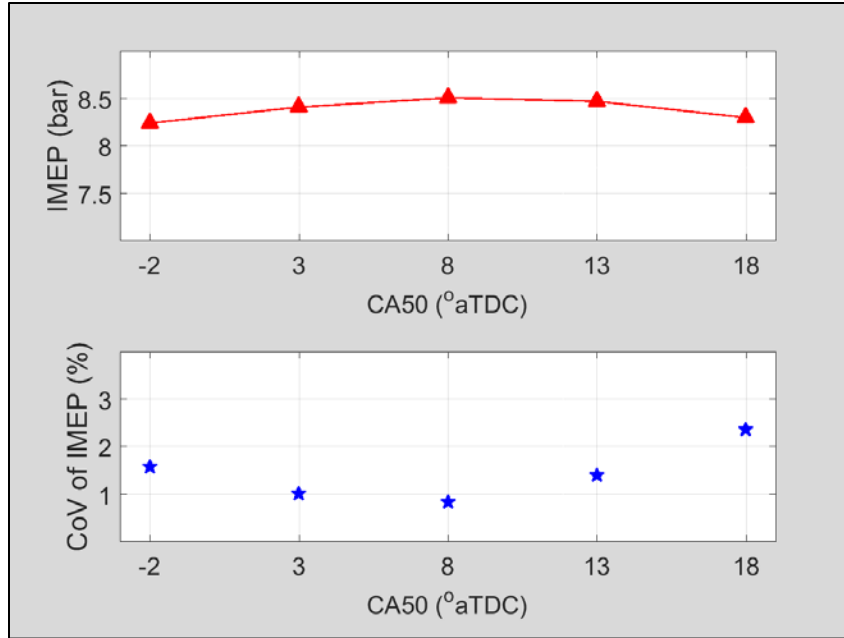


Figure 44. GX120 combustion phasing sweep IMEP and CoV of IMEP.

Combustion phasing and combustion duration for the combustion phasing sweep are shown in Figure 45 and Figure 46. Figure 45 shows that as the spark timing was increased to produce the desired changes in CA50, the slopes of the ignition timing, CA10, and CA50 remained essentially constant and equal. CA90 however slightly diverged from CA50 increasingly as CA50 was increased. This trend can be seen in Figure 46 as well where the total burn angle (θ_{0-90}) increased from 46.6 crank angle (CA) degrees at CA50 = 2° bTDC to 52.4 CA degrees at CA50 = 18° aTDC. Typically, as ignition timing is retarded, peak in-cylinder pressures are reduced [11], which explains the increase in θ_{0-90} .

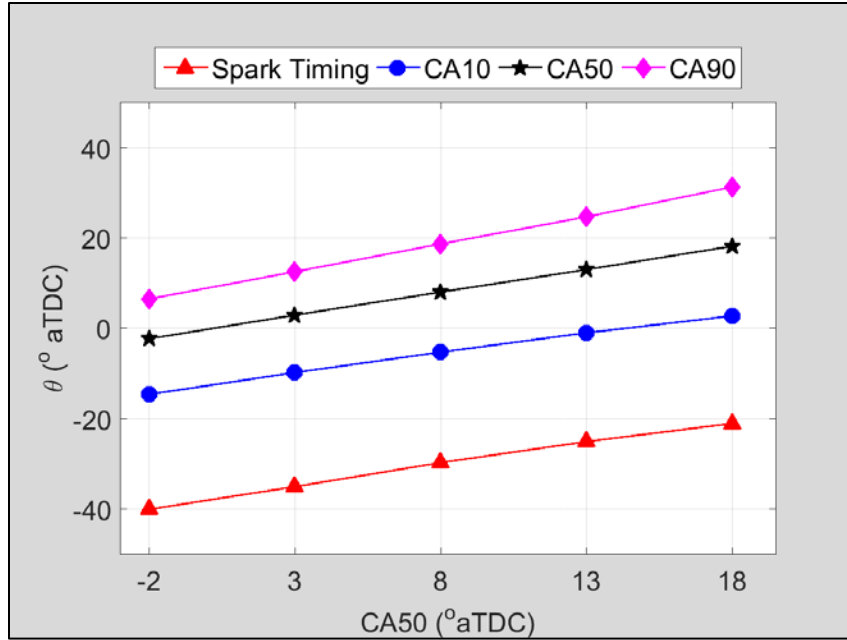


Figure 45. GX120 combustion phasing sweep combustion phasing.

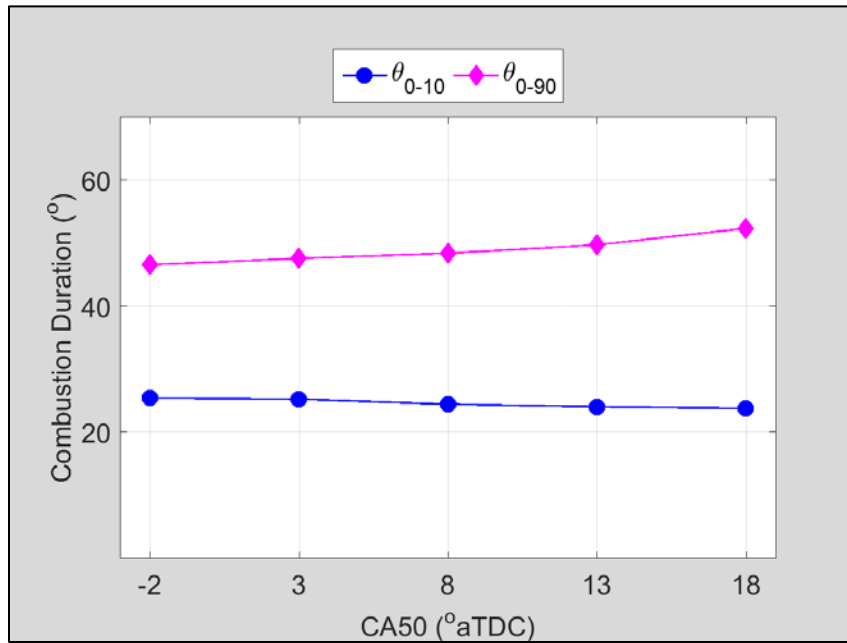
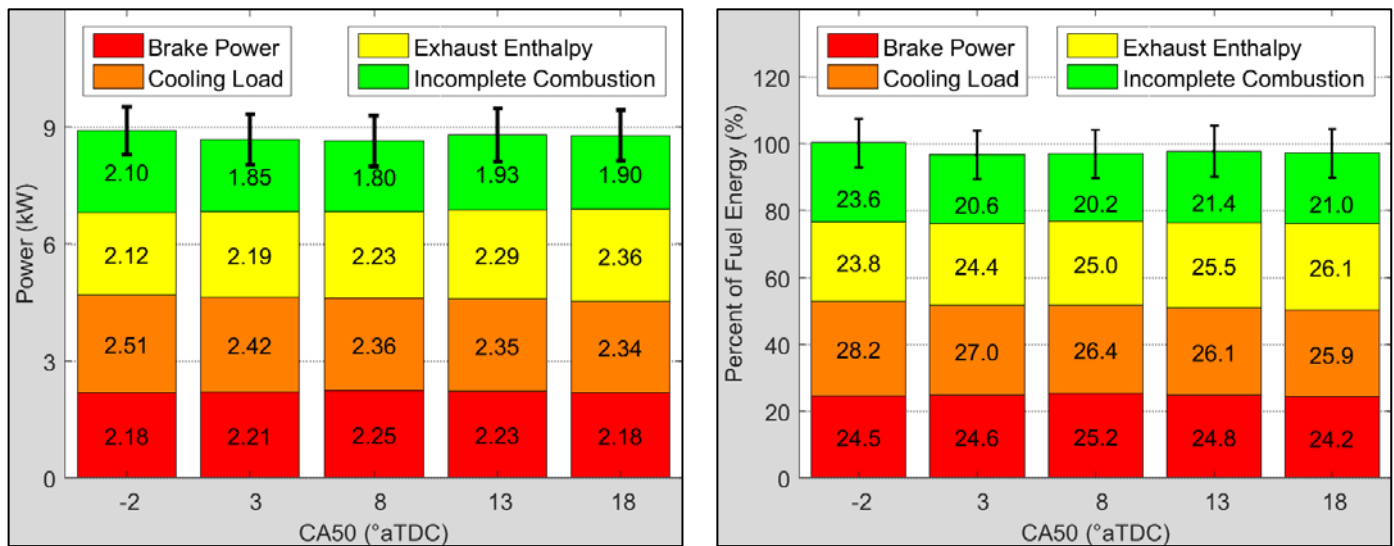


Figure 46. GX120 combustion phasing sweep combustion duration.

The energy balance results for the combustion phasing sweep are shown in Figure 47. Figure 47(a) shows the amount of energy in each pathway with the total uncertainty for the test point while Figure 47(b) shows the energy in each pathway as a percentage of fuel energy. Fuel conversion efficiency peaked at CA50 = 8° aTDC and tapered off slightly to 24.5% at CA50 = 2° bTDC and 24.2% at 18° aTDC, much like the brake power plot from Figure 43. Because the amount of fuel intake into the engine was essentially static for all test points, the exhaust enthalpy, cooling load, and incomplete combustion losses as a percent of fuel energy seen in Figure 47(b) followed the same trends as those previously discussed and seen in Figure 43 and Figure 47(a)



(a) Overall energy in each pathway (kW).

(b) Percentage of fuel energy in each pathway.

Figure 47. GX120 combustion phasing energy balance.

4.1.3.3. GX120 Cooling Load Sweep

For the cooling load sweep, cylinder head temperature (CHT) was varied from 125° C to 160° C. This was accomplished by varying the electrical power to the SERB

cooling blower with the LSDAQ LabVIEW interface while monitoring cylinder head temperature on the same LabVIEW interface. Other conditions held constant were: ϕ of 1.05 ± 0.02 , engine speed of 2800 ± 120 rpm, WOT, and CA50 of $8^\circ \pm 0.4^\circ$ aTDC. In the plots, the equivalent air speed of the cooling air was used to delineate test points in lieu of the cylinder head temperature. This generalized the data in a way that was applicable to Group 2 UAVs, because different small engines operate at various cylinder head temperatures. Figure 48 shows the relationship between cylinder head temperature and the equivalent air speed of the cooling air. The cooling air temperature was $27^\circ \pm 1^\circ\text{C}$.

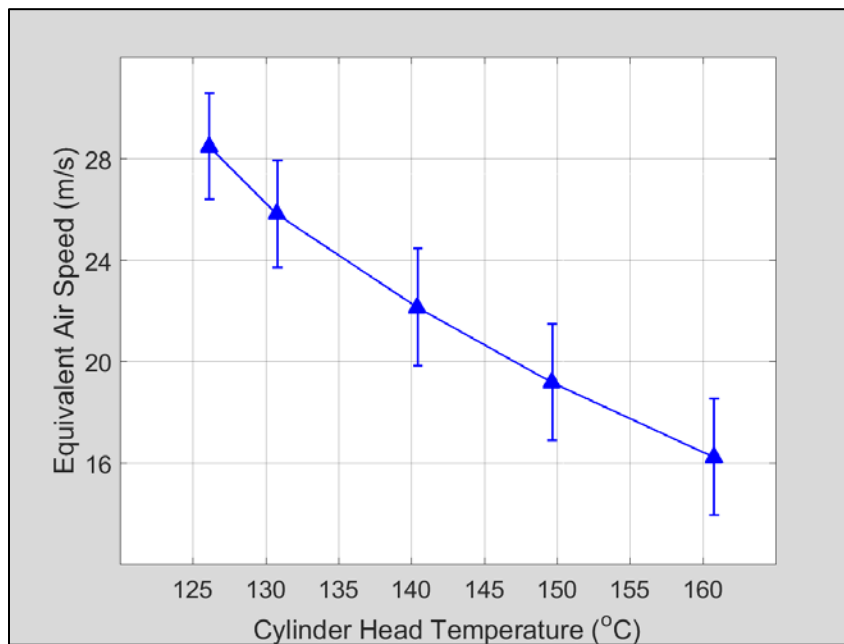


Figure 48. GX120 cooling load sweep cooling air speed versus cylinder head temperature.

Figure 49 shows the results of measuring the energy pathways in terms of the energy (in kW) contained in each of the four pathways. Brake power increased slightly but steadily from 2.13 kW at an equivalent air speed of 16.2 m/s (CHT = 160°C) to 2.24

kW at an equivalent air speed of 28.5 m/s (CHT = 125° C). This is contrary to Heywood’s flame quenching discussion, which states that increased CHT should improve combustion efficiency [11], but in agreement with Ausserer’s two-stroke small engine study [10], which postulates that the increase in brake power with decreasing CHT is the result of less heat transfer to the fresh charge. Cooling load clearly increased with equivalent air speed as would be expected, with a fairly large increase in uncertainty at low equivalent air speed (high CHT) due to the blower air speed being at the lower end of the range of the hot wire anemometer that was used to measure it. Exhaust enthalpy and incomplete combustion losses showed no significant variation in the cooling load sweep.

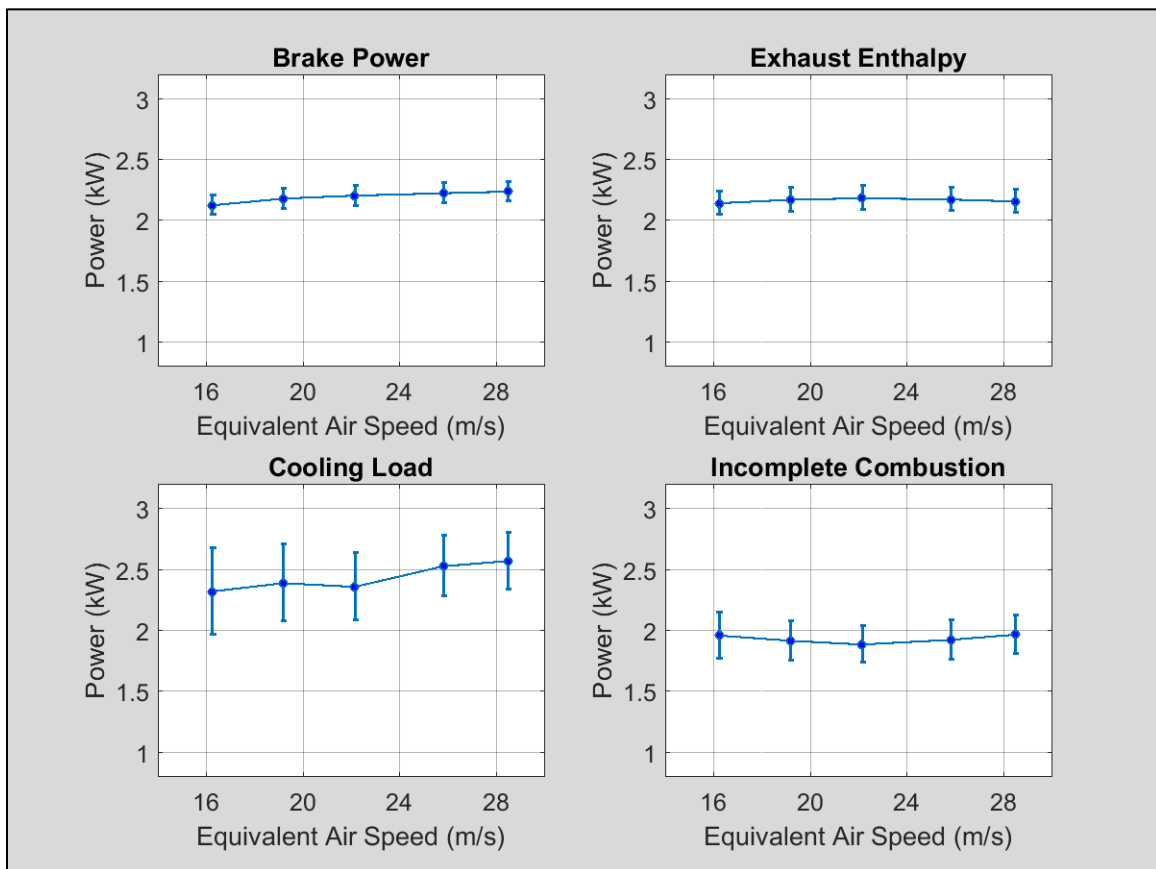


Figure 49. GX120 cooling load sweep energy pathways (in kW).

The IMEP and CoV of IMEP for the cooling load sweep are shown in Figure 50. Much like the trend seen in the brake power plot of Figure 49, IMEP increased slightly from 8.2 to 8.5 bar as equivalent air speed increased from 16.2 to 28.5 m/s. CoV of IMEP remained essentially constant at 0.80% - 0.87%. There were no significant changes in combustion phasing or combustion duration. They will not be discussed in this section; the plots are included in Appendix A for reference.

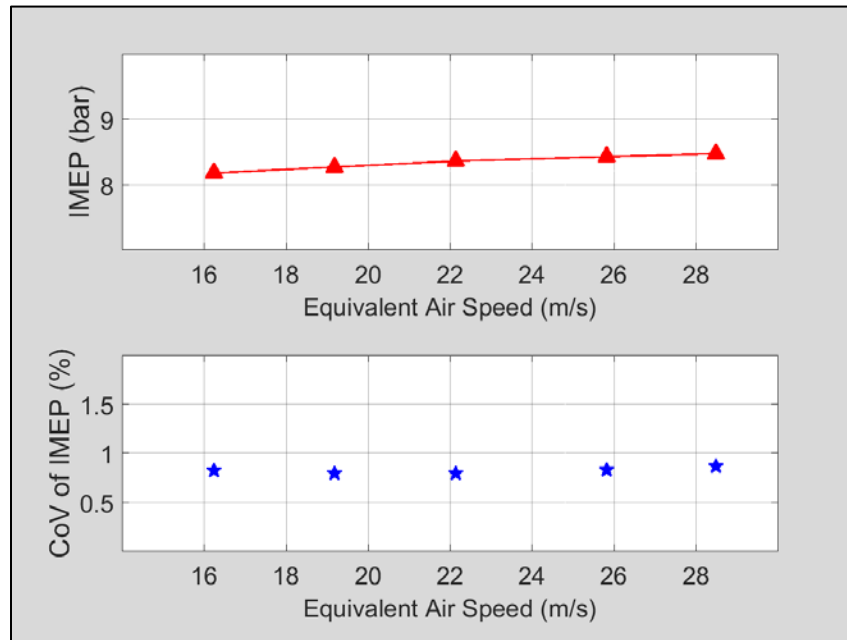
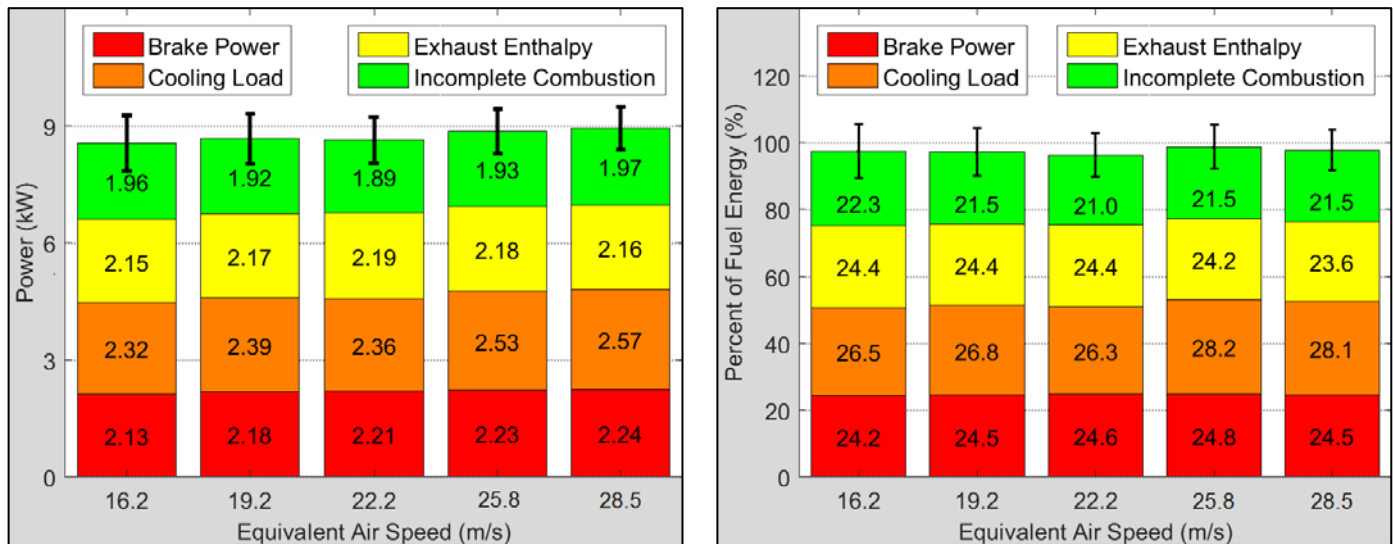


Figure 50. GX120 cooling load sweep IMEP and CoV of IMEP.

The energy balance results for the cooling load sweep are shown in Figure 51. Figure 51(a) shows the amount of energy in each pathway with the total uncertainty for the test point while Figure 51(b) shows the energy in each pathway as a percentage of fuel energy. Fuel conversion efficiency was again essentially constant, ranging from 24.2% to 24.8% throughout the sweep. Cooling load losses as a percentage of fuel

energy was the only energy pathway that showed a higher than negligible change, increasing from 26.5% to 28.2% of the fuel energy throughout the sweep.



(a) Overall energy in each pathway (kW).

(b) Percentage of fuel energy in each pathway.

Figure 51. Honda GX120 cooling load sweep energy balance.

4.1.3.4. GX120 Throttle Sweep

The final parametric sweep for the GX120 engine was a throttle sweep. In the throttle sweep the throttle body of the SERB EFI system was varied from 28% open to 100% open (WOT). Other conditions held constant were: ϕ of 1.05 ± 0.02 , engine speed of 2800 ± 120 rpm, cylinder head temperature of $140^\circ \pm 1^\circ$ C, and CA50 of $8^\circ \pm 0.4^\circ$ aTDC. To accomplish the throttle sweep, the mass flow rate of intake air was noted at WOT, and then the engine was throttled without stalling. Just before stall, the mass flow rate of the intake air was again noted. After establishing the WOT and stall limited settings, the throttle was opened back up in steps to incrementally increase the mass flow rate of intake air. When the results were plotted, the intake air mass flow rates were

converted to volumetric efficiency (η_v) to generalize the data. Figure 52 shows the relationship between volumetric efficiency and the mass flow rate of intake air. Additionally, it should be noted that maximum flow rate of intake air was achieved when the throttle was 72% open.

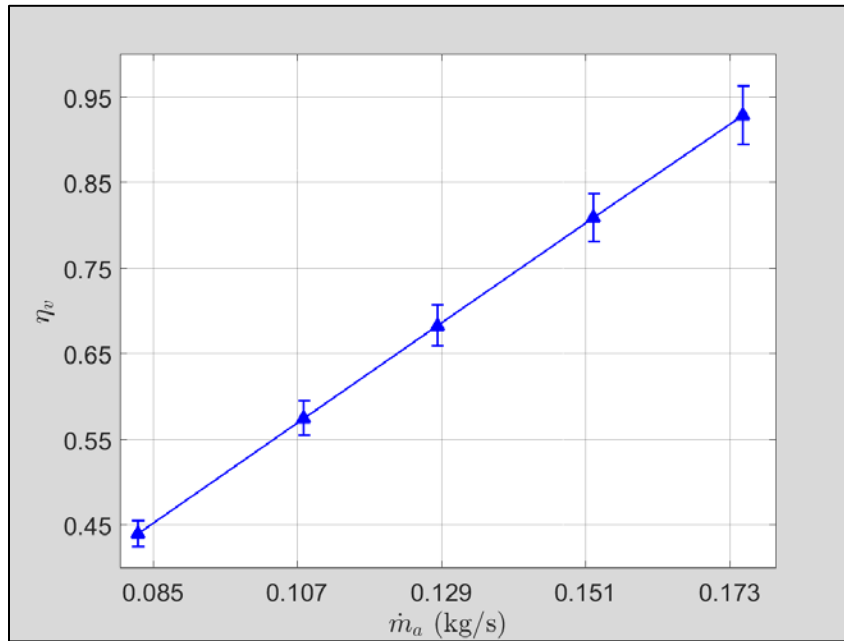


Figure 52. GX120 throttle sweep volumetric efficiency versus mass flow rate of intake air.

Figure 53 shows the results of measuring the energy pathways in terms of the energy (in kW) contained in each of the four pathways. Brake power, exhaust enthalpy and cooling load increased steadily as the throttle was opened from 28% ($\eta_v = 0.44$) to WOT ($\eta_v = 0.93$).⁷ Incomplete combustion losses decreased steadily from 1.83 kW at η_v

⁷ It should be noted that volumetric efficiency at WOT is not necessarily equal to unity as one may assume. There are many factors which may cause low η_v such as an undersized throttle body, pumping losses, etc. η_v values greater than one are possible as well. Boosted engines compress the intake air (utilizing either a turbocharger or supercharger) before it enters the engine, essentially “stuffing” more air into the combustion chamber than it could normally hold. Naturally aspirated engines may also attain η_v values greater than one, reaching values as high as 1.3, with proper tuning [52].

= 0.44 to 1.64 kW at $\eta_v = 0.73$ and $\eta_v = 0.81$, before increasing to 1.88 kW at $\eta_v = 0.93$ (WOT). This trend is explained by examining the concentrations of H₂ and CO in the exhaust gases, shown in Figure 54. As the throttle was opened from $\eta_v = 0.44$ to $\eta_v = 0.81$ H₂ concentration decreased from 3.7% to 1.7%, while CO concentration decreased from 8.1% to 4.5%. The increase in air and fuel flow produced a rise in mixing during combustion which clearly had a favorable effect on incomplete combustion. From $\eta_v = 0.81$ to $\eta_v = 0.93$, H₂ and CO levels remained stable however, while mass flow rate continued to increase. This trend shows that optimal incomplete combustion losses occurred at slightly less than WOT.

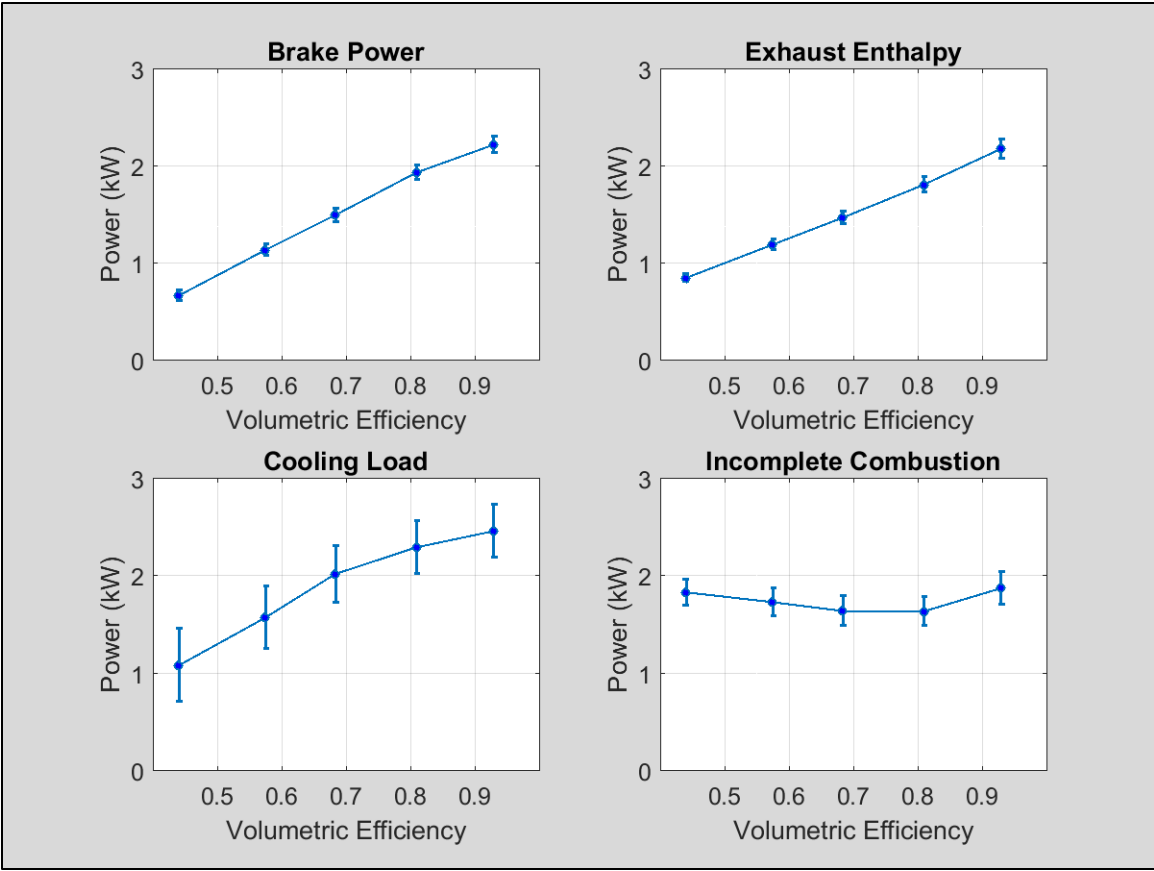


Figure 53. GX120 throttle sweep energy pathways (in kW).

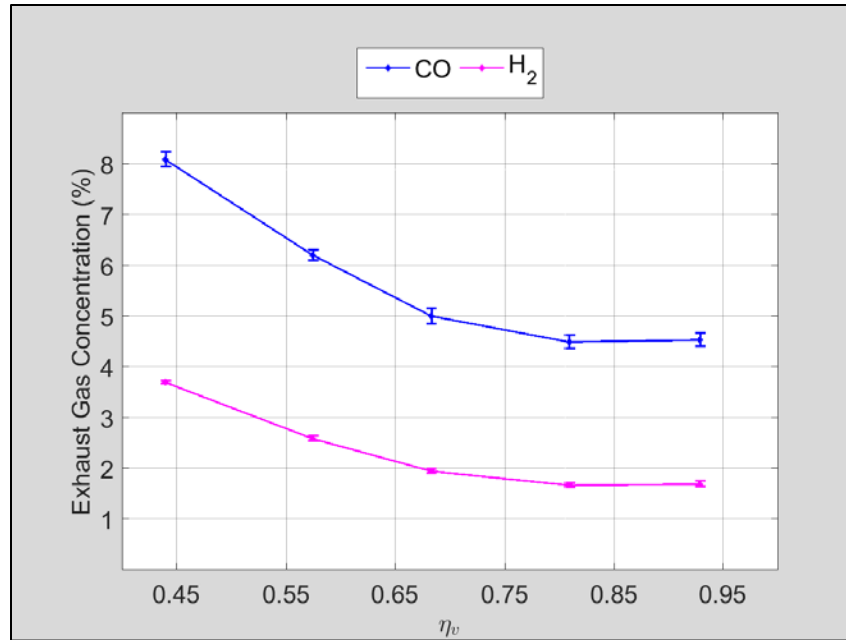


Figure 54. GX120 throttle sweep H₂ and CO concentration in exhaust gases.

IMEP and CoV of IMEP for the throttle sweep, shown in Figure 55, followed a predictable trend for IMEP, with slightly higher (albeit still quite low) instability of combustion at low throttle settings. Figure 56 and Figure 57 show the large decrease in CA degrees required to burn the fuel as the throttle was opened up, with a slight increase again when going from $\eta_v = 0.81$ to $\eta_v = 0.93$.

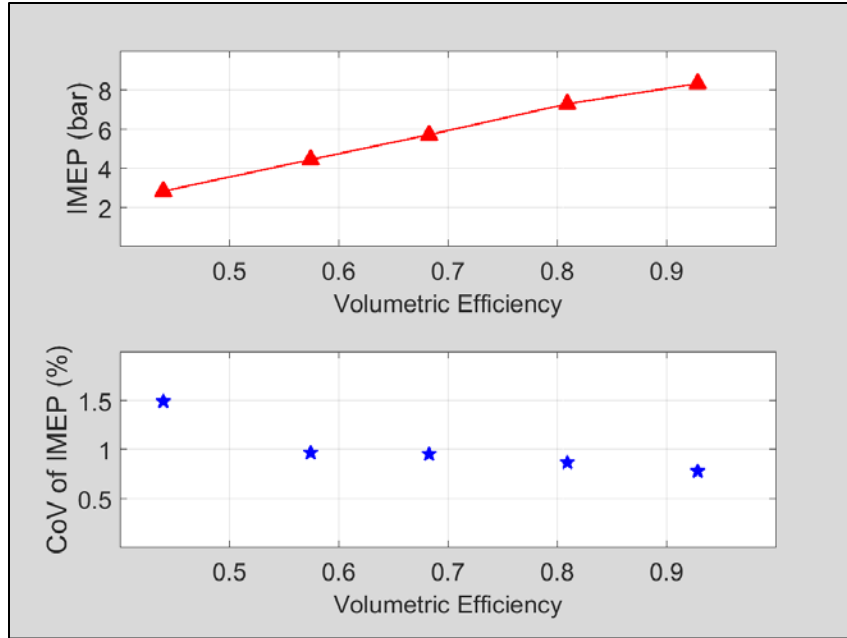


Figure 55. GX120 throttle sweep IMEP and CoV of IMEP.

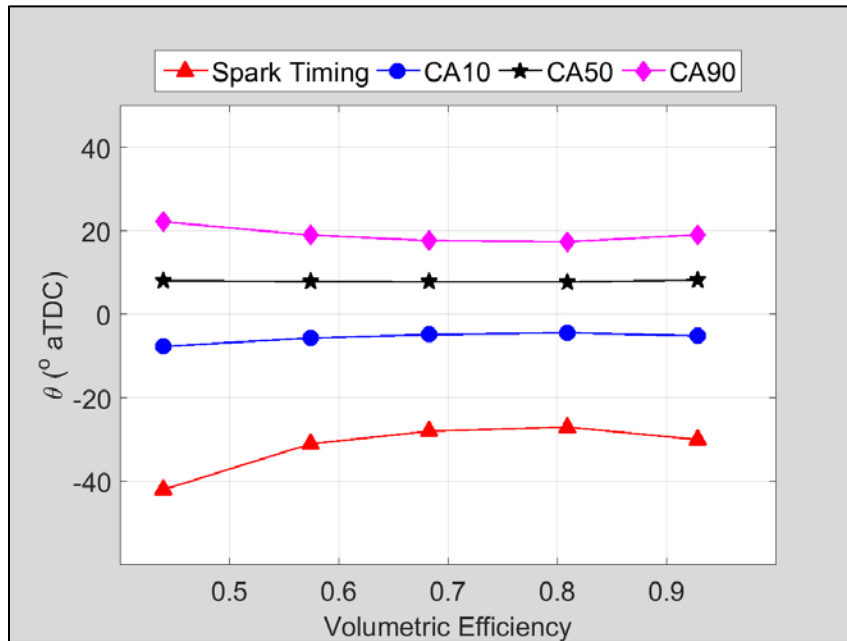


Figure 56. GX120 throttle sweep combustion phasing.

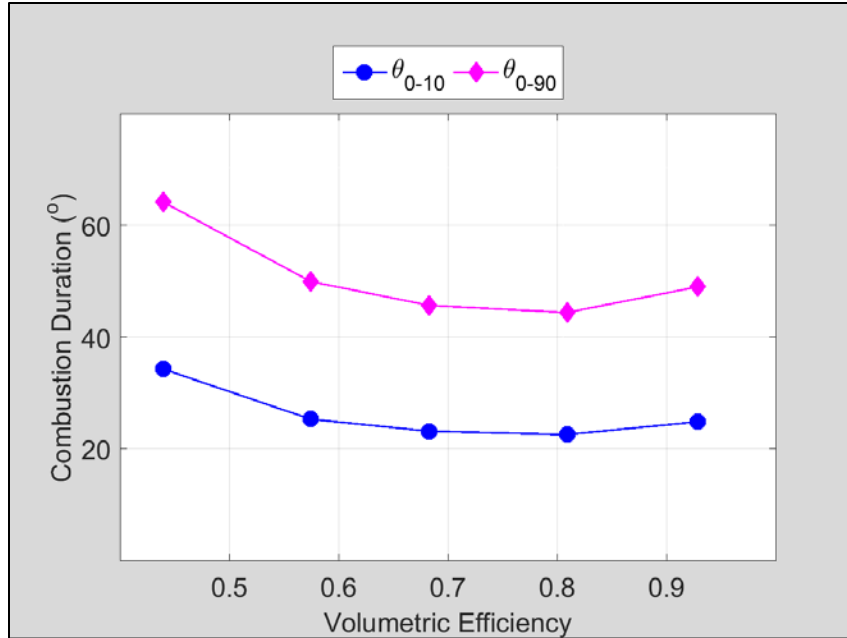
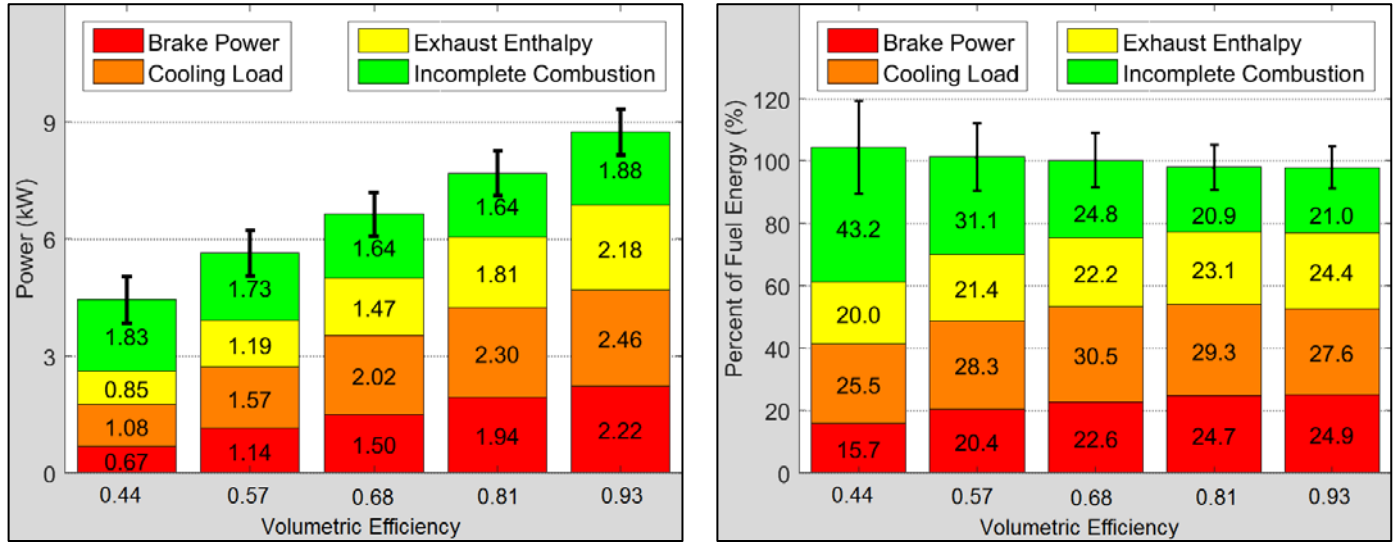


Figure 57. GX120 throttle sweep combustion duration.

The energy balance results for the throttle sweep are shown in Figure 58. Figure 58(a) shows the amount of energy in each pathway with the total uncertainty for the test point while Figure 58(b) shows the energy in each pathway as a percentage of fuel energy. Fuel conversion efficiency was 15.7% at $\eta_v = 0.44$, which was the lowest of any test condition for the GX120 engine. In Figure 58(b) it is shown that as the throttle was opened, η_f steadily increased to 24.9%. Exhaust enthalpy as a percentage of fuel energy increased steadily from 20% at $\eta_v = 0.44$ to 24.4% at $\eta_v = 0.93$. This was the result of both increased EGT and mass flow rate of intake air and fuel. Cooling load losses as a percentage of fuel energy showed an interesting trend, increasing steadily from 25.5% at $\eta_v = 0.44$ to 30.5% at $\eta_v = 0.68$, then decreasing to 27.6% at $\eta_v = 0.93$. Much like the speed sweep of Section 4.1.2, incomplete combustion losses dominated at low throttle

settings (43.2% at $\eta_v = 0.44$), and became much less significant at WOT (21% at $\eta_v = 0.93$), despite remaining comparatively constant in magnitude (1.64 kW – 1.88 kW) as seen in Figure 58(a).



(a) Overall energy in each pathway (kW).

(b) Percentage of fuel energy in each pathway.

Figure 58. GX120 throttle sweep energy balance.

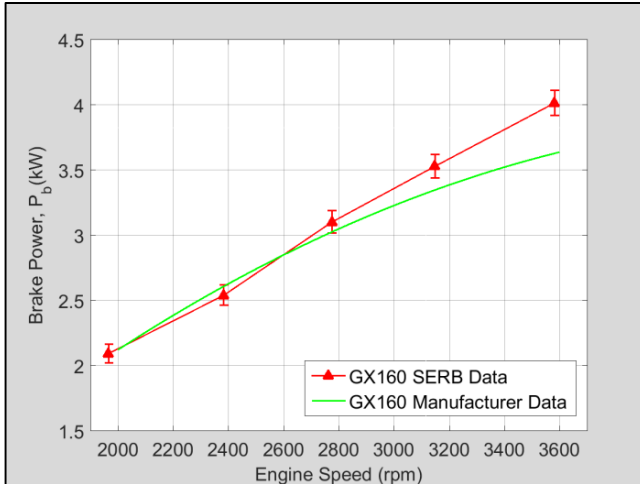
4.2. GX120, GX160, GX200

After running the set of tests discussed in Section 4.1 on the 120 cm³ displacement volume Honda GX120 engine, the same set of tests was run on two geometrically similar engines of 160 cm³ and 200 cm³ displacement volume, namely the Honda GX160 and Honda GX200 engines. An exhaust sampling validation similar to the one discussed in Section 4.1.1 was performed first to ensure no mixing in the exhaust was present. The results showed stable levels of H₂ and CO in the exhaust gases as samples were taken from exhaust Ports two, four, six, and eight. The results of the GX160 and

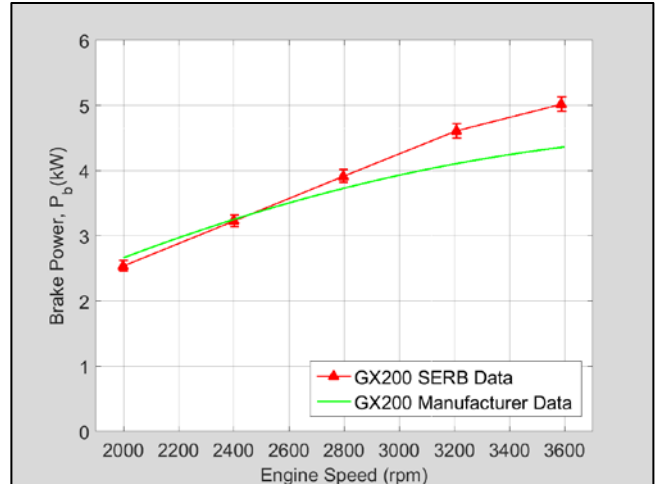
GX200 exhaust sampling validation tests will not be discussed further, however the results from the tests are included in Appendix A. Section 4.2.1 contains the results and discussion of the speed sweeps and comparison to the engine manufacturer data while Section 4.2.2 contains the results and discussion of the four remaining parametric studies of equivalence ratio, combustion phasing, cooling load, and throttle.

4.2.1. GX120, GX160, and GX200 Power Study (Speed Sweep)

The GX160 and GX200 engines were then run through their manufacturer recommended operating ranges from 1800 – 3600 rpm. Other conditions held constant were: WOT, ϕ of 1.05 ± 0.02 , CA50 of $8^\circ \pm 0.4^\circ$ aTDC, and cylinder head temperatures of $150^\circ \pm 1^\circ$ C for the GX160 and of $170^\circ \pm 1^\circ$ C for the GX200 engines. The changes in baseline head temperatures were necessary due to the limitations of the cooling blower motor. For the respective speed sweeps, the cooling blower motor was set to approximately 60% power, providing similar equivalent air speeds for the cooling air of each engine. Figure 59 shows results similar to the GX120 power curve from Figure 30, where the SERB measured power was greater than the manufacturer's advertised data at the higher end of the recommended engine speed range [53, 54].



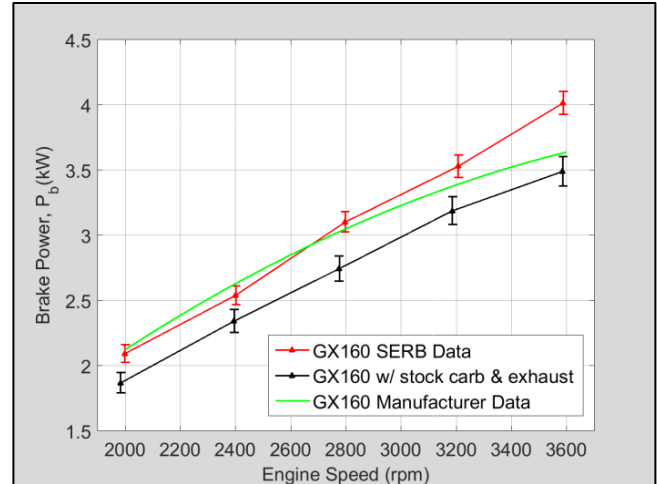
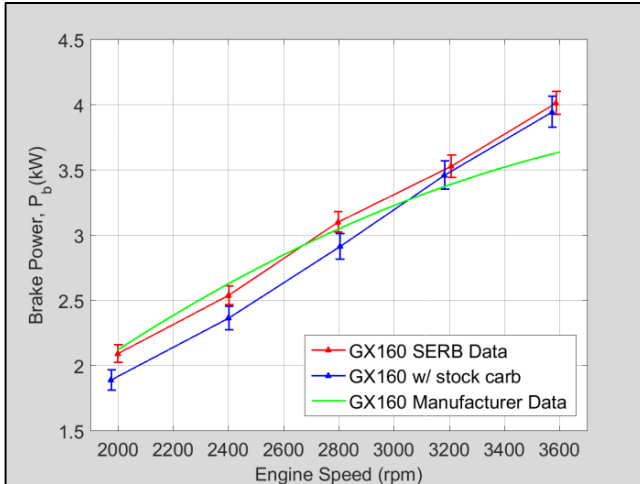
(a) GX160 engine power curve.



(b) GX200 engine power curve.

Figure 59. GX160 and GX200 power curves with the SERB exhaust versus the manufacturer's advertised power curves.

Recall from Section 4.1.2 that the GX120 engine was run with the stock muffler installed to examine the effect of the configuration change on the brake power of the engine. To further examine the effect of other configuration changes on the engine's speed sweep brake power measurements, the GX160 engine was put through the speed sweep test once with the stock carburetor installed, using the SERB exhaust system (which contains no muffler or internal baffling), and again utilizing the stock carburetor and stock exhaust. The results of these tests are shown in Figure 60.



(a) GX160 power curve with the stock carburetor and SERB exhaust.

(b) GX160 power curve with the stock carburetor and stock exhaust.

Figure 60. GX160 speed sweep using various equipment configurations.

Figure 60(a) shows that the stock carburetor limited the brake power of the GX160 engine at low engine speed, providing a 10.2% reduction in power at 2000 rpm which steadily declined to a 1.7% reduction at 3600 rpm. Recall from Figure 30 that the opposite trend was seen when the GX120 engine was tested with the stock exhaust and the SERB EFI system. In that test a greater reduction in brake power was seen at 3600 rpm while the low speed test points were very close. Figure 60(b) shows that installing the stock carburetor and exhaust together reduced the brake power across the entire speed range by an average value of 11.2%. The GX200 engine was only run using the SERB exhaust and the SERB EFI system for fuel delivery.

Combined plots showing the energy in each of the four energy balance pathways (in kW) for the three Honda engines are shown in Figure 61. The magnitude of brake power and exhaust enthalpy losses scaled in a consistent manner, while the cooling load

losses and incomplete combustion losses showed less consistent patterns. This is likely due in part to the cooling load and incomplete combustion loss energy pathways consistently showing greater uncertainty in the measurements and run-to-run repeatability (discussed in Sections 3.4 and 3.5). Overall, Figure 61 shows a general trend of the energy in each of the four pathways increasing with engine size.

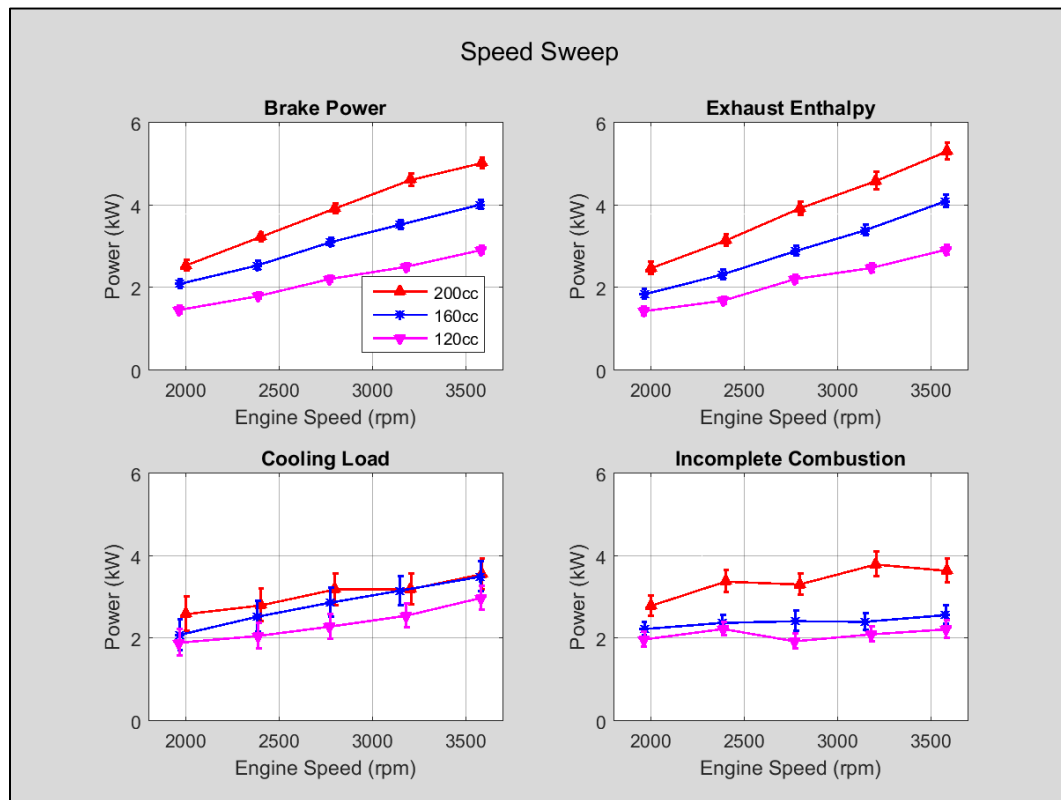


Figure 61. Combined speed sweep energy pathways (in kW).

Combined IMEP and CoV of IMEP plots are shown in Figure 62. The GX120 engine had consistently lower IMEP than the GX160 and GX200 engines, while the GX160 and GX200 engines had IMEP values that converged as engine speed increased.

CoV of IMEP values were very similar for all three engines, ranging mostly from 0.5% to 1%.

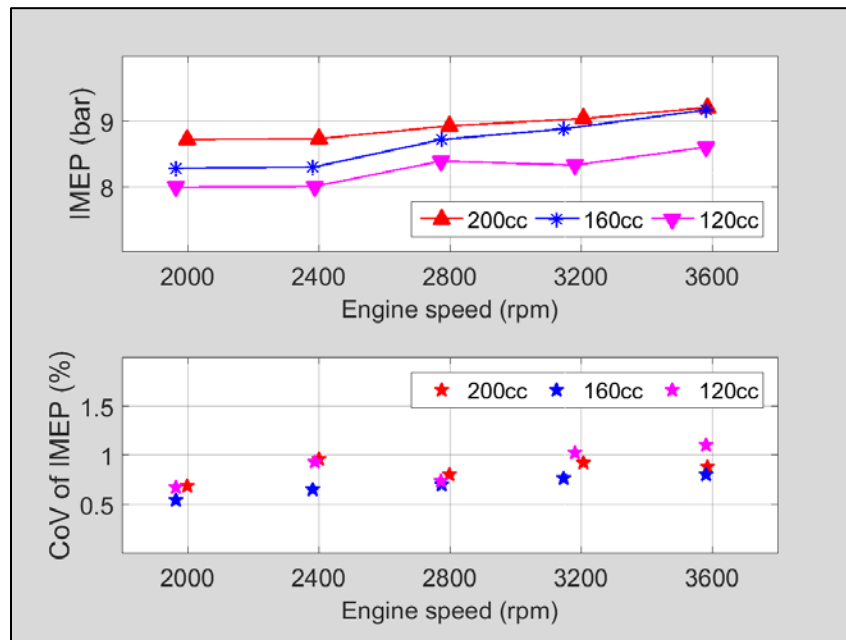
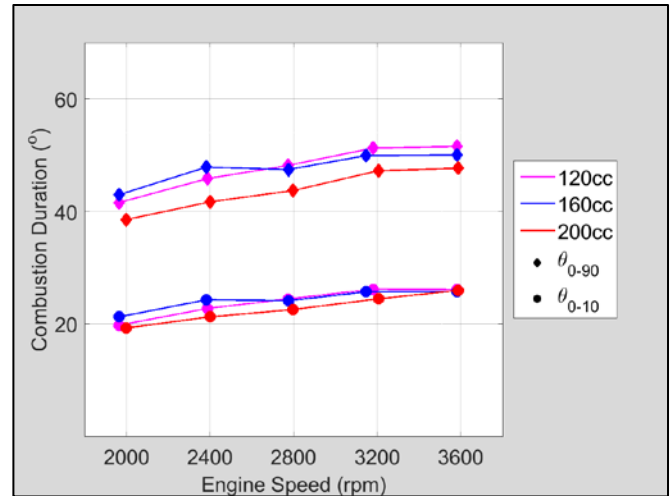
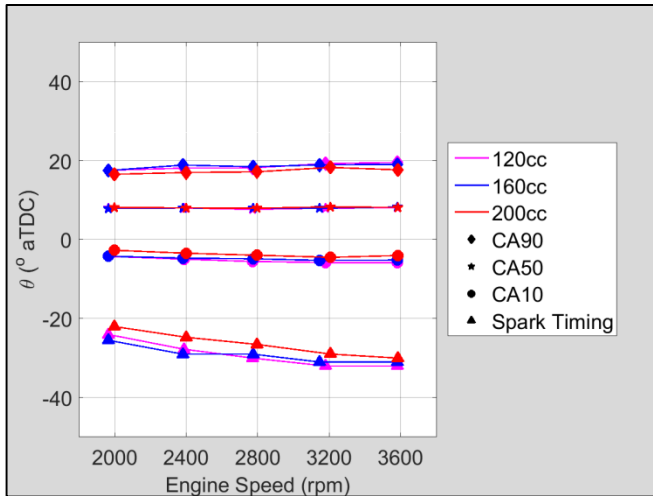


Figure 62. Combined speed sweep IMEP and CoV of IMEP.

The combined combustion phasing and combustion duration plots for the GX120, GX160, and GX200 engines are shown in Figure 63. These figures show that the trends in combustion phasing and combustion duration for the GX160 and GX200 engines were very similar to those of the GX120 engine, also shown in Section 4.1, Figure 35 and Figure 36.

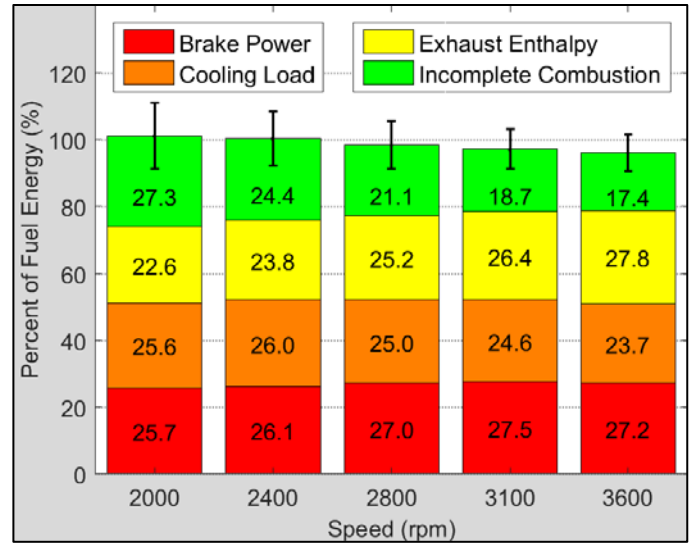
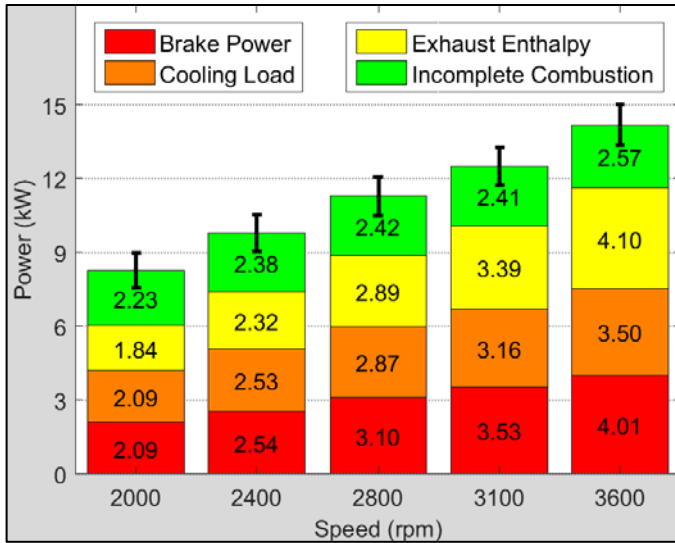


(a) Combined speed sweep combustion phasing.

(b) Combined speed sweep combustion duration.

Figure 63. Combined speed sweep combustion phasing and combustion duration.

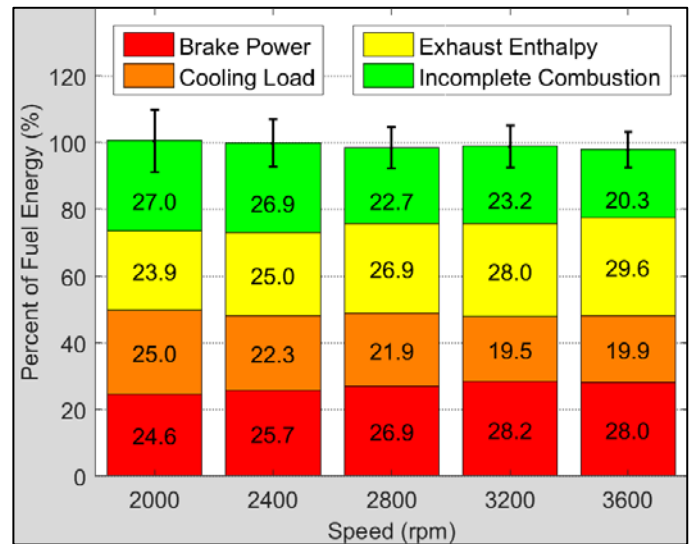
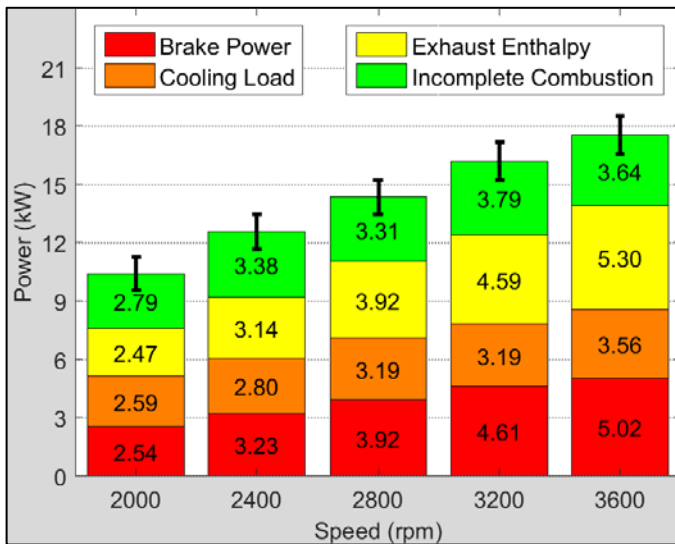
Energy balance results for the GX160 speed sweep and GX200 speed sweep are shown in Figure 64 and Figure 65, respectively. The trends from Figure 64(a) and Figure 65(a) were discussed previously, and are shown in Figure 61. Figure 66 was generated using the GX160 speed sweep percentage of fuel energy data from Figure 64(b), the GX200 data from Figure 65(b), and the GX120 data from Figure 37(b).



(a) Overall energy in each pathway (kW).

(b) Percentage of fuel energy in each pathway.

Figure 64. GX160 speed sweep energy balance.



(a) Overall energy in each pathway (kW).

(b) Percentage of fuel energy in each pathway.

Figure 65. GX200 speed sweep energy balance.

Figure 66 shows the combined percentage of fuel energy in each pathway from the speed sweeps of the GX120, GX160 and GX200 engines. The GX160 and GX200 engines had greater fuel conversion efficiency (brake power as a percentage of fuel

energy) than the GX120 throughout the entire operating range. The GX160 engine had greater efficiency at 2000 and 2400 rpm, while the GX200 was the most efficient of the three engines at 3200 and 3600 rpm. Exhaust enthalpy losses as a percentage of fuel energy increased consistently with engine displacement throughout the speed sweep. Cooling load losses as a percentage of fuel energy showed a general increase as displacement decreased. Incomplete combustion losses as a percentage of fuel energy did not appear to show a consistent trend with engine size, with the GX160 engine consistently having the least, and the GX120 having the highest incomplete combustion losses at 2000 and 2400 rpm, while the GX200 had the highest at 2800, 3200 and 3600 rpm.

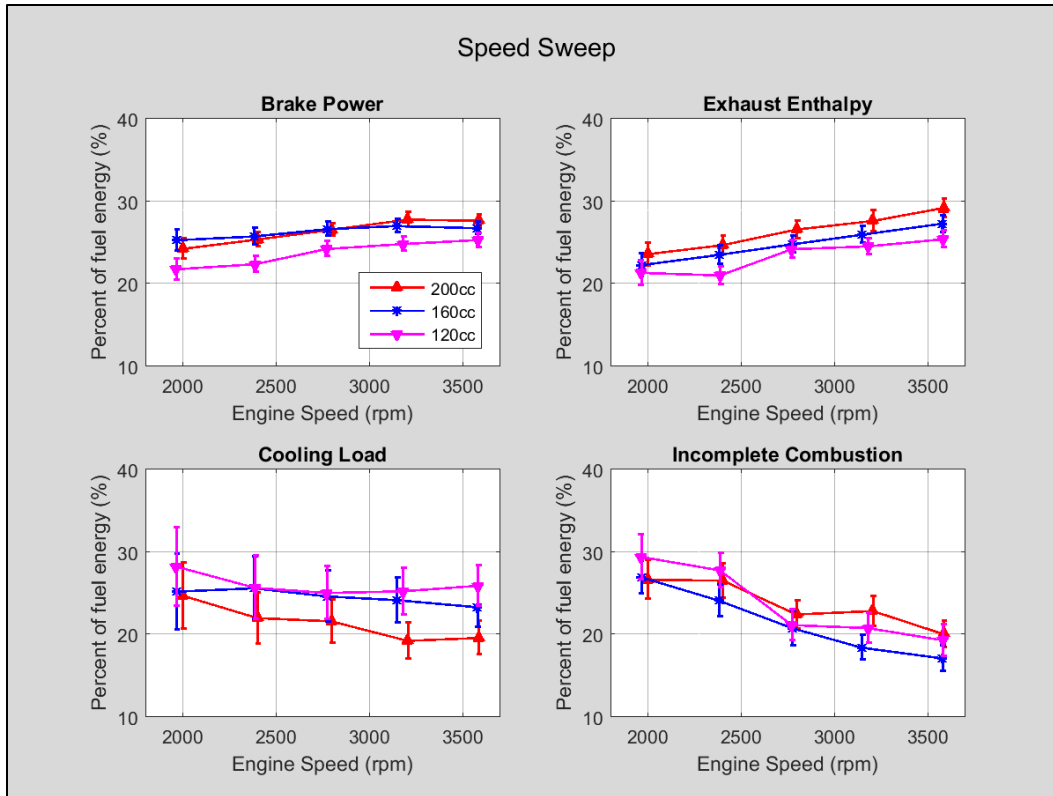


Figure 66. Combined speed sweep percentage of fuel energy in each energy pathway.

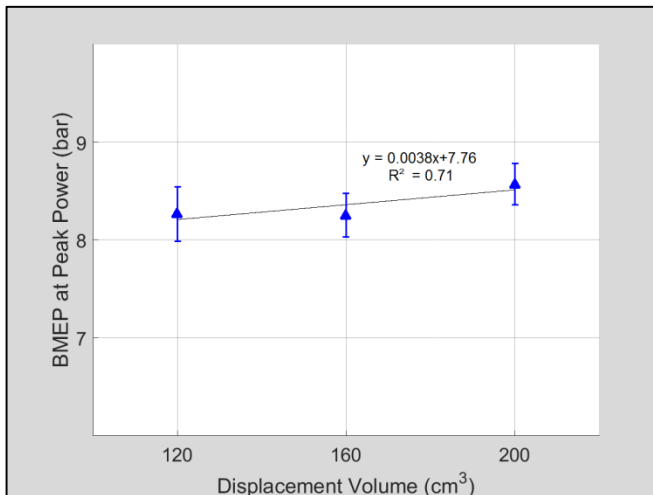
Recalling back to Section 2.4.3 and Section 2.4.4, it was a goal of Menon and Cadou [9, 33] and Ausserer et al. [7] to develop scaling laws in order to predict small ICE behavior on the basis of engine size. In Figure 12 and Figure 13 from Section 2.4.3, BMEP and fuel conversion efficiency for a wide variety of engines was plotted versus engine displacement. To generate the data for Figure 12 and Figure 13, BMEP and η_f were calculated using maximum brake power. Figure 67(a) and Figure 67(b) show the BMEP and η_f for the three Honda engines. Using these data points, Figure 12 and Figure 13 were updated to include the Honda GX120, GX160 and GX200 data, shown in Figure 68 and Figure 69. The figures show that the measured data from the three Honda

engines matches up well with the other data points on the figures and appear to corroborate the scaling laws of Menon and Cadou. As shown in Figure 67(a) and Figure 67(b), the BMEP and η_f at peak power points can be used with a linear least-squares regression to provide the following rudimentary scaling laws for four-stroke engines of 120 – 200 cm³ displacement volume (V_d):

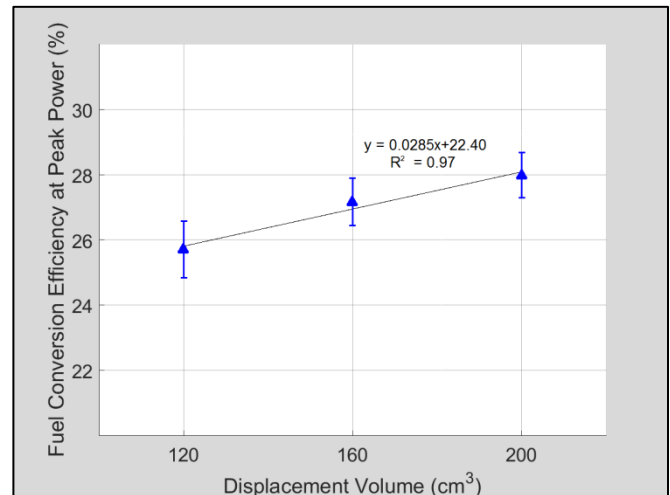
$$BMEP = 0.00382V_d + 7.76 \quad (58)$$

and

$$\eta_f = 0.0285V_d + 22.40 \quad (59)$$



(a) BMEP at peak power versus displacement volume.



(b) Fuel conversion efficiency versus displacement volume.

Figure 67. BMEP and fuel conversion efficiency (η_f) at peak power versus displacement volume for the Honda GX120, GX160, and GX200 engines.

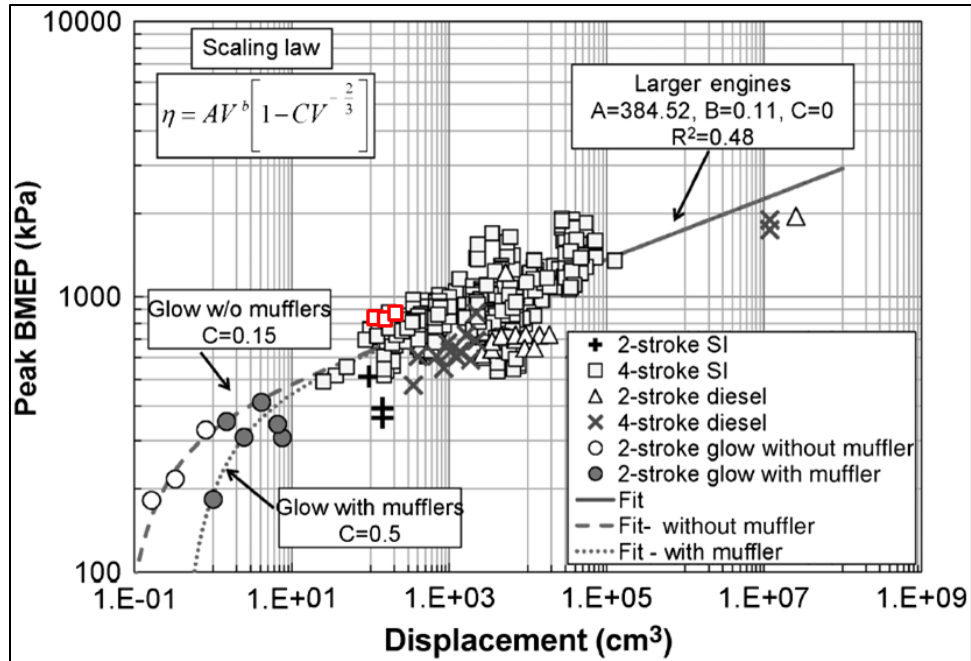


Figure 68. Menon and Cadou BMEP versus displacement plot [9] with data points from the Honda GX120, GX160, and GX200 added in red.

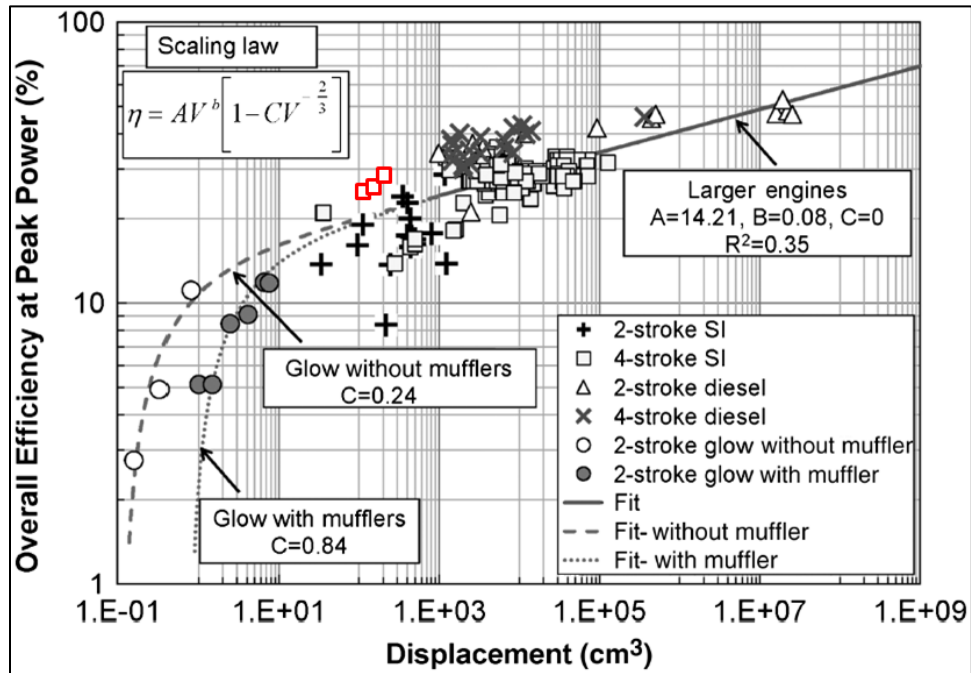


Figure 69. Menon and Cadou fuel conversion efficiency versus displacement plot [9] with data points from the Honda GX120, GX160, and GX200 added in red.

It may be more useful to include engine speed in the equations to estimate these properties under differing operating conditions. Section 2.3.4 introduced the notion of mean piston speed (\bar{S}_p), an engine speed normalized by engine stroke (L), which allows engines of different sizes and speeds to be compared to each other. To allow for a more universal application of the scaling laws developed in the following pages, the engine speeds of the three Honda engines tested were converted to mean piston speeds using Equation (13). The mean piston speed (in m/s) versus engine speed (in rpm) of the GX120, GX160 and GX200 engines are shown in Figure 70.

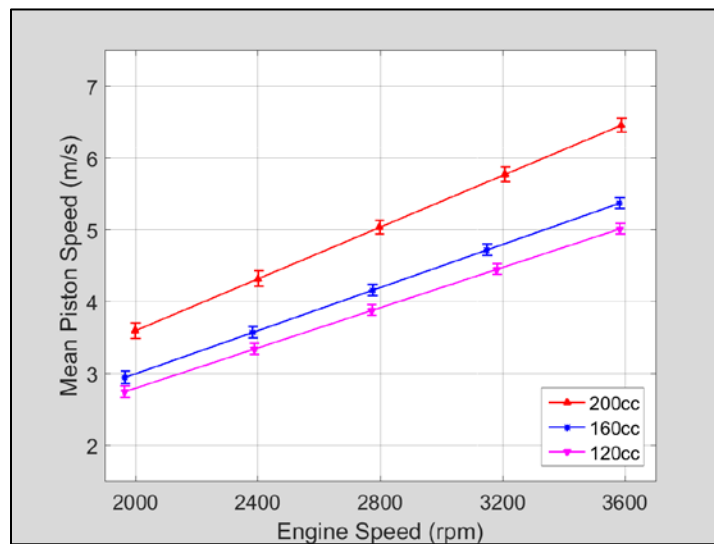


Figure 70. Mean piston speed versus engine speed for the Honda GX120, GX160 and GX200 engines.

After converting the engine speeds, contour plots of fuel conversion efficiency and BMEP as functions of mean piston speed and engine displacement were created and are shown in Figure 71 and Figure 72. A multivariable linear regression was then used to

generate equations for predicting BMEP and η_f as functions of both mean piston speed and displacement. The equations are of the form:

$$F(V_d(cm^3), \bar{S}_p(m/s)) = A + B * V_d + C * \bar{S}_p + D * \bar{S}_p^2 \quad (60)$$

The \bar{S}_p^2 term was included in the equations to improve the accuracy of the correlation. Adding a V_d^2 term slightly improved the accuracy, but was removed because the effects were negligible⁸. The equations fit the test data well, with an R^2 of 0.85 and a root mean square (RMS) error of 0.16 bar for the BMEP correlation and an R^2 of 0.73 and RMS error of 1.02 % of fuel energy for the η_f correlation. The BMEP and η_f equation coefficients for Equation (60) are listed in Table 5.

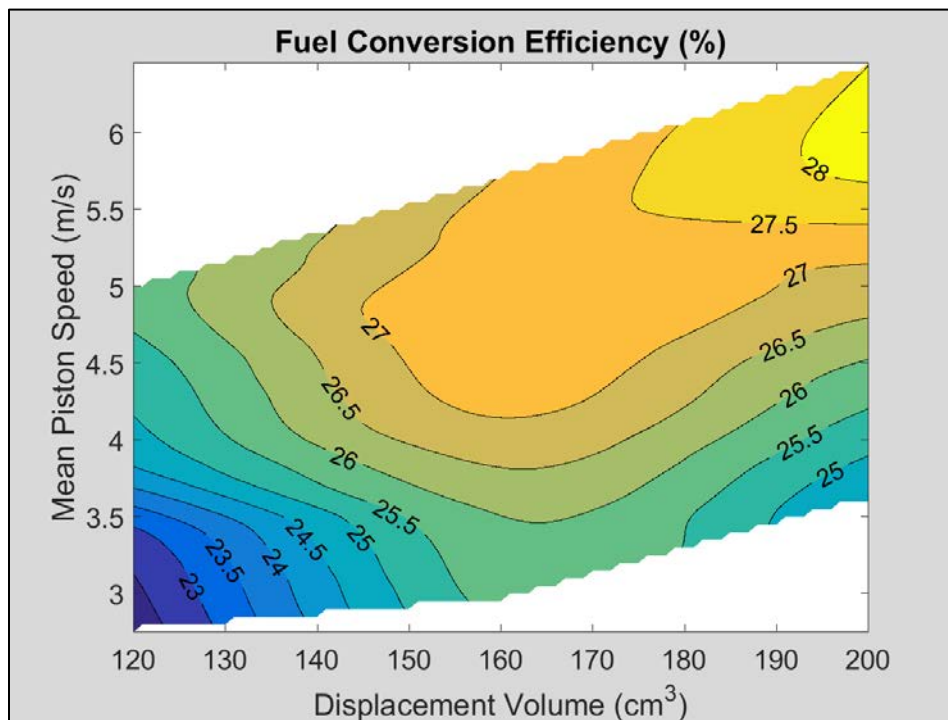


Figure 71. Fuel conversion efficiency as a function of mean piston speed and displacement volume.

⁸ A goal of the correlation equation analysis was to keep the equations as concise as possible while maintaining a high level of correlation to the collected data.

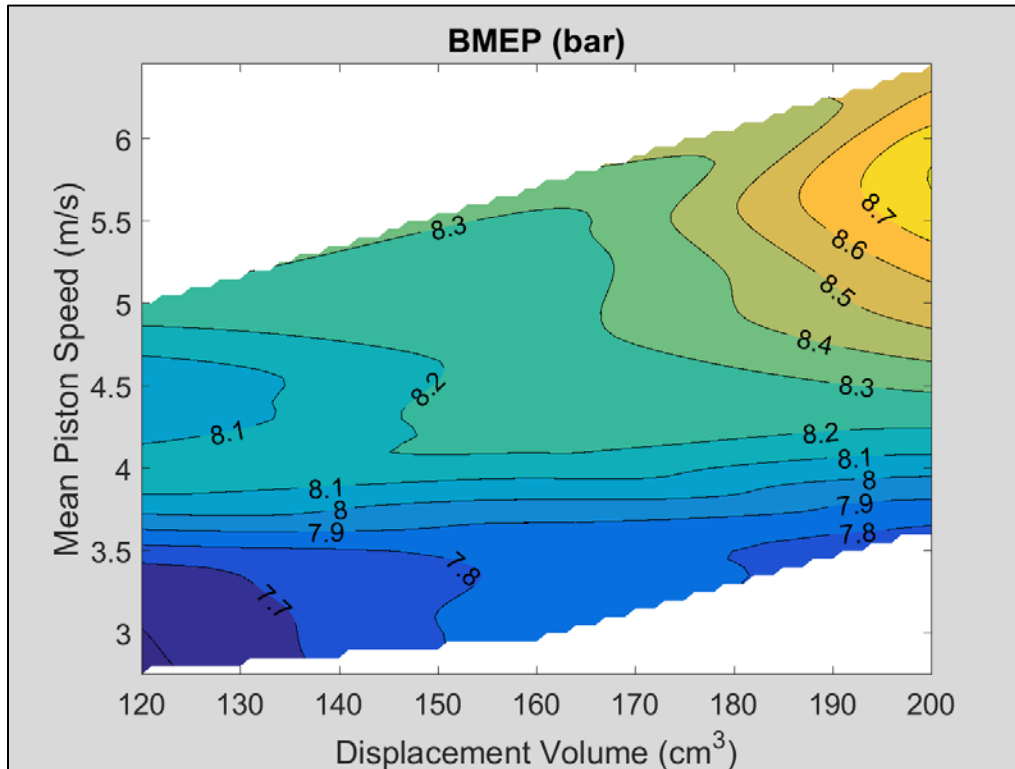


Figure 72. BMEP as a function of mean piston speed and displacement volume.

Table 5. BMEP and η_f coefficients for use with Equation (60).

Coefficient	A	B	C	D
BMEP (bar)	5.86	2.05E-03	0.63	-3.93E-02
η_f (%)	14.09	1.71E-02	3.08	-0.22

The form of Equation (60) was also used to generate scaling equations for exhaust enthalpy losses, cooling load losses, and incomplete combustion losses as a percentage of fuel energy for the three Honda engines. The equations had R^2 values of 0.95, 0.88, and 0.77, with RMS errors of 0.58%, 0.95%, and 2.01% of fuel energy, respectively.

Table 6. Exhaust enthalpy, cooling load, and incomplete combustion losses as a percentage of fuel energy coefficients for use with Equation (60).

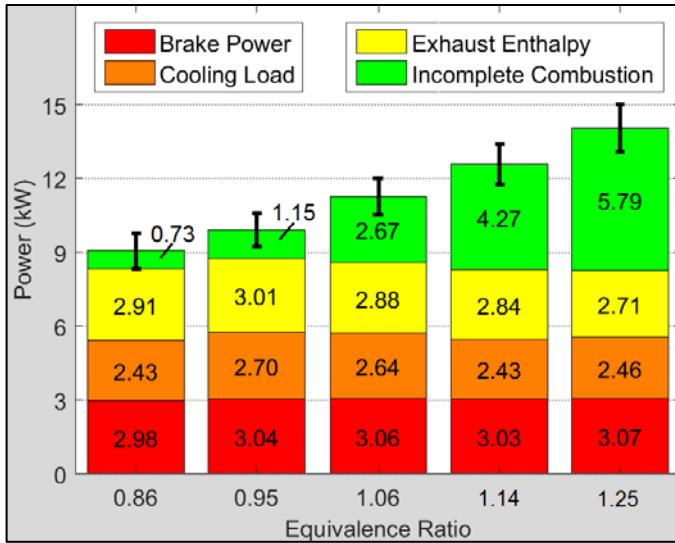
Coefficient	A	B	C	D
Exhaust Enthalpy (%)	13.99	8.65E-03	2.52	-5.88E-02
Cooling Load (%)	34.18	-3.90E-02	-0.29	-0.12
Incomplete Combustion (%)	50.31	4.16E-02	-12.41	1.02

4.2.2. GX120, GX160, and GX200 Parametric Studies

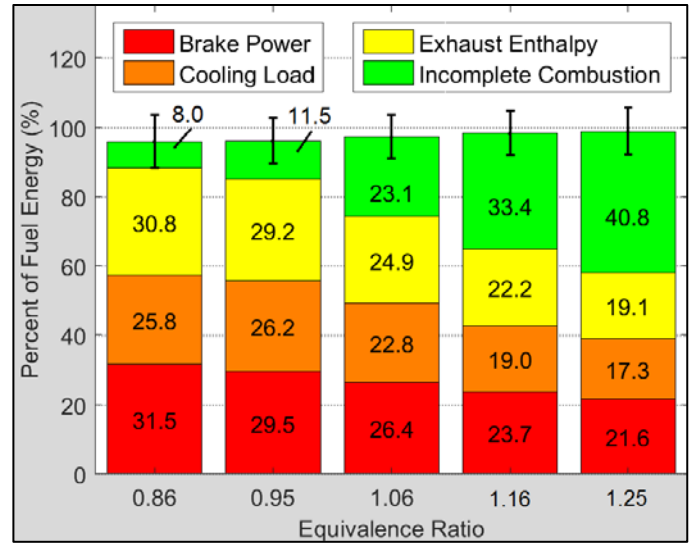
Similar to the GX120 engine, the GX160 and GX200 engines were run through a series of parametric studies to characterize the impact of five variables (equivalence ratio, combustion phasing, head temperature, engine speed and throttle setting) on the loss pathways. The speed sweeps were discussed in Section 4.2.1; the remainder of Section 4.2.2 will discuss the remaining parametric studies. The equivalence ratio sweeps are discussed in Section 4.2.2.1, the combustion phasing sweeps are in Section 4.2.2.2, the cooling load (or head temperature) sweeps are in Section 4.2.2.3, and the throttle sweeps are in Section 4.2.2.4.

4.2.2.1. GX120, GX160, and GX200 Equivalence Ratio Sweep

The GX160 and GX200 engines were run through a sweep of equivalence ratio from $\phi = 0.85$ to $\phi = 1.25 \pm 0.02$. Other conditions held constant were: WOT, engine speed of 2800 ± 120 rpm, CA50 of $8^\circ \pm 0.4^\circ$ aTDC, and cylinder head temperatures of $150^\circ \pm 1^\circ$ C for the GX160 and of $170^\circ \pm 1^\circ$ C for the GX200 engines. The energy balance results for the GX160 equivalence ratio sweep are shown in Figure 73, while the energy balance results for the GX200 equivalence ratio sweep are shown in Figure 74.

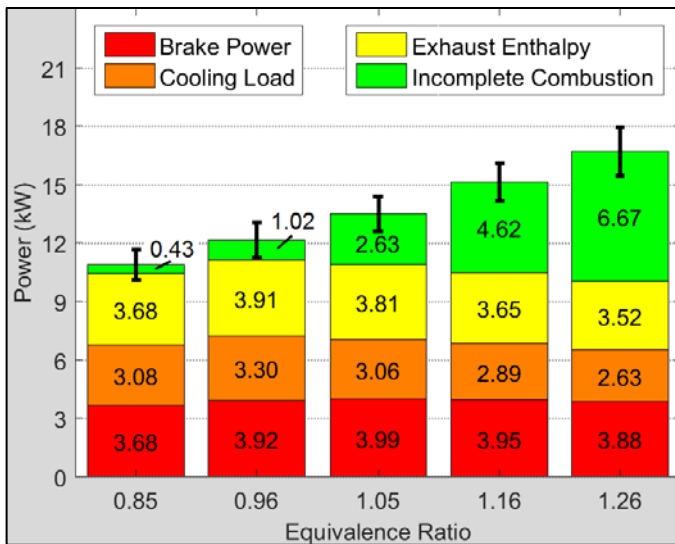


(a) Overall energy in each pathway (kW).

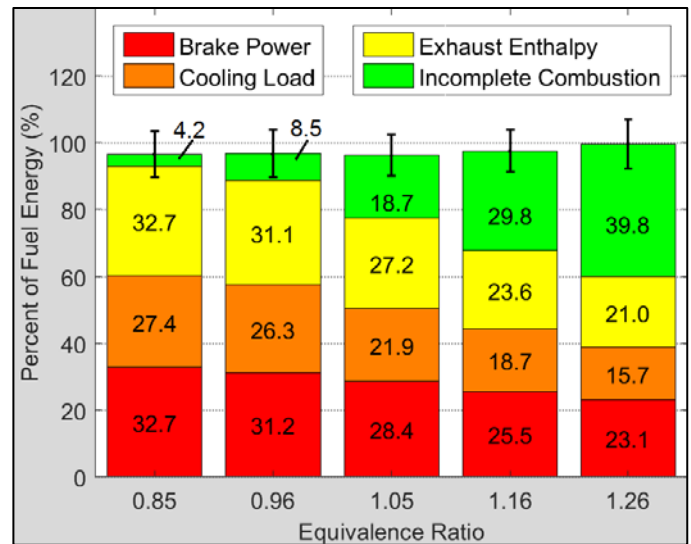


(b) Percentage of fuel energy in each pathway.

Figure 73. GX160 equivalence ratio sweep energy balance.



(a) Overall energy in each pathway (kW).



(b) Percentage of fuel energy in each pathway.

Figure 74. GX200 equivalence ratio sweep energy balance.

The energy balance results of both engines showed similar patterns of fuel energy distribution, which will be discussed further in the following pages. Looking at the energy distributions as a percentage of fuel energy, seen in Figure 73(b) and Figure 74(b),

the total measurement of energy ranged from 96.9% to 99.8% of the fuel energy entering the GX160 engine and 97.0% to 100.3% of the fuel energy entering the GX200 engine. Much like the GX120 equivalence ratio sweep from Figure 42, both sets of data tended to show greater deviation from 100% as the fuel mixture progressed from lean to rich, but are within the experimental uncertainty for achieving 100% fuel accountability.

Examining the energy pathway magnitude data in Figure 75, it can be seen that all three of the Honda engines had a peak in brake power at $\phi = 1.05$, with slight dips in output as the fuel/air mixtures became very lean or very rich. All three of the engines had a peak in exhaust enthalpy losses at $\phi = 0.95$, also with only slight drops as the mixture was leaned and richened. The GX160 and GX200 engines followed roughly the same trend as the GX120 engine for cooling load losses, showing a peak at either $\phi = 0.95$ or $\phi = 1.05$, with a steady decrease (or leveling for the GX160) as the mixture was leaned or richened, with minimum cooling load losses when the mixture was very rich ($\phi = 1.25$). Incomplete combustion losses showed a general trend of the GX120 having the lowest losses (except at $\phi = 0.85$), while the GX160 and GX200 had nearly identical losses at all but the very rich test points.

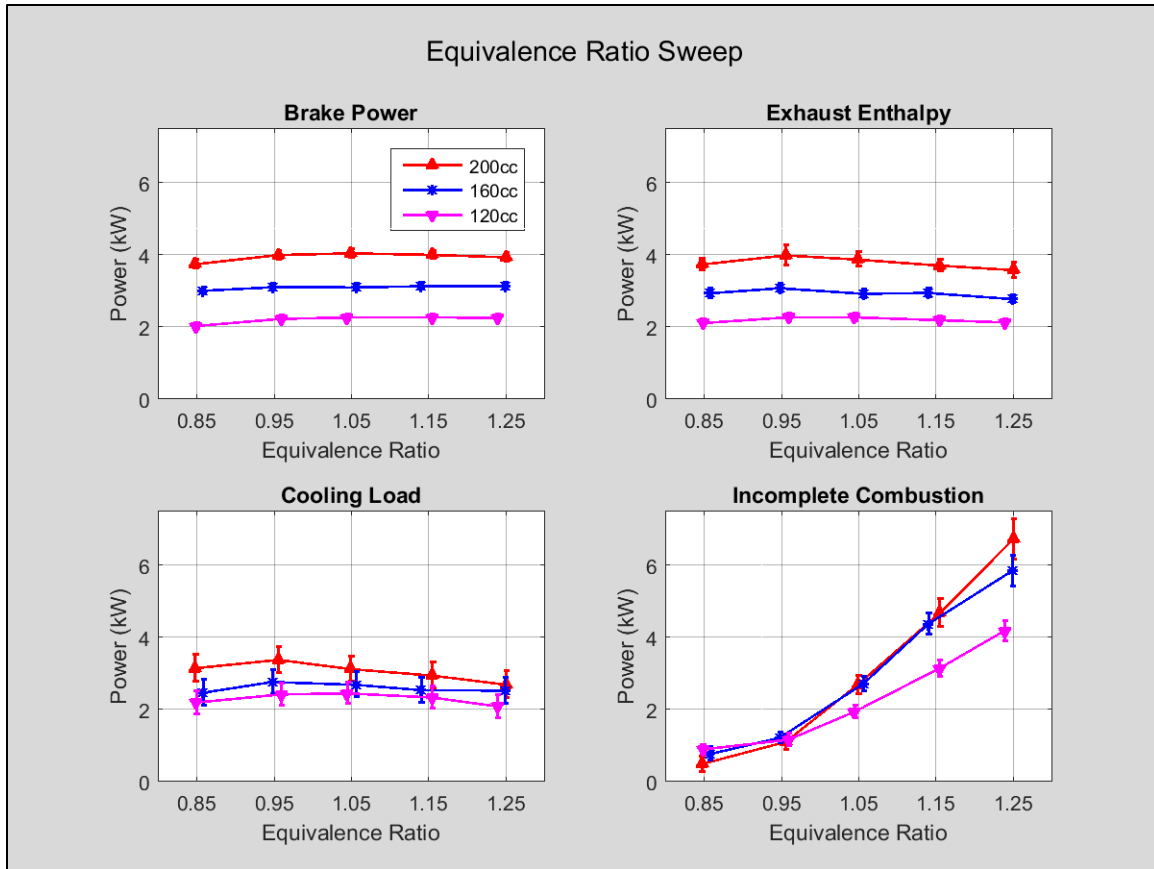


Figure 75. Combined equivalence ratio sweep energy pathways (in kW).

Figure 76 contains the IMEP and CoV of IMEP data from the equivalence ratio sweeps of the three Honda engines. The GX200 engine had consistently higher IMEP than the GX160 and GX120 engines throughout the equivalence ratio sweep, as expected, but decreased at $\phi = 0.85$ and $\phi = 0.95$ (possibly due to higher CoV of IMEP) where the GX200 IMEP was nearly identical to the GX160 IMEP. Recalling that Figure 75 clearly showed that brake power at $\phi = 0.85$ and $\phi = 0.95$ was considerably higher for the GX200 engine than the GX160, this may be an indication that the GX160 engine had greater friction losses under lean running conditions. Looking at the CoV of IMEP plots from Figure 76, it can be seen that there was greater combustion inconsistency in all three

of the engines when they were run lean, which may be another contributing factor in the IMEP similarities.

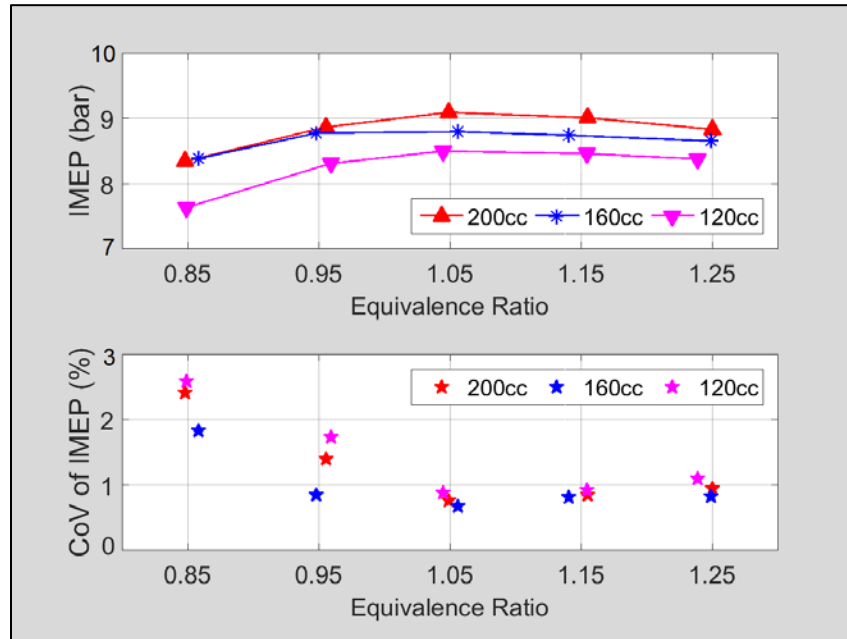
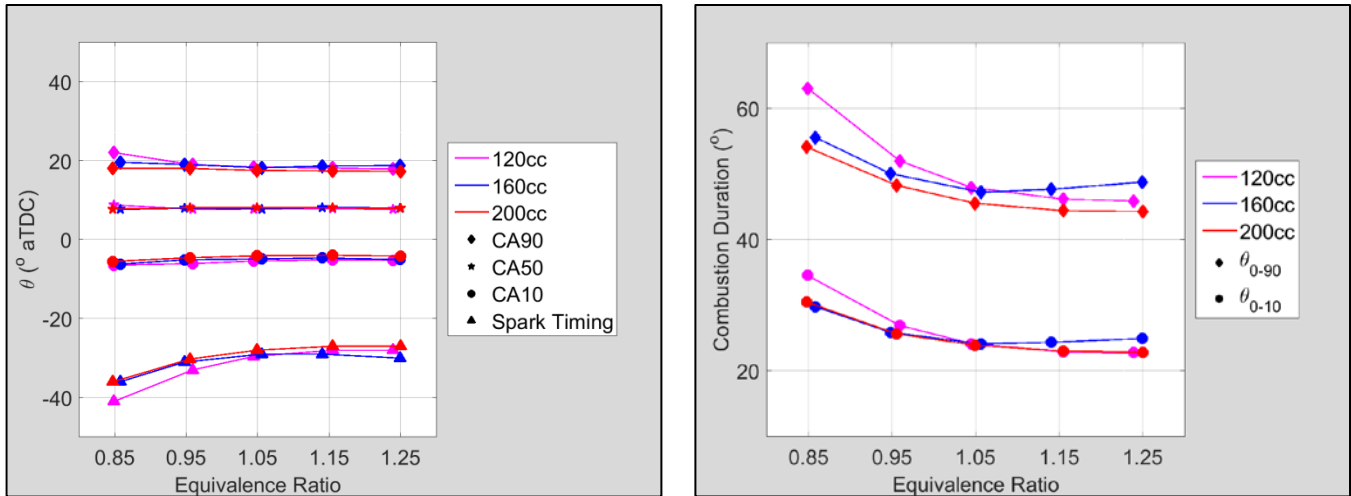


Figure 76. Combined equivalence ratio sweep IMEP and CoV of IMEP.

The combined plots showing combustion phasing and combustion duration in Figure 77 show a general trend of slightly shorter fuel burn times as the engines increased in displacement volume, with the exception of the GX160 showing a slight increase in θ_{0-10} and θ_{0-90} from $\phi = 1.05$ to $\phi = 1.25$. Looking at Figure 77(a), an increase in spark timing advance was seen as well for the GX160 engine from $\phi = 1.05$ to $\phi = 1.25$. This small change in spark timing to a possibly less than optimal setting may have resulted in slightly more crank angle degrees required for a 10% and 90% fuel burn, but generally the results match up well, showing that displacement volume had minimal impact on combustion phasing in this size range.



(a) Combined speed sweep combustion phasing.

(b) Combined speed sweep combustion duration.

Figure 77. Combined equivalence ratio sweep combustion phasing and combustion duration.

The combined plots of the percentage of fuel energy in each pathway for the equivalence ratio sweeps are shown in Figure 78. Generally, fuel conversion efficiency scaled with engine displacement, showing higher efficiency as engine displacement increased. Exhaust enthalpy losses as a percentage of fuel energy were highest across the board for the GX200 engine, while at lean conditions the GX160 engine showed a slightly higher percentage, until the GX120 and GX160 values converged from $\phi = 1.05$ to $\phi = 1.25$. Cooling load losses as a percentage of fuel energy were generally higher for the GX120 engine, and virtually impossible to distinguish for the GX160 and GX200 engines. Incomplete combustion losses as a percentage of fuel energy were generally lowest for the GX200 engine, while the GX120 showed a higher percentage at lean conditions, switching with the GX160 at rich conditions, and all three engines had incomplete combustion losses of approximately 40% at $\phi = 1.25$.

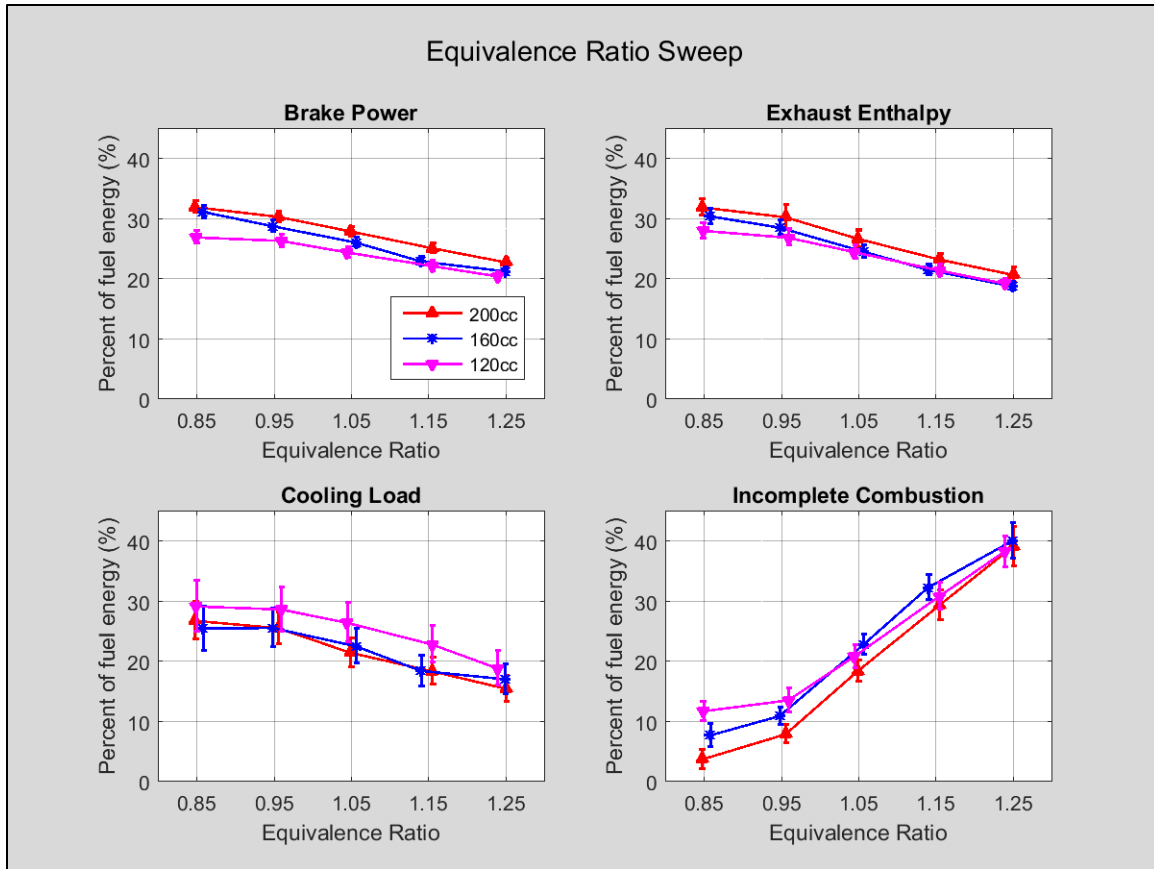


Figure 78. Combined equivalence ratio sweep percentage of fuel energy in each energy pathway.

Much like the analysis done on the combined speed sweep data in Figure 71 and Figure 72 from Section 4.2.1, it was beneficial to map η_f and BMEP in smoothed contour plots showing them as functions of both equivalence ratio and displacement volume. The results, seen in Figure 79 and Figure 80, show η_f increasing consistently to the right and bottom (displacement increasing, equivalence ratio decreasing) of Figure 79. In Figure 80, all three of the engines show peak BMEP at $\phi = 1.05$, but little change in BMEP for displacement volumes between 120 and 160 cm³ and $\phi = 1.0$ to $\phi = 1.25$.

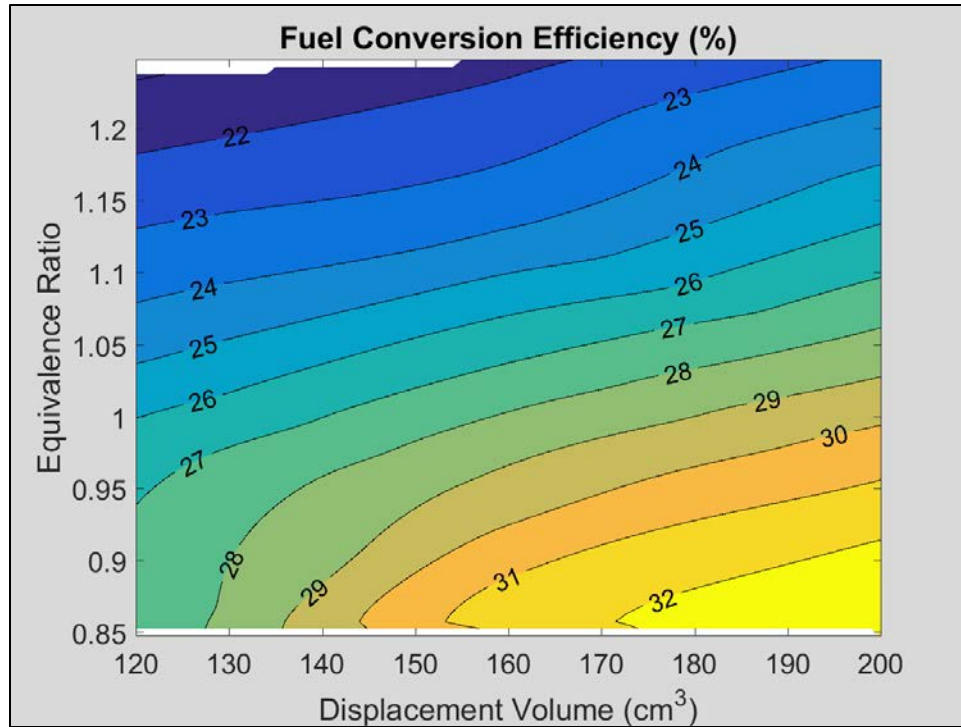


Figure 79. Fuel conversion efficiency as a function of equivalence ratio and displacement volume.

Finally, a set of multivariable equations was developed to predict BMEP, η_f , exhaust enthalpy losses as a percentage of fuel energy, cooling load losses as a percentage of fuel energy, and incomplete combustion losses as a percentage of fuel energy. The equations are for four stroke engines in the size range of 120 – 200 cm³ displacement, operating at equivalence ratios ranging from 0.85 to 1.25. The equations are of the form:

$$F(V_d(\text{cm}^3), \phi) = A + B * V_d + C * \phi + D * \phi^2 \quad (61)$$

Values for the coefficients A – D, R² values for the multiple linear regression analyses, and the RMS errors for the equations are listed in Table 7. RMS error for the BMEP equation has units of bar, while RMS error for the remaining four equations have units of percentage of fuel energy.

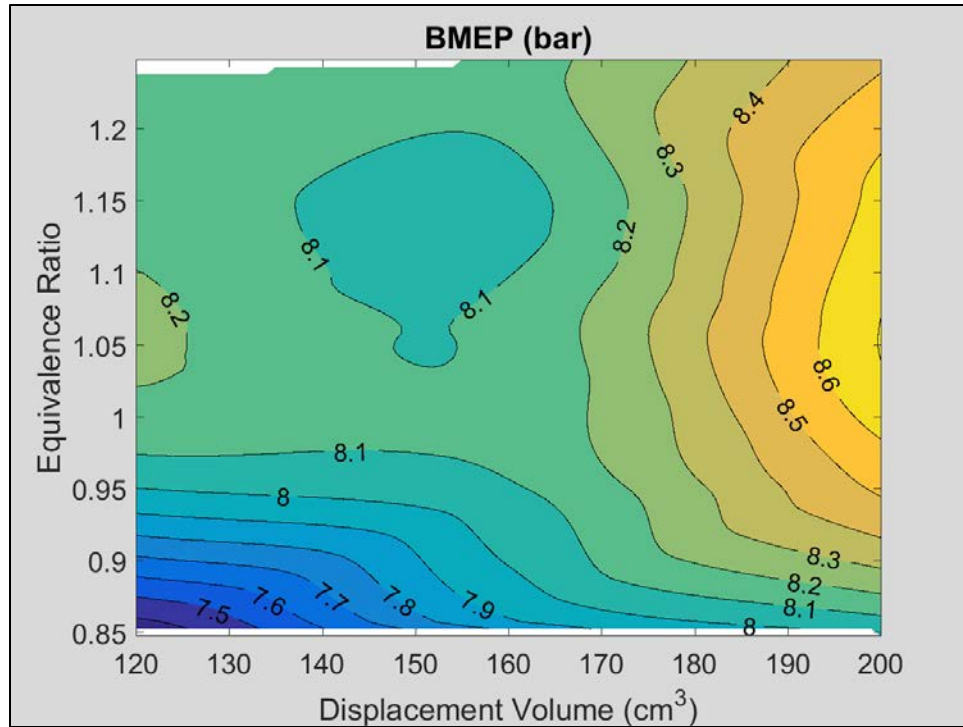


Figure 80. BMEP as a function of equivalence ratio and displacement volume.

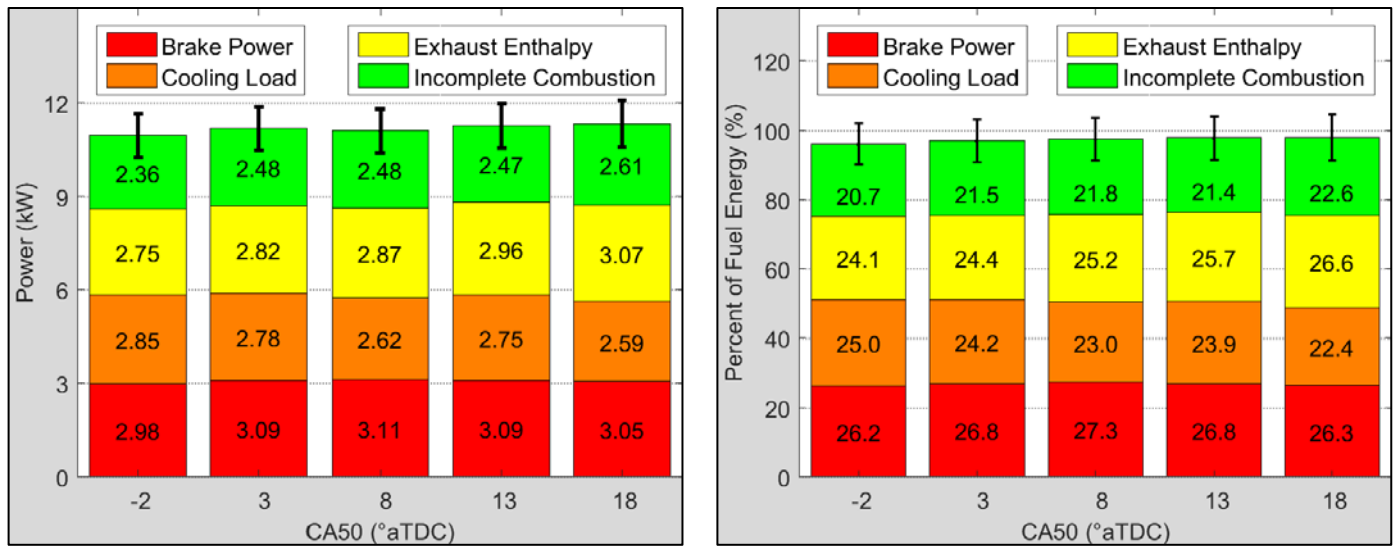
Table 7. BMEP, η_f , exhaust enthalpy, cooling load, and incomplete combustion losses as a percentage of fuel energy coefficients for use with Equation (61).

	A	B	C	D		R ²	RMS Error
BMEP (bar)	-3.89	6.28E-03	20.27	-9.13		0.83	0.16
η_f (%)	28.49	4.65E-02	4.81	-13.00		0.97	0.72
Exhaust Enthalpy (%)	31.13	3.40E-02	7.81	-17.09		0.97	0.77
Cooling Load (%)	18.28	-4.37E-02	51.50	-37.47		0.94	1.23
Incomplete Combustion (%)	32.65	-4.43E-02	-93.78	84.83		0.97	2.27

4.2.2.2. GX120, GX160, and GX200 Combustion Phasing Sweep

The GX160 and GX200 engines were run through a combustion phasing sweep where CA50 was varied from 2° bTDC to 18° ± 0.4° aTDC. Other conditions held

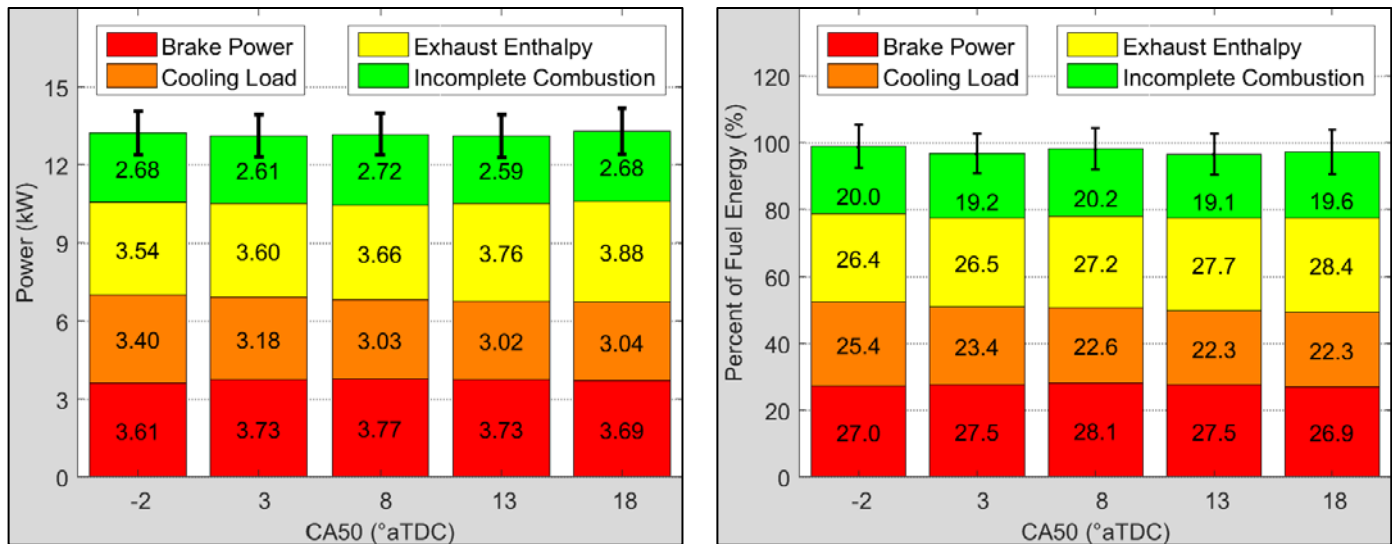
constant were: WOT, ϕ of 1.05 ± 0.02 , engine speed of 2800 ± 120 rpm, and cylinder head temperatures of $150^\circ \pm 1^\circ$ C for the GX160 and $170^\circ \pm 1^\circ$ C for the GX200 engines. The energy balance results for the GX160 combustion phasing sweep are shown in Figure 81, while the energy balance results for the GX200 combustion phasing sweep are shown in Figure 82.



(a) Overall energy in each pathway (kW).

(b) Percentage of fuel energy in each pathway.

Figure 81. GX160 combustion phasing sweep energy balance.



(a) Overall energy in each pathway (kW).

(b) Percentage of fuel energy in each pathway.

Figure 82. GX200 combustion phasing sweep energy balance.

The most apparent trend seen in Figure 81 and Figure 82 is the lack of obvious trends in the data. Compared to the data from the speed and equivalence ratio sweeps, the energy distributions of the combustion phasing sweeps were relatively constant. The energy distributions as a percentage of fuel energy, seen in Figure 81(b) and Figure 82(b), showed total measurements of energy ranged from 96.8% to 98.6% of the fuel energy entering the GX160 engine and 97.3% to 99.5% of the fuel energy entering the GX200 engine.

Examining the magnitude of energy in each pathway, seen in Figure 83, all of the measurements increased with engine size, with the cooling load losses and incomplete combustion losses again showing some deviation in relative distance from one another. All three engines showed a peak in brake power at CA50 = 8° aTDC. Exhaust enthalpy

losses steadily increased as CA50 was advanced throughout the sweeps. Cooling load losses decreased slightly with increasing CA50. Incomplete combustion losses showed slight variations but remained essentially stable throughout the sweeps. This shows that, while the raw values of power change with engine size, the percent distributions, as seen in Figure 81(b) and Figure 82(b), had very little change with engine displacement.

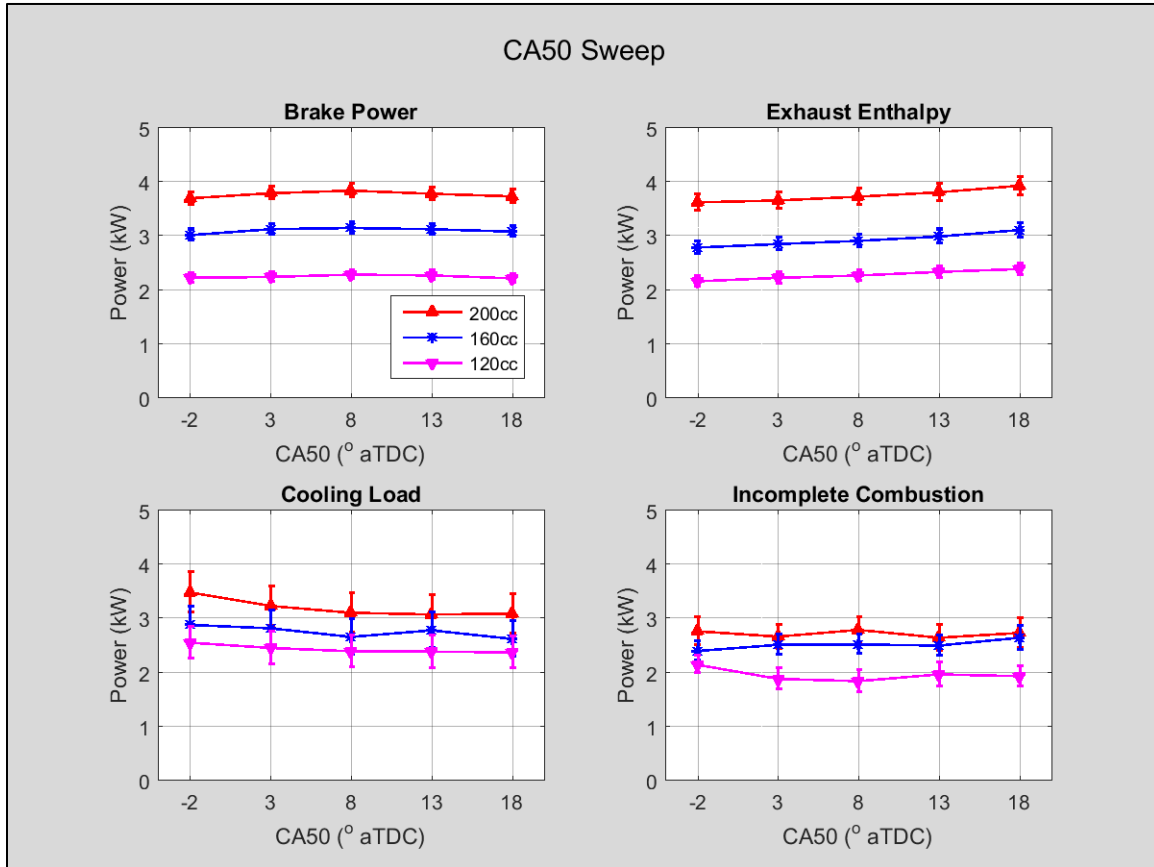


Figure 83. Combined combustion phasing sweep energy pathways (in kW).

IMEP and CoV of IMEP for the three engines, shown in Figure 84, followed very similar trends, showing maximum IMEP and minimum CoV of IMEP at CA50 = 8°

aTDC. The GX120 engine had lower levels of IMEP throughout the sweeps while the GX160 and GX200 engines had essentially the same IMEP.

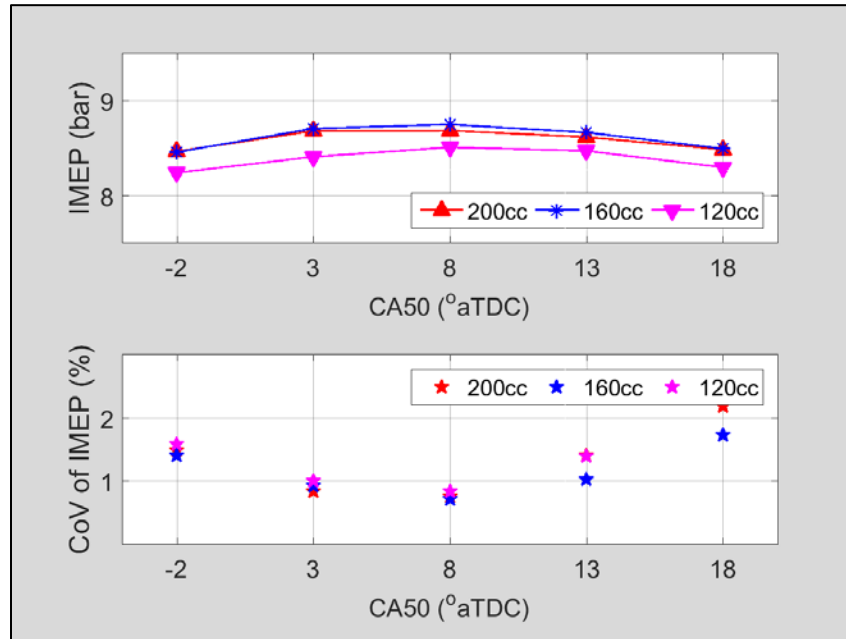
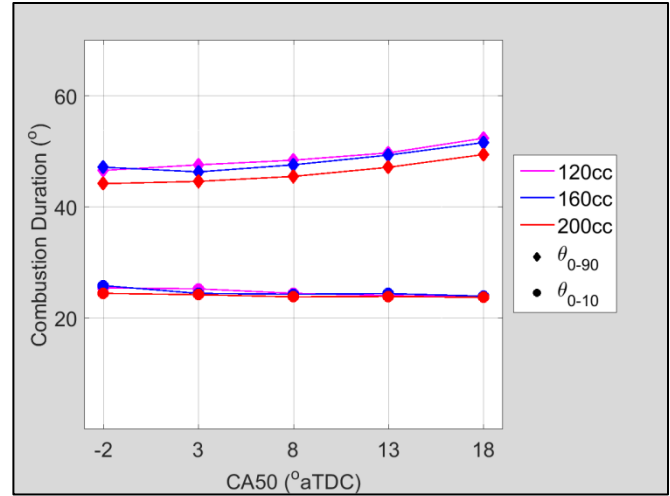
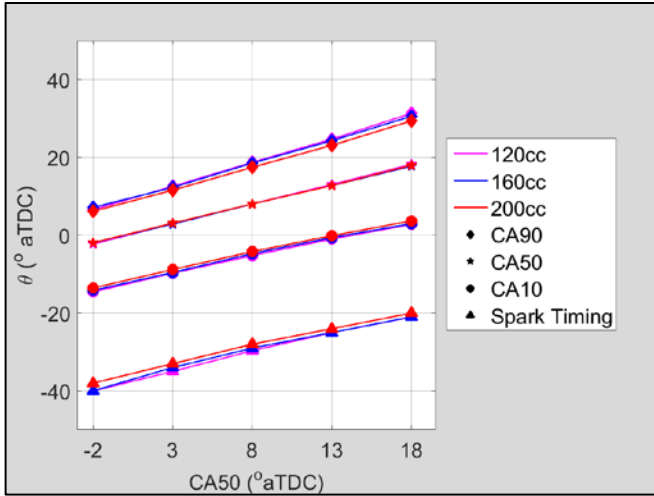


Figure 84. Combined combustion phasing sweep IMEP and CoV of IMEP.

Figure 85 shows the combustion phasing and combustion duration of the combustion phasing sweeps for the three engines. There were no significant deviations from the trends discussed for the GX120 engine discussed in Section 4.1.3.2. Figure 86 shows the energy pathways as a percentage of fuel energy for the combustion phasing sweeps of the three engines. The trends in the data are essentially the same as those for the energy pathway data from Figure 83, with no discernable trend in the incomplete combustion losses as a percentage of fuel energy.



(a) Combined speed sweep combustion phasing.

(b) Combined speed sweep combustion duration.

Figure 85. Combined combustion phasing sweep combustion phasing and combustion duration.

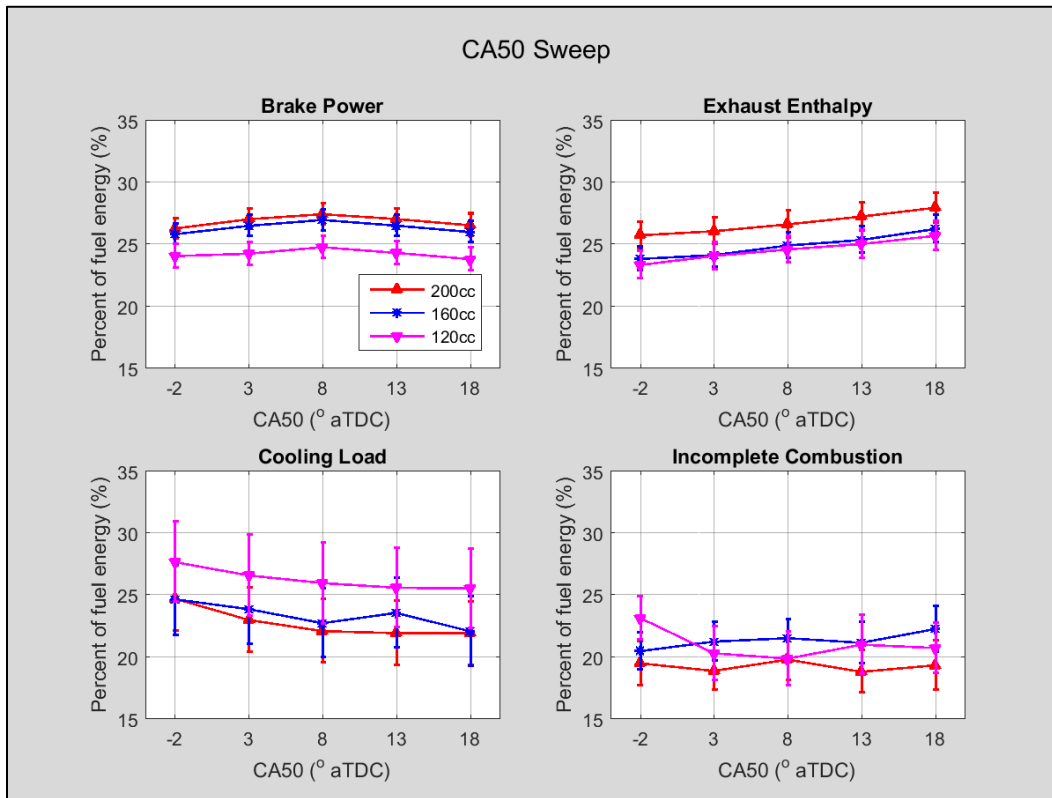
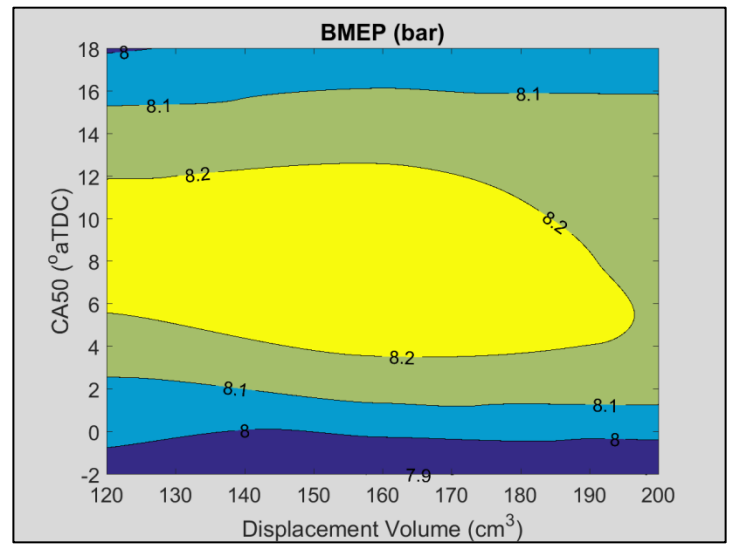
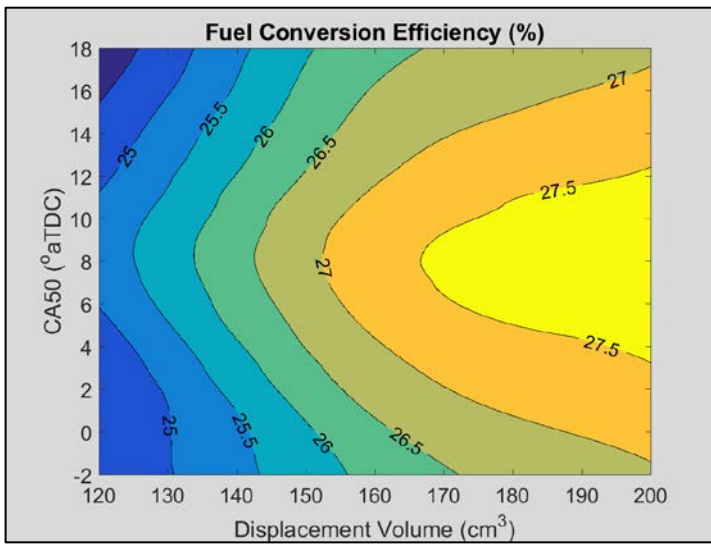


Figure 86. Combined combustion phasing sweep percentage of fuel energy in each energy pathway.

Contour plots for η_f and BMEP as a function of CA50 and displacement volume are shown in Figure 87(a) and Figure 87(b). Both figures were somewhat symmetric about the horizontal dividing line of CA50 = 8° aTDC, showing η_f at a maximum when CA50 was 8° aTDC and increasing with displacement volume and BMEP having little dependence on displacement volume.



(a) Fuel conversion efficiency as a function of CA50 and displacement volume.

(b) BMEP as a function of CA50 and displacement volume.

Figure 87. Fuel conversion efficiency and BMEP as functions of CA50 and displacement volume.

A set of multivariable equations was developed from the combustion phasing data to predict BMEP, η_f , exhaust enthalpy losses as a percentage of fuel energy, cooling load losses as a percentage of fuel energy, and incomplete combustion losses as a percentage of fuel energy. The equations are for four stroke engines in the size range of 120 – 200

cm³ displacement, operating at CA50 ranging from 2° bTDC to 18° aTDC. The equations are of the form:

$$F(V_d(cm^3), CA50(^{\circ}aTDC)) = A + B * V_d + C * CA50 + D * CA50^2 \quad (62)$$

Values for the coefficients A – D, R² values for the multiple linear regression analyses, and the RMS errors for the equations are listed in Table 8. For this set of correlations, the CA50² term had only a small effect on the equation outcome, evidenced by the small magnitude of the “D” coefficients in Table 8, however it was left into the form of Equation (62) for consistency. RMS error for the BMEP equation has units of bar, while RMS error for the remaining four equations have units of percentage of fuel energy.

Table 8. BMEP, η_f , exhaust enthalpy, cooling load, and incomplete combustion losses as a percentage of fuel energy coefficients for use with Equation (62).

	A	B	C	D		R ²	RMS Error
BMEP (bar)	8.04	-5.99E-05	4.51E-02	-2.52E-03		0.94	3.30E-02
η_f (%)	20.79	3.34E-02	0.13	-8.42E-03		0.91	0.41
Exhaust Enthalpy (%)	20.49	2.78E-02	8.61E-02	1.54E-03		0.89	0.49
Cooling Load (%)	32.60	-4.38E-02	-0.23	6.84E-03		0.86	0.79
Incomplete Combustion (%)	24.56	-2.14E-02	-0.12	6.97E-03		0.42	1.05

4.2.2.3. GX120, GX160, and GX200 Cooling Load Sweep

The GX160 and GX200 engines were run through a cooling load sweep where the cylinder head temperatures were varied from 130° C to 170° C ± 1° C for the GX160 engine and from 150° C to 190° C ± 1° C for the GX200 engine. Other conditions held

constant were: WOT, ϕ of 1.05 ± 0.02 , engine speed of 2800 ± 120 rpm, and CA50 of $8^\circ \pm 0.4^\circ$ aTDC. To generalize the data, the results were plotted on the basis of the equivalent air speed (in m/s) of the cooling air rather than cylinder head temperature. A plot of cooling air speed versus cylinder head temperature for the three Honda engines is shown in Figure 88. Converting from cylinder head temperature to cooling air speed allowed the data to be plotted on a common scale (approximately 16 to 28 m/s).

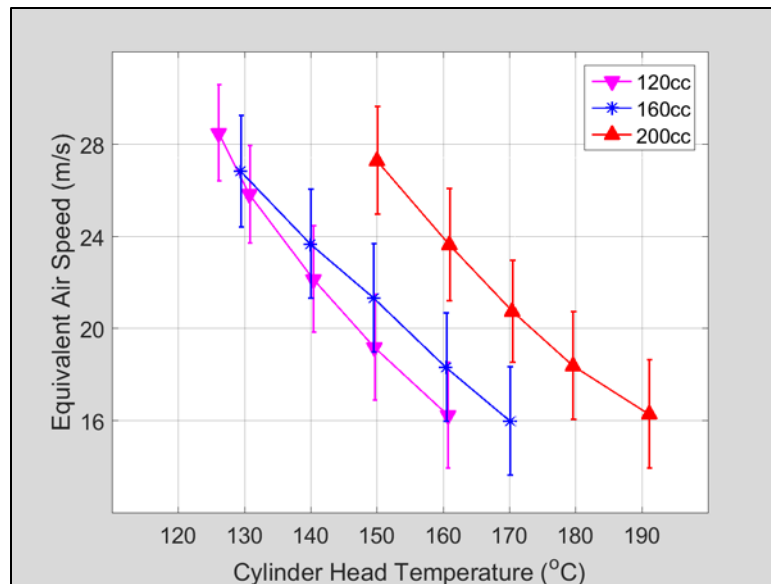
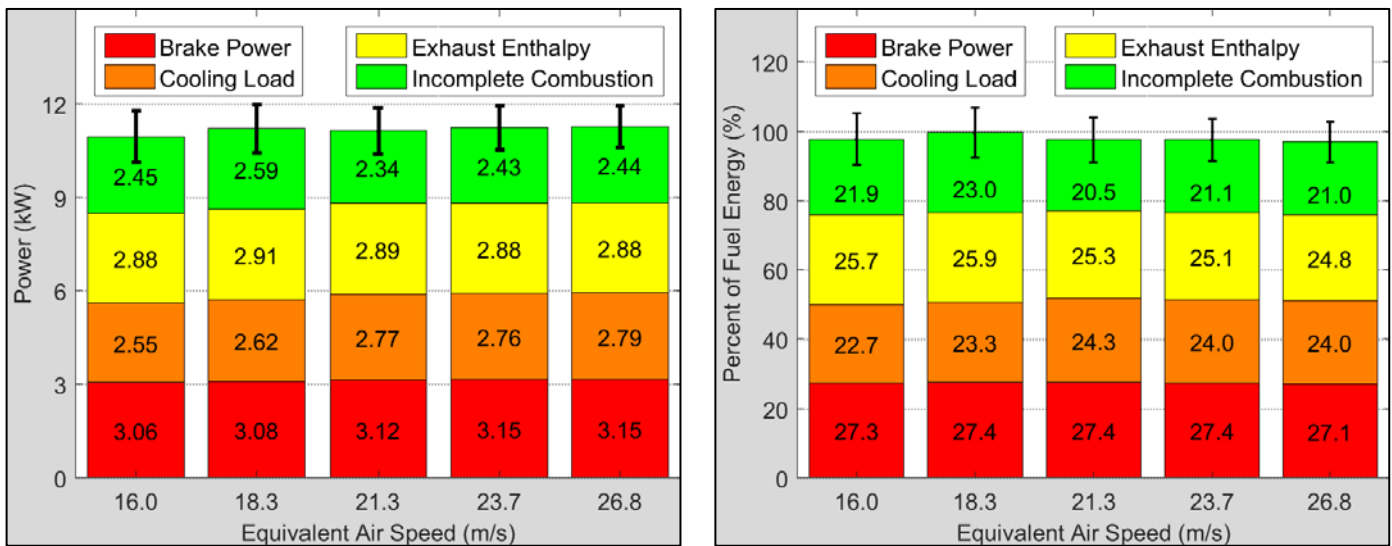


Figure 88. Equivalent air speed of cooling air versus cylinder head temperature for the Honda GX120, GX160, and GX200 engines.

The energy balance results for the GX160 cooling load sweep are shown in Figure 89, while the energy balance results for the GX200 cooling load sweep are shown in Figure 90. Examining the energy balance figures shows that there was little to no significant change in the magnitudes or percentages of fuel energy in the four pathways as the cooling air velocity increased. The engines required some amount of cooling air to operate effectively, and did show slight reductions in brake power at high cylinder head

temperatures (low equivalent air speed), but the overall trends did not change considerably as a function of cylinder head temperature. The energy distributions as a percentage of fuel energy, seen in Figure 89(b) and Figure 90(b), showed total measurements of energy ranged from 97.7% to 100.4% of the fuel energy entering the GX160 engine and 96.6% to 97.9% of the fuel energy entering the GX200 engine.

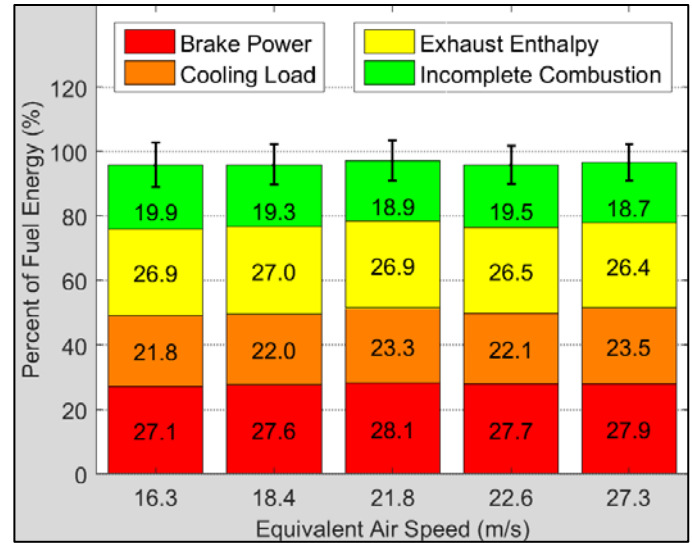
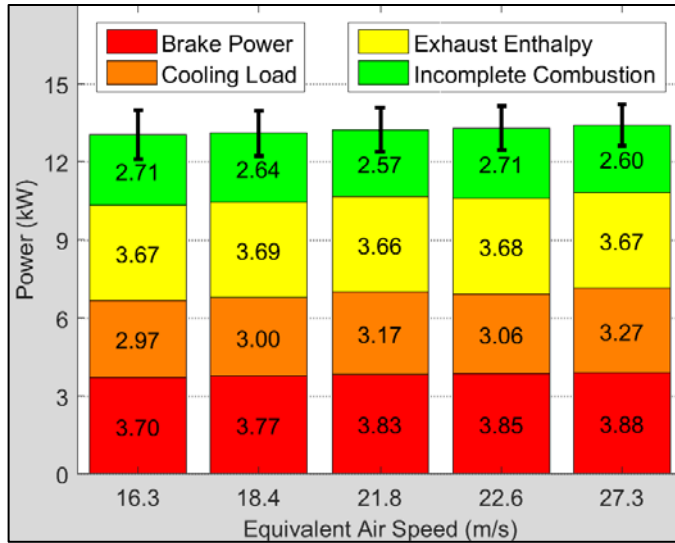
The IMEP and CoV of IMEP for the three engines was plotted as seen previously in the combined speed, equivalence ratio, and combustion phasing sweep plots from the preceding sections, but they showed very little variation and will not be discussed in this section. They have been included in Appendix A for reference with combined plots showing the combustion phasing and combustion duration.



(a) Overall energy in each pathway (kW).

(b) Percentage of fuel energy in each pathway.

Figure 89. GX160 cooling load sweep energy balance.



(a) Overall energy in each pathway (kW).

(b) Percentage of fuel energy in each pathway.

Figure 90. GX200 cooling load sweep energy balance.

BMEP and η_f contour plots were not generated due to the lack of variability in the cooling load sweep data as cylinder head temperature changed. As an alternative, the mean BMEP values for the cooling load sweeps of the GX120, GX160, and GX200 engines were calculated and plotted versus displacement volume, shown in Figure 91.

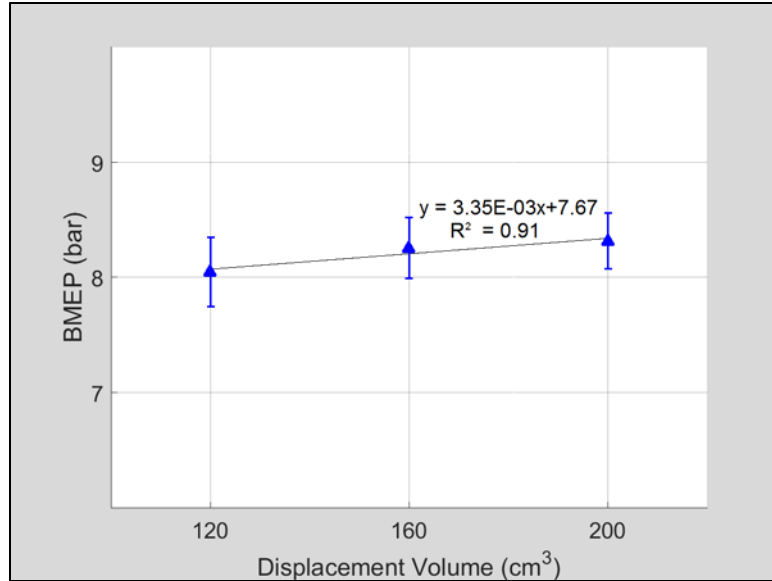


Figure 91. Average BMEP versus displacement volume for the combined cooling load sweeps.

Averaged brake power, exhaust enthalpy, cooling load, and incomplete combustion losses as percentage of fuel energy were also plotted as a function of displacement volume, as seen in Figure 92. Using linear regression analysis, single variable equations were generated to predict BMEP, η_f , exhaust enthalpy losses, cooling load losses, and incomplete combustion losses as a percentage of fuel energy as a function of displacement volume. The equations only have a V_d term because the cylinder head temperature had little effect on the quantities being predicted in the correlations. The equations were of the form:

$$F(V_d(\text{cm}^3)) = A + B * V_d \quad (63)$$

Values for the coefficients A – B, R^2 values for the linear regression analyses, and the RMS errors for the equations are given in Table 8. RMS error for the BMEP equation

has units of bar, while RMS error for the remaining four equations have units of percentage of fuel energy.

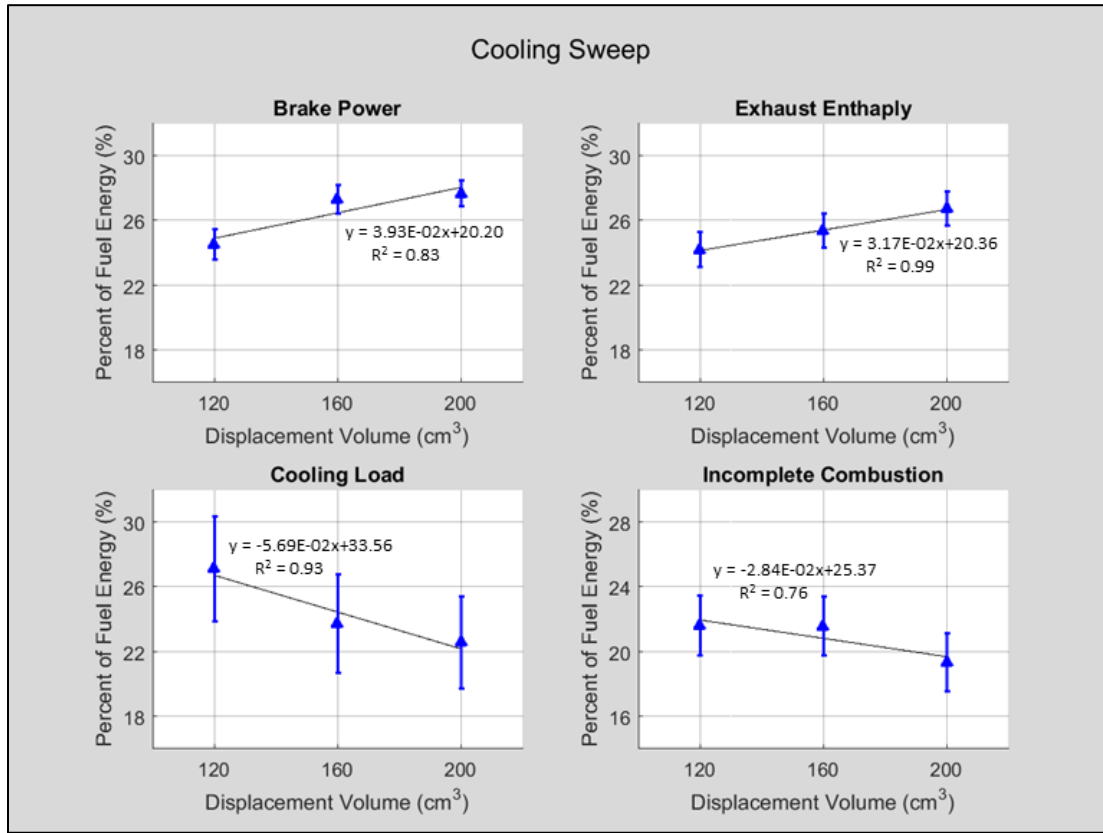


Figure 92. Average brake power, exhaust enthalpy, cooling load, and incomplete combustion losses as a percentage of fuel energy versus displacement volume for the combined cooling load sweeps.

Table 9. BMEP, η_f , exhaust enthalpy, cooling load, and incomplete combustion losses as a percentage of fuel energy coefficients for use with Equation (63).

	A	B		R ²	RMS Error
BMEP (bar)	7.67	3.35E-03		0.91	0.06
η_f (%)	20.20	3.93E-02		0.83	1.00
Exhaust Enthalpy (%)	20.36	3.17E-02		0.99	0.08
Cooling Load (%)	33.56	-5.69E-02		0.93	0.91
Incomplete Combustion (%)	25.37	-2.84E-02		0.76	0.90

4.2.2.4. GX120, GX160, and GX200 Throttle Sweep

The GX160 and GX200 engines were run through a throttle sweep where the GX160 throttle was swept from 28.6% open to 100% open and the GX200 throttle was swept from 35.7% open to 100% open. Other conditions held constant were: ϕ of 1.05 ± 0.02 , engine speed of 2800 ± 120 rpm, CA50 of $8^\circ \pm 0.4^\circ$ aTDC, and cylinder head temperatures of $150^\circ \pm 1^\circ$ C for the GX160 and $170^\circ \pm 1^\circ$ C for the GX200 engine. To accomplish the throttle sweeps, the mass flow rates of intake air were noted at WOT, then the engines were progressively throttled without stalling. Just before stall, the mass flow rates of the intake air were again noted. After establishing the WOT and stall limited settings, the throttles were opened back up in steps to incrementally increase the mass flow rates of intake air. To generalize the data, the mass flow rates of intake air for the engines were converted to volumetric efficiency (η_v) using Equation (23). Figure 93 shows the relationship between volumetric efficiency and the mass flow rates of intake air. Additionally, it should be noted that maximum flow rate of intake air for the GX160 and GX200 engines was achieved when the throttle was 75% and 80% open, respectively.

The energy balance results for the GX160 throttle sweep are shown in Figure 94, while the energy balance results for the GX200 throttle sweep are shown in Figure 95. The energy distributions as a percentage of fuel energy, seen in Figure 94(b) and Figure 95(b), showed total measurements of energy ranged from 98.0% to 101.7% of the fuel energy entering the GX160 engine and 97.8% to 103.7% of the fuel energy entering the GX200 engine. The data sets for both engines tended to measure slightly more than

100% of the fuel energy at low throttle settings. This was most likely due to the higher uncertainty in the measurements as the lower limits of the SERB hot wire anemometer measuring cooling air velocity and the piston type flow meter measuring fuel volumetric flow rate were approached.

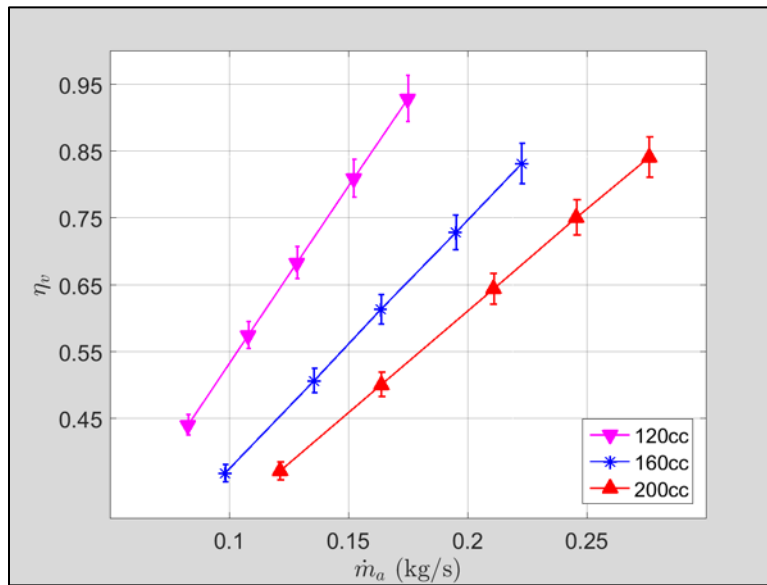
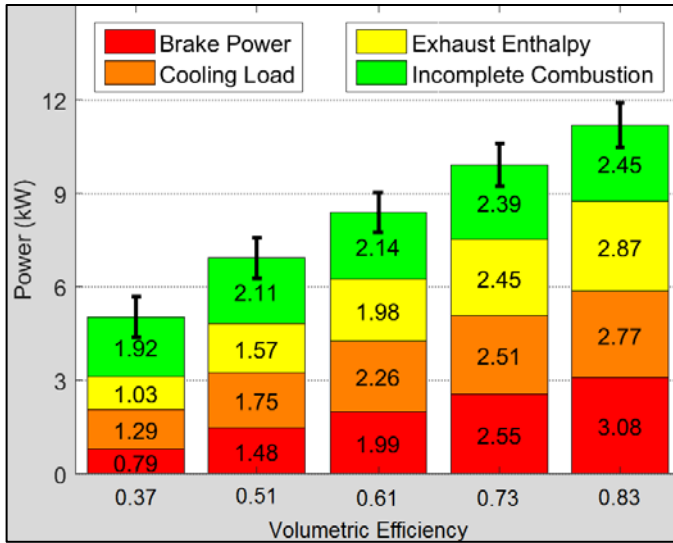
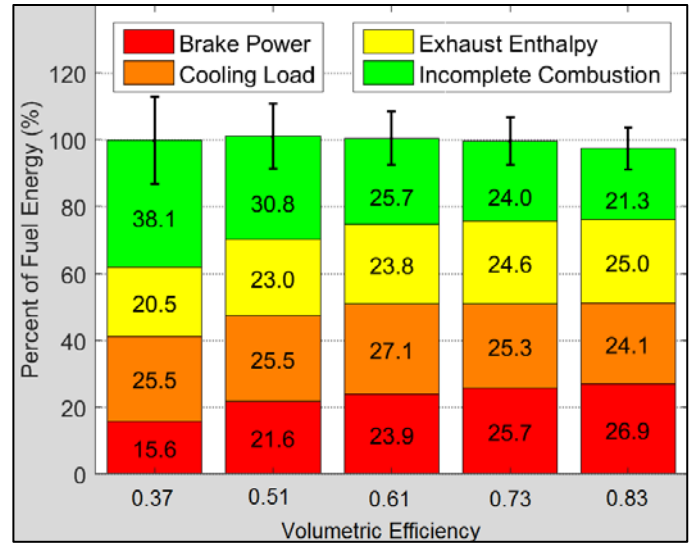


Figure 93. Combined throttle sweep volumetric efficiency versus mass flow rate of intake air.

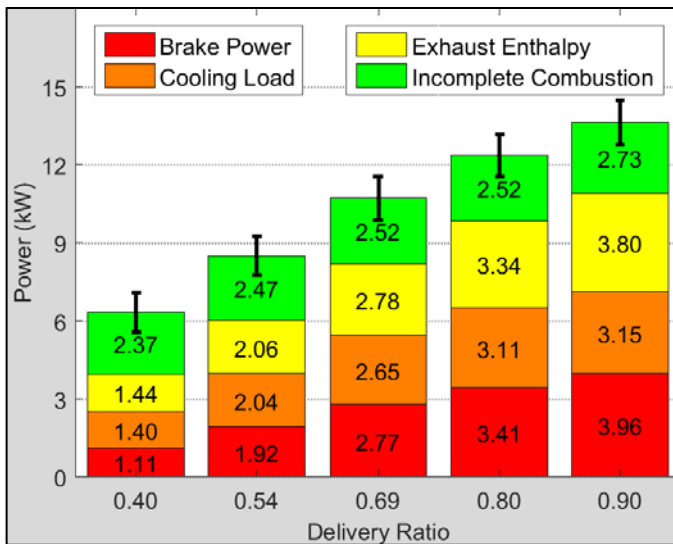


(a) Overall energy in each pathway (kW).

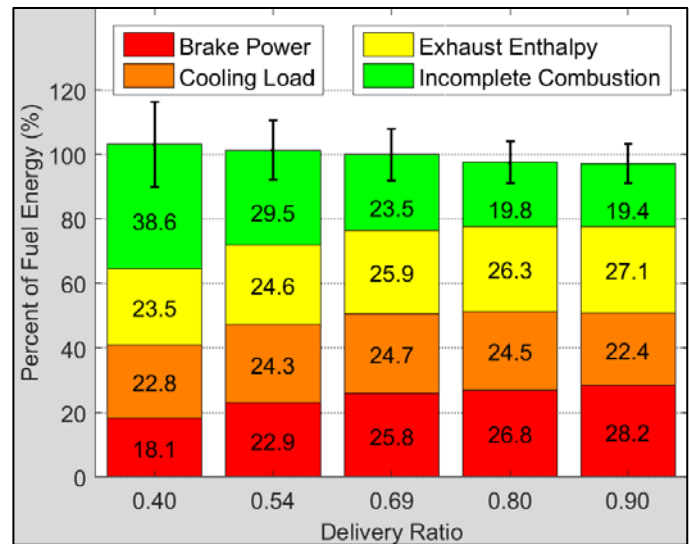


(b) Percentage of fuel energy in each pathway.

Figure 94. GX160 throttle sweep energy balance.



(a) Overall energy in each pathway (kW).



(b) Percentage of fuel energy in each pathway.

Figure 95. GX200 throttle sweep energy balance.

The magnitude of energy in each of the four pathways, shown in Figure 96, consistently increased with larger displacement volume. Brake power, exhaust enthalpy,

and cooling load losses increased significantly (roughly 1.5 – 3.0kW) as the throttle opening increased, while incomplete combustion losses showed a much smaller change (0.1 – 0.3 kW). This phenomena was explained in the GX120 throttle sweep discussion (Section 4.1.3.4), where the H₂ and CO levels in the exhaust gases decreased with increasing volumetric efficiency, but were offset by increasing mass flow of exhaust air as volumetric efficiency increased.

IMEP and CoV of IMEP levels for the throttle sweeps of the three engines, shown in Figure 97, were very similar. Given the results of the four previous parametric studies, this was not a surprising result.

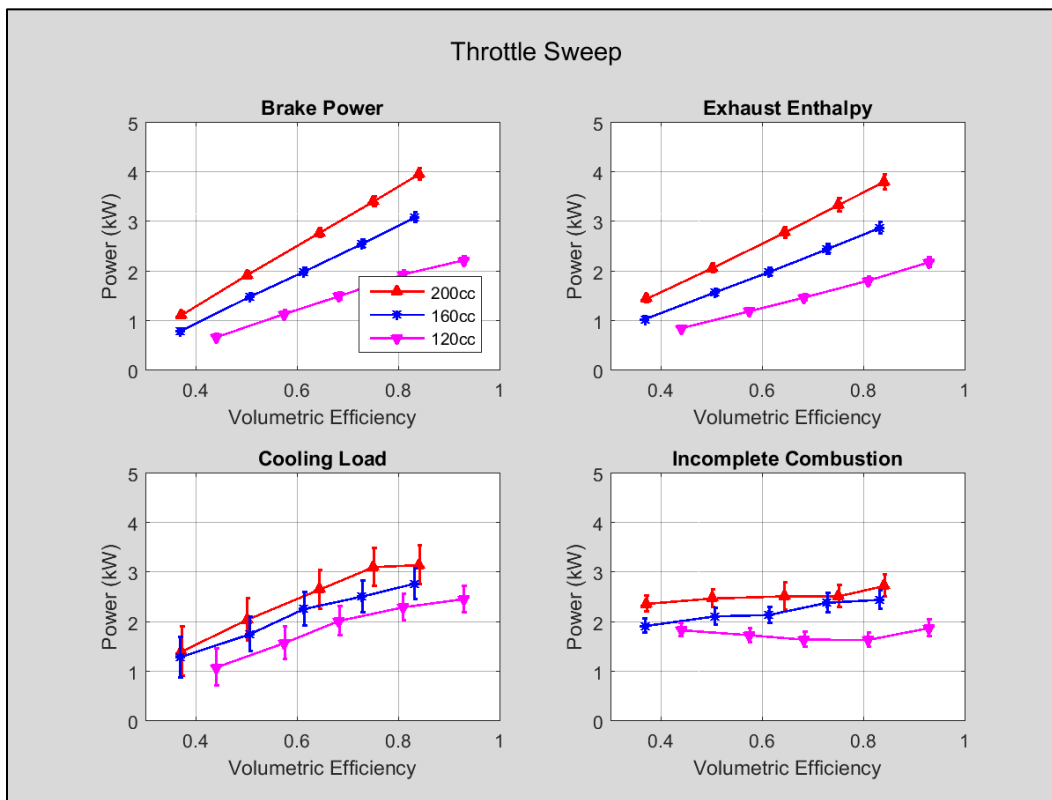


Figure 96. Combined throttle sweep energy pathways (in kW).

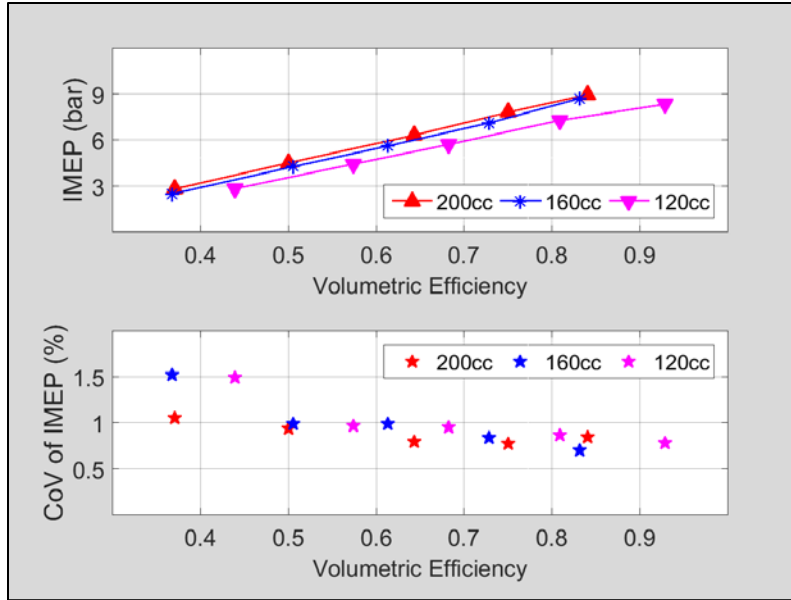
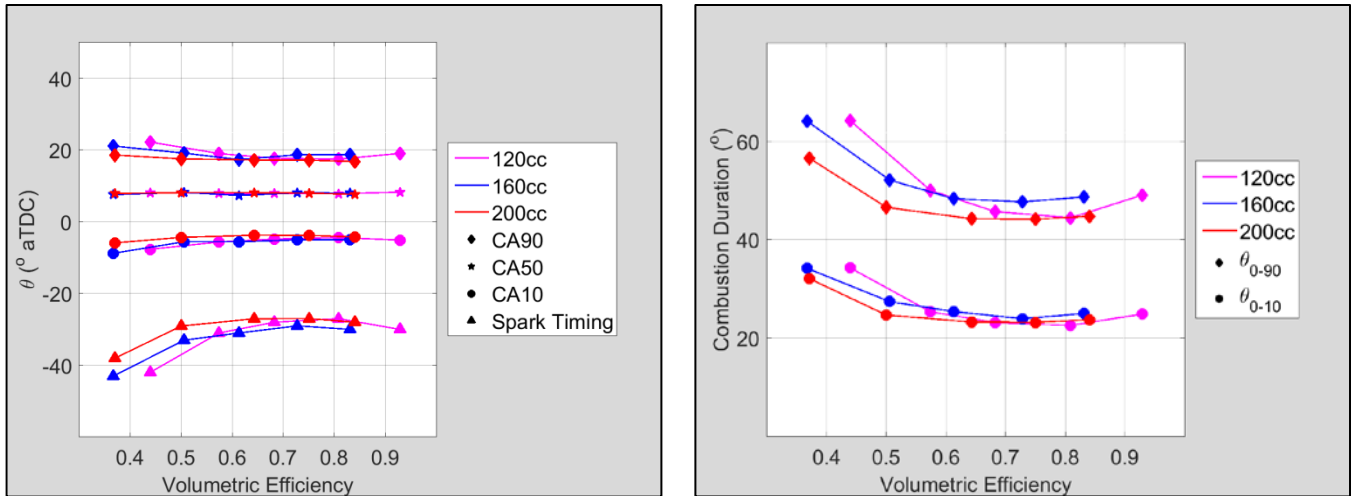


Figure 97. Combined throttle sweep IMEP and CoV of IMEP.

Figure 98 show the combined combustion phasing and combustion duration plots for the throttle sweeps of the three Honda engines. Again, similar behavior was seen for the three engines, indicating that engine displacement did not have a strong effect on these parameters.



(a) Combined throttle sweep combustion phasing. (b) Combined throttle sweep combustion duration.

Figure 98. Combined throttle sweep combustion phasing and combustion duration.

Examining the energy pathways as a percentage of fuel energy from Figure 99, it can be seen that fuel conversion efficiency again increased with engine displacement. The throttle sweeps also produced the largest change in fuel conversion efficiency for all three of the engines, increasing from 15.4% to 25.4% for the GX120 engine, from 15.4% to 26.4% for the GX160 engine, and from 17.8% to 27.7% for the GX200 engine. Exhaust enthalpy losses as a percentage of fuel energy consistently increased with displacement and volumetric efficiency, although in a less pronounced manner than the fuel conversion efficiency. Cooling load losses as a percentage of fuel energy results were somewhat harder to interpret, but showed generally higher loss percentages in the smaller engines. Incomplete combustion losses as a percentage of fuel energy changed dramatically as the throttles were opened, decreasing from approximately 40% to

approximately 20% in all three of the engines, with the smaller engines having slightly higher levels.

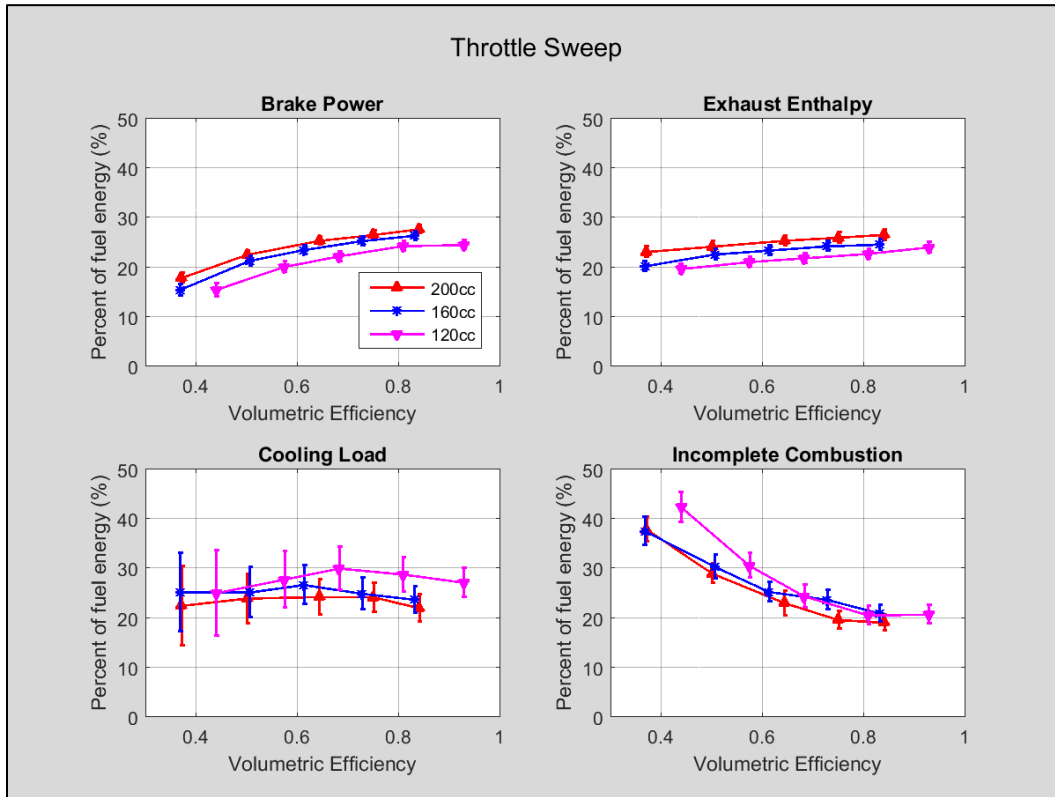
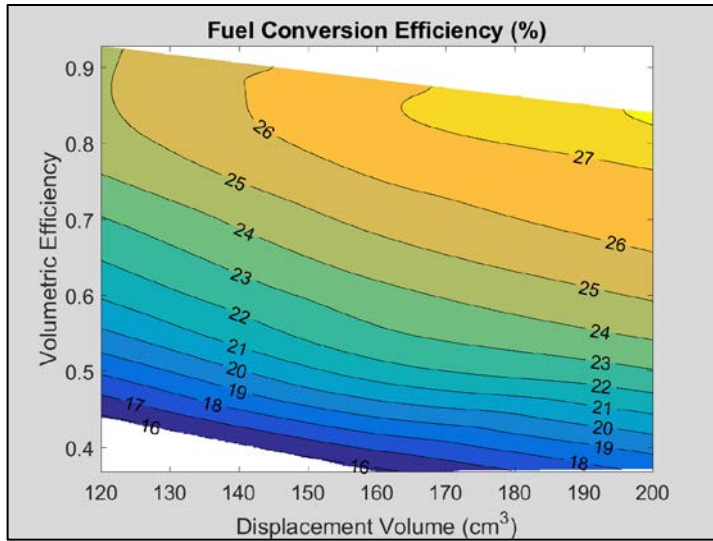
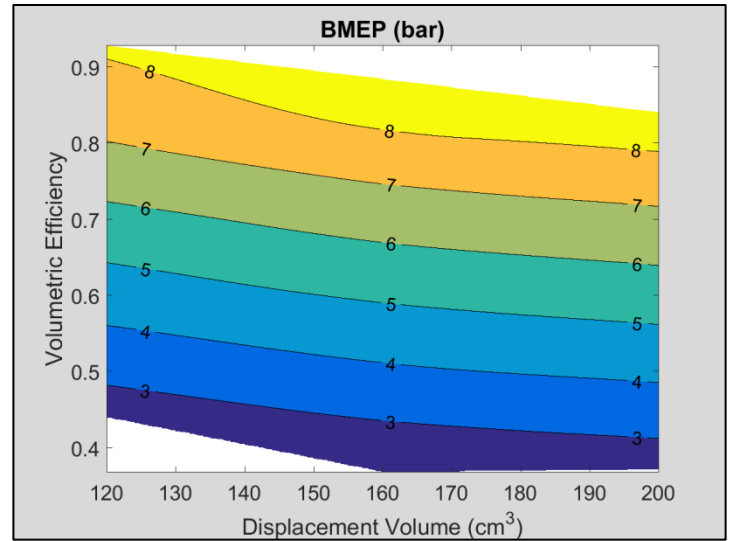


Figure 99. Combined throttle sweep percentage of fuel energy in each energy pathway.

Contour plots for η_f and BMEP as a function of volumetric efficiency and displacement volume are shown in Figure 100(a) and Figure 100(b). The figures show BMEP and η_f increasing with displacement volume and volumetric efficiency.



(a) Fuel conversion efficiency as a function of volumetric efficiency and displacement volume.



(b) BMEP as a function of volumetric efficiency and displacement volume.

Figure 100. Fuel conversion efficiency and BMEP as functions of volumetric efficiency and displacement volume.

Finally, a set of multivariable equations was developed from the throttle sweep data to predict BMEP, η_f , exhaust enthalpy losses as a percentage of fuel energy, cooling load losses as a percentage of fuel energy, and incomplete combustion losses as a percentage of fuel energy. The equations are for four stroke engines in the size range of 120 – 200 cm³ displacement, operating at volumetric efficiencies ranging from 0.35 to 0.95. The equations are of the form:

$$F(V_d(cm^3), \eta_v) = A + B * V_d + C * \eta_v + D * \eta_v^2 \quad (64)$$

Values for the coefficients A – D, R² values for the multiple linear regression analyses, and the RMS errors for the equations are listed in Table 10. RMS error for the BMEP equation has units of bar, while RMS error for the remaining four equations have units of percentage of fuel energy.

Table 10. BMEP, η_f , exhaust enthalpy, cooling load, and incomplete combustion losses as a percentage of fuel energy coefficients for use with Equation (64).

	A	B	C	D		R ²	RMS Error
BMEP (bar)	-6.03	1.38E-02	16.93	-3.45		0.99	0.15
η_f (%)	-11.26	4.84E-02	66.49	-36.64		0.98	0.55
Exhaust Enthalpy (%)	9.06	4.65E-02	14.70	-5.02		0.98	0.32
Cooling Load (%)	25.19	-5.51E-02	31.27	-24.13		0.77	1.23
Incomplete Combustion (%)	82.92	-5.46E-02	-112.77	57.75		0.94	2.02

4.3. GF40, TP70

After collecting the data for the three geometrically similar Honda engines, it was desirable to determine what results would be obtained from running the same set of tests on two smaller four-stroke engines that were designed to power small remotely piloted hobbyist aircraft. The 40 cm³ displacement volume OS GF40 and the 70 cm³ displacement Torqpro TP70 engines, shown in Figure 101, were selected.



(a) GF40 engine.

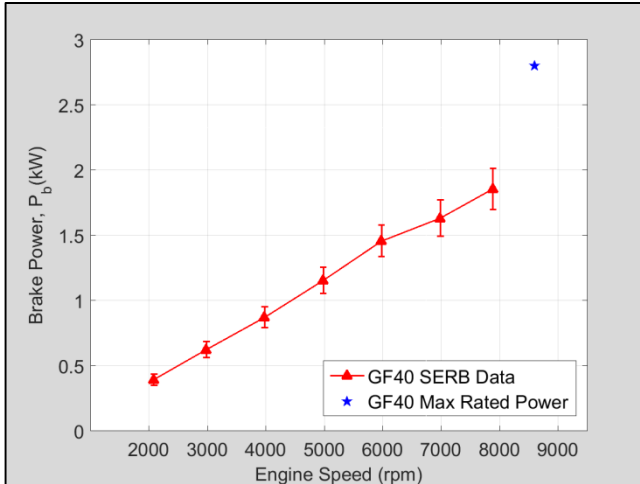


(b) TP70 engine.

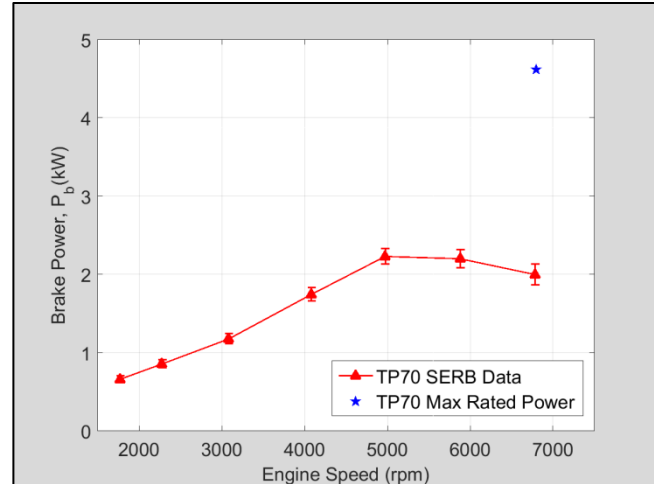
Figure 101. OS GF40 and Torqpro TP70 engines.

4.3.1. GF40 and TP70 Speed Sweep

The GF40 engine was run from 2000 – 7900 rpm and the TP70 engine was run from 1800 – 6800 rpm. Other conditions held constant were: WOT, ϕ of 1.05 ± 0.02 , CA50 of $8^\circ \pm 0.4^\circ$ aTDC, and cylinder head temperatures of $150^\circ \pm 1^\circ$ C for the GF40 and of $145^\circ \pm 1^\circ$ C for the TP70 engines. For the respective speed sweeps, the cooling blower motor was set to approximately 60% power, providing similar equivalent air speeds for the cooling air of each engine. Figure 102 shows the results of comparing the SERB measured brake power to the manufacturer's advertised peak power ratings.



(a) GF40 engine power curve.



(b) TP70 engine power curve.

Figure 102. GF40 and TP70 power curves with the SERB exhaust versus the manufacturer's advertised power curves.

The most immediate result seen in Figure 102 is that neither engine produced the manufacturer's maximum rated power. The GF40 engine produced a maximum of 1.88 kW at 7900 rpm, 33% less than the advertised maximum power of 2.8 kW at 9000 rpm. It should be noted that the advertised maximum power for the GF40 was for an engine speed of 9000 rpm, and the engine was only tested up to 7900 rpm on the SERB. This was done due to constraints of the JABtronic ECU. However, it appears from the data in Figure 102 that even if the engine was able to operate at 9000 rpm on the SERB, it would not have reached 2.8 kW. The TP70 engine produced a maximum of 2.27 kW at 5000 rpm, 51% less than the advertised maximum power of 4.62 kW at 6800 rpm. The TP70 engine ran very poorly at engine speeds above 5000 rpm, as seen in Figure 103, where a sharp drop in IMEP and a rise in CoV of IMEP occurred when the engine speed exceeded 5000 rpm. When the TP70 engine was run at 6800 rpm, the consistency of combustion

was so poor at WOT that the throttle had to be slightly closed, reducing volumetric efficiency from 0.87 at 5900 rpm (WOT) to 0.68 at 6800 rpm. It is unclear why the peak power measurements for the GF40 and TP70 engines were so much lower on the SERB when compared to the manufacturer's advertised power ratings. Perhaps a model or estimate of peak power was used for the advertised power ratings.

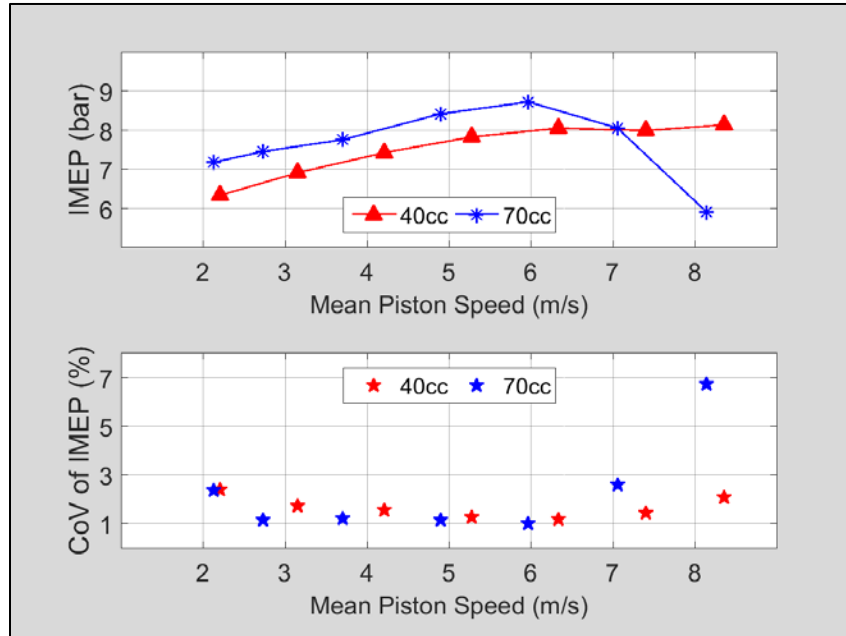


Figure 103. Combined GF40 and TP70 speed sweep IMEP and CoV of IMEP.

It should be noted that the results shown in Figure 103 are presented on a mean piston speed scale, rather than rpm. This transformation was calculated due to the differences in engine speed between the two engines. Figure 104 shows the relationship between mean piston speed and engine speed in rpm for the two engines.

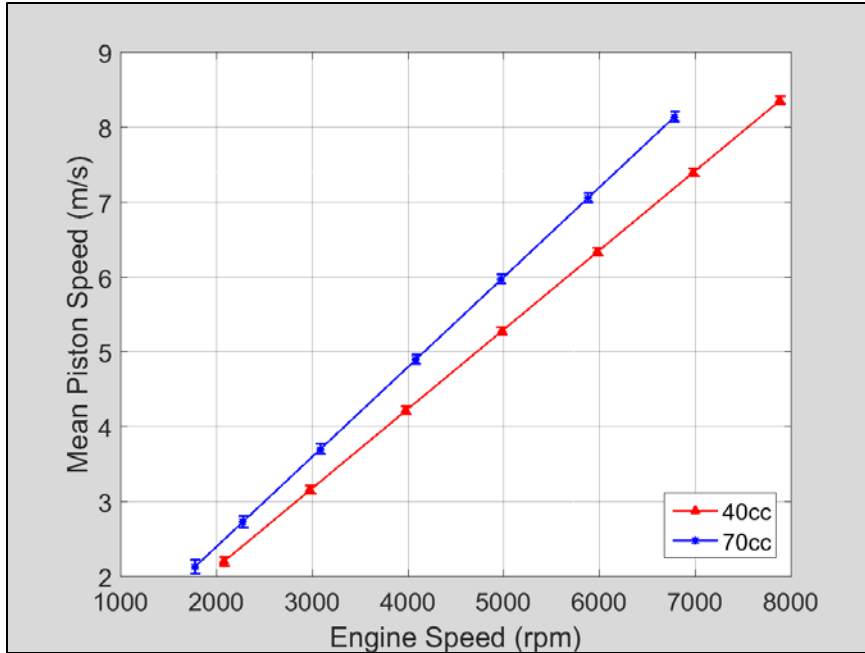


Figure 104. Mean piston speed (m/s) versus engine speed (rpm) for the GF40 and TP70 engines.

Combined plots showing the energy in each of the four energy balance pathways (in kW) for the three GF40 and TP70 engines are shown in Figure 105. As expected, the TP70 consistently had a larger magnitude of energy in each of the four pathways, with the exception of reduced cooling load losses at 6800 rpm. This was likely the result of the poor combustion quality and reduction in brake power and exhaust enthalpy losses seen in Figure 105. Incomplete combustion losses spiked dramatically for the TP70 engine at 5800 rpm, probably due to a combination of poor combustion quality at WOT, and the general uncertainty of the incomplete combustion loss calculations seen throughout the study for all of the engines.

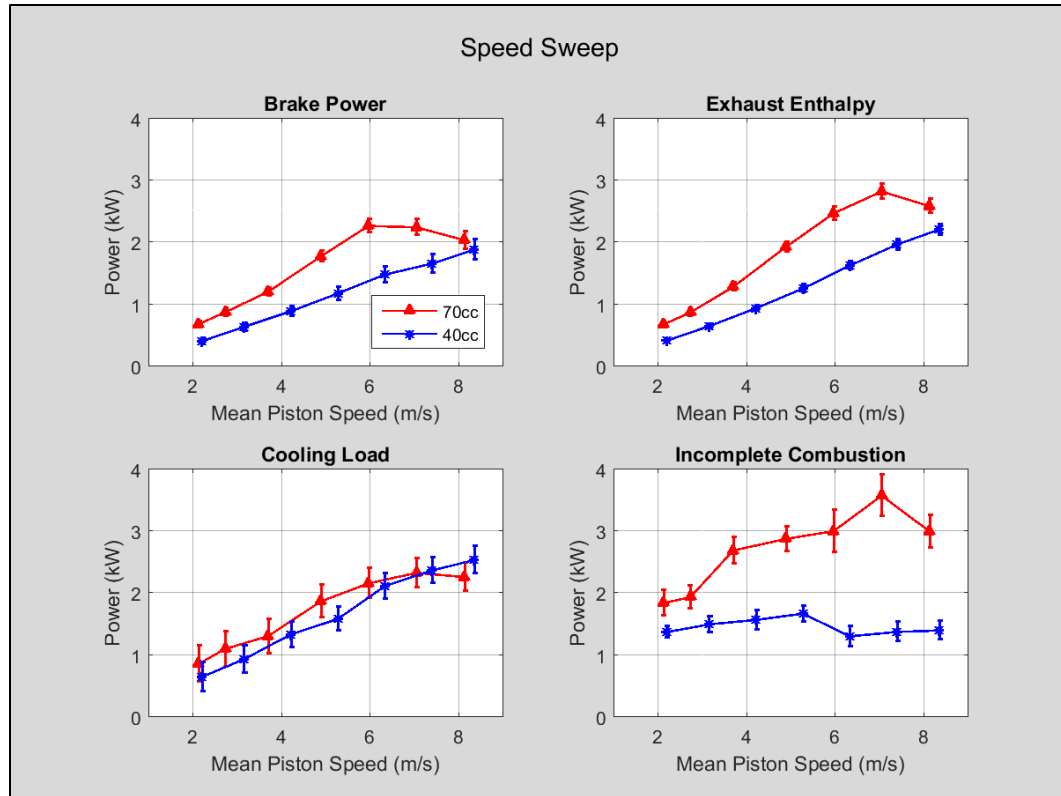
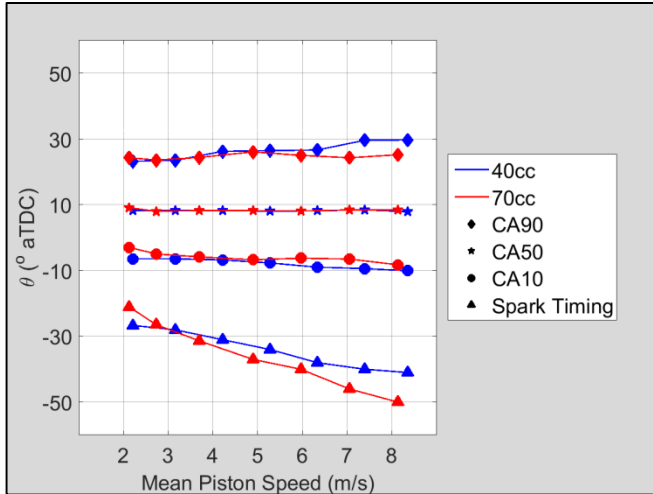
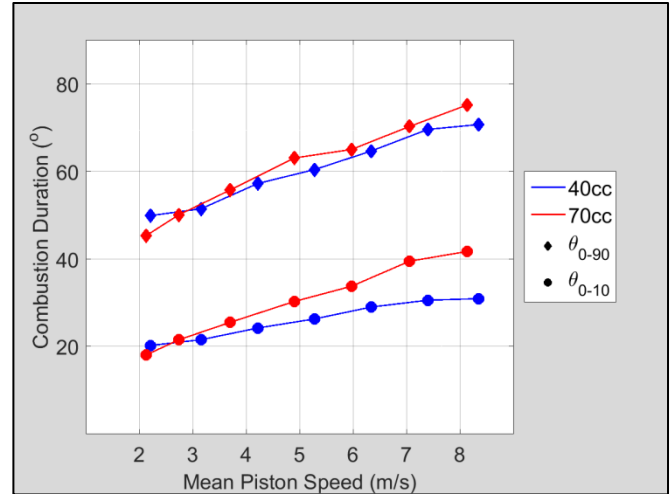


Figure 105. Combined GF40 and TP70 speed sweep energy pathways (in kW).

The combined GF40 and TP70 combustion phasing and combustion duration plots are shown in Figure 106. These figures show that the trends in combustion phasing and combustion duration for the GF40 and TP70 engines were very similar to those of the three previous engines, and that the TP70 engine displayed a large increase in flame development angle at engine speeds above 5000 rpm, again the likely result of the poor combustion quality (high CoV of IMEP).



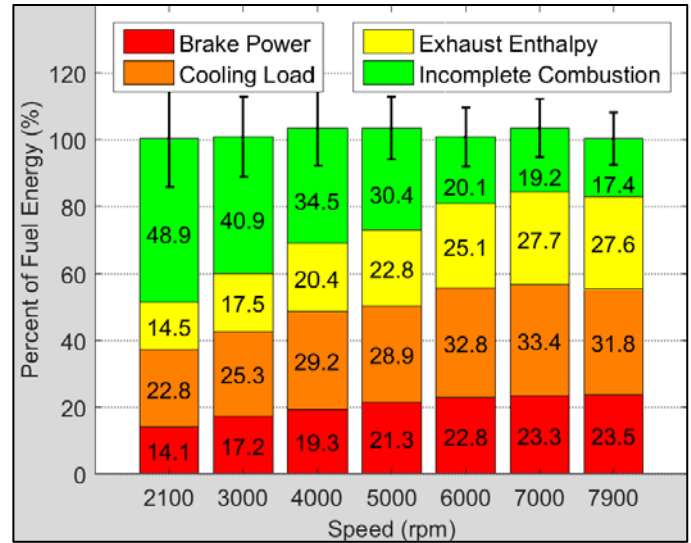
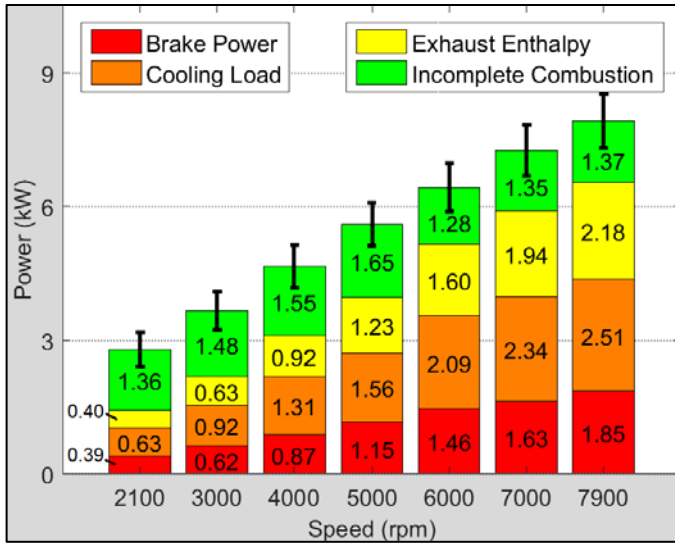
(a) Combined GF40 and TP70 speed sweep combustion phasing.



(b) Combined GF40 and TP70 speed sweep combustion duration.

Figure 106. Combined GF40 and TP70 speed sweep combustion phasing and combustion duration.

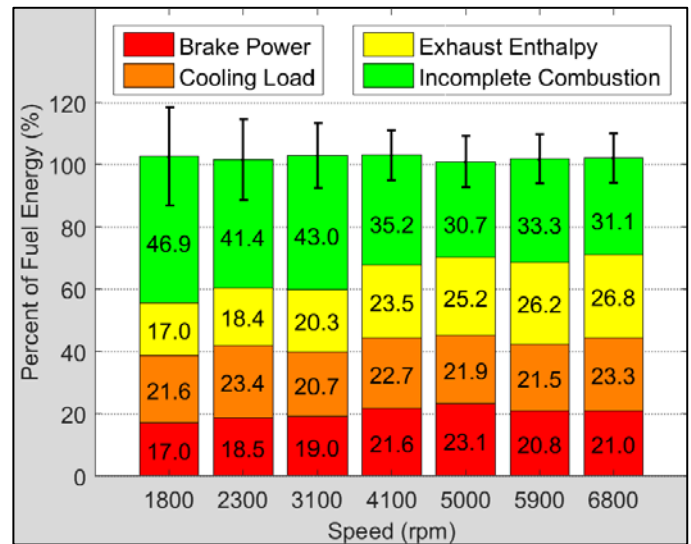
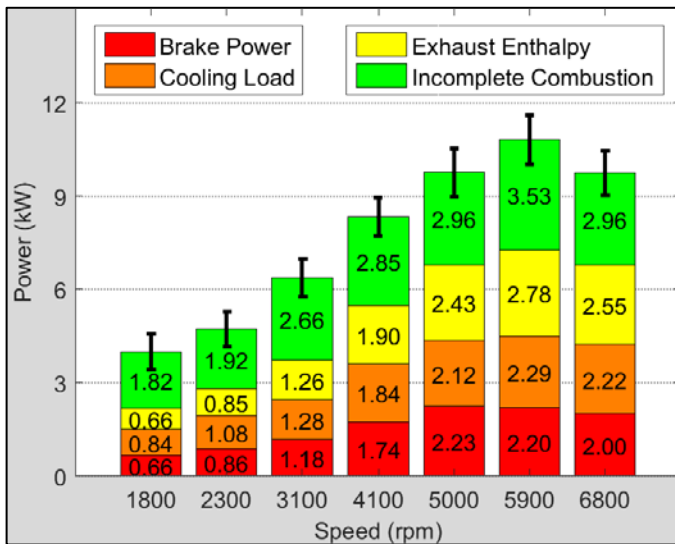
Energy balance results for the GF40 speed sweep and TP70 speed sweep are shown in Figure 107 and Figure 108, respectively. The trends from Figure 107(a) and Figure 108(a) were discussed previously, and are shown in Figure 105. The energy distributions as a percentage of fuel energy, seen in Figure 107(b) and Figure 108(b), show the total measurement for the energy balance ranged from 100.8% to 104.1% of the fuel energy entering the GF40 engine and 101.5% to 103.6% of the fuel energy entering the TP70 engine. When compared to the total measurement for the energy balances of the three larger Honda engines, a slight trend toward energy balance total measurements greater than 100% of fuel energy can be seen.



(a) Overall energy in each pathway (kW).

(b) Percentage of fuel energy in each pathway.

Figure 107. GF40 speed sweep energy balance.



(a) Overall energy in each pathway (kW).

(b) Percentage of fuel energy in each pathway.

Figure 108. TP70 speed sweep energy balance.

Figure 109 shows the combined percentage of fuel energy in each pathway from the speed sweeps of the GF40 and TP70 engines. The results are logical given the

magnitudes of energy in each pathway shown in Figure 105, however the higher fuel conversion efficiency (brake power as a percentage of fuel energy) of the GF40 engine at high mean piston speeds is somewhat surprising. The much higher cooling load losses as a percentage of fuel energy for the GF40 engine may signal that somewhere between 70 cm³ and 40 cm³ the cooling load losses as a percentage of fuel energy begin to increase sharply. It would be interesting to investigate how this trend increases for four-stroke engines as engine displacement decreases.

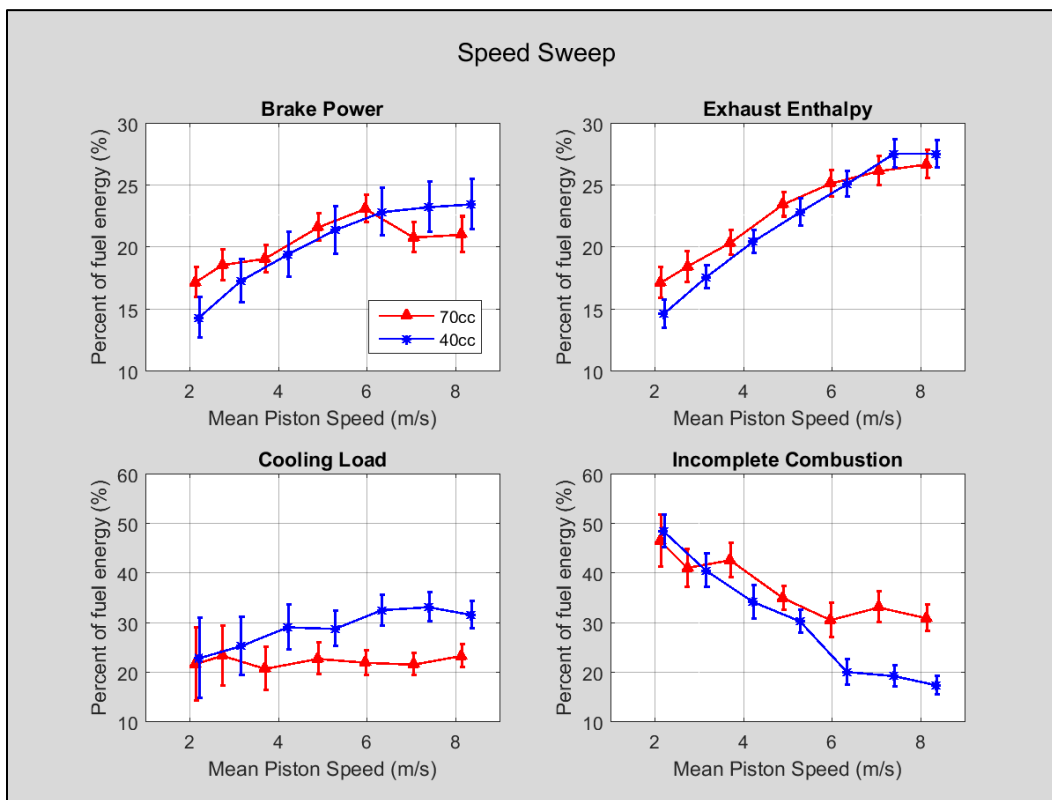
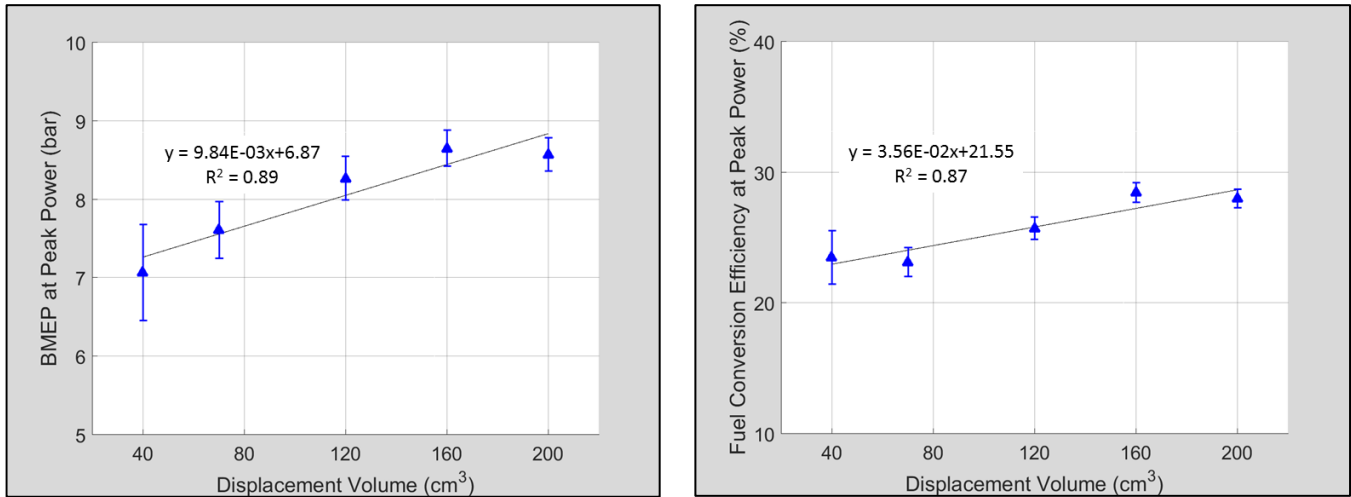


Figure 109. Combined GF40 and TP70 speed sweep percentage of fuel energy in each energy pathway.

The remainder of the analysis performed in this section aggregates the combined data from all five of the engines tested in the study, beginning with plots of peak BMEP

and fuel conversion efficiency at peak BMEP versus engine displacement, shown in Figure 110.



(a) BMEP at peak power versus displacement volume.

(b) Fuel conversion efficiency versus displacement volume.

Figure 110. BMEP and fuel conversion efficiency (η_f) at peak power versus displacement volume for the GF40, TP70, GX120, GX160, and GX200 engines.

Using the results shown in Figure 110, the rudimentary BMEP and η_f at peak power scaling laws introduced in Section 4.2.1 were updated to expand their applicability to four-stroke engines of 40 – 200 cm³ displacement volume (V_d):

$$BMEP = 0.00984V_d + 6.87 \quad (65)$$

and

$$\eta_f = 0.0356V_d + 21.55 \quad (66)$$

Additionally, the Menon and Cadou [9, 33] figures showing BMEP and fuel conversion efficiency as a function of displacement volume (Figure 12 and Figure 13), were updated as well to contain data for the five engines tested in this study, shown in

Figure 111 and Figure 112. As expected, the five four-stroke engines showed consistently higher overall efficiency at peak power than the two-stroke engines of the same size range.

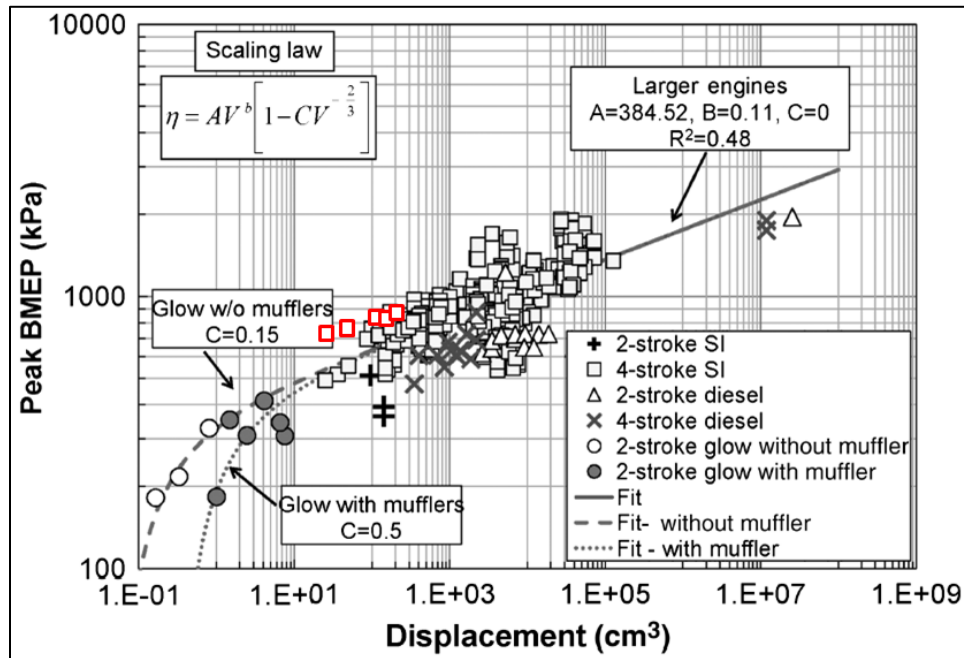


Figure 111. Menon and Cadou BMEP versus displacement plot [9] with data points from the GF40, TP70, GX120, GX160, and GX200 added in red.

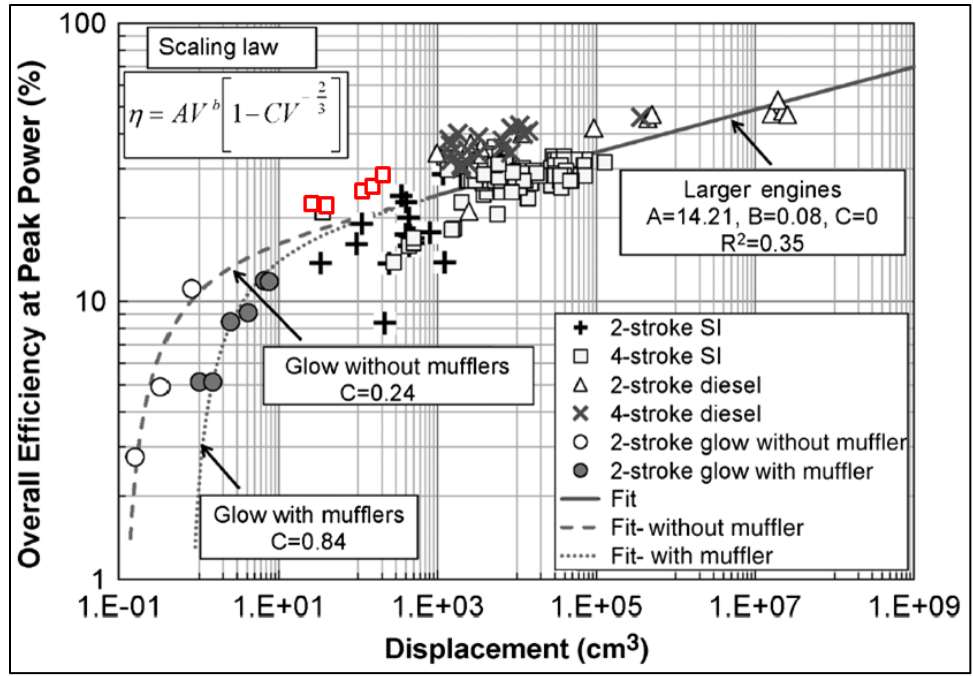
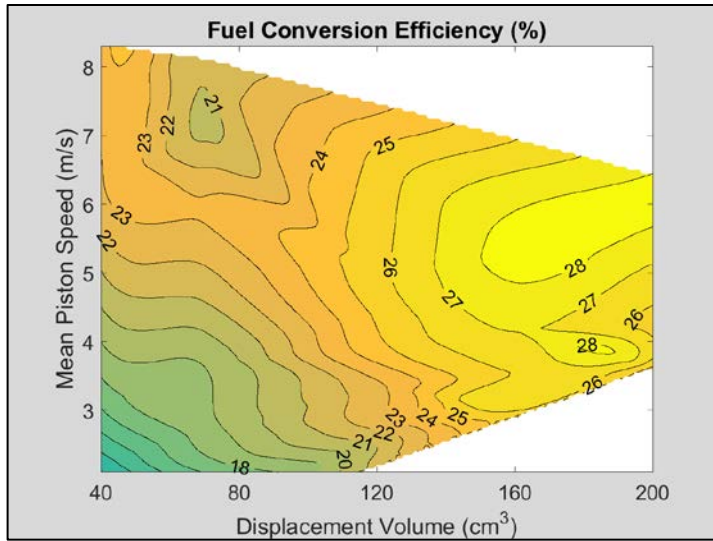
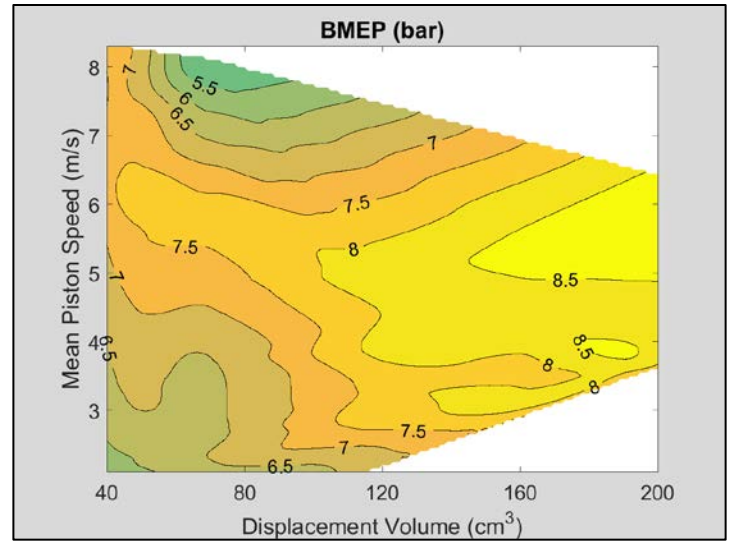


Figure 112. Menon and Cadou fuel conversion efficiency versus displacement plot [9] with data points from the GF40, TP70, GX120, GX160, and GX200 added in red.

Similar to the analysis done previously for the GX120, GX160, and GX200 engines, speed sweep data from all five engines was used to create fuel conversion efficiency and BMEP contour maps to illustrate these operating characteristics as functions of displacement volume and mean piston speed, shown in Figure 113. The results were somewhat similar to those seen in Figure 71 and Figure 72, with η_f and BMEP generally increasing with increased mean piston speed and displacement volume.



(a) Fuel conversion efficiency as a function of mean piston speed and displacement volume.



(b) BMEP as a function of mean piston speed and displacement volume.

Figure 113. Fuel conversion efficiency and BMEP for the GF40, TP70, GX120, GX160, and GX200 engines as functions of mean piston speed and displacement volume.

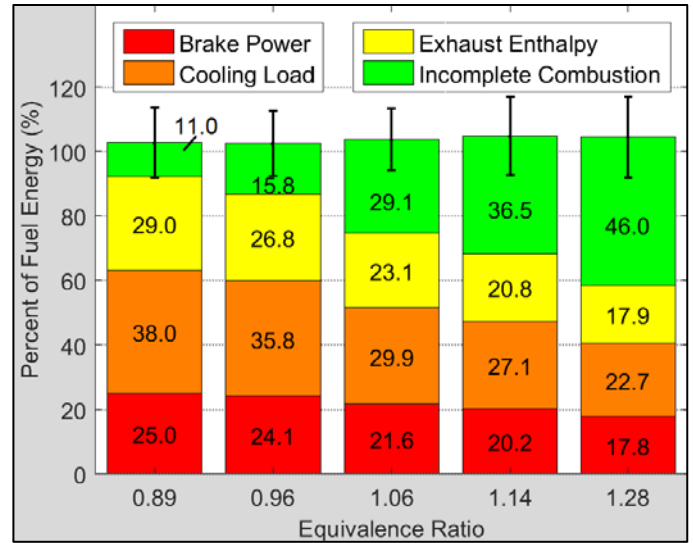
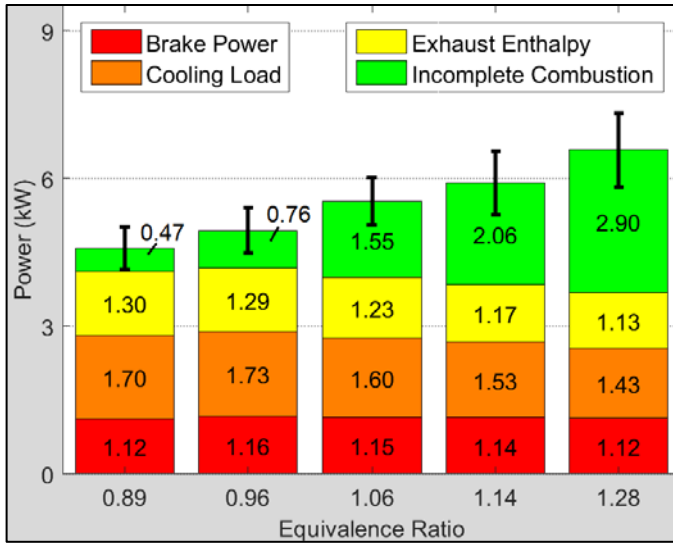
Finally, data from the speed sweeps of all five engines was used to update the coefficients for Equation (60), which can be used to predict BMEP, η_f , exhaust enthalpy losses, cooling load losses, and incomplete combustion losses as a percentage of fuel energy for 40 – 200 cm³ four-stroke engines as functions of both mean piston speed and displacement. The coefficients, R² values, and RMS error for the equations are listed in Table 11. Expanding the correlation data from the three Honda engines to all five engines improved (increased) the R² values by an average of 5%, while increasing the RMS errors by an average of 216%. RMS error for the BMEP equation has units of bar, while RMS error for the remaining four equations have units of percentage of fuel energy.

Table 11. BMEP, η_f , exhaust enthalpy, cooling load, and incomplete combustion losses as a percentage of fuel energy coefficients for use with Equation (60).

	A	B	C	D		R ²	RMS Error
BMEP (bar)	0.20	9.17E-03	2.57	-0.24		0.97	0.57
η_f (%)	0.48	4.32E-02	6.69	-0.55		0.97	1.58
Exhaust Enthalpy (%)	0.51	2.80E-02	6.71	-0.46		0.99	1.20
Cooling Load (%)	1.67	-3.42E-02	10.77	-0.96		0.85	4.15
Incomplete Combustion (%)	4.24	-9.06E-02	16.33	-1.76		0.60	8.92

4.3.2. GF40 and TP70 Equivalence Ratio Sweep

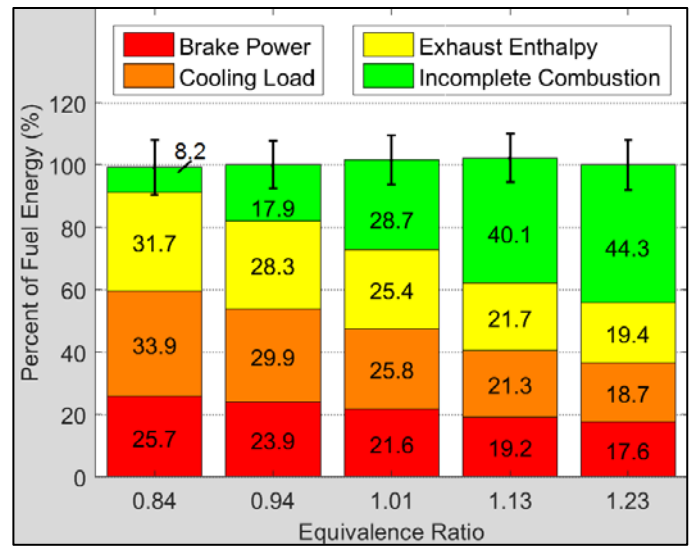
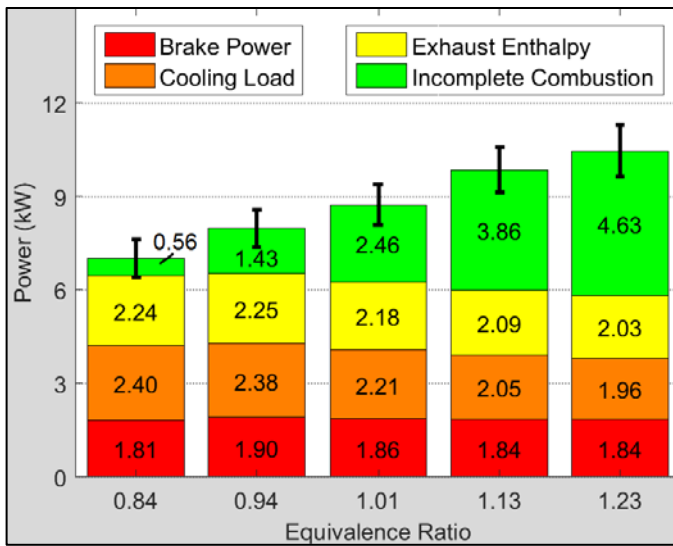
The GF40 and TP70 engines were run through a sweep of equivalence ratio from $\phi = 0.85$ to $\phi = 1.25 \pm 0.04$. Other conditions held constant were: WOT, mean piston speed of 5.28 ± 0.15 m/s, CA50 of $8^\circ \pm 0.4^\circ$ aTDC, and cylinder head temperatures of $150^\circ \pm 1^\circ$ C for the GF40 and of $145^\circ \pm 1^\circ$ C for the TP70 engines. The energy balance results for the GF40 equivalence ratio sweep are shown in Figure 114, while the energy balance results for the TP70 equivalence ratio sweep are shown in Figure 115.



(a) Overall energy in each pathway (kW).

(b) Percentage of fuel energy in each pathway.

Figure 114. GF40 equivalence ratio sweep energy balance.



(a) Overall energy in each pathway (kW).

(b) Percentage of fuel energy in each pathway.

Figure 115. TP70 equivalence ratio sweep energy balance.

The energy balance results of both engines showed similar patterns of fuel energy distribution, which were also similar to the results of the GX120, GX160, and GX200

engines discussed in Section 4.1.3.1 and Section 4.2.2.1. The energy distributions as a percentage of fuel energy, seen in Figure 114(b) and Figure 115(b), showed the total measurement of energy ranged from 102.9% to 105.1% of the fuel energy entering the GF40 engine and 99.7% to 102.7% of the fuel energy entering the TP70 engine.

Examining the energy pathway magnitude data, similar patterns to those seen previously in the three Honda engines were observed in the GF40 and TP70 engines. A plot showing the trends in the four energy pathways, similar to Figure 75, containing the data found in Figure 114(a) and Figure 115(b), can be found in Appendix A.

Figure 116 contains the IMEP and CoV of IMEP data from the equivalence ratio sweeps of the GF40 and TP70 engines. The GF40 engine had consistently lower IMEP than the TP70 engine at all points in the equivalence ratio sweep. Both the GF40 and TP70 engines had difficulty running consistently under lean conditions, but the GF40 ran especially poorly when the mixture was leaned beyond an equivalence ratio of 0.90. Figure 116 shows a very high CoV of IMEP of 7% at an equivalence ratio of 0.89. When the fuel/air mixture was leaned beyond that point, the combustion quality of the GF40 engine was too poor to consistently obtain credible data.

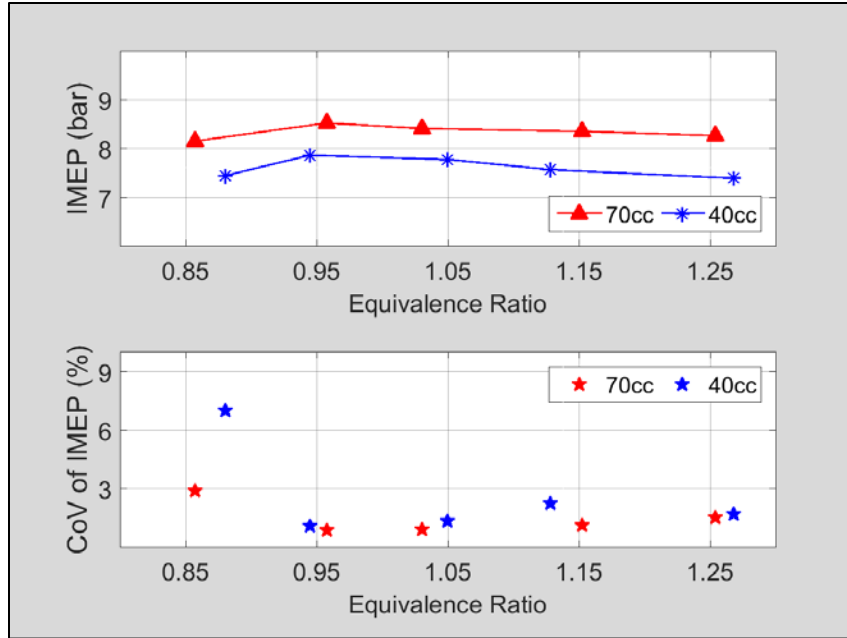
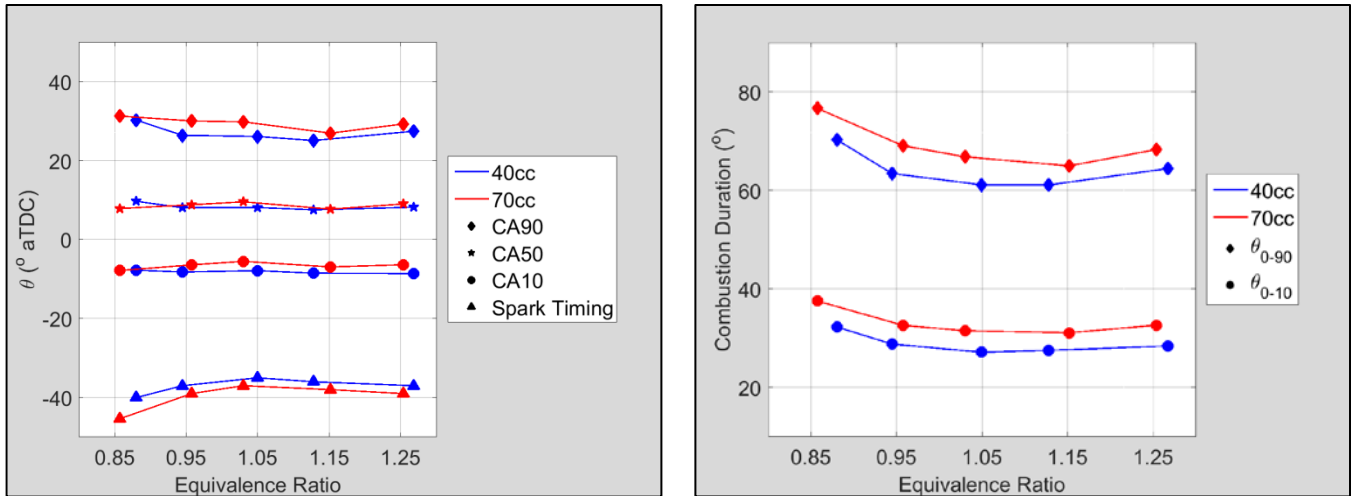


Figure 116. Combined GF40 and TP70 equivalence ratio sweep IMEP and CoV of IMEP.

The combined GF40 and TP70 equivalence ratio sweep combustion phasing and combustion duration plots, seen in Figure 117, showed very similar patterns to those of the GX120, GX160, and GX200 engines (found in Section 4.2.2.1, Figure 77), with the GF40 and TP70 engines having consistently longer flame development and rapid burn angles than the larger Honda engines. This pattern shows the fuel burn times increasing with decreasing displacement, however the TP70 engine displayed consistently longer flame development and rapid burn angles than the GF40 engine. Although both engines were tested at the same mean piston speed (5.28 m/s), the difference in engine speed, (5000 rpm for the GF40, 4400 rpm for the TP70), was likely the cause of the different fuel burn angles.



(a) Combined equivalence ratio sweep combustion phasing.

(b) Combined equivalence ratio sweep combustion duration.

Figure 117. Combined equivalence ratio sweep combustion phasing and combustion duration.

The combined plots of the percentage of fuel energy in each pathway for the equivalence ratio sweeps of the GF40 and TP70 are shown in Figure 118. Fuel conversion efficiency, exhaust enthalpy losses, and incomplete combustion losses as a percentage of fuel energy showed very little dependence on engine displacement. Cooling load losses as a percentage of fuel energy were approximately 5% higher for the GF40 engine than for the TP70. The increase in cooling load loss percentage while the other four pathways were essentially the same accounts for the overall increase in total energy measurement shown in Figure 114(b) and Figure 115(b), although it is likely that the trend toward total measurements greater than 100% of fuel energy are the result of greater uncertainty in the measurement of all four energy pathways as engine displacement decreased.

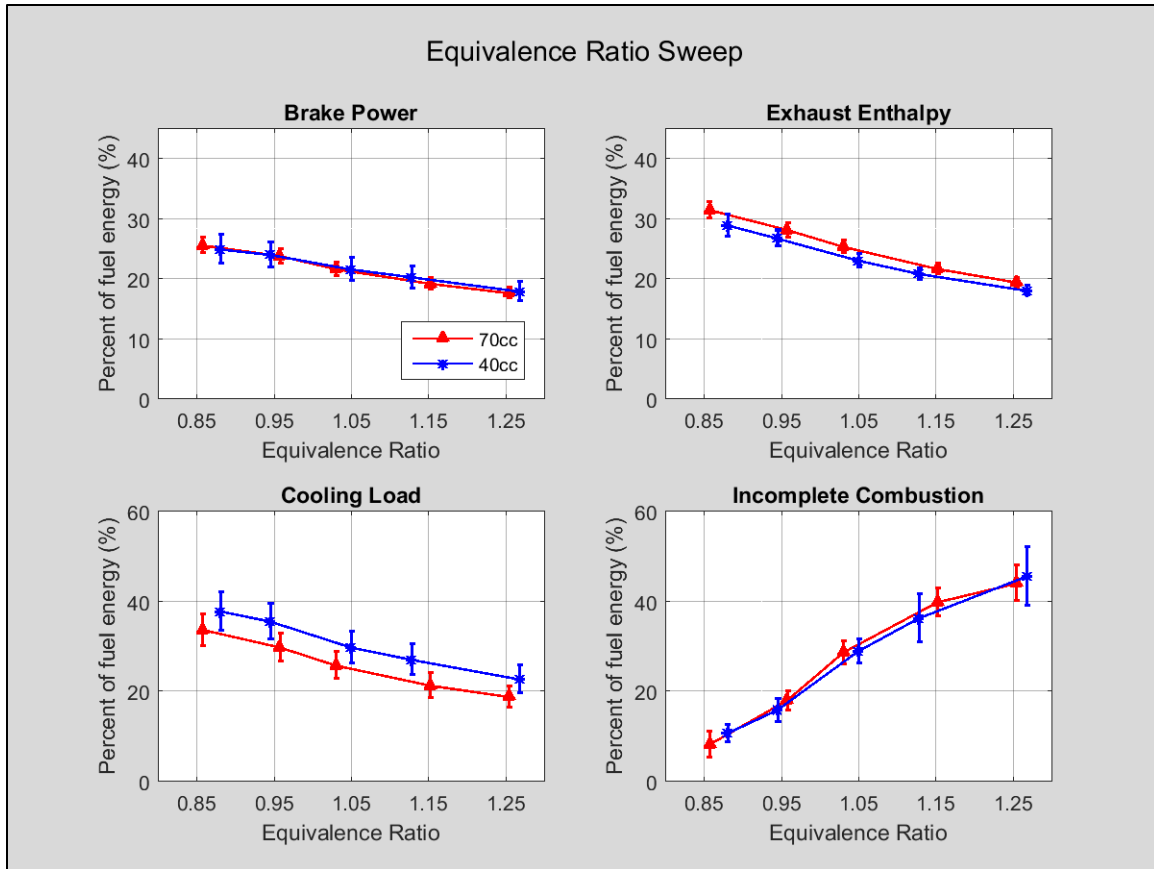
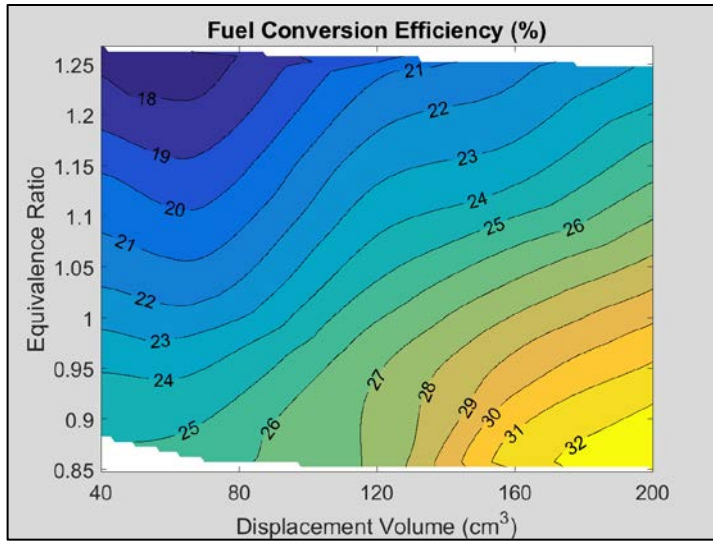
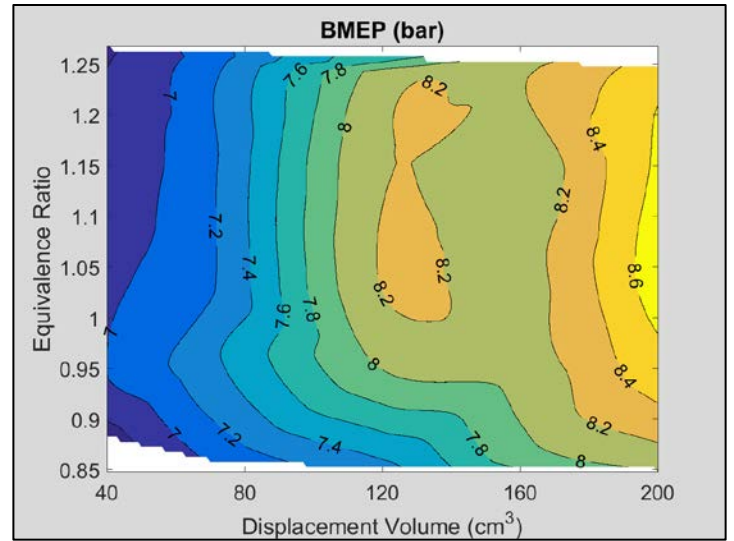


Figure 118. Combined GF40 and TP70 equivalence ratio sweep percentage of fuel energy in each energy pathway.

BMEP and η_f values for the equivalence ratio sweeps of all five engines were mapped out in smoothed contour plots showing them as functions of both equivalence ratio and displacement volume, shown in Figure 119. The results in Figure 119(a) show η_f increasing as displacement increased and equivalence ratio decreased. In Figure 119(b), all of the engines show peak BMEP near $\phi = 1.0 \pm 0.05$, with less dependency on displacement volume for the larger engines.



(a) Fuel conversion efficiency as a function of equivalence ratio and displacement volume.



(b) BMEP as a function of equivalence ratio and displacement volume.

Figure 119. Fuel conversion efficiency and BMEP as functions of equivalence ratio and displacement volume.

Finally, data from the equivalence ratio sweeps of all five engines was used to update the coefficients for Equation (61), which can be used to predict BMEP, η_f , exhaust enthalpy losses, cooling load losses, and incomplete combustion losses as a percentage of fuel energy for 40 – 200 cm³ four-stroke engines as functions of both equivalence ratio and displacement. The coefficients, R^2 values, and RMS error for the equations are listed in Table 12. Expanding the correlation data from the three Honda engines to all five engines improved (increased) the R^2 values by an average of 1%, while increasing the RMS errors by an average of 25%. RMS error for the BMEP equation has units of bar, while RMS error for the remaining four equations have units of percentage of fuel energy.

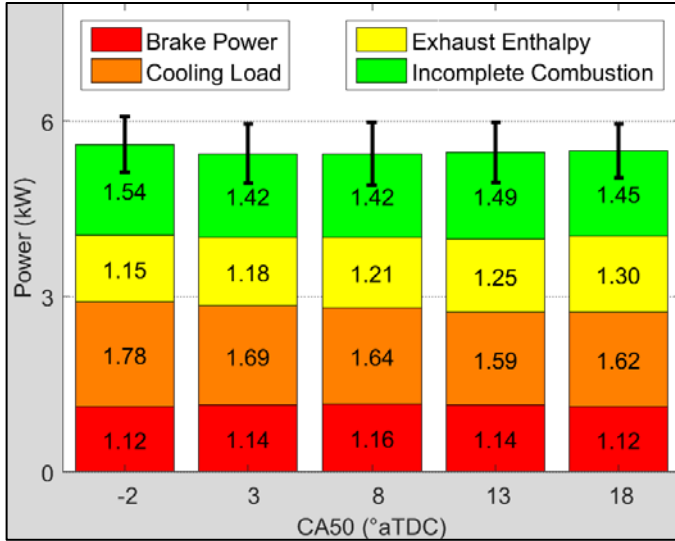
Table 12. BMEP, η_f , exhaust enthalpy, cooling load, and incomplete combustion losses as a percentage of fuel energy coefficients for use with Equation (61).

	A	B	C	D		R ²	RMS Error
BMEP (bar)	-3.04	1.01E-02	17.74	-8.09		0.93	0.19
η_f (%)	38.07	4.35E-02	-14.17	-3.38		0.96	0.82
Exhaust Enthalpy (%)	53.61	1.64E-02	-29.21	0.24		0.95	0.98
Cooling Load (%)	45.36	-4.97E-02	5.34	-17.63		0.91	1.83
Incomplete Combustion (%)	-43.11	-4.61E-02	50.49	17.69		0.97	2.60

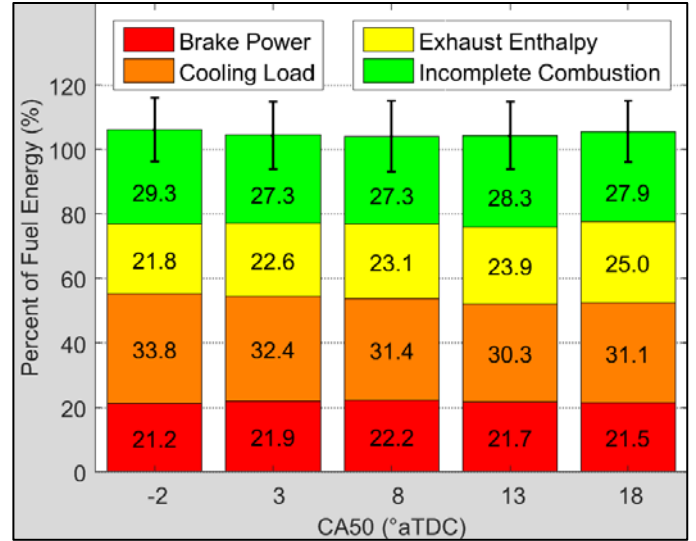
4.3.3. GF40 and TP70 Combustion Phasing Sweep

The GF40 and TP70 engines were run through a combustion phasing sweep where CA50 was varied from 2° bTDC to 18° ± 0.4° aTDC. Other conditions held constant were: WOT, ϕ of 1.05 ± 0.02, mean piston speed of 5.28 ± 0.15 m/s, and cylinder head temperatures of 150°± 1° C for the GF40 and 145°± 1° C for the TP70 engines. The energy balance results for the GF40 combustion phasing sweep are shown in Figure 120, while the energy balance results for the TP70 combustion phasing sweep are shown in Figure 121.

Much like the results shown for the GX120, GX160, and GX200 engines, the GF40 and TP70 engines showed little change in the energy distributions of the combustion phasing sweeps over the range of CA50 values tested. The energy distributions as a percentage of fuel energy, seen in Figure 120(b) and Figure 121(b), showed total measurements of energy ranged from 104.4% to 106.5% of the fuel energy entering the GF40 engine and 100.5% to 102.2% of the fuel energy entering the TP70 engine.

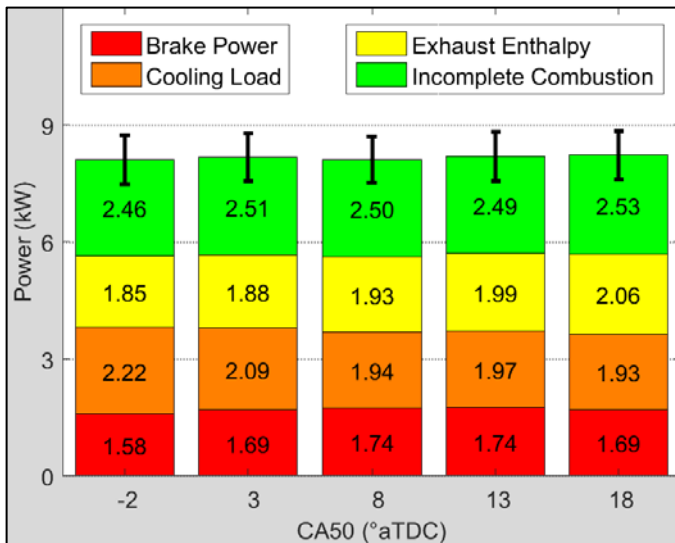


(a) Overall energy in each pathway (kW).

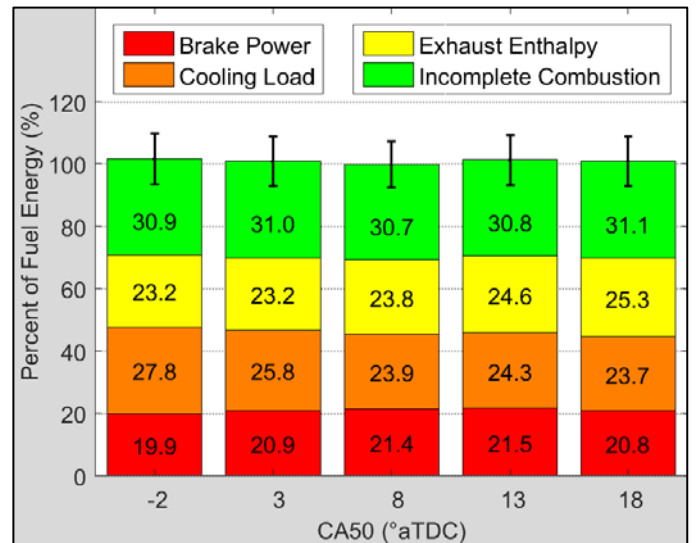


(b) Percentage of fuel energy in each pathway.

Figure 120. GF40 combustion phasing sweep energy balance.



(a) Overall energy in each pathway (kW).



(b) Percentage of fuel energy in each pathway.

Figure 121. TP70 combustion phasing sweep energy balance.

The energy pathway magnitude data for the GF40 and TP70 combustion phasing sweeps had very similar patterns to those seen previously in the three Honda engines. A plot showing the trends in the four energy pathways, similar to Figure 83, containing the data found in Figure 120(a) and Figure 121(b), is included in Appendix A. IMEP and CoV of IMEP for the two engines, shown in Figure 122, followed very similar trends to the previous three engines, showing maximum IMEP (scaling with engine size) and minimum CoV of IMEP at CA50 = 8° aTDC.

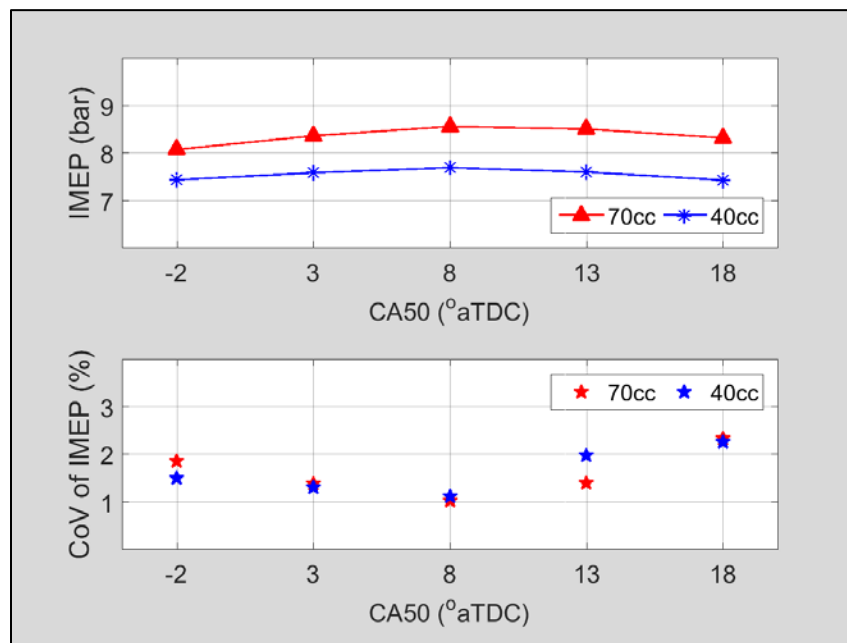


Figure 122. Combined GF40 and TP70 combustion phasing sweep IMEP and CoV of IMEP.

The combustion phasing and combustion duration of the combustion phasing sweeps for the GF40 and TP70 engines were nearly indiscernible. The flame development and rapid burning angles were longer than those for the larger Honda engines as seen in the speed and equivalence ratio sweeps. Plots of combustion phasing

and combustion duration for the GF40 and TP70 combustion phasing sweep are included in Appendix A for reference.

The energy pathways as a percentage of fuel energy for the combustion phasing sweeps of the GF40 and TP70 engine is shown in Figure 123. An unusual trend in the data is that the GF40 had a fuel conversion efficiency approximately 1% higher than the TP70 for all but the $CA_{50} = 13^\circ$ aTDC points. Given the similarity in η_f for the two engines in the equivalence ratio sweep, it is possible that the difference seen here was attributable to day-to-day variation or experimental uncertainty. As with the previous sweeps, the exhaust enthalpy and incomplete combustion losses as a percentage of fuel energy were relatively similar for both engines, with the cooling load as a percentage of fuel energy losses approximately 5% higher for the GF40 engine.

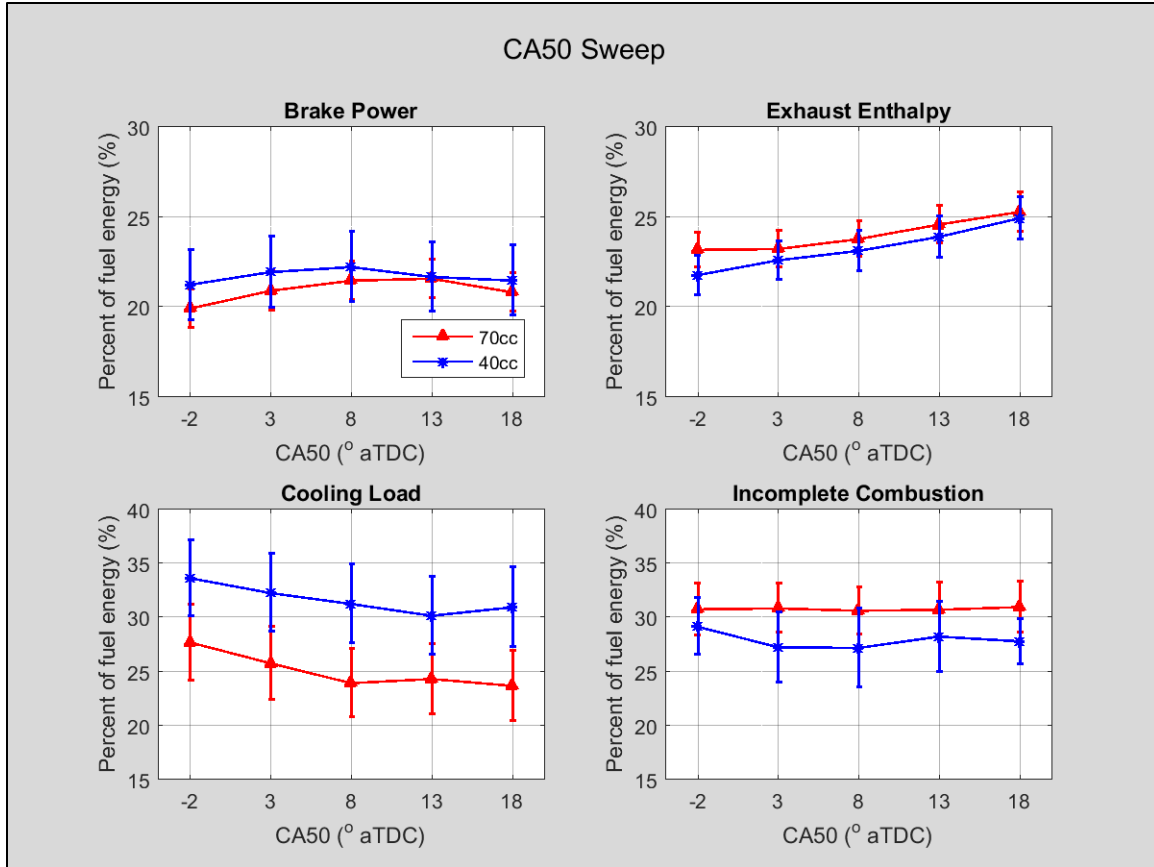
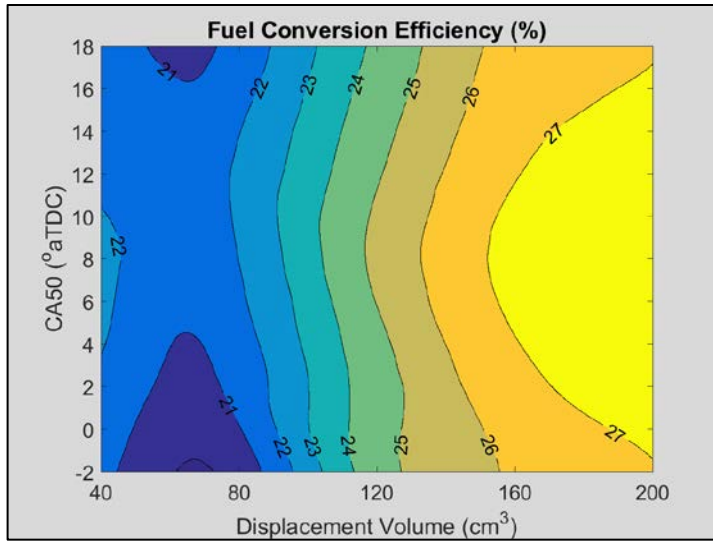
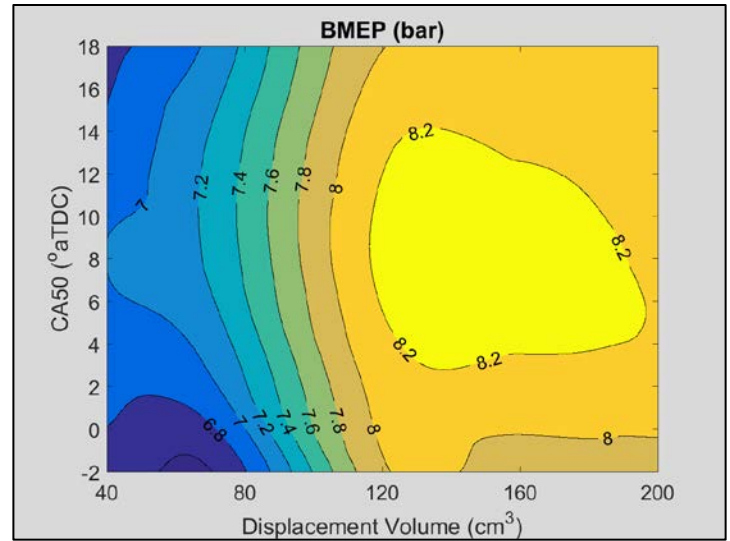


Figure 123. Combined GF40 and TP70 combustion phasing sweep percentage of fuel energy in each energy pathway.

Contour plots for BMEP and η_f as a function of CA50 and displacement volume for all five engines are shown in Figure 124. Both figures were again somewhat symmetric about the horizontal dividing line of CA50 = 8° aTDC, showing BMEP and η_f at a maximum when CA50 was 8° aTDC and increasing with displacement volume. Both BMEP and η_f were relatively stable in the ranges of 40 – 80 cm³ displacement volume and 120 – 200 cm³ displacement volume at CA50 = 8° aTDC.



(a) Fuel conversion efficiency as a function of CA50 and displacement volume.



(b) BMEP as a function of CA50 and displacement volume.

Figure 124. Fuel conversion efficiency and BMEP as functions of CA50 and displacement volume.

Data from the combustion phasing sweeps of all five engines was used to update the coefficients for Equation (62), which can be used to predict BMEP, η_f , exhaust enthalpy losses, cooling load losses, and incomplete combustion losses as a percentage of fuel energy for 40 – 200 cm³ four-stroke engines as functions of both combustion phasing (CA50) and displacement. The coefficients, R² values, and RMS error for the equations are listed in Table 13. Expanding the correlation data from the three Honda engines to all five engines improved (increased) the R² values by an average of 10%, while increasing the RMS errors by an average of 230%. RMS error for the BMEP equation has units of bar, while RMS error for the remaining four equations have units of percentage of fuel energy.

Table 13. BMEP, η_f , exhaust enthalpy, cooling load, and incomplete combustion losses as a percentage of fuel energy coefficients for use with Equation (62).

	A	B	C	D		R ²	RMS Error
BMEP (bar)	6.49	8.87E-03	5.19E-02	-2.81E-03		0.80	0.29
η_f (%)	19.08	4.23E-02	0.15	-8.81E-03		0.91	0.86
Exhaust Enthalpy (%)	21.40	2.21E-02	8.40E-02	2.19E-03		0.94	0.43
Cooling Load (%)	32.37	-4.27E-02	-0.29	9.28E-03		0.69	1.97
Incomplete Combustion (%)	32.10	-6.43E-02	-0.12	6.86E-03		0.75	2.36

4.3.4. GF40 and TP70 Cooling Load Sweep

The GF40 and TP70 engines were run through a cooling load sweep where the cylinder head temperatures were varied from 130° C to 170° C \pm 1° C for the GF40 engine and from 125° C to 165° C \pm 1° C for the TP70 engine. Other conditions held constant were: WOT, ϕ of 1.05 \pm 0.02, mean piston speed of 5.28 \pm 0.15 m/s, and CA50 of 8° \pm 0.4° aTDC. To generalize the data, the results were plotted on the basis of the equivalent air speed (in m/s) of the cooling air rather than cylinder head temperature. A plot of cooling air speed versus cylinder head temperature for the GF40 and TP70 engines is shown in Figure 125. Converting from cylinder head temperature to cooling air speed allowed the data to be plotted on a common scale (approximately 19 to 31 m/s).

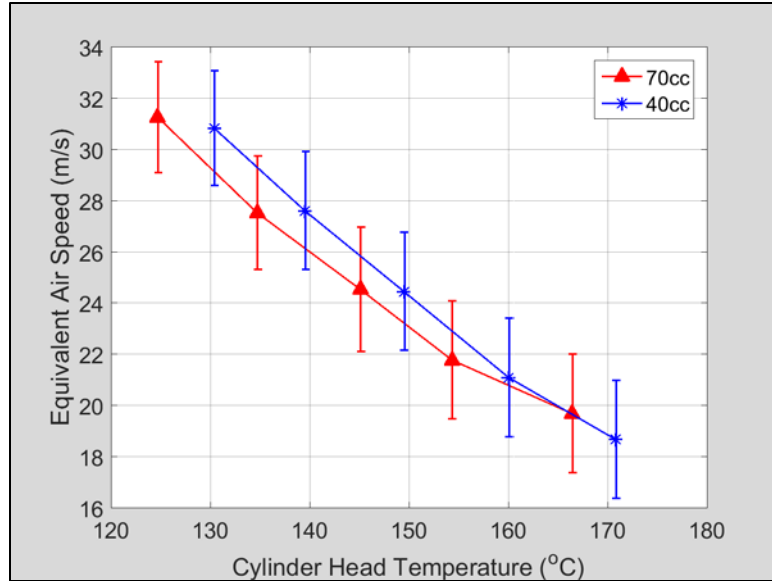
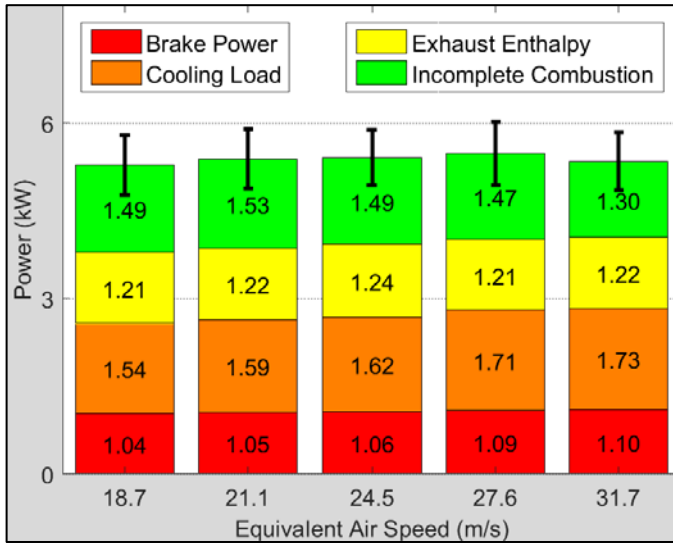


Figure 125. Equivalent air speed of cooling air versus cylinder head temperature for the GF40 and TP70 engines.

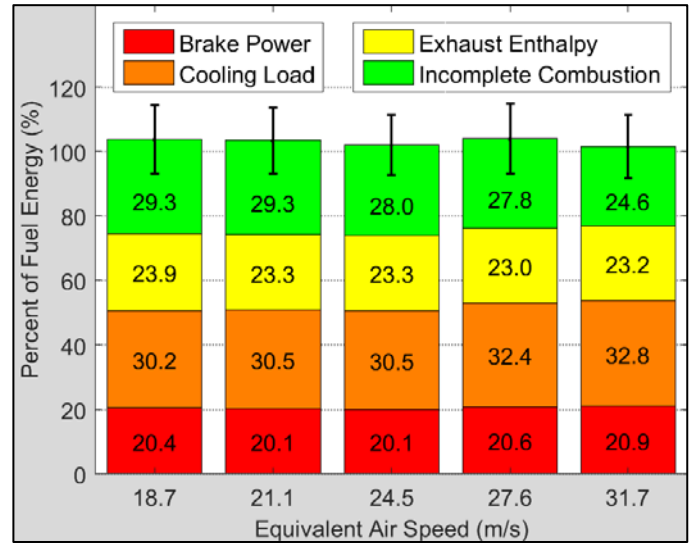
The energy balance results for the GF40 cooling load sweep are shown in Figure 126, while the energy balance results for the TP70 cooling load sweep are shown in Figure 127. Examining the energy balance figures shows that there was little to no significant change in the magnitudes or percentages of fuel energy in the four pathways as the cooling air velocity increased (i.e. cylinder head temperature decreased). The energy distributions as a percentage of fuel energy, seen in Figure 126(b) and Figure 127(b), had total measurements of energy ranging from 101.9% to 104.2% of the fuel energy entering the GF40 engine and 99.6% to 101.9% of the fuel energy entering the TP70 engine.

The IMEP and CoV of IMEP for the two engines was plotted as shown previously in the preceding sections, but the plot displayed very little variation and is not discussed in this section. It has been included in Appendix A for reference, as well as combined

plots showing the combustion phasing and combustion duration of the GF40 and TP70 engines.

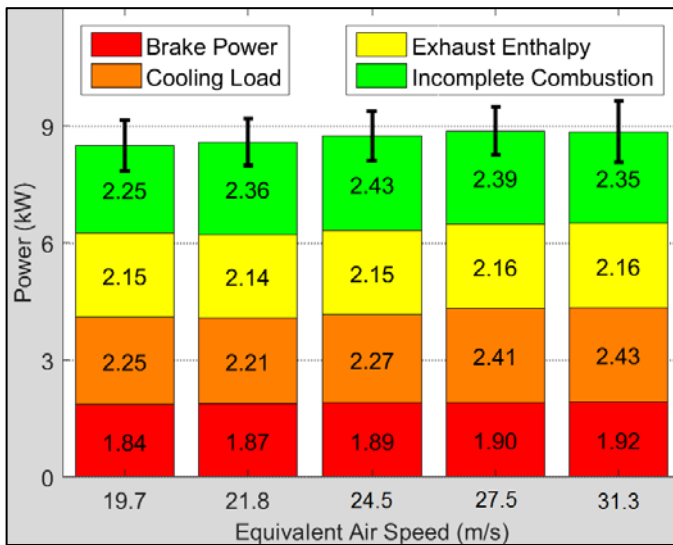


(a) Overall energy in each pathway (kW).

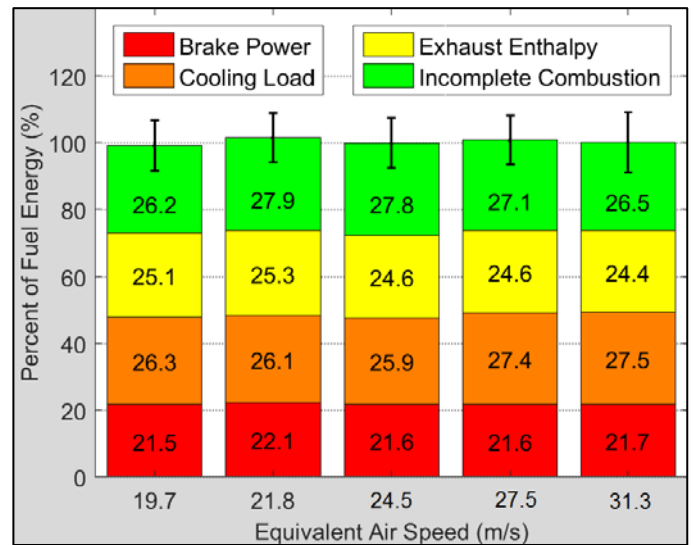


(b) Percentage of fuel energy in each pathway.

Figure 126. GF40 cooling load sweep energy balance.



(a) Overall energy in each pathway (kW).



(b) Percentage of fuel energy in each pathway.

Figure 127. TP70 cooling load sweep energy balance.

BMEP and η_f contour plots were not generated due to the lack of variability in the cooling load sweep data as cylinder head temperature was varied. As an alternative, the mean values for BMEP for all five engines were calculated and plotted versus displacement volume, shown in Figure 128.

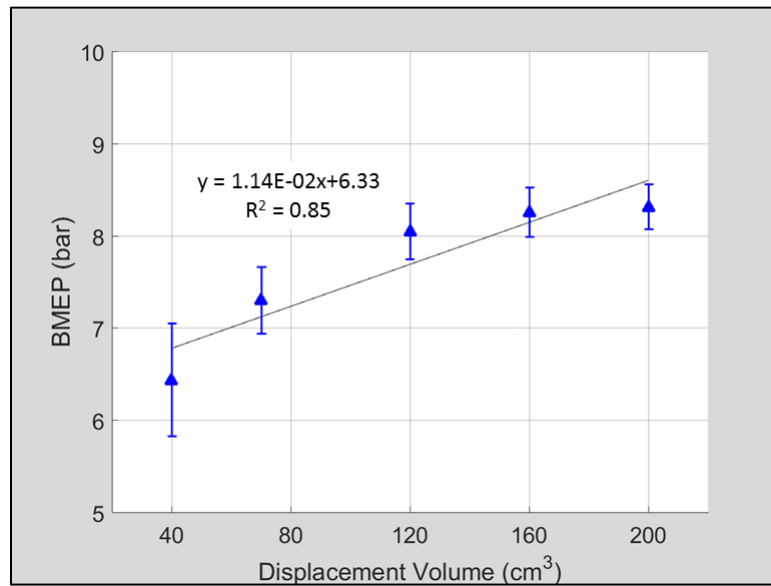


Figure 128. Average BMEP versus displacement volume for the cooling load sweeps of all five engines.

Averaged brake power, exhaust enthalpy, cooling load, and incomplete combustion losses as percentage of fuel energy were also plotted as a function of displacement volume, as seen in Figure 129. Using linear regression analysis, single variable equations were generated to predict BMEP, η_f , exhaust enthalpy losses, cooling load losses, and incomplete combustion losses as a percentage of fuel energy as a function of displacement volume. Values for the coefficients A – B, R^2 values for the linear regression analyses, and the RMS errors for the equations are given in Table 8. Expanding the correlation data from the three Honda engines to all five engines improved

(increased) the R^2 values by an average of 1%, while increasing the RMS errors by an average of 254%. RMS error for the BMEP equation has units of bar, while RMS error for the remaining four equations have units of percentage of fuel energy.

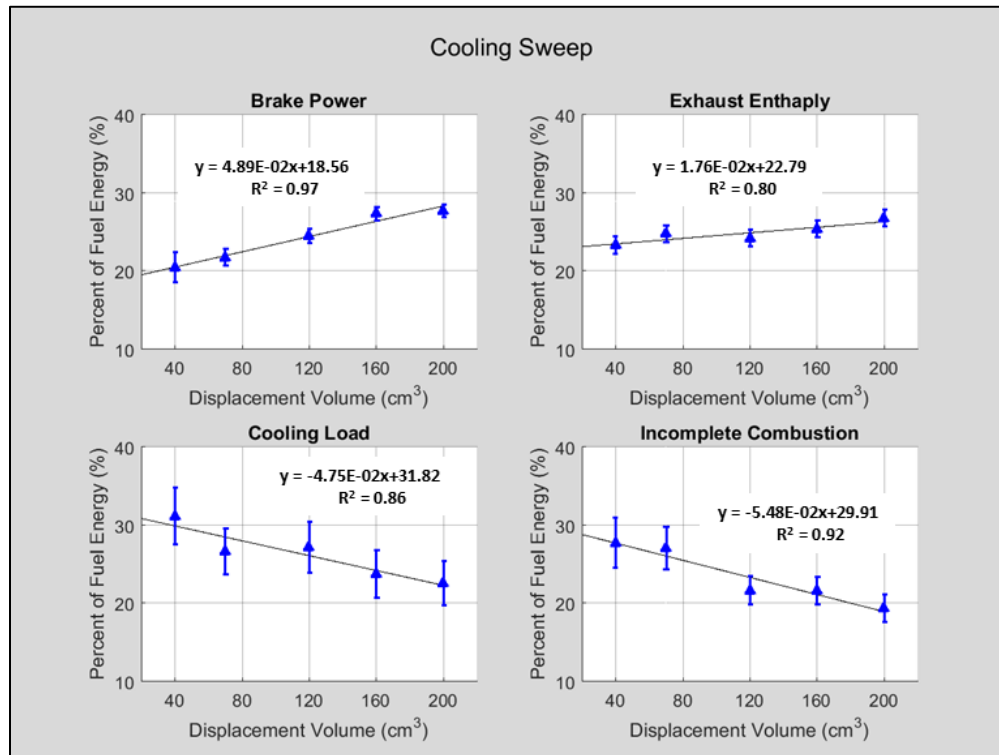


Figure 129. Average brake power, exhaust enthalpy, cooling load, and incomplete combustion losses as a percentage of fuel energy versus displacement volume for the combined cooling load sweeps of all five engines.

Table 14. BMEP, η_f , exhaust enthalpy, cooling load, and incomplete combustion losses as a percentage of fuel energy coefficients for use with Equation (63).

	A	B	R^2	RMS Error
BMEP (bar)	6.33	1.14E-02	0.85	0.35
η_f (%)	18.56	4.89E-02	0.97	0.68
Exhaust Enthalpy (%)	22.79	1.77E-02	0.80	0.66
Cooling Load (%)	31.82	-4.75E-02	0.86	1.46
Incomplete Combustion (%)	29.91	-5.48E-02	0.92	1.19

4.3.5. GF40 and TP70 Throttle Sweep

The GF40 and TP70 engines were run through throttle sweeps where the throttle for both engines was swept from 21.4% open to 100%. Other conditions held constant were: ϕ of 1.05 ± 0.02 , mean piston speed of 5.28 ± 0.15 m/s, CA50 of $8^\circ \pm 0.4^\circ$ aTDC, and cylinder head temperatures of $150^\circ \pm 1^\circ$ C for the GF40 engine and $145^\circ \pm 1^\circ$ C for the TP70 engine. To accomplish the throttle sweeps, the mass flow rates of intake air were noted at WOT, then the engines were progressively throttled without stalling. Just before stall, the mass flow rates of intake air were again noted. After establishing the WOT and stall limited settings, the throttles were opened back up in steps to incrementally increase the mass flow rates of intake air. To generalize the data, the mass flow rates of intake air for the engines were converted to volumetric efficiency (η_v) using Equation (23). Figure 130 shows the relationship between volumetric efficiency and the mass flow rates of intake air for the GF40 and TP70 engines. Additionally, it should be noted that maximum flow rate of intake air for the GF40 and TP70 engines was achieved when the throttle was 48% and 71% open, respectively.

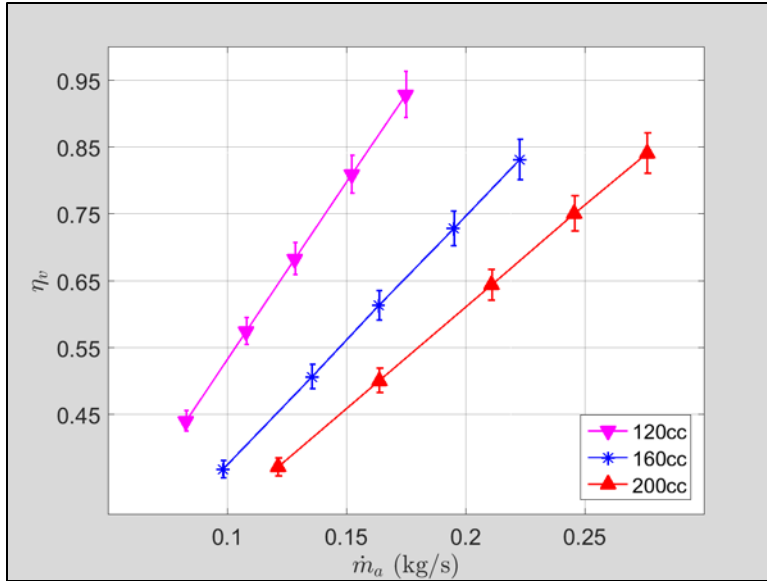
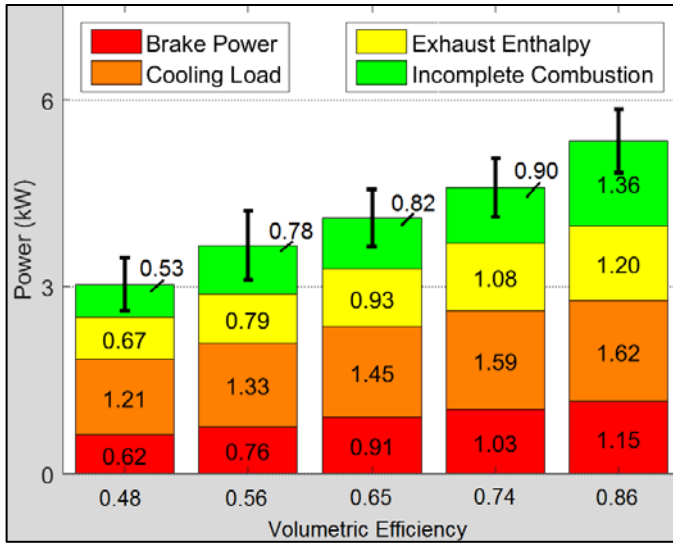
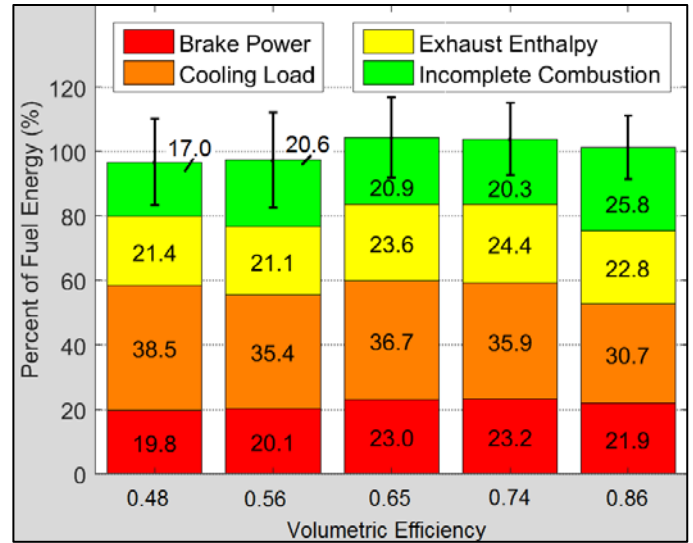


Figure 130. Combined GF40 and TP70 throttle sweep volumetric efficiency versus mass flow rate of intake air.

The energy balance results for the GF40 throttle sweep are shown in Figure 131, while the energy balance results for the TP70 throttle sweep are shown in Figure 132. The energy distributions as a percentage of fuel energy, seen in Figure 131(b) and Figure 132(b), showed total measurements of energy ranged from 97.3% to 104.7% of the fuel energy entering the GF40 engine and 98.6% to 107.7% of the fuel energy entering the TP70 engine.

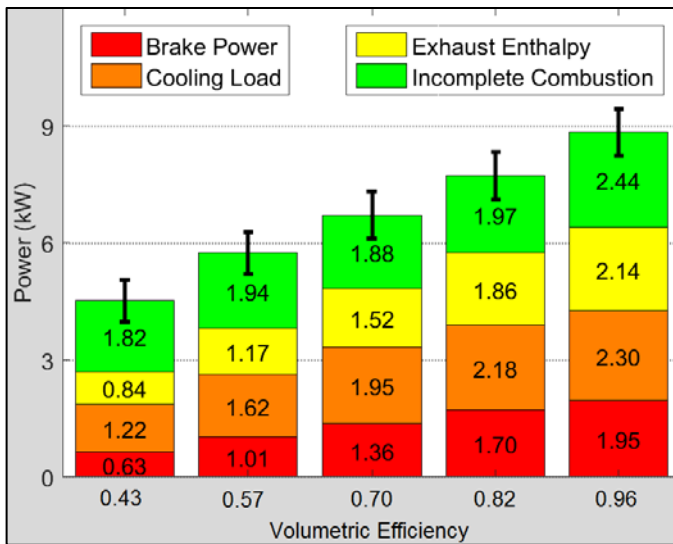


(a) Overall energy in each pathway (kW).

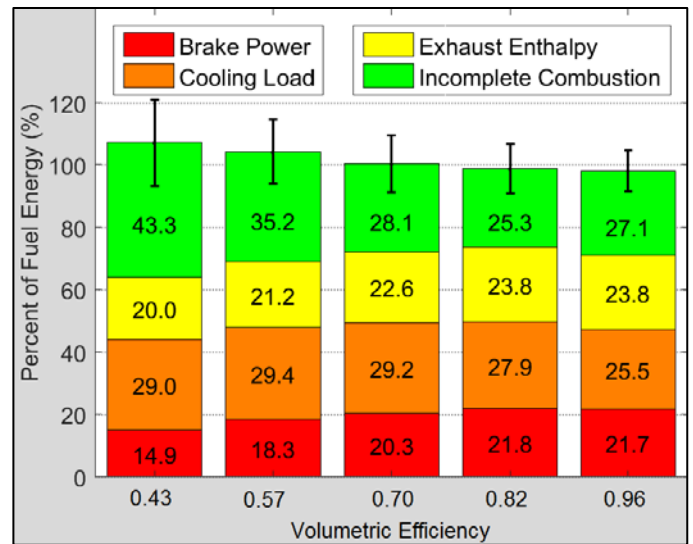


(b) Percentage of fuel energy in each pathway.

Figure 131. GF40 throttle sweep energy balance.



(a) Overall energy in each pathway (kW).



(b) Percentage of fuel energy in each pathway.

Figure 132. TP70 throttle sweep energy balance.

The magnitude of energy in each of the four pathways, shown in Figure 133, consistently increased with larger displacement volume. Unlike the GX120, GX160, and GX200 combined throttle sweep plots in Figure 96, where incomplete combustion losses

showed only a small increase relative to the increases in brake power, exhaust enthalpy, and cooling load, the incomplete combustion losses rose significantly for both the GF40 and TP70 engines at WOT. This may have been the result of using the same throttle body for all five engines, which was larger than the carburetor throats of the GF40 and TP70 carburetors.

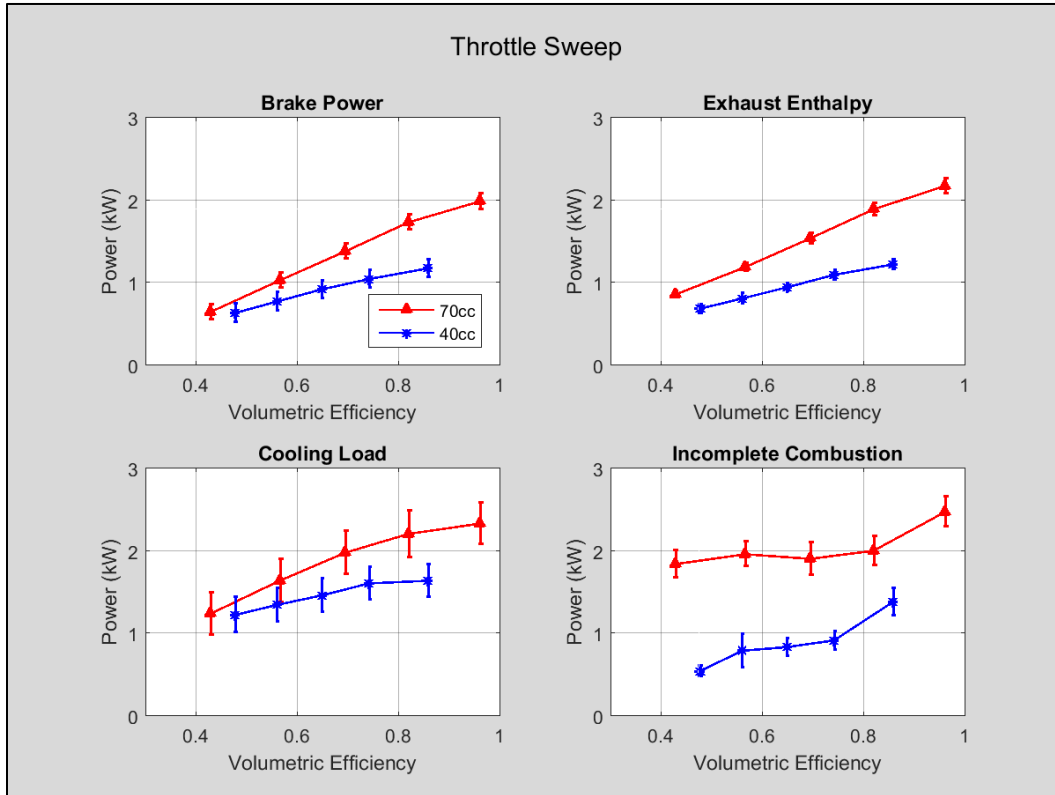


Figure 133. Combined GF40 and TP70 throttle sweep energy pathways (in kW).

IMEP and CoV of IMEP levels for the throttle sweeps of the GF40 and TP70 engines, seen in Figure 134, show that the the GF40 typically had slightly higher IMEP for a given volumetric efficiency, however the TP70 had greater IMEP at WOT. Figure 134 also shows that the GF40 engine ran very poorly at low throttle conditions, with CoV of IMEP of 6.8% at a volumetric efficiency of 0.48.

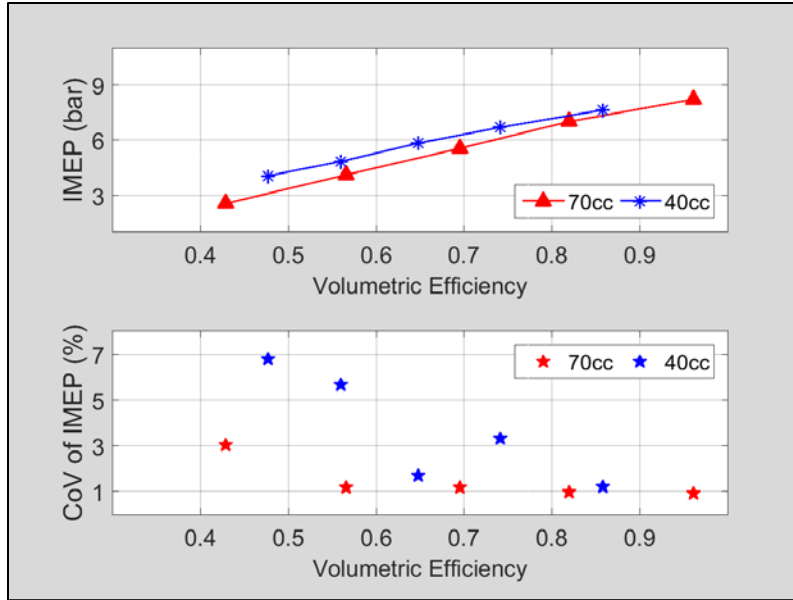
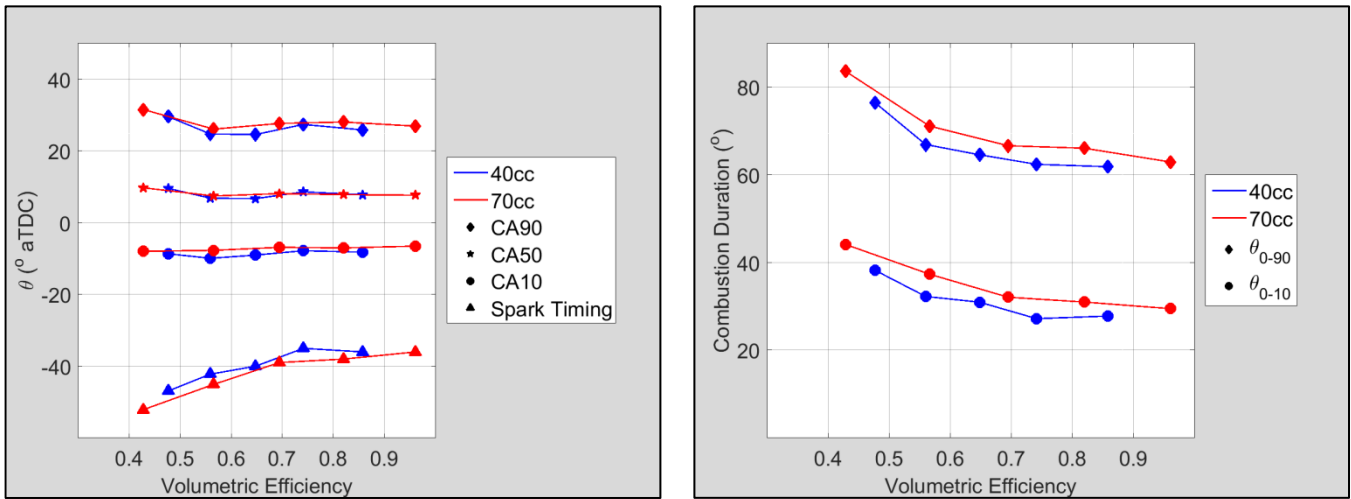


Figure 134. Combined GF40 and TP70 throttle sweep IMEP and CoV of IMEP.

Figure 135 shows the combined combustion phasing and combustion duration plots for the throttle sweeps of the GF40 and TP70 engines. As seen in the plots, engine displacement had very little effect on the combustion phasing and combustion duration.



(a) Combined throttle sweep combustion phasing.

(b) Combined throttle sweep combustion duration.

Figure 135. Combined GF40 and TP70 throttle sweep combustion phasing and combustion duration.

Examining the energy pathways as a percentage of fuel energy from Figure 136, similar patterns to those seen in the other GF40 and TP70 combined sweeps were seen for fuel conversion efficiency, exhaust enthalpy losses, and cooling load losses as a percentage of fuel energy, but incomplete combustion losses decreased as the throttle was closed in the GF40 engine. This was the only engine which displayed this behavior. It is not known at the time of this writing why this engine produced this result.

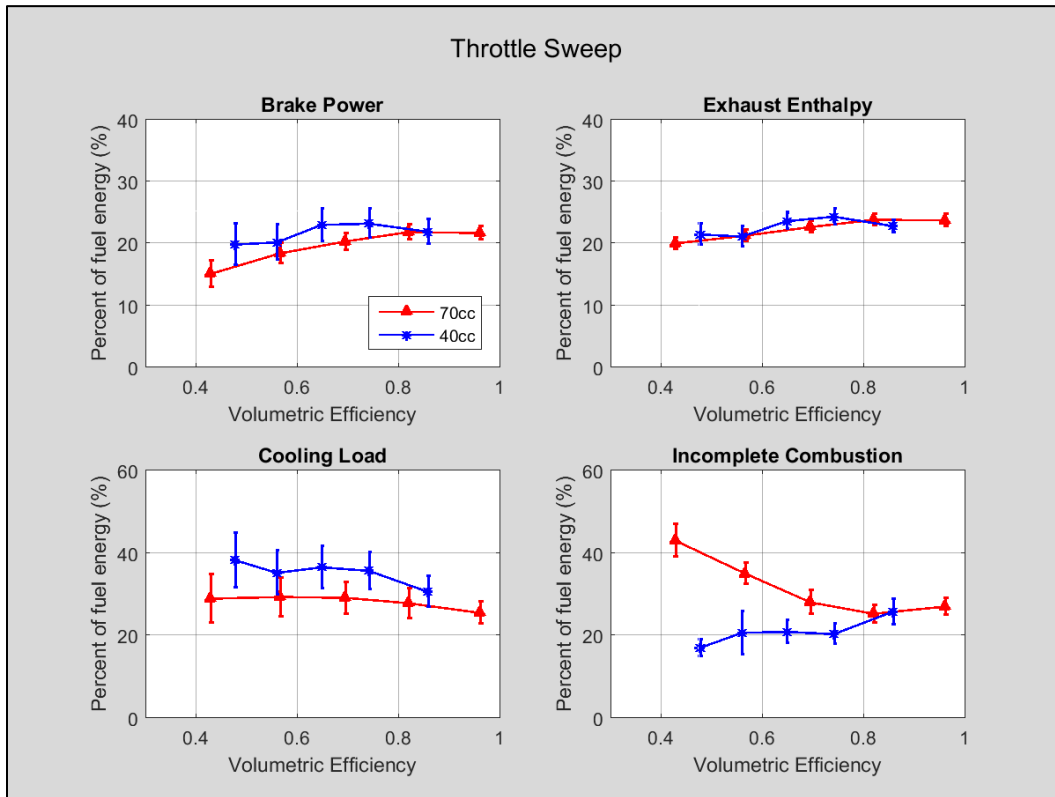
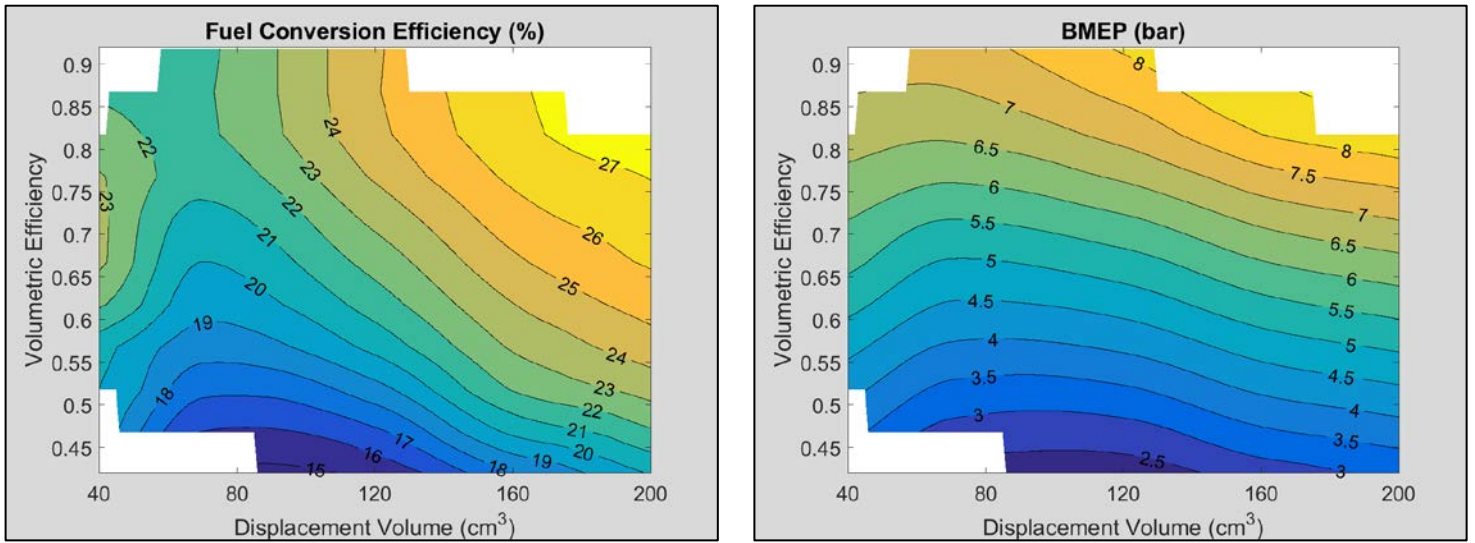


Figure 136. Combined GF40 and TP70 throttle sweep percentage of fuel energy in each energy pathway.

Contour plots for η_f and BMEP as a function of volumetric efficiency and displacement volume are shown in Figure 137(a) and Figure 137(b). The figures show

BMEP and η_f increasing with displacement volume and volumetric efficiency, with a slight increase in η_f at low displacement, as seen in Figure 136.



(a) Fuel conversion efficiency as a function of volumetric efficiency and displacement volume.

(b) BMEP as a function of volumetric efficiency and displacement volume.

Figure 137. Fuel conversion efficiency and BMEP as functions of volumetric efficiency and displacement volume for all five engines.

Data from the throttle sweeps of all five engines was used to update the coefficients for Equation (64), which can be used to predict BMEP, η_f , exhaust enthalpy losses, cooling load losses, and incomplete combustion losses as a percentage of fuel energy for 40 – 200 cm³ four-stroke engines as functions of both volumetric efficiency and displacement. The coefficients, R² values, and RMS error for the equations are listed in Table 15. Expanding the correlation data from the three Honda engines to all five engines worsened (decreased) the R² values by an average of 15%, while increasing the RMS errors by an average of 152%. RMS error for the BMEP equation has units of bar,

while RMS error for the remaining four equations have units of percentage of fuel energy.

Table 15. BMEP, η_f , exhaust enthalpy, cooling load, and incomplete combustion losses as a percentage of fuel energy coefficients for use with Equation (64).

	A	B	C	D		R ²	RMS Error
BMEP (bar)	-5.91	6.74E-03	21.74	-8.11		0.96	0.41
η_f (%)	-10.65	3.00E-02	77.30	-47.02		0.87	1.35
Exhaust Enthalpy (%)	11.15	1.95E-02	23.63	-12.45		0.75	1.00
Cooling Load (%)	21.22	-6.09E-02	50.98	-42.13		0.80	2.08
Incomplete Combustion (%)	84.47	-1.02E-03	-156.51	98.53		0.56	5.26

5. Conclusions and Recommendations

Chapter Overview

Chapter five is divided into three subsections. Section 5.1 contains a review and discussion on the completion of the research objectives developed in Section 1.2. Section 5.2 contains key findings and conclusions from the research contained in the study. Section 5.3 discusses recommendations for improvements and future research.

5.1. Research Objectives

A brief discussion of each of the three research objectives found in Section 1.2 and how they were met follows.

5.1.1. Objective 1

Objective 1 was concerned with comparing actual measured power to manufacturer's advertised power ratings for a selection of single cylinder, 40 – 200 cm³ displacement volume, four-stroke ICEs.

The five engines tested in the study were installed on the SERB and run through their manufacturer's recommended engine speed ranges. When compared to the manufacturer's advertised power ratings, the Honda GX120 engine produced 14% more brake power than the advertised maximum power rating, the Honda GX160 engine produced 19% more brake power than the advertised maximum power rating and the Honda GX200 engine produced 18% more brake power than the advertised maximum power rating. The peak power ratings found on the SERB utilized the SERB exhaust, EFI, and ECU systems, which provided the increased outputs in brake power. When

tested with stock exhaust systems, the Honda engines performed much closer to the manufacturer's advertised power ratings. Using the same SERB exhaust (with very slight modification), EFI, and ECU setups, the Torqpro TP70 engine produced 51% less brake power than the advertised maximum power rating, and the OS GF40 engine produced 33% less brake power than the advertised maximum power rating. It is not known at this time if the power levels advertised for the GF40 and TP70 engines were achieved through manufacturer testing or if they were estimates. Additionally, η_f and BMEP at peak power for the five engines were plotted and an equation was developed to predict η_f and BMEP at peak power for small four-stroke engines based on engine displacement.

5.1.2. Objective 2

Objective 2 was concerned with performing first law of thermodynamics energy balances for five engines. All energy pathways are to be measured experimentally. Examined energy pathways were:

- a) Brake power
- b) Cooling load
- c) Sensible enthalpy of exhaust gases
- d) Incomplete combustion

A total of 129 energy balances were performed for various test conditions for the OS GF40, Torqpro TP70, and Honda GX120, GX160, and GX200 engines. Total energy measurements for all 129 test conditions were between 96% and 107% of fuel energy, with 68 of 129 energy balance totals between 98% and 102% of fuel energy. In general, the results showed typical fuel conversion efficiencies of 20 – 25%, exhaust enthalpy

losses of 20 – 30% of fuel energy, cooling load or thermal losses of 20 – 30% of fuel energy, and incomplete combustion losses of 15 – 40% of fuel energy. Incomplete combustion losses had a prominent role in the engine speed, equivalence ratio, and throttle sweeps, but the findings did not suggest a single dominant loss pathway for all test conditions, as was found in the previous two-stroke engine study of Ausserer [10].

5.1.3. Objective 3

Objective 3 was the summation of the effort covering parametric studies to characterize the impact of five variables (equivalence ratio, combustion phasing, cylinder head temperature, engine speed, and throttle setting) on the loss pathways.

Five parametric studies were performed for the Honda GX120, GX160, and GX200 engines. For all three of the Honda engine studies engine speed was swept from 2000 – 3600 rpm, equivalence ratio was swept from 0.85 – 1.25, and CA50 was swept from 2° bTDC to 8° aTDC. For the GX120 engine, cylinder head temperature was swept from 125° C - 160° C and throttle was swept from 28.6% open to 100% open (WOT). For the GX160 engine, cylinder head temperature was swept from 130° C - 170° C and throttle was swept from 28.6% open to 100% open (WOT). For the GX200 engine, cylinder head temperature was swept from 150° C - 190° C and throttle was swept from 35.7% open to 100% open (WOT).

Five parametric studies were also performed for the OS GF40 and Torqpro TP70 engines. In the parametric studies engine speed was swept from 2000 – 7900 rpm for the GF40 engine and from 1800 – 6800 rpm for the TP70 engine. Equivalence ratio was swept from 0.85 – 1.25 for both the GF40 and TP70 engines. CA50 was swept from 2°

bTDC to 8° aTDC for both the GF40 and TP70 engines. Cylinder head temperature was swept from 130° C - 170° C for the GF40 engine and from 125° C - 165° C for the TP70 engine. Finally, throttle was swept from 21.4% open to 100% open (WOT) for both the GF40 and TP70 engines.

The parametric studies showed that engine speed, equivalence ratio, and throttle setting had large impacts on both the magnitude of energy in the loss pathways and the percentage of fuel energy the losses accounted for, particularly in the incomplete combustion energy pathway, which showed losses as a percentage of fuel energy from under 10% to nearly 50%. Combustion phasing and cylinder head temperature had minimal impact on the magnitude of energy in the loss pathways and the percentage of fuel energy, with the largest changes in the cooling load and exhaust enthalpy losses as a percentage of fuel energy, which changed by approximately 3 – 5% as the engines were swept through the test conditions.

5.2. Key Findings and Conclusions

The most relevant parameters of interest to most engine researchers are maximum brake power (P_b) and fuel conversion efficiency (η_f). The OS GF40 engine had a maximum brake power of 1.85 kW at 7900 rpm. Maximum fuel conversion efficiency was 25% when run with a ϕ of 0.89. Minimum fuel conversion efficiency was 17.8% when run with a ϕ of 1.28. The Torqpro TP70 engine had a maximum brake power of 2.23 kW at 5000 rpm. Maximum fuel conversion efficiency was 25.7% when run with a ϕ of 0.85. Minimum fuel conversion efficiency was 14.9% when run under highly throttled conditions. The Honda GX120 engine had a maximum brake power of 2.91 kW

at 3600 rpm. Maximum fuel conversion efficiency was 27.3% when run with a ϕ of 0.85. Minimum fuel conversion efficiency was 15.7% when run under highly throttled conditions. The Honda GX160 engine had a maximum brake power of 4.01 kW at 3600 rpm. Maximum fuel conversion efficiency was 31.5% when run with a ϕ of 0.85. Minimum fuel conversion efficiency was 15.6% when run under highly throttled conditions. The Honda GX200 engine had a maximum brake power of 5.02 kW at 3600 rpm. Maximum fuel conversion efficiency was 32.7% when run with a ϕ of 0.85. Minimum fuel conversion efficiency was 18.1% when run under highly throttled conditions. These findings show that maximum fuel conversion efficiency improved with increased engine displacement, as the literature suggests.

In addition to these findings and the research undertaken to satisfy the research objectives from Section 1.2, a set of equations was developed from the test data to predict BMEP, fuel conversion efficiency, exhaust sensible enthalpy losses, cooling load losses, and incomplete combustion losses as percentages of fuel energy. The equations allow researchers to predict these five operating parameters for single cylinder four-stroke engines ranging in displacement volume from 40 – 200 cm³ operating under a variety of conditions. Perhaps these equations may be used to identify areas of potential energy loss reduction and fuel conversion efficiency improvement in future small engine research.

5.3. Recommendations for Future Research

Although much effort was devoted to collecting the best possible test data to present in this study, there were some areas which could be improved. The uncertainty in

the cooling load loss measurements were generally larger than the uncertainty in the brake power and exhaust sensible enthalpy losses by a factor of two or greater. A recommendation for future research is to change test bench configurations in the cooling system to better suit different engines and test conditions. The “one size fits all” approach used in this study worked well for many test conditions, but was less effective for smaller flow rates.

The energy pathway that would likely be of the most interest to future researchers seeking to improve the efficiency of small COTS four stroke engines would be incomplete combustion. Efforts to improve the mixing characteristics, turbulence in the combustion chamber, or optimization of fuel spray patterns and atomization are recommended.

Another recommendation is to obtain more test data in the below 120 cm³ displacement range. Difficulties with running the Torqpro TP70 engine consistently warrant further exploration of the range between 40 cm³ and 120 cm³ in particular. Obtaining a larger data set and integrating it into the equations developed in Section 4.3 will help to improve the accuracy of the correlations and broaden their application. Additional analysis of the correlation equations to make them dimensionally correct is recommended as well.

Appendix A

Figure A - 1 through Figure A - 4 and Table A - 1 through Table A - 4 contain repeatability data for the GF40, TP70, GX160, and GX200 engines.

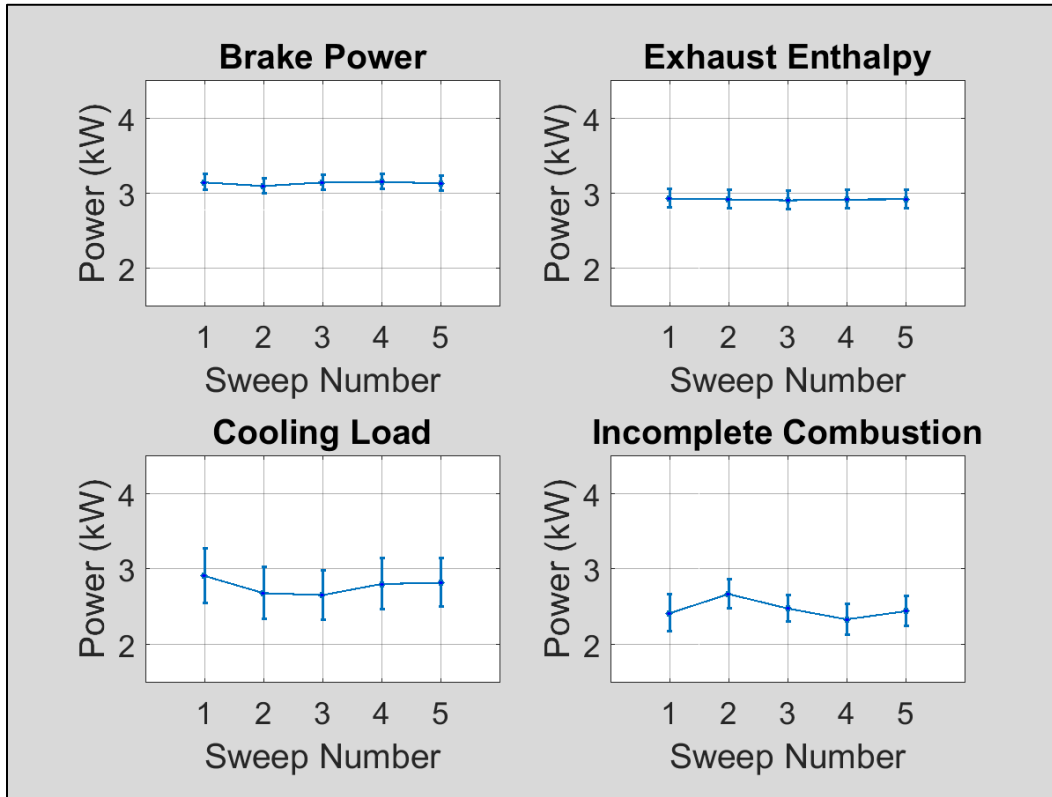


Figure A - 1. Repeatability of GX160 engine.

Table A - 1. Repeatability analysis results for GX160 engine.

Sweep	Brake Power (kW)	Exhaust Enthalpy (kW)	Cooling Load (kW)	Incomplete Combustion (kW)
1	3.150	2.935	2.915	2.419
2	3.101	2.924	2.687	2.674
3	3.150	2.911	2.660	2.484
4	3.159	2.922	2.807	2.339
5	3.136	2.925	2.824	2.447
Mean (kW)	3.139	2.923	2.779	2.472
Std Dev (kW)	0.020	0.008	0.094	0.111
95% CI (kW)	0.052	0.020	0.241	0.287
Variation (%)	1.7	0.7	8.7	11.6

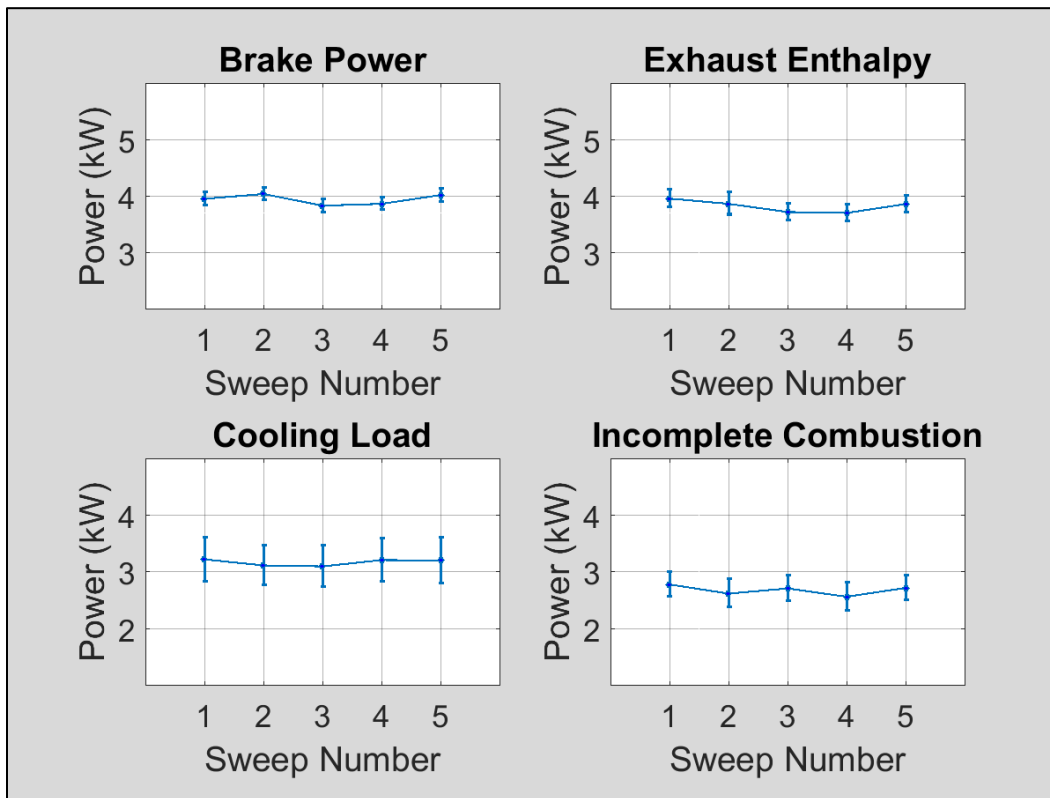


Figure A - 2. Repeatability of GX200 engine.

Table A - 2. Repeatability analysis results for GX200 engine.

Sweep	Brake Power (kW)	Exhaust Enthalpy (kW)	Cooling Load (kW)	Incomplete Combustion (kW)
1	3.961	3.966	3.231	2.788
2	4.048	3.873	3.125	2.627
3	3.841	3.728	3.107	2.718
4	3.872	3.711	3.219	2.571
5	4.028	3.869	3.213	2.727
Mean (kW)	3.950	3.830	3.179	2.686
Std Dev (kW)	0.082	0.097	0.052	0.077
95% CI (kW)	0.211	0.248	0.134	0.198
Variation (%)	5.3	6.5	4.2	7.4

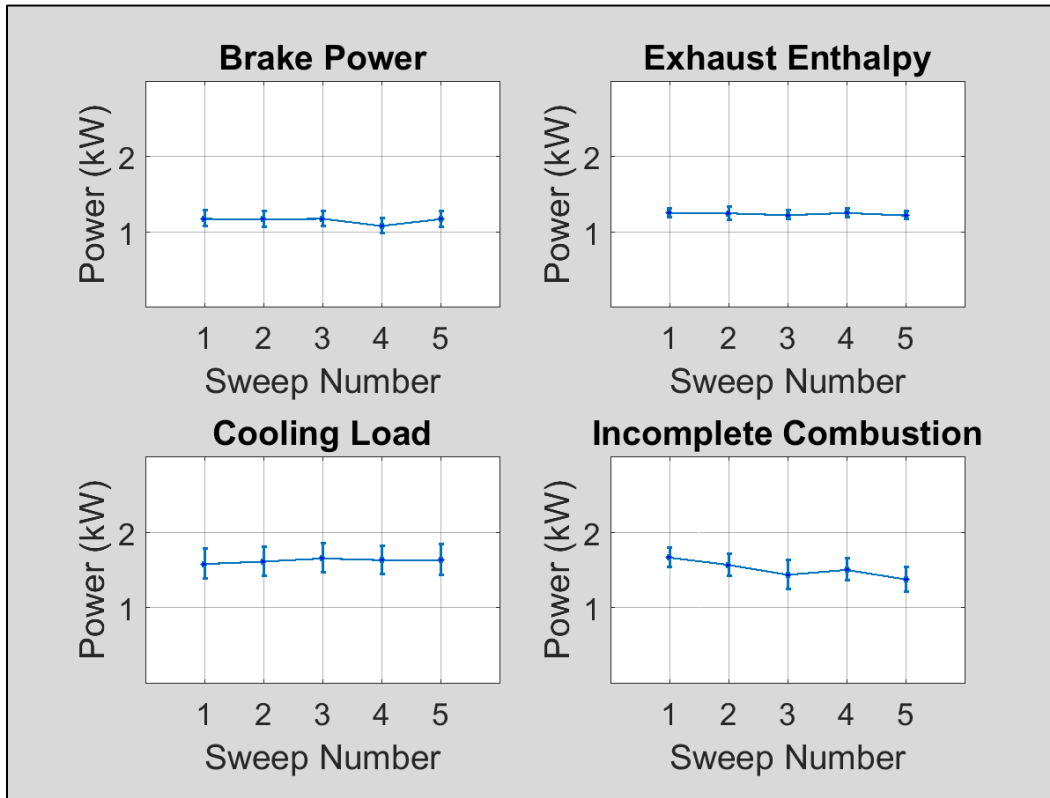


Figure A - 3. Repeatability of GF40 engine.

Table A - 3. Repeatability analysis results for GF40 engine.

Sweep	Brake Power (kW)	Exhaust Enthalpy (kW)	Cooling Load (kW)	Incomplete Combustion (kW)
1	1.178	1.258	1.585	1.670
2	1.173	1.252	1.618	1.573
3	1.179	1.227	1.659	1.442
4	1.084	1.257	1.637	1.507
5	1.174	1.223	1.639	1.382
Mean (kW)	1.158	1.243	1.628	1.515
Std Dev (kW)	0.037	0.015	0.025	0.101
95% CI (kW)	0.095	0.039	0.064	0.259
Variation (%)	8.2	3.2	3.9	17.1

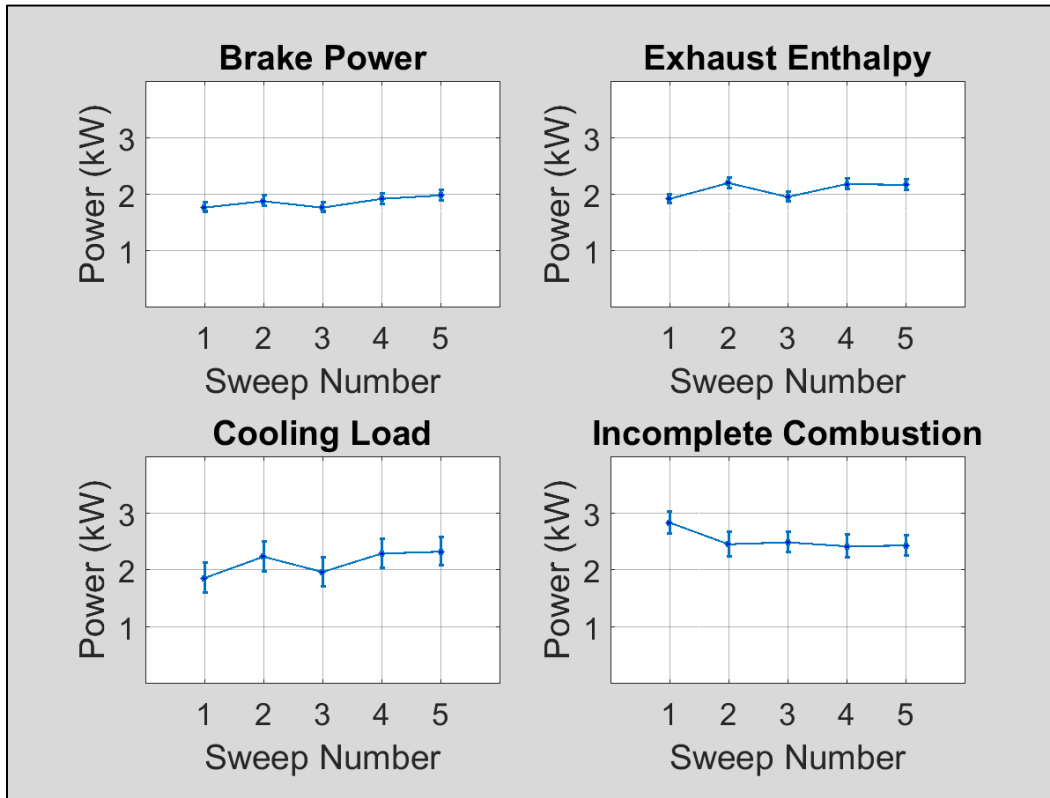


Figure A - 4. Repeatability of TP70 engine.

Table A - 4. Repeatability analysis results for TP70 engine.

Sweep	Brake Power (kW)	Exhaust Enthalpy (kW)	Cooling Load (kW)	Incomplete Combustion (kW)
1	1.772	1.925	1.865	2.846
2	1.884	2.207	2.243	2.463
3	1.770	1.960	1.973	2.497
4	1.926	2.187	2.298	2.427
5	1.987	2.174	2.332	2.440
Mean (kW)	1.868	2.091	2.142	2.535
Std Dev (kW)	0.086	0.122	0.188	0.158
95% CI (kW)	0.220	0.314	0.483	0.405
Variation (%)	11.8	15.0	22.5	16.0

Figure A - 5 contains exhaust validation results for the GF40, TP70, GX160, and GX200 engines.

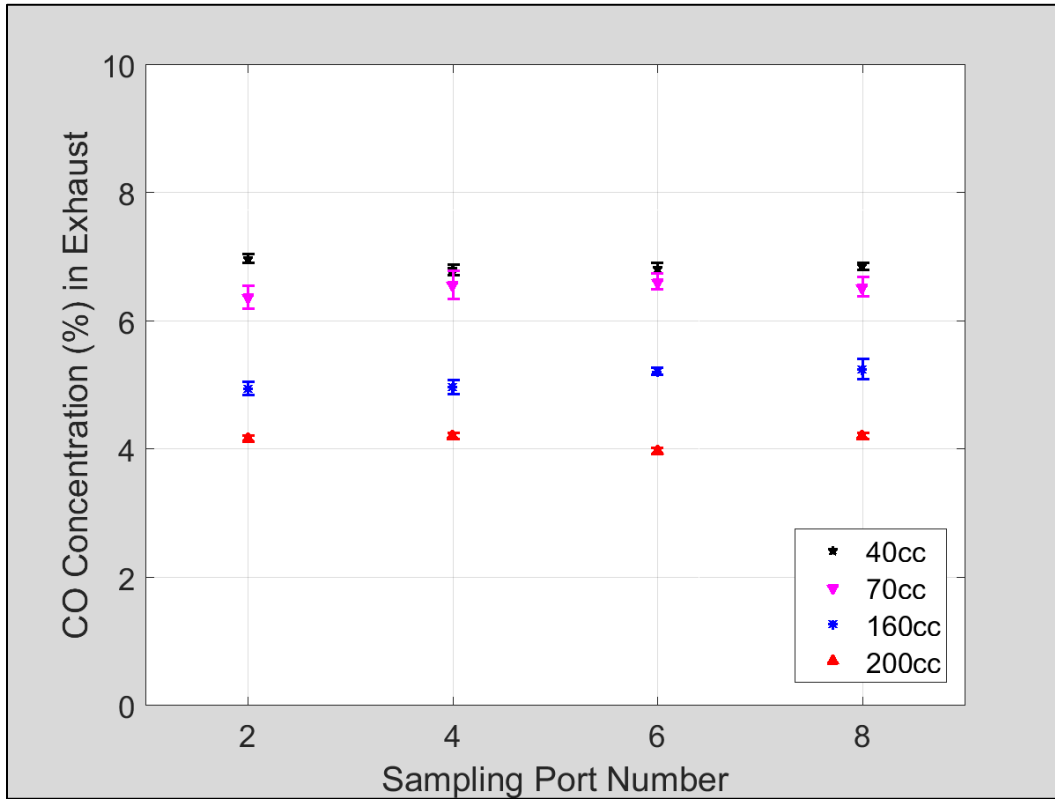


Figure A - 5. Exhaust validation results for the GF40, TP70, GX160, and GX200 engines. CO concentrations remained stable from exhaust sampling Port 2 to exhaust sampling Port 8.

Figure A - 6 and Figure A - 7 contain results for the GX120 engine cooling load sweep.

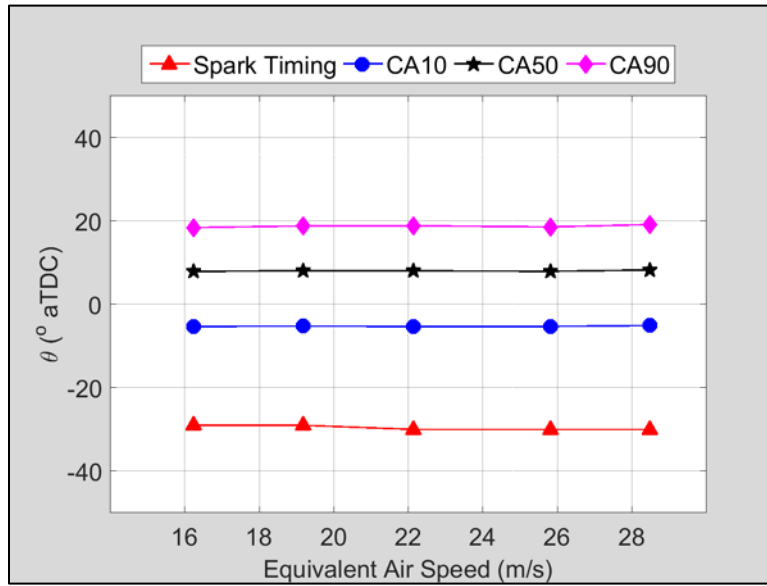


Figure A - 6. GX120 cooling load sweep combustion phasing.

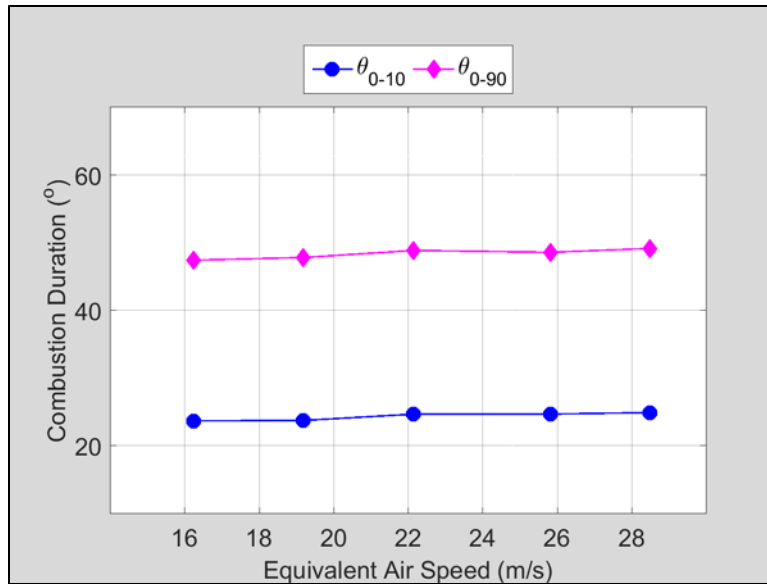


Figure A - 7. GX120 cooling load sweep combustion duration.

Figure A - 8 and Figure A - 9 contain results for the GX120, GX160, and GX200 cooling load sweeps.

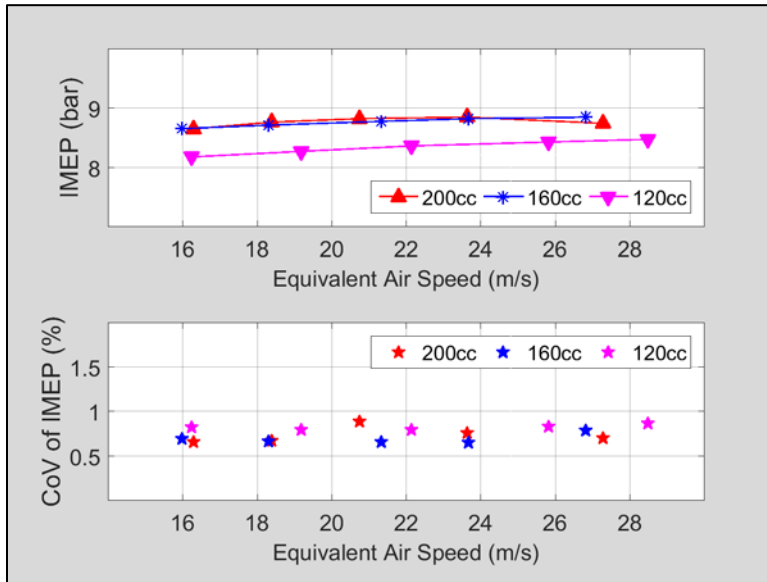
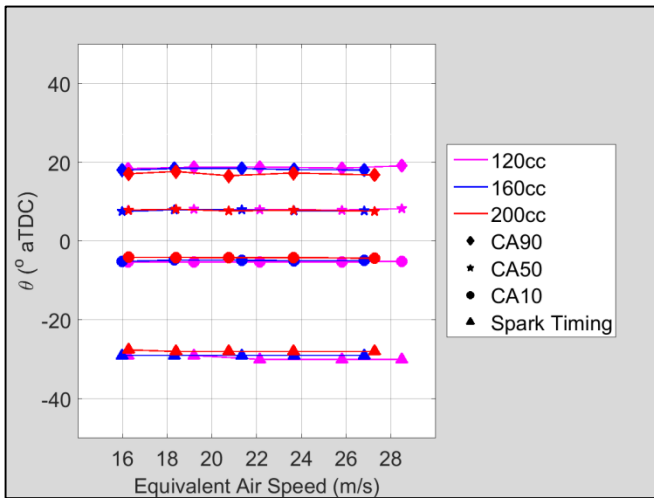
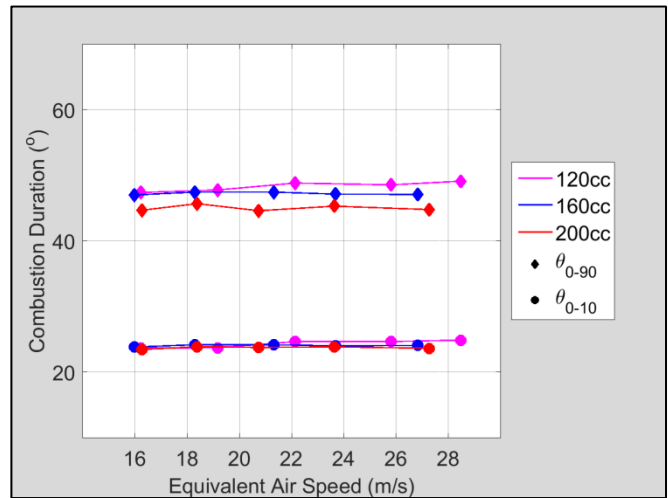


Figure A - 8. Combined cooling load sweep IMEP and CoV of IMEP.



(a) Combined cooling load sweep combustion phasing.



(b) Combined cooling load sweep combustion duration.

Figure A - 9. Combined GX120, GX160, and GX200 cooling load sweep combustion phasing and combustion duration.

Figure A - 10 through Figure A - 14 contain results for the GF40 and TP70 parametric sweeps.

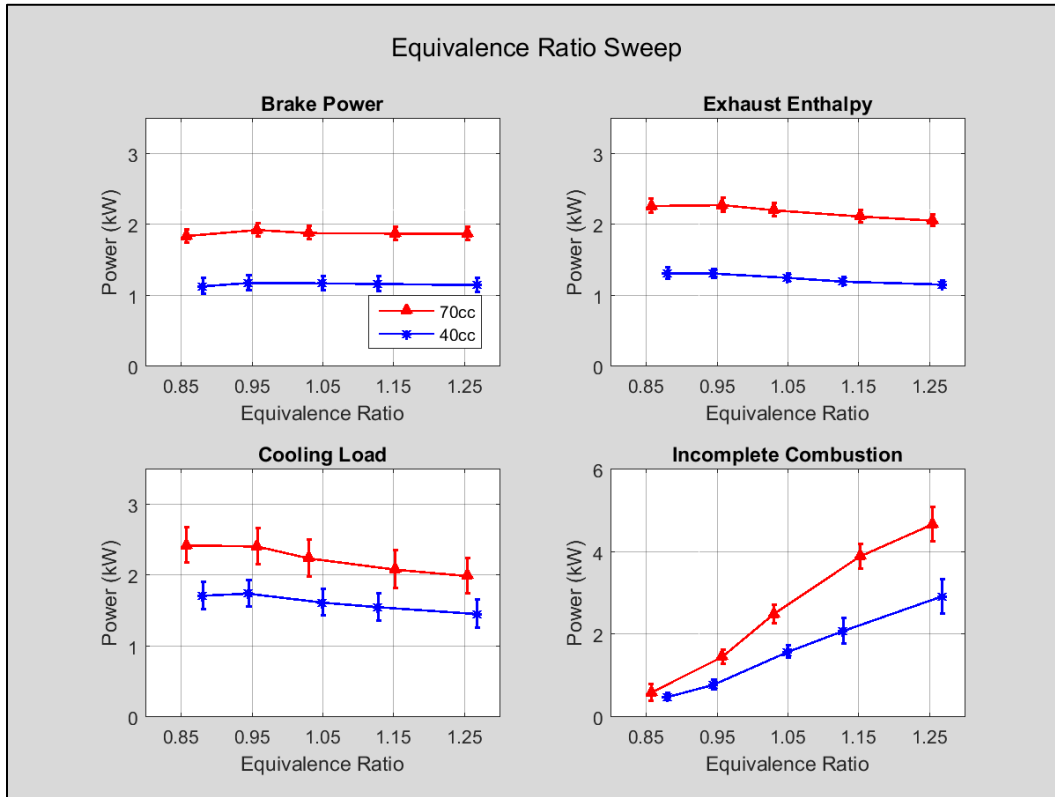


Figure A - 10. Combined GF40 and TP70 equivalence ratio sweep energy pathways (in kW).

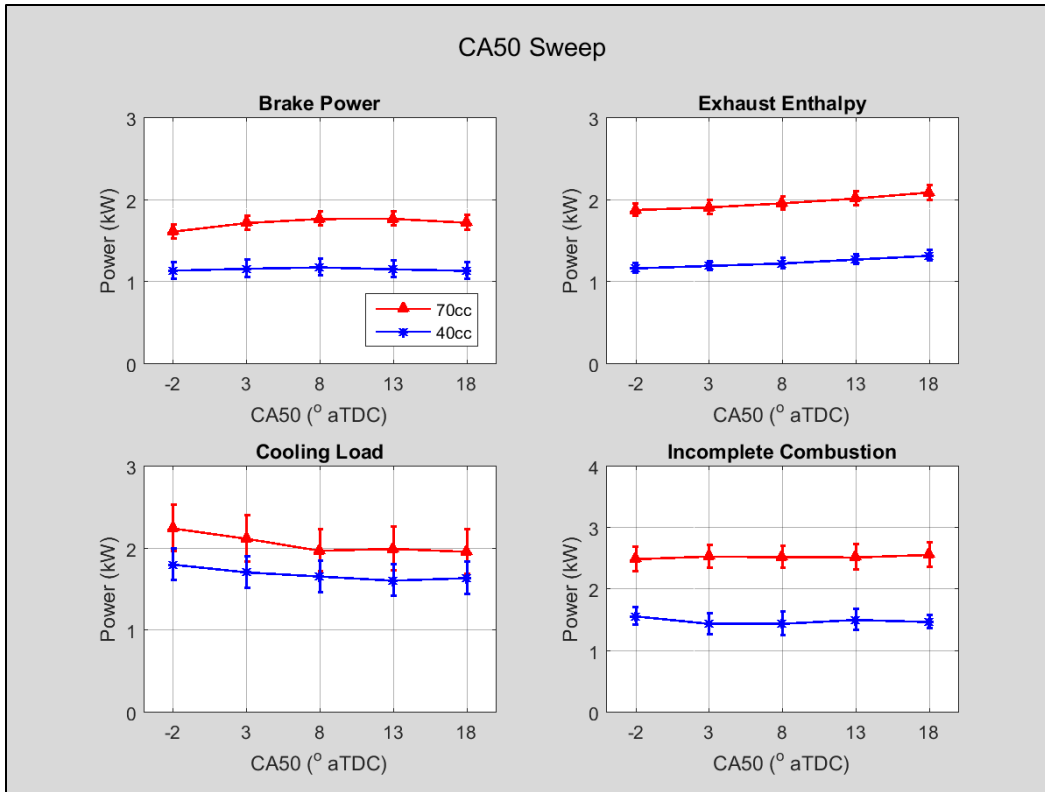
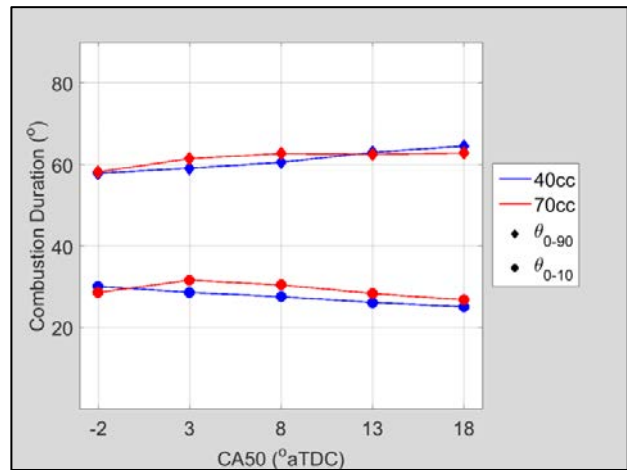
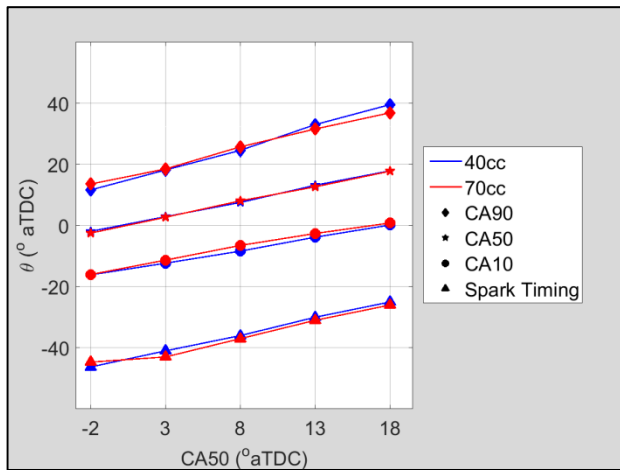


Figure A - 11. Combined GF40 and TP70 combustion phasing sweep energy pathways (in kW).



(a) Combined combustion phasing sweep combustion phasing.

(b) Combined combustion phasing sweep combustion duration.

Figure A - 12. Combined GF40 and TP70 combustion phasing sweep combustion phasing and combustion duration.

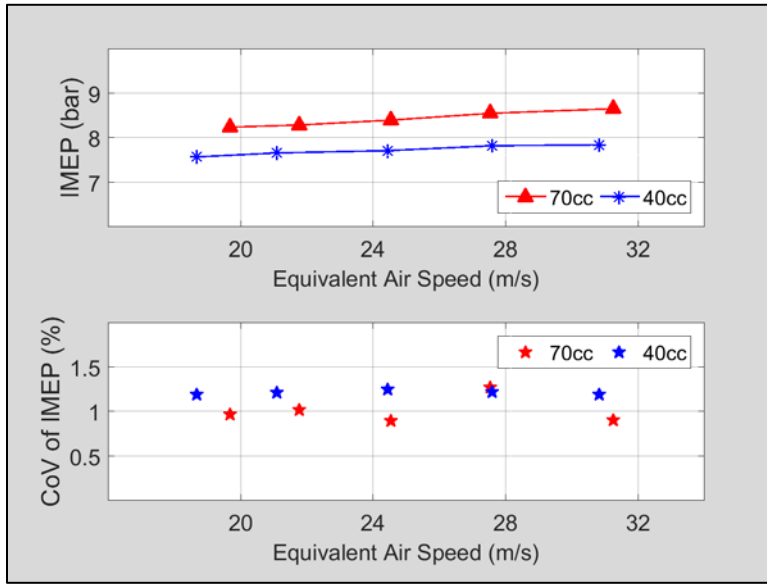
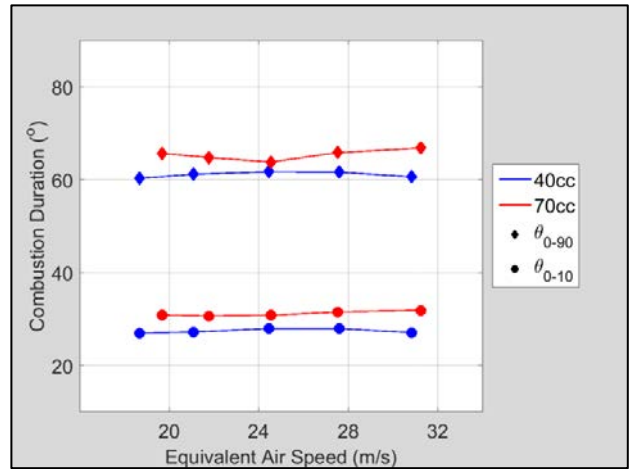
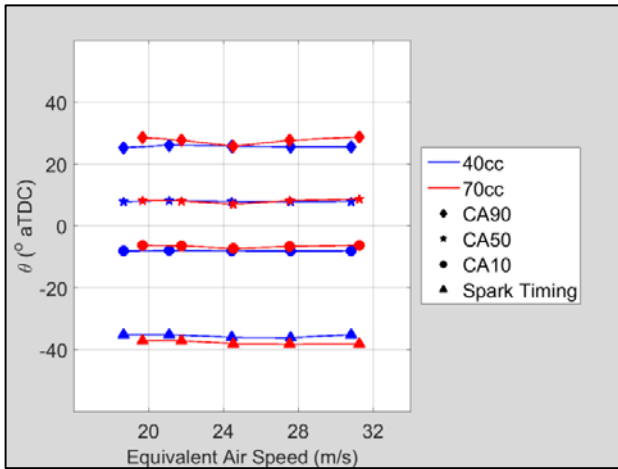


Figure A - 13. Combined GF40 and TP70 cooling load sweep IMEP and CoV of IMEP.



(a) Combined cooling load sweep combustion phasing.

(b) Combined cooling load sweep combustion duration.

Figure A - 14. Combined GF40 and TP70 cooling load sweep combustion phasing and combustion duration.

Bibliography

- [1] Strategic Defence Intelligence, "The Global Unmanned Aerial Vehicle Market 2015-2025 - Major Programs: Market Profile," 2015.
- [2] D. Jenkins and B. Vasigh, "The Economic Impact of Unmanned Aircraft Systems Integration in the United States," Association for Unmanned Vehicle Systems International, Arlington, Virginia, March 2013.
- [3] United States Air Force, "Global Integrated Intelligence, Surveillance, & Reconnaissance Operations: Air Force Doctrine Document 2-0," Department of the Air Force, Ed., ed. LeMay Center, 2012.
- [4] United States Air Force, "United States Air Force RPA Vector: Vision and Enabling Concepts 2013 - 2038 ", Department of the Air Force, Ed., ed, 2014.
- [5] United States Air Force, "United States Air Force Unmanned Aircraft Systems Flight Plan 2009-2047," Department of the Air Force, Ed., ed. Headquarters, United States Air Force, Washington DC, 2009.
- [6] Department of Defense, "The U.S. Air Force Remotely Piloted Aircraft and Unmanned Aerial Vehicle Strategic Vision," ed. United States Air Force, 2005.
- [7] J. K. Ausserer, M. Polanka, P. J. Litke, and K. Grinstead, "The Scaling of Loss Mechanisms in 1-10 kW Two-Stroke Internal Combustion Engines," *SAE International Journal of Engines*, 2017.
- [8] J. R. Blantin, J. K. Ausserer, M. Polanka, P. J. Litke, and J. Baranski "Power Loss Pathways and Energy Balance of a Small Four-Stroke Internal Combustion Engine," AIAA SciTech, Grapevine, TX, 2017.
- [9] S. Menon and C. Cadou, "Scaling of Miniature Piston-Engine Performance Part 1: Overall Engine Performance," *Journal of Propulsion and Power*, vol. 29, pp. 774-787, July-August 2013, doi: 10.2514/1.B34638.
- [10] J. K. Ausserer, "The Scaling Of Loss Pathways And Heat Transfer In Small Scale Internal Combustion Engines," Ph.D. Dissertation, Department of Aeronautics and Astronautics, Air Force Institute Of Technology, Wright-Patterson Air Force Base, Ohio, 2016.
- [11] J. B. Heywood, *Internal Combustion Engine Fundamentals*. New York: McGraw-Hill, 1988.
- [12] C. F. Taylor, *The Internal Combustion Engine in Theory and Practice: Volume 1: Thermodynamics, Fluid Flow, Performance*, 2nd, revised ed. vol. 1: First MIT Press, 1985.
- [13] W. W. Pulkrabek, *Engineering Fundamentals of the Internal Combustion Engine*. Upper Sadle River, New Jersey: Prentice Hall, 1997.
- [14] C. A. Amann, "Cylinder-Pressure Measurement and Its Use in Engine Research," SAE Paper 852067, 1985.
- [15] J. K. Ausserer, P. J. Litke, J.-R. Groenewegen, A. Rowton, M. Polanka, and K. Grinstead, "Development of Test Bench and Characterization of Performance in Small Internal Combustion Engines," 19th Small Engine Technology Conference, Taipei, Taiwan, SAE Technical Paper 2013-32-9036, 2013, doi: 10.4271/2013-32-9036.

- [16] M. L. Smith, J. Owen, E. Buxton and K. Y. Tang, "Study of Miniature Engine-Generator Sets," The Ohio State University Research Foundation, 1956.
- [17] I. N. Bishop, "Effect of Design Variables on Friction and Economy," *SAE Transactions*, vol. 73, pp. 334-358, SAE Technical Paper 640807, 1 January 1965, doi: 10.4271/640807.
- [18] D. Gierke. (1973) Part III: Dynamometer: An Engine Performance Analysis. *Flying Models*. pp. 38-47.
- [19] D. Gierke. (1973) Part II: Dynamometer: An Engine Performance Analysis. *Flying Models*. pp. 43-51.
- [20] D. Gierke. (1973) Part I: Dynamometer: An Engine Performance Analysis. *Flying Models*. pp. 21-25.
- [21] J. D. McCullough, "Engine Cylinder Pressure Measurements," *SAE Transactions*, vol. 61, p. 17, 1963.
- [22] W. L. Brown, "Methods for Evaluating Requirements and Errors in Cylinder Pressure Measurement," presented at the Automotive Engineering Conference, Detroit, MI, SAE Technical Paper 670008, 1967, doi: 10.4271/670008.
- [23] W. L. Brown, "The Caterpillar IMEP Meter and Engine Friction," presented at the Industrial Automotive Engineering Conference, Detroit, MI, 730150, 1973, doi: 10.4271/730150.
- [24] R. S. Benson and R. Pick, "Recent Advances in Internal Combustion Engine Instrumentation with Particular Reference to High-Speed Data Acquisition and Automated Test Bed," SAE Technical Paper 740695, 1974, doi: 10.4271/740695.
- [25] R. V. Fisher and J. P. Macey, "Digital Data Acquisition with Emphasis on Measuring Pressure Synchronously with Crank Angle," presented at the Automotive Engineering Congress and Exposition, Detroit, MI, 750028, 1975, doi: 10.4271/750028.
- [26] D. R. Lancaster, R. B. Krieger, and J. H. Lienesch, "Measurement and Analysis of Engine Pressure Data," presented at the Automotive Engineering Congress and Exposition, Detroit, MI, SAE Technical Paper 750026, 1975, doi: 10.4271/750026.
- [27] G. P. Blair, "Prediction of Two-Cycle Engine Performance Characteristics," *SAE Transactions*, vol. 85, SAE Technical Paper 760645, 1 February 1976, doi: 10.4271/760645.
- [28] G. P. Blair and M. C. Ashe, "The Unsteady Gas Exchange Characteristics of a Two-Cycle Engine," presented at the Off-Highway Vehicle Meeting, Milwaukee, WI, SAE Technical Paper 760644, 1976, doi: 10.4271/760644.
- [29] G. A. Lavoie and P. N. Blumberg, "A Fundamental Model for Prediction Fuel Consumption, NO_x and HC Emissions of the Conventional Spark-Ignited Engine," *Combustion Science and Technology*, vol. 21, p. 34, 6 July 1979 1980, doi: 0010-2202/80/2105-0225.
- [30] C. Cadou, S. Menon, N. Moulton, and T. Leach, "Performance Scaling and Measurement for Hydrocarbon-Fueled Engines with Mass Less Than 1kg," presented at the AIAA's 1st Technical Conference and Workshop on Unmanned Aerospace Vehicles, Portsmouth, Virginia, 2002.

- [31] C. Cadou, N. Moulton, and S. Menon, "Performance Measurement and Scaling in Small Internal Combustion Engines," 41st Aerospace Sciences and Exhibit, Reno, NV, 2003.
- [32] C. Cadou and S. Menon, "Scaling of Losses in Small IC Aero Engines with Engine Size," 42nd AIAA Aerospace Sciences Meeting and Exhibit, Reno, NV, 2004.
- [33] S. Menon and C. Cadou, "Scaling of Miniature Piston-Engine Performance Part 2: Energy Losses," *Journal of Propulsion and Power*, vol. 29, pp. 788-799, July-August 2013, doi: 10.2514/1.B34639.
- [34] J. B. Heywood and E. Sher, *The Two-Stroke Cycle Engine*. New York: Taylor & Francis Group, 1999.
- [35] S. Menon and C. Cadou, "Investigation of Combustion Processes in Miniature Internal Combustion Engines," *Combustion Science and Technology*, vol. 185, pp. 1667-1695, 2013, doi: 10.1080/00102202.2013.829720.
- [36] J.-R. J. Groenewegen, "The Performance and Emissions Characteristics of Heavy Fuels in a Small Spark Ignition Engine," M.S. in Mechanical Engineering, School of Engineering, University of Dayton, Dayton, OH, 2011.
- [37] J.-R. J. Groenewegen, S. S. Sidhu, J. L. Hoke, C. W. Wilson, and P. J. Litke, "The Performance and Emissions Effects of Utilizing Heavy Fuels and Algae Based Biodiesel in a Port-Fuel-Injected Small Spark Ignition Internal Combustion Engine," 47th AIAA/ASME/SAE/ASEE Joint Propulsion Conference & Exhibit, San Diego, California, 2011.
- [38] J. Baranski, "Experimental Investigation of Octane Requirement in a Turbocharged Spark-Ignition Engine," M.S. in Mechanical Engineering, School of Engineering, University of Dayton, Dayton, Ohio, 2013.
- [39] J. Baranski, E. Anderson, K. Grinstead, J. Hoke, and P. J. Litke, "Control of Fuel Octane for Knock Mitigation on a Dual-Fuel Spark-Ignition Engine," SAE World Congress, Detroit, Michigan, SAE Technical Paper 2013-01-0320, 2013, doi: 10.4271/2013-01-0320.
- [40] J. A. Rittenhouse, A. K. Rowton, J. K. Ausserer, and M. D. Polanka, "Preliminary Thermal Loss Measurements for a Small Internal Combustion Engine," SciTech 2014, National Harbor, MD, AIAA 2014-0529, 2014, doi: 10.2514/6.2014-0529.
- [41] K. P. Horn, J. K. Ausserer, M. D. Polanka, P. J. Litke, and K. D. Grinstead, "Dynamic Friction Measurements on a Small Engine Test Bench," SciTech 2015, Kissimmee, Florida, AIAA 2015-1473, 2015.
- [42] J. A. Rittenhouse, "Thermal Loss Determination for a Small Internal Combustion Engine," M.S. in Aeronautical Engineering M.S. in Aeronautical Engineering, Department of Aeronautics and Astronautics, Air Force Institute of Technology, WPAFB, Ohio, 2014.
- [43] National Institute of Standards and Technology. NIST Chemistry WebBook [Online]. Available: <http://webbook.nist.gov/chemistry/>
- [44] J. K. Ausserer, K. Horn, M. Polanka, Paul Litke, and Kieth Grinstead, "Quantification of Short-Circuiting and Trapping Efficiency in a Small Internal

- Combustion Engine by GC-MS and GC-TCD," 2015 SAE Small Engine Technology Conference, Osaka, Japan, 2015.
- [45] SAE International, "Surface Vehicle Information Report," in *Instrumentation and Techniques for Exhaust Gas Emissions Measurements* vol. J254, ed: SAE International, 2011.
- [46] R. J. Moffat, "Describing the Uncertainties in Experimental Results," *Experimental Thermal and Fluid Science*, pp. 3-17, 1988.
- [47] R. J. Moffat, "Contributions to the Theory of Single-Sample Uncertainty Analysis," *Journal of Fluids Engineering*, vol. 104, pp. 250-260, 1982.
- [48] Honda Motor Co., "Honda GX120 Horizontal Shaft Gasoline Engine," ed. www.honda-engines-eu.com, 2014.
- [49] A. K. Rowton, J. K. Ausserer, K. D. Grinstead, P. J. Litke, and M. D. Polanka, "Measuring Scaling Effects in Small Two-Stroke Internal Combustion Engines," 2014 Small Engine Technology Conference & Exposition, Pisa, Italy, SAE Technical Paper 2014-32-0010, 2014, doi: 20.4271/2014-32-0010.
- [50] A. K. Rowton, "Measuring Scaling Effects in Small Two-Stroke Internal Combustion Engines," M.S. in Aeronautical Engineering, Department of Aeronautical and Astronautical Engineering, Air Force Institute of Technology, WPAFB, Ohio, 2014.
- [51] S. R. Turns, *An Introduction to Combustion: Concept and Applications*: McGraw Hill, 2000.
- [52] K. Aoi, K. Nomura, and H. Matsuzaka, "Optimization of Multi-Valve Four Cycle Engine Design-The Benefit of Five-Valve Technology," SAE Technical Paper 860032, 1986, doi: 10.4271/860032.
- [53] Honda Motor Co., "Honda GX160 Horizontal Shaft Gasoline Engine," ed. www.honda-engines-eu.com, 2014.
- [54] Honda Motor Co., "Honda GX200 Horizontal Shaft Gasoline Engine," ed. www.honda-engines-eu.com, 2014.

REPORT DOCUMENTATION PAGE

Form Approved
OMB No. 0704-0188

Public reporting burden for this collection of information is estimated to average 1 hour per response, including the time for reviewing instructions, searching existing data sources, gathering and maintaining the data needed, and completing and reviewing this collection of information. Send comments regarding this burden estimate or any other aspect of this collection of information, including suggestions for reducing this burden to Department of Defense, Washington Headquarters Services, Directorate for Information Operations and Reports (0704-0188), 1215 Jefferson Davis Highway, Suite 1204, Arlington, VA 22202-4302. Respondents should be aware that notwithstanding any other provision of law, no person shall be subject to any penalty for failing to comply with a collection of information if it does not display a currently valid OMB control number. **PLEASE DO NOT RETURN YOUR FORM TO THE ABOVE ADDRESS.**

1. REPORT DATE (DD-MM-YYYY) 15-09-2017		2. REPORT TYPE Thesis		3. DATES COVERED (From - To) Sept 2015 – Sept 2017	
4. TITLE AND SUBTITLE CHARACTERIZATION AND SCALING STUDY OF ENERGY PATHWAYS IN SMALL FOUR-STROKE INTERNAL COMBUSTION ENGINES				5a. CONTRACT NUMBER	
				5b. GRANT NUMBER	
				5c. PROGRAM ELEMENT NUMBER	
6. AUTHOR(S) Blantin, Jason R., Capt, USAF				5d. PROJECT NUMBER	
				5e. TASK NUMBER	
				5f. WORK UNIT NUMBER	
7. PERFORMING ORGANIZATION NAME(S) AND ADDRESS(ES) Air Force Institute of Technology Graduate School of Engineering and Management (AFIT/ENY) 2950 Hobson Way, Building 640 WPAFB OH 45433-8865				8. PERFORMING ORGANIZATION REPORT NUMBER AFIT-ENY-MS-17-S-054	
9. SPONSORING / MONITORING AGENCY NAME(S) AND ADDRESS(ES) Air Force Research Laboratory, Aerospace Systems Directorate 2130 8 th St. WPAFB, OH 45433 937-904-4807 ATTN: Fred Schauer				10. SPONSOR/MONITOR'S ACRONYM(S)	
				11. SPONSOR/MONITOR'S REPORT NUMBER(S)	
12. DISTRIBUTION / AVAILABILITY STATEMENT DISTRUBTION STATEMENT A. APPROVED FOR PUBLIC RELEASE; DISTRIBUTION UNLIMITED.					
13. SUPPLEMENTARY NOTES This material is declared a work of the U.S. Government and is not subject to copyright protection in the United States.					
14. ABSTRACT A study of the efficiency and energy losses of a selection of five small (40 – 200 cm ³ displacement) single cylinder, four-stroke engines was accomplished. The study was performed as part of a larger effort to improve the range and endurance of small internal combustion engines (ICE) that power Group II Unmanned Aerial Vehicles (UAVs). Little is known about the performance, efficiency, and allocation of energy losses for four-stroke ICEs in this size range. The goal of the study was to characterize these parameters for use in future research efforts. Three research objectives were developed to guide the study contained herein. The first objective was to reliably measure the brake power output of each engine and compare the measurements to the manufacturer's advertised power ratings. The second objective was to perform an energy balance, experimentally measuring the fuel energy entering the system (engine), and all of the energy exiting the system. Energy exiting the system was categorized as useable energy (brake power), or energy losses due to exhaust sensible enthalpy, thermal losses, or incomplete combustion. The third objective (which encompassed the first two) was to perform as series of parametric sweeps on the engines, examining the effect of varying engine speed, equivalence ratio, combustion phasing, cylinder head temperature, and throttle position. The characterization data from the five engines was then used to develop a set of correlations that could be used to predict brake mean effective pressure (BMEP), fuel conversion efficiency (η_f), exhaust sensible enthalpy losses, thermal (cooling load) losses, and incomplete combustion losses as a percentage of fuel energy for small four-stroke engines with displacement volumes of 40 – 200 cm ³ . Accurate correlations for this size class currently do not exist in the literature.					
15. SUBJECT TERMS internal combustion engine, scaling, loss pathways					
16. SECURITY CLASSIFICATION OF:			17. LIMITATION OF ABSTRACT UU	18. NUMBER OF PAGES 243	19a. NAME OF RESPONSIBLE PERSON Marc D. Polanka, AFIT/ENY
a. REPORT U	b. ABSTRACT U	c. THIS PAGE U			19b. TELEPHONE NUMBER (include area code) (937) 255-6565, ext 4714 (COMM)